N° d'ordre : 332/21

Université Sultan Moulay Slimane
Faculté des Sciences et Techniques
Beni Mellal

Centre d'Études Doctorales : Sciences et Techniques
Formation Doctorale : **Ressources Naturelles, Environnement Et Santé**

THÈSE

Présentée par
Hamza OUATIKI

Pour l'obtention du grade de
DOCTEUR

Spécialité **: Géologie**
Option **: Hydrologie et Télédétection**

Large Scale Remote Sensing Spatial Rainfall Data for Water Resources Monitoring and Modeling over the Oum Er-Rbia River Basin

Soutenue le Samedi 03 Avril 2021 à 9h devant la commission d'examen:

Abdelghani CHEHBOUNI	Directeur de Recherche, IRD Toulouse, France	Président
Mohammed El Mehdi SAIDI	Professeur, Fac. Sc.et Techniques - Guéliz, Marrakech, Maroc	Rapporteur
Samira KRIMISSA	Professeur, Fac. Polydisciplinaire, Béni Mellal, Maroc	Rapporteur
Jalal MOUSTADRAF	Professeur, Fac. Polydisciplinaire, Khouribga, Maroc	Rapporteur
Carmen DE JONG	Professeur, Fac. de géographie et d'aménagement, Strasbourg, France	Examinateur
Ahmed BARAKAT	Professeur, Fac. Sc. et Techniques, Béni Mellal, Maroc	Examinateur
Abdelghani BOUDHAR	Professeur, Fac. Sc. et Techniques, Beni Mellal, Maroc	Directeur de thèse
Aziz OUHINOU	Professeur, Fac. Sc. et Techniques, Beni Mellal, Maroc	Co-Directeur

Thesis Presentation Sheet

Author: **Hamza OUATIKI**

Water Resources Management and Valorization and Remote Sensing Team (GEVARET), Faculty of Sciences and Technics, Sultan Moulay Slimane University, Beni Mellal 23000, Morocco;

E-mail: h.ouatiki@usms.ma

Title: Large Scale Remote Sensing Spatial Rainfall Data for Water Resources Monitoring and Modeling over the Oum Er-Rbia River Basin

Specialty: Hydrology & Remote Sensing

Supervisor: **Dr. Abdelghani BOUDHAR**

Water Resources Management and Valorization and Remote Sensing Team (GEVARET), Faculty of Sciences and Technics, Sultan Moulay Slimane University, Beni Mellal 23000, Morocco;

Co-Supervisor: **Dr. Aziz OUHINOU**

Department of Mathematics, Faculty of Sciences and Technics, Sultan Moulay Slimane University, Beni Mellal 23000, Morocco;

Articles:

- **Hamza Ouatiki**, Abdelghani Boudhar, Yves Tramblay, Lionel Jarlan, Tarik Benabdelouhab, Lahoucine Hanich, M. El Meslouhi, and Abdelghani Chehbouni. 2017.

"Evaluation of TRMM 3B42 V7 Rainfall Product over the Oum Er Rbia Watershed in Morocco." Climate 5 (1): 1–17. https://doi.org/10.3390/cli5010001.

- **Hamza Ouatiki**, Abdelghani Boudhar, Aziz Ouhinou, Abdelkrim Arioua, Mohammed Hssaisoune, Hafsa Bouamri, and Tarik Benabdelouahab. 2019. "Trend Analysis of Rainfall and Drought over the Oum Er-Rbia River Basin in Morocco during 1970–2010." Arabian Journal of Geosciences 12 (128): 1–11. https://doi.org/10.1007/s12517-019-4300-9.

- Hadria, Rachid, Abdelghani Boudhar, **Hamza Ouatiki**, Youssef Lebrini, Loubna Elmansouri, Fouad Gadouali, Hayat Lionboui, and Tarik Benabdelouahab. 2019. "Combining Use of TRMM and Ground Observations of Annual Precipitations for Meteorological Drought Trends Monitoring in Morocco Combining Use of TRMM and Ground Observations of Annual Precipitations for Meteorological Drought Trends Monitoring in Morocco." American Journal of Remote Sensing 7 (2): 25–34. https://doi.org/10.11648/j.ajrs.20190702.11.

- Rachid Hadria, Tarik Benabdelouahab, Loubna Elmansouri, Fouad Gadouali, **Hamza Ouatiki**, Youssef Lebrini, Abdelghani Boudhar, Adil Salhi, and Hayat Lionboui. 2019. "Derivation of Air Temperature of Agricultural Areas of Morocco from Remotely Land Surface Temperature Based on the Updated Köppen-Geiger Climate Classification." Modeling Earth Systems and Environment 5 (4): 1883–92. https://doi.org/10.1007/s40808-019-00645-4.

- Abdelghani Boudhar, **Hamza Ouatiki**, Hafsa Bouamri, Youssef Lebrini, Ismail Karaoui, Mohammed Hssaisoune, Abdelkrim Arioua, and Tarik Benabdelouahab. 2020. "Hydrological Response to Snow Cover Changes Using Remote Sensing over the Oum Er Rbia Upstream Basin, Morocco." In Mapping and Spatial Analysis of Socio-Economic and Environmental Indicators for Sustainable Development, edited by N. Rebai and M. Mastere, 95–102. Cham, Switzerland: Springer, Cham. https://doi.org/10.1007/978-3-030-21166-0_9.

- **Hamza Ouatiki**, Abdelghani Boudhar, Aziz Ouhinou, Abdelaziz Beljadid, Marc Leblanc, and Abdelghani Chehbouni. 2020. "Sensitivity and Interdependency Analysis of the HBV

Conceptual Model Parameters in a Semi-Arid." Water 12 (9): 2440. https://doi.org/10.3390/w12092440.

Presentations:

- Poster presentation: Estimation des précipitations à partir du produit radar TRMM à l'échelle du bassin versant d'Oum-Er-Rbia. In "Forum International sur les Changements climatiques ATLASCop : La lutte contre le changement climatique, vecteur de développement économique et social durable et intégré" . Beni Mellal, Morocco, 18th & 19th October 2016.

- Poster presentation: Les estimations des précipitations par TRMM en amont du Bassin Versant d'Oum Er-Rbia. In "Congrès international Eau Déchets & Environnement (EDE6)". Université Sultan Moulay Slimane University, Faculty of Sciences and Techniques, Beni Mellal, Morocco, from 12th to 14th December 2017.

- Oral presentation: Importance of remote sensing to estimate rainfall over a scarce data basin in Morocco. In the 4th Remote Sensing and Hydrology Symposium (RSHS'18). Cordoba, Spain, from 8th to 10th May 2018.

- Oral presentation: Apport des issues de la télédétection spatiale pour le suivie de la variabilité climatique du Maroc. In "la 2ème édition du congrès international sur Les zones humides - Bassins versants et le développement local". Nador, Morocco, from 25th to 27th April 2019.

- Oral presentation: Elaboration d'une base de données climatique de la plaine de tarifa et analyse de la variabilité des pluies dans la plaine entre 1992 et 2017. In "la 2ème édition du congrès international sur Les zones humides - Bassins versants et le développement local". Nador, Morocco, from 25th to 27th April 2019.

- Oral presentation: Rainfall trends and streamflow simulation over Oum Er-Rbia river basin in Morocco using remote sensing rainfall products. In "the 1st summer school on Hydro-informatics". Mohammed IV Polytechnic University, Benguerir, Morocco, from 8th to 12th July 2019.

Acknowledgment

First of all, I would like to thank my thesis supervisor, Professor Abdelghani Boudhar, for the confidence he has shown in me, for his support and constructive instructions throughout my thesis. His availability and invaluable support, humanly and scientifically, made this work possible.

I would also like to thank Professor Aziz Ouhinou, my co-supervisor, for his contribution to the success of this work.

I thank the Tadla Regional Office for Agricultural Development, The IMPETUS program, and the Oum Er Rbia Hydraulic Basin Agency for providing me with the necessary hydroclimatic data to carry out this work.

I express my gratitude to all spatial agencies around the world to NASA for providing free access to a large part of their satellite data.

My sincere thanks also go to the members of the jury for the interest they gave to this work by agreeing to examine it and enrich it with their comments.

Thanks to all members of the GEVARET team for their help and support during all the years that I have spent with the team.

I would like to especially thank my family who gave me the freedom to act and the wisdom to inlight my way. I thank them for encouraging me to pursue this adventure and for their support, morally and financially.

Abstract

In the context of water scarcity in Morocco, the proper management of water resources is becoming a national priority. However, the strong spatiotemporal fluctuation of rainfall, which characterizes the OERB (Oum Er-Rbia River Basin), combined with the sparsity of the RG (Rain Gauge) networks constitute real constraints for water resources management. In the last decades, several satellite-based rainfall estimates have become available. These estimates can be a potential source of rainfall data over poorly gauged watersheds. Therefore, the main aim of this work is to investigate the suitability of eight SRP (Spatial Rainfall Product) datasets (ARC, CHIRPSp25, CHIRPSp5, CMORPH-CRT v1, GPM IMERG v6, PERSIANN-CDR, RFE, and TRMM 3B42 v7) for water resources monitoring and modeling over the OERB. The SRP estimates were evaluated at daily and monthly time scales adopting GC-based (Grid cell) and hydrologic modeling evaluation approaches. The HBV (Hydrologiska Byråns Vattenbalansavedlning) conceptual rainfall-runoff model was investigated over the Ait Ouchene sub-watershed using a set of nine years (2001 – 2009) of hydroclimatic measurements and remotely sensed SCA (Snow Cover Area). The results showed that the HBV model can fairly reproduce the observed daily streamflow in the Ait Ouchene sub-watershed with variable reliability. Overall, the changes in hydroclimatic conditions seemed to actuate the interdependency of the model parameters. The latter were found to combine either to shrink the storage capacity of the model's reservoirs under extremely high peak flows or to enlarge them under overestimated water supply, mainly provoked by abundant snow cover. Regarding the SRPs evaluation, the rainfall estimates performed poorly at the daily time scale for both direct comparison and hydrologic modeling approaches. While most PCCs (Pearson Correlation Coefficients) were below 0.5, the SRPs performance in hydrologic modeling varied depending on years and products. Generally, the SRPs yielded better streamflow simulations than the RG data obtained from the unevenly distributed network of Tilouguite sub-watershed. At the monthly time scale, the SRPs correlated better with the RGs, except in the mountainous region, with the precedence of IMERG (with a short-term record) and PERSIANN (with a long-term

record) over the remaining products. Still, the monthly SRP estimates were significantly biased, particularly large rainfall totals were frequently underestimated for most SRPs. Remarkable improvement in the SRPs performance was observed after bias correction techniques were applied. The latter yielded close results, with a slight prevalence of the CDF (Cumulative Distribution Function) over the LS (Linear Scaling) and SLR (Simple Linear Regression) techniques. However, LS and SLR appeared to be more suitable than CDF over the OERB, as their performance was more spatially consistent after validation.

Keywords: Oum Er-Rbia, Semi-Arid, Trend, Hydrologic Modeling, HBV model, Sensitivity, Interdependency, Spatial Rainfall Products, Bias Correction.

ملخص الرسالة

في سياق ندرة المياه التي يعرفها المغرب، أصبحت الإدارة السليمة للموارد المائية أولوية وطنية. لكن التقلبات الزمانية والمكانية القوية التي تميز هطول الأمطار على مستوى الحوض المائي لنهر ام الربيع، جنبًا إلى جنب مع محدودية التغطية المجالية لشبكات القياس يشكلان قيودًا حقيقية فيما يخص سيرورة عملية إدارة موارد المياه. خلال العقود الماضية الاخيرة، أصبحت العديد من قياسات الأمطار الشبكية، التي تعتمد على بيانات الأقمار الاصطناعية، متاحة للعموم بشكل مجاني. يمكن لهذه القياسات أن تشكل مصدرا مهما لبيانات الأمطار على مستوى الأحواض التي تعاني من محدودية شبكة محطات القياس. في هذا الصدد، إن الهدف الرئيسي من هذا العمل هو التحقق من مدى ملاءمة مجموعة من البيانات الشبكية لقياسات الأمطار (ARC، CHIRPSp25، CHIRPSp5، CMORPH-CRT v1، GPM IMERG v6، PERSIANN-CDR، RFE، TRMM 3B42 v7)لرصد موارد المياه على مستوى النطاق الجغرافي للحوض المائي المذكور أعلاه. قمنا بتقييم هذه البيانات باعتماد نهج أول قائم على المقارنة المباشرة بين قياسات الامطار المقدرة وتلك المسجلة عن طريق محطات القياس الأرضية، ونهج ثاني قائم على النمذجة الهيدرولوجية.

بعد ذلك، قمنا باختبار نموذج تدفق مياه الامطار "HBV" على مستوى مستجمع المياه الفرعي آيت أوشن، وذلك بالاعتماد على ما يقارب تسع سنوات (2001 - 2009) من القياسات الهيدرومناخية وبيانات ال "SCA" المقاسة عن طريق تقنية الاستشعار عن بعد. أظهرت النتائج على أن النموذج الهيدرولوجي "HBV" قادر الى حد ما على محاكات التدفق اليومي للمجرى المائي لمستجمع آيت أوشن، بدقة تختلف من سنة إلى أخرى. بشكل عام، تم تبيان أن لتغيرات الظروف الهيدرومناخية دور مهم في تحفيز الاعتماد المتبادل بين معاملات النموذج. لقد وجدنا أن هذه الأخيرة تتفاعل فيما بينها إما لتقليص سعة خزانات النموذج تحت تأثير وجود تدفقات ذروة مهمة، أو لتوسيعها في ظل إمدادات مياه مبالغ فيها الناتجة بشكل أساسي عن الغطاء الثلجي. فيما يتعلق بتقييم بيانات ال "SRPs"، أشارت النتائج إلى أن أداء مختلف تقديرات الامطار كان ضعيفًا على النطاق الزمني اليومي باعتبار مقاربتي المقارنة المباشرة والنمذجة الهيدرولوجية. بينما كانت أغلب ال "PCCs" المحصل عليها أصغر من 0.5، عندما تم استخدامهم في معايرة نموذج ال "HBV"، بدا أداء ال "SRPs" في النموذج الهيدرولوجية غير مستقر ويتغير باختلاف السنوات. بشكل عام، أسفرت بيانات ال "SRPs" عن إنتاج محاكاة لتدفق المجاري المائية أفضل من تلك التي أسفرت عنها بيانات ال "RG" على مستوى مستجمع المياه الفرعي تيلوكيت، حيث شبكة القياس موزعة بشكل غير متساو. على مستوى النطاق الزمني الشهري كان مستوى التوافق بين مصدري البيانات أقوى. من بين جميع ال "SRPs"، كان أداء بيانات "IMERG" و"PERSIANN" الأفضل على مستوى الحوض المائي لنهر أم الربيع. ومع ذلك، فإن تقديرات الأمطار الشهرية تحوي تحيزا كبيرا بالمقارنة مع بيانات ال "RGs"، ولا سيما عندما يتعلق الأمر بمستويات الأمطار المهمة. بعد تطبيق تقنيات تصحيح التحيز، أظهرت النتائج

تحسنا ملحوظا في التقديرات الشهرية لل "SRPs". كانت النتائج المحصل عليها من طرف مختلف تقنيات التصحيح متقاربة مع تفوق نسبي لتقنية ال "CDF" مقارنتا بتقنيتي ال "LS" و"SLR". بالرغم من ذلك، بدت تقنيتي ال "LS" و "SLR" أكثر ملاءمة من نظيرتها ال "CDF" على مستوى الحوض المائي لنهر أم الربيع، حيث كان أداؤهما أكثر اتساقًا من الناحية المكانية بعد عملة التحقق.

الكلمات المفتاحية: أم الربيع، شبه قاحلة، اتجاه، النمذجة الهيدرولوجية، HBV، تحليل الحساسية، تحليل الاعتماد المتبادل، منتجات هطول الأمطار المكانية، تصحيح التحيز

Résumé

Dans le contexte de pénurie d'eau au Maroc, la bonne gestion des ressources en eau devient une priorité nationale. Cependant, la forte fluctuation spatio-temporelle des précipitations, qui caractérise l'OERB, combiné à la disponibilité limitée des réseaux de mesure constituent de réelles contraintes pour la gestion de ces ressources. Au cours des dernières décennies, plusieurs produits d'estimation de la pluviométrie distribuée, à la base des données satellitaires, sont devenus disponibles. Ces produits peuvent être une source potentielle de données pluviométriques à l'échelle des bassins mal ou non gaugés. En effet, l'objectif principal de ce travail est d'étudier la pertinence de huit données pluviométriques distribuées (ARC, CHIRPSp25, CHIRPSp5, CMORPH-CRT v1, GPM IMERG v6, PERSIANN-CDR, RFE, et TRMM 3B42 v7) pour la surveillance et ma modélisation des ressources en eau à l'échelle de l'OERB. Ces données ont été évaluées à différentes échelles de temps en adoptant une première approche qui repose sur la comparaison directe entre les données issues des différents produits et les mesures in situ (pluviomètres et la moyenne régionale), et une deuxième qui se base sur la modélisation hydrologique.

En outre, le modèle conceptuel pluie-débit HBV a été investigué sur le sous-bassin versant de l'Ait Ouchene en utilisant un ensemble de neuf ans (2001 – 2009) de mesures hydro-climatiques et de "SCA" mesuré par télédétection. Les résultats montraient que le modèle HBV peut reproduire le débit journalier observé à l'échelle du sous-bassin d'Ait Ouchene avec une fiabilité variable. Dans l'ensemble, les changements des conditions hydro-climatiques peuvent stimuler l'interdépendance entre les paramètres du modèle. Ces derniers se combinent soit pour réduire la capacité de stockage des réservoirs du modèle en cas de débits de pointe extrêmement élevés, soit pour les augmenter en cas d'approvisionnement en eau surestimé, principalement provoqué par une couverture neigeuse abondante. En ce qui concerne l'évaluation des SRPs, les résultats indiquaient que les estimations des SRPs étaient peu performantes à l'échelle temporelle quotidienne, tant pour

la comparaison directe que pour la modélisation hydrologique. Alors que la plupart des PCCs étaient inférieurs à 0.5, les performances des SRP en modélisation hydrologique variaient en fonction des années et des produits. En général, les SRPs ont donné une meilleure simulation du débit que les données RG sur le sous-bassin Tilouguite, où le réseau de jaugeage est inégalement réparti. A l'échelle mensuelle, les SRPs se sont révélées bien corrélées avec les observations des stations, sauf dans la partie montagneuse, avec une précédence d'IMERG et PERSIANN contre le reste des produits. Néanmoins, les estimations mensuelles des SRPs étaient significativement biaisées, en particulier les grands totaux des pluies étaient fréquemment sous-estimés pour la plupart des SRPs. Une amélioration remarquable des performances des SRPs a été observée après l'application des techniques de correction du biais En outre, ces dernières ont montré des très proches. La CDF a relativement surpassé les techniques LS et SLR. Cependant, LS et SLR semblent être plus adaptés à l'OERB, vue la cohérentes de leurs performances dans l'espace après validation.

Mots-clés : Oum Er-Rbia, Semi-Aride, Tendance, Modélisation Hydrologique, , Pluie-Débit, Modèle HBV, Sensibilité, Interdépendance, Produits Spatiaux de Pluie, Correction du Biais

Table of Contents

Acronyms

ABHOER	Agence du Bassin Hydrolique de l'Oum Er-Rbia (the Oum Er Rbia Hydraulic Basin Agency)
AMSR-E	Advanced Microwave Scanning Radiometer for the Earth Observing System
AMSU-B	Advanced Microwave Sounding Unit-B
ARC	Africa Rainfall Climatology
ATMS	The Advanced Technology Microwave Sounder
CCD	Cold Cloud Duration
CDF	Cumulative Distribution Function
CERES	Clouds and the Earth's Radiant Energy System
CFS	Coupled Forecast System
CHC	Climate Hazards Center
CHIRPS	Climate Hazards group Infrared Precipitation with Stations
CHPclim	Climate Hazards group Precipitation climatology
CHRS	Center for Hydrometeorology and Remote Sensing
CMORPH	Climate Prediction Center Morphing Technique
CMORPH-CRT	CPC Morphing Technique-bias corrected
CMORPH-KF	CPC Morphing-Kalman Filter
CPC	Climate Prediction Center
CSR	Center for Space Research
DLR	Deutsche Forschungsanstalt für Luft und Raumfahrt/German Research Center for Aeronautics and Space
DMSP	Defense Meteorological Satellite Program
DPR	Dual-frequency Precipitation Radar
FAO	Agriculture Organization of the United Nations
FEWS-NET	Famine Early Warning Systems Network
FY	Fen-Yung
GC	Grid-cell
GCOM-W1	Global Change Observation Mission - Water 1
GEO	Geostationary
GEOS	Geostationary Operational Environmental Satellite
GEOS-FP	Goddard Earth Observing System model - Forward Processing
GFZ	German Research Centre for Geosciences
GHCN	Global Historical Climate Network
GIS	Geographic Information System
GMI	GPM Microwave Imager

GMS	Geostationary Meteorological Satellite
GPCP	Global Precipitation Climatology Project
GPI	Global Precipitation Index
GPM	Global Precipitation Measurement
GPROF	Goddard PROFiling
GPS	Global Positioning System
GRACE	Gravity Recovery and Climate Experiment
GRACE-FO	Gravity Recovery and Climate Experiment Follow-on
GridSat	Gridded Satellite infrared data
GSFC	Goddard Space Flight Center
GSOD	Global Summary of the Day
GTS	World Meteorological Organization's Global Telecommunication System
GWS	Ground Water Storage
HBV	Hydrologiska Byråns Vattenbalansavedlning
IMERG	Integrated Multi-satellitE Retrievals for GPM
IFA	Insignificant False Alarms
IR	InfraRed
IRWIN	InfraRed WINdow
ISBA	Interactions between Soil, Biosphere, and Atmosphere
ISCCP	International Satellite Cloud Climatology Project
JAXA	Japan Aerospace eXploration Agency
JMA	Japan Meteorological Agency
JPL	Jet Propulsion Laboratory
LDAS	Land Data Assimilation Systems
LEO	Low Earth Orbit
LIS	Lightning Imaging Sensor
LS	Linear Scaling
LST	Land Surface Temperature
MATLAB	MATrix LABoratory
MERRA-2	Modern Era Retrospective Reanalysis 2
Meteosat	METEOrological SATellite
MetOp	Operational Meteorological satellite
MHS	Microwave Humidity Sounders
MODIS	Moderate Resolution Imaging Spectroradiometer
MSPPS	Microwave Surface and Precipitation Products System
MTSat	Multi-functional Transport Satellite
MWCOMB	COMBined MicroWave
NASA	National Aeronautics and Space Administration
NASDA	National Space Development Agency of Japan
NCDC	National Climatic Data Center
NDSI	Normalized Difference Snow Index
NESDIS	National Environmental Satellite Data and Information Service

NMA	National Meteorological Agencies
NOAA	National Oceanic and Atmospheric Administration
NOAA-CPC	NOAA Climate Prediction Center
NOHRSC	National Operational Hydrologic Remote Sensing Center
OERB	Oum Er-Rbia River Basin
ORMVAT	L'Office Régional de Mise en Valeur Agricole du Tadla (The Tadla Regional Office for Agricultural Development)
PCC	Pearson Correlation Coefficient
PERSIANN-CCS	Precipitation Estimation from Remotely Sensed Information using Artificial Neural Networks – Cloud Classification System
PERSIANN-CDR	Precipitation Estimation from Remotely Sensed Information using Artificial Neural Networks – Climate Data Record
PMM	Precipitation Measurement Missions
PMW	Passive Microwave
PPS	Precipitation Processing System
PR	Precipitation Radar
PRPS	Precipitation Retrieval and Profiling Scheme
RFE	Rainfall Estimator
RG	Rain Gauge
SAPHIR	multi-channel microwave humidity sounder/Sondeur Atmosphérique du Profil d'Humidité Intertropicale par Radiométrie
SASSCAL	Southern African Science Service Centre for Climate Change and Adaptive Land Management
SCA	Snow Cover Area
SFA	Significant False Alarms
SLR	Simple Linear Regression
SM	Soil Moisture
SNPP	Suomi National Polar-orbiting Partnership
SPI	Standardized Precipitation Index
SRM	Snowmelt Runoff Model
SRP	Spatial Rainfall Product
SSMI	Special Sensor Microwave Imager
SSMIS	Special Sensor Microwave Imager/Sounder
SURFEX	Surface Externalisée
TLR	Temperature Lapse Rate
TMI	TRMM Microwave Imager
TMPA	TRMM Multi-satellite Precipitation Analysis
TRIP	Total Runoff Integrating Pathways
TRMM	Tropical Rainfall Measuring Mission
TWS	Total Water Storage
USAID	United States Agency for International Development
USGS	US Geological Survey
VIRS	Visible and Infrared Scanner
WAvg	Watershed Average
WMO	World Meteorological Organization

List of Figures

List of Tables

General Introduction

These last years, serious concerns have been raised about potential changes in water resources supplies and their influence on the environmental and social components. Hence, several debates and studies have discussed the spatiotemporal evolution of climatic variables as an indicator of these changes. However, unlike temperature that present significant changes, consistent with the global warming tendency, rainfall exhibit a strong temporal variability and spatial incoherent patterns in terms of tendencies (IPCC, 2014, 2012). Still, rainfall has sparked a lot of interest in various climatic contexts, particularly in semi-arid regions, since it constitutes the primary source of surface water. On the one hand, many studies were developed to explore the potentials of collecting rainwater in small catchments through rainwater harvesting systems (Terêncio et al., 2018, 2017). On the other hand, numerous works were conducted to assess rainfall variability in space and time. Around the world, wide changes in this resource have been reported over the 20th century (Bates et al., 2008). While the rainfall has significantly increased in some regions during the last half of the 20th century (Boyles and Raman, 2003; Burns et al., 2007; Lu et al., 2015), it showed serious declines in others (Li et al. 2013; Li et al. 2014). Still, mixed trend patterns were reported around the world (Chen et al. 2007; Liu et al. 2011), even at one same site, the tendency of total rainfall can exhibit a high complexity as it can change of direction from one season to another (Ahmad et al., 2015). Since the 1970s the water sector in Morocco has taken a major place among the concerns of the public authorities because of its decisive role in the country's food security (CESE 2014). This interest has been expressed by a set of policies and strategies that concern water conservation and management, within the framework of the national goals of socioeconomic development (Lionboui et al. 2016a). However, in the current context of climate change, the country is strongly confronted with water scarcity (Schilling et al., 2012), given the sensitivity of this resource to the variability of the climatic conditions (Benabdelouahab et al., 2015; Gosain et al., 2006). This situation appears to get accentuated in recent decades due to a significant decrease in rainfall with irregular spatiotemporal distribution and frequent prolonged dry spells

that seem to persist in the future (Driouech, 2010; Esper et al., 2007). Tramblay et al., (2013) evaluated the rainfall trends over North African countries (Morocco, Algeria, and Tunisia) and noticed a decline in total annual rainfall, linked to a decrease in wet days and an increase of dry periods in the extreme northern part of Morocco. Filahi et al., (2015) reported mixed spatial patterns and a small number of significant changes. According to the same author, the extreme north of Morocco exhibits wetter conditions against drier ones in the south. At watersheds' scale, Khomsi et al., (2016) found that rainfall presents different trends inside each of Bouregreg and Tensift, while an overall rainfall decrease was reported by Bouchaou et al., (2011) and Abahous et al., (2017) over the arid watershed of Souss-Massa. For a renewable water potential of 22 billion m^3, the ratio per capita over Morocco is around 600 m^3 per capita per year. Under the general decreasing tendency in rainfall combined with the rapid demographic, the ratio is projected to reach 500 m^3 per capita per year (water shortage threshold set by the WHO) by 2025 (JICA, 2007; USAID, 2010). Furthermore, Morocco is largely dependent on agricultural productivity. The latter is one of the major drivers of the Moroccan economy with an important contribution to the Gross Domestic Product and a high rate of employment (Lionboui et al. 2016b). It is one of the most sectors affected by climate conditions variability (Mougou et al., 2011). In fact, the socio-economic stability of Morocco is highly sensitive to climate change, especially that most of the agricultural activities occupy rainfed lands (Schilling et al., 2012). Yet, with limited adaptation capacities, severe changes in climatic conditions greatly impact living conditions and food security in the country, mainly in poorer and rural areas (Lionboui et al. 2016b). Thus, the quantification of water supply and the understanding of major factors that control water availability and distribution within a given watershed is of great importance. It helps managers to evaluate the potential reserves and efficiently program dams' release and water allocation to the various consuming sectors under the growing demand. The efficient management of water resources in a context of scarcity requires a solid understanding of both human interaction and the different physical processes that control the movement of water at lager and smaller scales (Davie, 2008). However, the quantitative impact of human activities on the water during its trajectory towards the outlet remains one of the most challenging aspects to consider in water management. Hence, the changes due to relevant physical processes that occur within the unit watershed took the major interest. The latter articulates around the accurate estimation of runoff, taking into consideration the influence of each of the processes

that describe the rainfall-runoff relationship at the watershed scale (Abdulla and Al-Badranih, 2010).

Mathematical models have been widely used in water resources-related applications, and they have become essential tools for management and planning purposes (Bergström and Lindström, 2015). Various structures are available with different degrees of complexity, from simple conceptual lumped models to more physically-based distributed ones (Arnold and Fohrer, 2005; Bergström and Forsman, 1973; Liang et al., 1994; Rango and Martinec, 1979; Todini, 1996; Vandewiele et al., 1992; Zhao, 1992). Conceptual models based on physical concepts, which are approximations of the real system with inherent uncertainties (Beven, 1989), have been more attractive to the hydrological community due to their low requirements of input data and simplicity in application. Their performance can be comparable to even more physically based models in contexts of low-quality input data (Beven and Freer, 2001; Orth et al., 2015). Therefore, a trade-off between complexity, efficiency, and data availability is unavoidable (Bergström and Lindström, 2015), particularly over watersheds in semi-arid regions with limited gauging networks. However, a poorly gauged watershed in terms of meteorological variables, in both spatial and temporal dimensions, may not be the ideal scenario for hydrologic modeling (Wilk and Hughes, 2002; Xu et al., 2013). The shortage in gauging networks makes it difficult to find a regional average that closely represents the real distribution of meteorological variables over the watershed of interest, particularly rainfall. The RGs are the main instruments that provide basic measures of rainfall within a watershed. Each RG provides a continuous measurement over time that can be representative only for relatively small areas (Love et al., 2004). In 1994, the WMO (World Meteorological Organization) indicated that for optimal coverage in mountainous regions one RG is required every 250 km^2 (OMM, 1994). Thus, the sparsity of the gauging networks in developing countries, particularly in mountainous areas, can strongly limit the reliability of rainfall measurements at the watershed scale. Numerous studies were conducted to assess the changes in model performances depending on the density and distribution of the RGs. Xu et al. (2013) reported that good model performance requires a higher number of RGs. However, the gauging networks' density demonstrates no significant improvements when it exceeds a certain threshold (Dong et al., 2005; Xu et al., 2013). Xue et al., (2013), Arsenault and Brissette, (2014), and Zeng et al., (2018) agreed that optimal performance may be achieved with fewer RGs optimally distributed. However,

a well distributed gauging network cannot be always found in regions where the topography and financial conditions can be limiting factors.

In recent years, remote sensing data have been widely used in the hydroclimatic field, particularly in rainfall estimation (Adler et al., 1994, 1993; Bennartz et al., 2002; Muñoz et al., 2016). Several gridded rainfall datasets derived from various remote sensing data have been released. They provide quasi-global coverage of rainfall estimates at high spatiotemporal resolution (Huffman et al., 2001). On the one hand, some algorithms rely on data from passive sensors to provide the rainfall estimates, such as the case of the ones that use the IR (InfraRed) imagery, namely ARC and PERSIANN (Ashouri et al., 2015; Novella and Thiaw, 2013; Sorooshian et al., 2000), and others that combine IR and PMW (Passive Microwave) satellite data, such as CMORPH, CHIRPS, and RFE (Funk et al., 2015a; Joyce et al., 2004; Love et al., 2004). On the other hand, there are space missions, like TRMM and GPM, that are fully dedicated to rainfall monitoring from space (George J Huffman et al., 2019; George J. Huffman et al., 2019; Huffman et al., 2010a; Macritchie, 2015). They provide several products of rain estimates by combining PMW, visible/IR, and rainfall radar system data. The quality of the SRP estimates was evaluated in various contexts around the world (Almazroui, 2011; Ma et al., 2020; Serrat-capdevila et al., 2016; Xue et al., 2013). Studies were performed in the Conterminous US (Beck et al., 2019), West Africa (Poméon et al., 2017; Satgé et al., 2020), several regions over Asia (Anjum et al., 2019; Tang et al., 2020; Wang et al., 2020), Peru (Mantas et al., 2014; Satgé et al., 2019), Egypt (Nashwan et al., 2019), and Algeria (Babaousmail et al., 2019). The reliability and accuracy of the different products differ depending on climatic and topographic contexts (Nashwan et al., 2019). In Morocco, only few studies were undertaken. Milewski et al., (2015) evaluated four TMPA 3B42 products (V6, V7 temporary, V7, reel time V7) against rain gauges data considering different climatic zones and elevation bands. The study covered a large part of the Moroccan territory, but the analysis was focused only on the average annual precipitation. The work of Tramblay et al., (2016) and Saouabe et al., (2020) highlighted the potential of the SRP datasets in hydrologic modeling over El Makhazine (northern Morocco) and Ghdat (southern Morocco) watersheds, respectively. Indeed, these datasets can be an important source of information at regional and local scales, due to their global availability and high measurement frequencies. Combining rainfall data derived from these missions with in situ measurements can greatly improve the accuracy of rainfall

estimations at the catchment scale, overcoming the challenges related to data availability (Rozante et al., 2010; Vila et al., 2009). In this context, the objectives of this thesis are:

- In Chapter 3: Provide an analysis of the variability of hydroclimatic variables over the OERB, using in situ and remote sensing data.
- In Chapter 4: Evaluate the capability of a conceptual hydrologic model to reproduce the daily streamflow gauged at the outlet of a sub-watershed of the OERB.
- In Chapters 5: Investigate the suitability of the SRPs (ARC, CHIRPSp25, CHIRPSp5, CMORPH-CRT v1, GPM IMERG v6, PERSIANN-CDR, RFE, and TRMM 3B42 v7), over the OERB, for reproducing and simulating the daily rainfall and streamflow, respectively.
- In Chapters 6: Evaluate the ability of the SRPs to estimate the monthly observed rainfall and, then, apply bias correction techniques and assess their spatial reliability in bias removal over multiple sub-watersheds.

Chapter 1. Fundamental Backgrounds

In this chapter, we present a summary of the theoretical basics of hydrology and remote sensing. We tried to provide the information and definitions that the reader may need to go through the manuscript pages with ease. For in-depth details, the reader is advised to refer to the references below, on which I relied to collect most of the scientific information reported here.

For hydrology: Davie (2008), WMO-UNESCO (2012), Viessman and Lewis (1996), and Robinson and Wars (2017).

For remote sensing: Davie (2008); Campbell and Wynne (2011), Egan (2003), NRCAN (2019), and Graham (1999).

1.1. Hydrology

From a literal stand of point, the term hydrology refers to the science (logy) of water (hydro). However, the scientific meaning of the term can be quite hard to discern. It changes over time and space being fitted to numerous applications that involve water as a subject (Chaponnière, 2005; Perrin, 2000). The International Glossary of Hydrology provides a general scientific approximation of the term hydrology. The latter is considered as the "science that deals with the waters around the globe; their occurrence, circulation, and distribution, both in time and space; their biological, chemical and physical properties; and their interaction with their environment, including their relation to living beings" (WMO-UNESCO, 2012). The definition underlined two main aspects through which hydrology deals with waters. A qualitative aspect that focuses on the quality of the available water within the biosphere, with an emphasis on the changes of its physical and biochemical indicators. A quantitative aspect where the evaluation of water spatiotemporal availability and distribution is the main concern. The latter, which takes the widest remit of hydrology (Davie, 2008), studies the movements of the water molecule above and under the earth's surface, and through the atmosphere. It is often linked to the water cycle, particularly in its

continental section (Perrin, 2000). Numerous scientists adhere to defining hydrology as the science that deals with the water cycle and the different accompanying fluxes (Chaponnière, 2005; Dooge, 1988; Mathevet, 2005; Oudin, 2005; Penman, 1961; Perrin, 2000). Thus, hydrology overlaps with numerous other science fields, such as geology and meteorology, and divaricate into numerous branches (Surface Water Hydrology, Cryology, Hydrogeology,…) each one concentrates on a specific component of the water cycle (Chaponnière, 2005; Mathevet, 2005; WMO-UNESCO, 2012). Still, these branches are interdependent, as water availability and distribution are linked to various processes that take place in tandem or simultaneously at different phases of the water cycle.

1.2. Water Cycle

Water is a vital and important natural resource for life-sustaining. It is available within the hydrosphere in solid, liquid, and gaseous forms. Around 97% of the earth's water is stored in the ocean (Davie, 2008). The remaining 3% includes atmospheric and continental biospheric water, where only less than 1% is available as continental liquid freshwater (Frédéric FRAPPART, 2006). Water is in continuous movement between its various reservoirs around the globe (equator-poles). These movements are maintained and balanced within the Water Cycle through numerous natural processes driven by solar energy that controls the ocean-land-atmosphere water exchanges (Figure 1 and Figure 2). The energy balance during this exchange process is responsible to a larger extent for the regulation of the earth's climate (Robinson and Wars, 2017; Viessman and Lewis, 1996). Under the effect of solar radiation, the water stored in the surface water bodies and the topsoil layers absorbs enough energy that causes the hydrogen bonds (that connect the water molecules) to weaken and break, transforming the liquid water into a gaseous form. In the meantime, a non-negligible portion of the soil water is sucked by the plants' roots (for their photosynthetic activity) and gets transpired through the leaves. Both of these processes (evaporation and transpiration), combined as evapotranspiration, allows water to escape the earth's surface towards the atmosphere as water vapor. In particular, evapotranspiration has significant control over water movements and redistribution in semi-arid regions (Chaponnière, 2005; Hernandez et al., 2000). Around 80% of the precipitated water returns to the atmosphere as water vapor (Chaponnière, 2005; Pilgrim et al., 1988). The latter travels through the atmosphere in both vertical and horizontal directions. The warm moist air is subject to cooling processes as it reaches higher and cooler layers of the atmosphere. The H_2O molecules condense around condensation

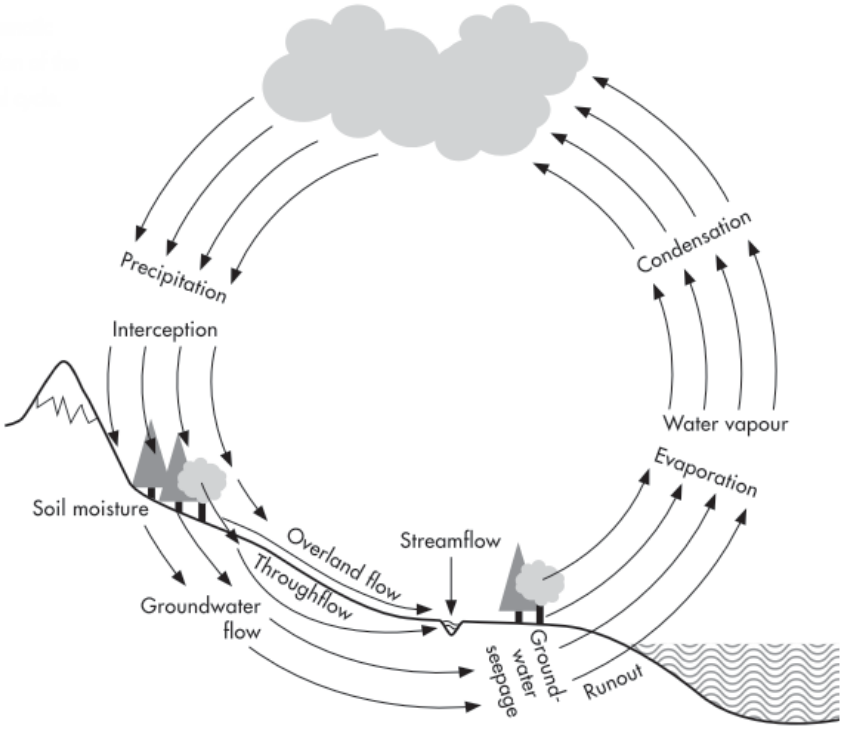

Figure 1. Schematic representation of the water cycle (source: Robinson and Wars 2017).

nuclei (aerosols) and form water droplets and ice flakes. The condensation process continues and water droplets and ice flakes grow in size, mainly through collision, until they are heavy enough (3 mm) so that the gravity forces takeover the uplifting forces and pulls them towards the ground as precipitation (Davie, 2008; Robinson and Wars, 2017). Depending on the temperature, the precipitation can be in liquid (rainfall) or solid (snow or hail) form. The solid precipitation generally forms under very low temperatures and falls as is, unless it passes through a warmer layer of the atmosphere (Robinson and Wars, 2017; Viessman and Lewis, 1996). A portion of the precipitated water is intercepted by the canopy. Its significance to the runoff generation highly depends on the development and the density of the vegetation cover. In dense forests, the canopy tends to hold important amounts of water and make them directly available for evaporation (Brooks et al., 2013; Davie, 2008). This process can be of less impact in semi-arid regions where the canopy is often of less density. The portion of water that reaches the ground is either fully or partly infiltrated into the soil depending on topography, soil biophysical properties (texture, structure, and biological activities), and rainfall characteristics (type, intensity, and duration) (Beven et al., 1988; Gnouma, 2006). The soil biophysical properties regulate the infiltration process by controlling the maximum rate (infiltration capacity) at which the water moves through the soil layers. Rainfall of

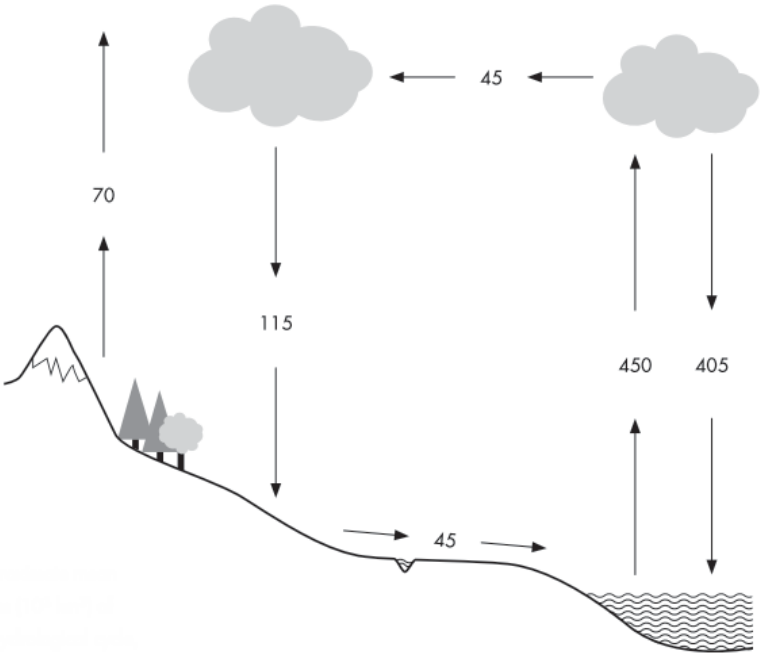

Figure 2. Estimates of mean annual fluxes (in 10^3 km^3) of the water cycle according to Rodell et al (2015) (source: Robinson and Wars 2017).

intensity smaller than the infiltration capacity is most favorable for infiltration. Moreover, the water movements through the soil are mainly governed by the capillary, adsorption, and gravitational forces. The capillarity and adsorption generally work against gravity as they are responsible for maintaining water as soil moister, between and on top of the soil particles. The gravity, on the other hand, pulls the water mostly vertically to percolate towards the underground reservoirs to be stored as groundwater. The latter can circulate within the saturated zone following the hydraulic gradient (saturated hydraulic conductivity) until it reaches the outlet through which it may contribute to the streamflow. This groundwater flow is the main water resource responsible for feeding the streams' baseflow, particularly during dry seasons (Chaponnière, 2005). Moreover, infiltration capacity higher than the rainfall intensity can also lead to surface runoff. In such a scenario the rainfall is expected to fully infiltrate the soil until saturated up to capacity leading to a surface flow referred to as saturated-excess overland flow (Dunnen and Black, 1970; Hewlett and Hibbert, 1965). The latter is mainly observed in mid-latitude regions with humid temperate climates (rainfall events of low intensity and long duration) and highly permeable soils (Bonell, 1993; Gnouma, 2006; Hewlett and Hibbert, 1965). This runoff generation mechanism predominantly occurs over lands where the water tables are high and can rapidly reach near-surface soil layers, allowing preliminary saturation (Davie, 2008; Koivusalo, 2003). When rainfall intensity exceeds the soil infiltration capacity, the

infiltration process is much less significant compare to the rapid overland flow. The latter, referred to as the infiltration-excess overland flow (Horton, 1933), is the most common mechanism responsible for runoff generation in semi-arid regions (Chaponnière, 2005; Davie, 2008; Gnouma, 2006; Koivusalo, 2003). The latter is characterized by predominant convective storms (short duration and high intensity) and low porosity due to compacted soils and sparsely vegetated areas (Chaponnière, 2005).

1.3. Measurement of the Water Cycle Components

1.3.1. Ground-based Measurements

1.3.1.1. Rainfall

The conventional instruments widely used for rainfall measurements, so-called RGs, are sort of funnel-shaped containers with a known surface opening (WMO, 2008a, 2008b). The funnel is equipped with a collection tank where the water is stored (Figure 3). This setup is not arbitrary, it helps to reduce the direct contact of collected water with sunlight and the air outside the gauge, and thus minimizes the loss of water due to evaporation (Davie, 2008). The gauges are usually set at a certain height (2 meters) above the surface to avoid over-measurement due to water splash and surface flooding, and the risk of the gauge being covered by snow (Davie, 2008; Robinson and Wars, 2017). They are placed high enough to overcome the aforementioned issues without exposing the gauge to significant under-measurement due to air turbulence.

Figure 3. Funnel-shaped manual RG (source: https://the-weather-station.com/).

The conventional gauges are manually operated to record the water volume. More sophisticated instruments that provide automatic measurements are available (WMO, 2008a, 2008b). These instruments are based on the Tipping-buckets principle, where the gauges are equipped with two small attached and balanced containers (Figure 4). The collected rainwater passes through the funnel to fill the buckets underneath. As soon as the first bucket is filled it tips over and the collected water flows out of the gauge body. In the meantime, the opposite bucket is aligned with the funnel aperture collecting rainwater until filled. Every time a bucket tips over, an electric pulse is generated and water amounts corresponding to the bucket volume are recorded.

Figure 4. The tipping-bucket automatic RG (source: https://www.ssh.co.th/).

1.3.1.2. Snowfall

There are several techniques for snowfall measurements. The two that provide direct measures of snow depth and snow water equivalent (the amount of water contained in a given snowpack) are the most commonly used (WMO, 2008a, 2008b). The snow depth method is intended to measure the thickness of a given snowpack with reference to the ground surface. Thus, it is expressed as the distance (in meter units) separating the surface of the snowpack and the earth's surface. The snow depth measurements can be made with manual methods using a gradual ruler and carrot sampler (Figure 5). The latter consists of using a metal tube to take a sample out of the snowpack and record its depth (Davie, 2008). Automatic measurements are also possible by employing an ultrasonic sensor that can be mounted on meteorological stations (Figure 5). The sensor emits a pulse of ultrasonic frequency which hits the snowpack surface and returns to the

sensor (Davie, 2008; WMO, 2008a, 2008b). The distance between the sensor and the snowpack surface, and hence the snowpack depth, can be determined based on the time the pulse took to travel between the sensor and the snowpack surface. The snow water equivalent is measured using the same gauges used for rainfall measurement equipped with heated panels. The snow accumulated on the gauge is melted by the panel and recorded as liquid water.

Figure 5. Left: snow depth sampler. Right: measurement station holding an ultrasonic snow depth sensor (source: https://www.nrcs.usda.gov/).

1.3.1.3. Radar Systems

Active Radars (radio detection and ranging) are ground instruments that provide indirect estimates of precipitation based on the interaction of the microwave spectrum with the water droplets contained in the clouds (WMO, 2008a, 2008b). The setup consists, in general, of an antenna beam and a receiver. The antenna emits a microwave beam that hits the cloud, and the precipitation is derived proportionally to the amount of the energy backscattered to the receiver. A cloud with abundant water droplets returns more energy to the receiver. In addition to their capacity to differentiate between the droplets' size (depending on the adopted wavelength or frequency), the ground radars can provide information about the movements of precipitation areas for a large spatial coverage (40 to 200 km) at a finer spatial (e.g., 5 km) and temporal (e.g., 15 min) resolutions (Davie, 2008; WMO, 2008a, 2008b).

Even though the obvious advantages of the Radar measurements, when it comes to estimating the amount of precipitated water, they remain of less accuracy compared to the RGs. Therefore, calibration against RG observations is often required before any quantitative analysis. The main drawbacks of this measurement technique are the difficulty of choosing the adequate wavelength and, particularly, The high management cost that makes it less popular around the world (WMO, 2008a, 2008b).

1.3.2. Remote Sensing Observations

1.3.2.1. Remote Sensing Theoretical Basics

Generally, remote sensing stands for the operation of detecting information about an object without being in physical contact with it (NRCAN, 2019). From a geoscience stand of point, remote sensing describes the science of collecting information about targets (object or phenomenon) from the Earth's terrestrial, atmospheric, and aquatic ecosystems using radiation sensors onboard aerospace ships (Campbell and Wynne, 2011; NRCAN, 2019). The distant sensing of the earth's surface started with cameras secured on tethered balloons back in the 1840s for topographic mapping (Graham, 1999). More sophisticated platforms emerged over time, namely aircraft and spacecraft. The development of these platforms was mainly motivated by the need for military surveillance and reconnaissance (Campbell and Wynne, 2011). Aerial photography (cameras mounted on airplanes) was brought to existence by World War I, while spacecraft-based photography (cameras mounted on artificial satellites) started with the emergence of space programs in the 1960s (Campbell and Wynne, 2011; Graham, 1999). Henceforth, remote sensing techniques have been used in numerous civil applications related to natural resources monitoring.

Remote sensing includes the full process of illumination, atmospheric and target interactions, information recording by the sensors, and storage and data processing in the ground reception units (Figure 6). For it to be detected from space, the targets must first be illuminated. This can be through electromagnetic radiation naturally produced by the sun (passive remote sensing) or artificially produced (active remote sensing) based on radar instruments (Campbell and Wynne, 2011; Graham, 1999; NRCAN, 2019).

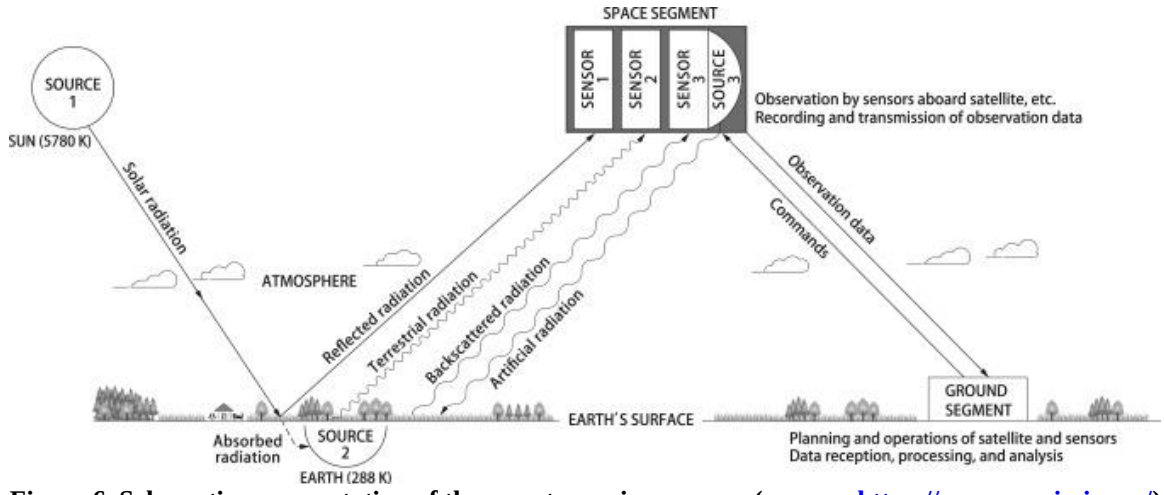

Figure 6. Schematic representation of the remote sensing process (source: https://www.omnisci.com/)

The electromagnetic radiation, a result of combined electric and magnetic waves, comprises multiple regions (Figure 7). The latter are categorized by the wavelength (the distance between successive wave crests, measured in Meters), or by the frequency (number of cycles of a wave per unit time, measured in Hertz) in what is called the electromagnetic spectrum. The latter, range from the gamma radiation bands (the shortest wavelength and highest frequency) to the radio waves (the longest wavelengths and lowest frequencies). However, the radiation that is practical for remote sensing is limited to those regions lying between the visible wavelengths and the microwaves. The visible region of the electromagnetic spectrum, which occupies wavelengths between 0.4 and 0.7 µm, is the only part that is perceptible to the human eyes. Right after the visible region, there is the infrared radiation where the associated wavelength lies between 0.7 and 100 µm. The infrared comprises three subregions, namely the near-IR, the mid-IR, and the far-IR (Figure 7). The near and mid-IR waves (from 0.7 to 3 µm) are used the same way as the visible ones as all of them are captured by the sensors as reflected energy. The far-IR (from 3 to 100 µm), on the other hand, is mostly the radiation released from the terrestrial targets as heat depending on the target's temperature, and thus recorded as thermal energy (Campbell and Wynne, 2011; Graham, 1999; NRCAN, 2019). Above 100 µm until 1 m in wavelength, the radiation belongs to the microwave region. It is the part of the electromagnetic spectrum that encompasses the longest wavelengths used in remote sensing. The shorter microwave wavelengths have similar concepts as the thermal-IR, and thus they are referred to as PMW (NRCAN, 2019). The microwave region can be divided into several bands (Ka, K, Ku, X, C, S, L, and P) that can be artificially produced and recorded by the radar systems (Figure 7).

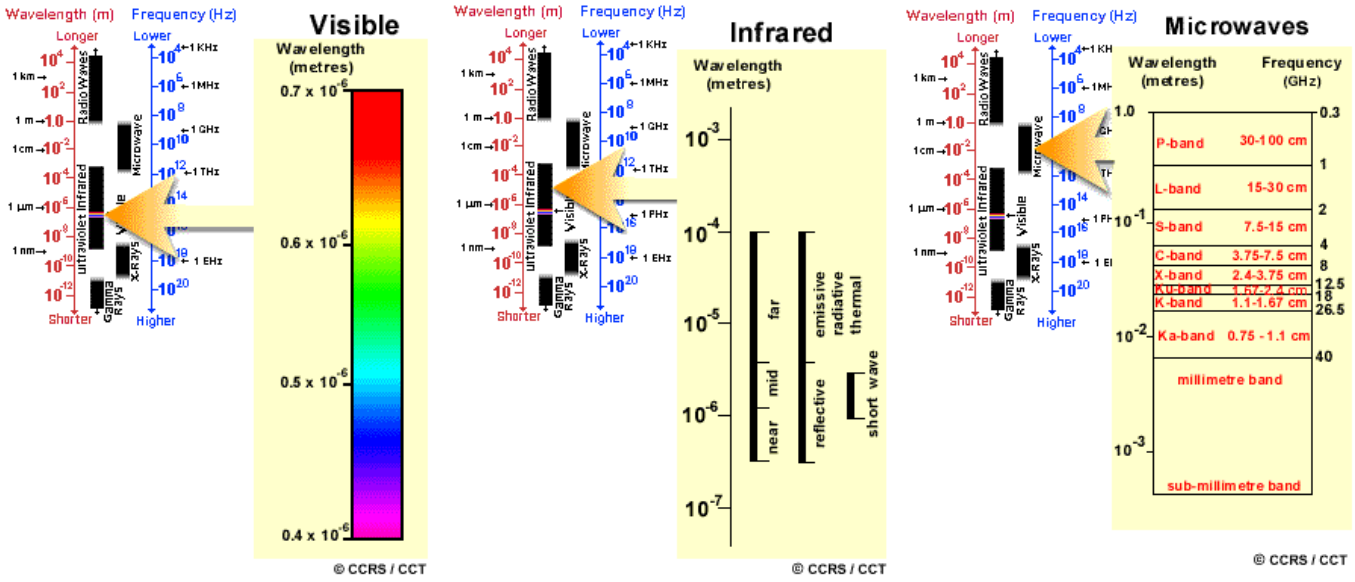

Figure 7. The electromagnetic spectrum (Source: www.nrcan.gc.ca/).

In the passive system, after the radiation reaches the surface it interacts with the various terrestrial targets. Depending on the physical characteristics of the target, the radiation is either reflected towards the sensors or absorbed by the targets and later released in longer wavelength as heat (Campbell and Wynne, 2011; NRCAN, 2019). However, during its travel through the atmosphere, the radiation interacts with the various atmospheric particles and molecules (aerosols) through the scattering and absorption phenomena. Both of these, disturb the electromagnetic radiation when it travels from the sun towards the terrestrial targets and when it is reflected or emitted by these targets towards the sensors in orbit. They specifically take place when the aerosols are in the propagation path of the radiation. The latter is either subject to a change of trajectory or absorbed by the aerosols. The amount of radiation disturbed or blocked from attending the passive sensors depends on the wavelength of the incoming radiation and the density of aerosols in the atmospheric column the radiation is traveling through (Campbell and Wynne, 2011; Graham, 1999). The atmospheric effect generally occurs when the aerosols are about the same or greater size than the wavelength radiation. Aerosols of large sizes such as water droplets are capable to influence a wide range of wavelengths (NRCAN, 2019).

Molecules constituting the atmosphere absorb the radiation at specific wavelengths. The absorption phenomenon is mainly caused by ozone, carbon dioxide, and water vapor. Each of these molecules absorbs specific radiation wavelengths at various regions of the electromagnetic spectrum (Figure 8). The Ozone-induced absorption mostly blocks the ultraviolet radiation from

getting to the earth's surface. The carbon dioxide mostly absorbs radiation in the first half of the far-IR preventing it from escaping the atmosphere. The water vapor presents various absorption windows throughout the electromagnetic spectrum. The most significant of these concerns the emitted radiation located in the second half of the far-IR region and the shorter microwaves. The vast majority of remote sensing applications mainly rely on the electromagnetic radiation that belongs to the regions, called atmospheric bands, where the absorption is at its minimum. The weather applications, on the other hand, make use of both of the aforementioned atmospheric distortion phenomena.

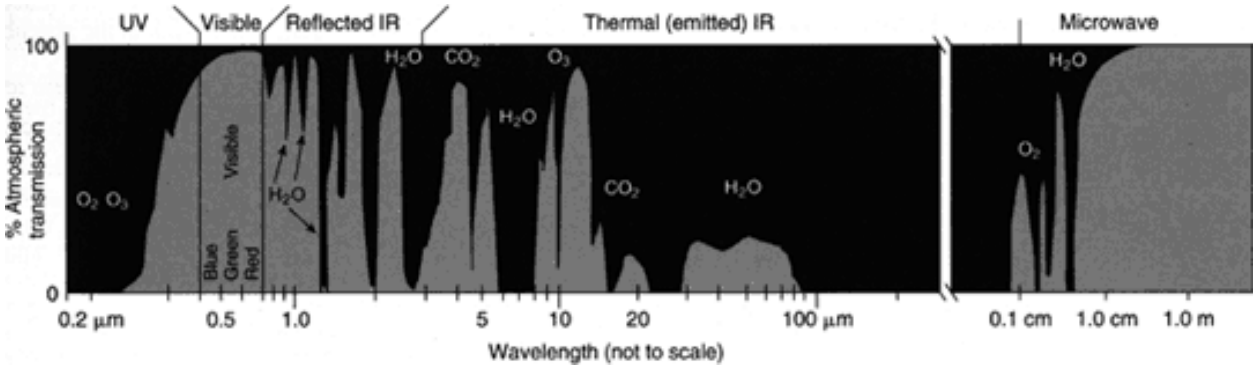

Figure 8. Diagram of absorption bands and atmospheric windows (source: NASA's Earth Observatory, www.earthobservatory.nasa.gov).

1.3.2.2. Rainfall Measurements

Infrared

The sensors that operate in the infrared bands mainly measure the energy emitted by the top of the cloud systems. And, the rainfall estimates are derived according to the amount of immitted energy. The IR-based estimation method, so-called Cloud-Indexing, mainly uses data from GEO (geostationary) satellites (Davie, 2008; WMO, 2008b). The latter consist of aerospace platforms placed in orbit parallel to the equator at approximately 35000 km high. They revolve in the same direction and speed the earth rotates on itself (Campbell and Wynne, 2011; NRCAN, 2019). This allows the satellites to be stationary relative to the earth’s surface and continuously observe the same area. The latter is usually wide and covers multiple continents under the same scene (about 40 percent of the earth's surface). The full IR coverage of the earth’s disk, except for small regions in the north and south poles, is obtained by combining observations from a constellation of GEO satellites installed at relatively the same orbital plane (Figure 9). These characteristics make the

GEO satellites the key tools for weather applications, particularly in monitoring the cloud dynamics and meteorological forecasts at the global scale.

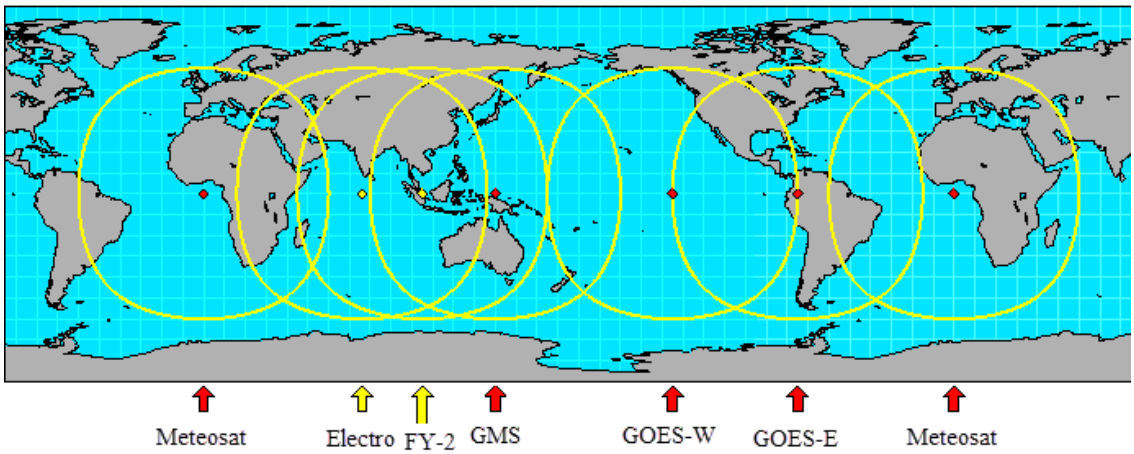

Figure 9. The global spatial coverage of GEO satellites (source: www.ral.ucar.edu/).

The Cloud-Indexing method assumes that the electromagnetic properties of the cloud tops are related to the intensity of rainfall that these clouds may hold. The clouds systems that show important vertical development and their top surface reaches high atmospheric layers (associated with very cold top temperatures) are the ones that present a high probability of precipitation (WMO, 2008b). Thus, algorithms were developed to classify the cloud systems based on their top temperature. Generally, these classification schemes assume that clouds with top temperatures below a given threshold are more likely to precipitate at a certain rate. One of the well-known Cloud-Indexing algorithms is GPI (GEOS Precipitation Index, Arkin and Meisner, 1987). The latter is based on an earlier work where Arkin, (1979) was able to find significant links between radar-derived rainfall estimates and infrared observations. These links were significant when the cloud top brightness temperature was less than the temperature threshold of 235°K. The GPI assumes that clouds with top temperatures less than 235°K can be associated with a rain rate of 3 $mm.h^{-1}$ in the tropics (30°N – 30°S, WMO 2008). Another approach, called life-history (Stout et al., 1979), is available. It accounts for the temporal evolution of the cloud systems based on GEO data. The life-history approach principle consists of analyzing multiple images acquired consecutively for the same spatial coverage. This analysis allows to emphasize the stage of development of the cloud system and determine whether it is about to grow or to reduce in size. The life-history rainfall estimates are computed by combining the cloud-indexing outputs with information about the cloud evolution derived from two consecutive images.

Passive microwave

This technique relies on data collected by PMW sensors. The latter are mainly mounted on LEO (Low Earth Orbit) satellites that fly the earth's surface following orbits of low altitudes (a few hundred kilometers) and different inclination angles (e.g., 65° relative to the equatorial plane). These satellites revolve around the earth's surface following a fixed orbit and, with a fly period that varies in the range of 90–120 min, they make 12–16 Earth turns per day. The orbital travel in conjunction with the Earth's rotation allows the LEO satellites to cover most of the Earth's surface. However, with a limited residence time, these satellites observe smaller scenes and take longer periods to rescan the same region. Thus, individual LEO satellites are less useful for weather studies. Instead, a constellation of multiple satellites with the same or similar characteristics is considered to provide temporally continuous coverage (Figure 10).

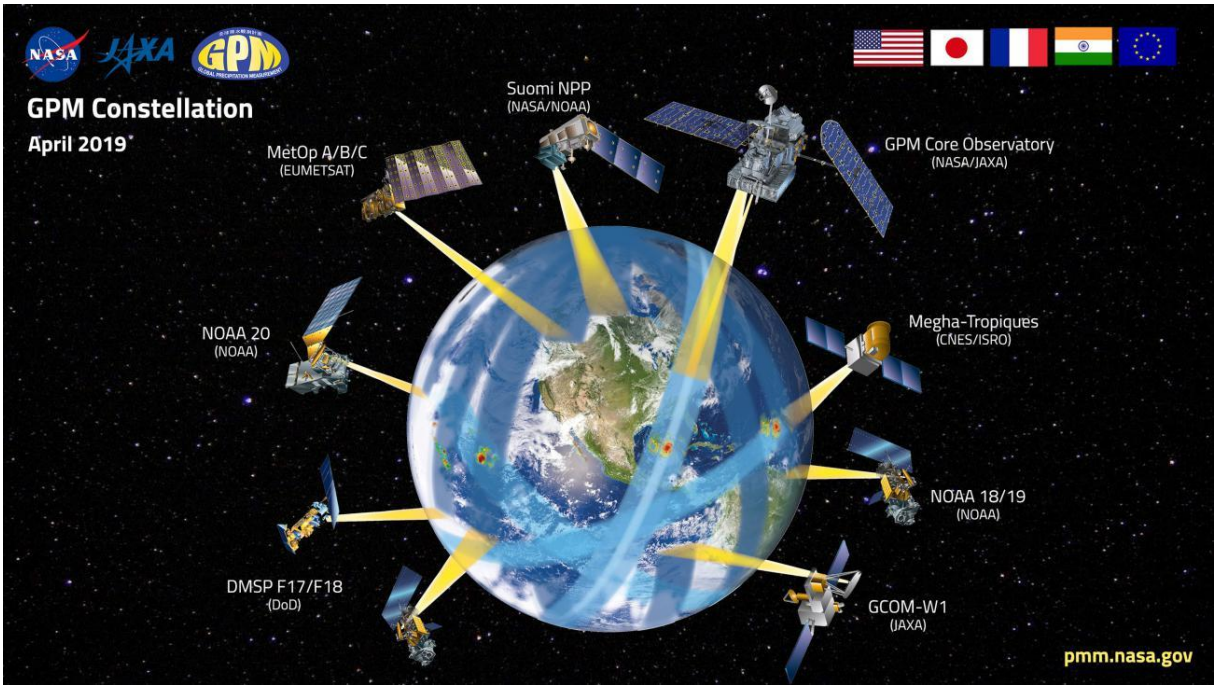

Figure 10. LEO satellites holding PMW sensors employed for rainfall estimation under the GPM space mission (source: www.gpm.nasa.gov).

The PMW-based rainfall estimation techniques are considered to be more physically sound compared to the IR techniques. They are built around the changes in brightness temperature caused by the presence of cloud systems between the source of energy and the PMW sensors (Davie, 2008; WMO, 2008b). These changes are provoked by the two natural mechanisms through which the atmosphere interacts with the electromagnetic radiation, namely the absorption and the scattering.

At low frequencies (below 22 GHz), the raindrops in the atmosphere absorb the radiation (Stout et al., 1979) and emit it towards the orbiting sensors as microwaves. The energy emitted is associated with the amount of water present within the cloud. The absorption-based rainfall retrievals are particularly powerful over surface objects of low emissivity levels, such as the sea and ocean. The latter emit the energy at a very low rate and appear radiometrically cold. Hence, the increase of brightness temperature provoked by the raindrop-induced emission allows the sensors to easily distinguish the rainy cloud systems (Stout et al., 1979). Overland, on the other hand, the information retrieved based on the absorption mechanism is of less significance. The different degrees of emissivity from the multiple earth's landscapes overwhelms the raindrops' emission and makes it hardly distinguishable. Thus, the PMW technics mainly employ the scattering mechanism for rainfall estimation. At high frequencies (above 50 GHz), the relatively large water droplets, particularly ice particles, tend to scatter the microwave radiation (Petty and Katsaros, 1992). The scattering mechanism leads to a decrease in the emitted radiation, and thus the sensor observes the clouds with abundant droplets aloft radiometrically colder than the surrounding areas of the earth's surface (Petty, 1994). The intensity of scattering is proportional to the number of droplets present within the cloud.

Active microwave

The active microwave sensors for weather monitoring from space are less common compared to the other sensors. Their era began with the TRMM satellite mission back in 1998, and it is maintained by its successor GPM satellite mission launched in 2014. More details about these missions are presented later in the manuscript (see section 2.3.1.). The active microwave sensors in orbit work similarly to those sited on the earth's surface (Davie, 2008; WMO, 2008b). The main difference resides in the fact that the sensors in space observe the clouds systems from the top while the ground sensors observe them from the bottom. The ability of cloud penetration (depending on the wavelength) allows the active radars to provide a three-dimensional representation of the cloud systems.

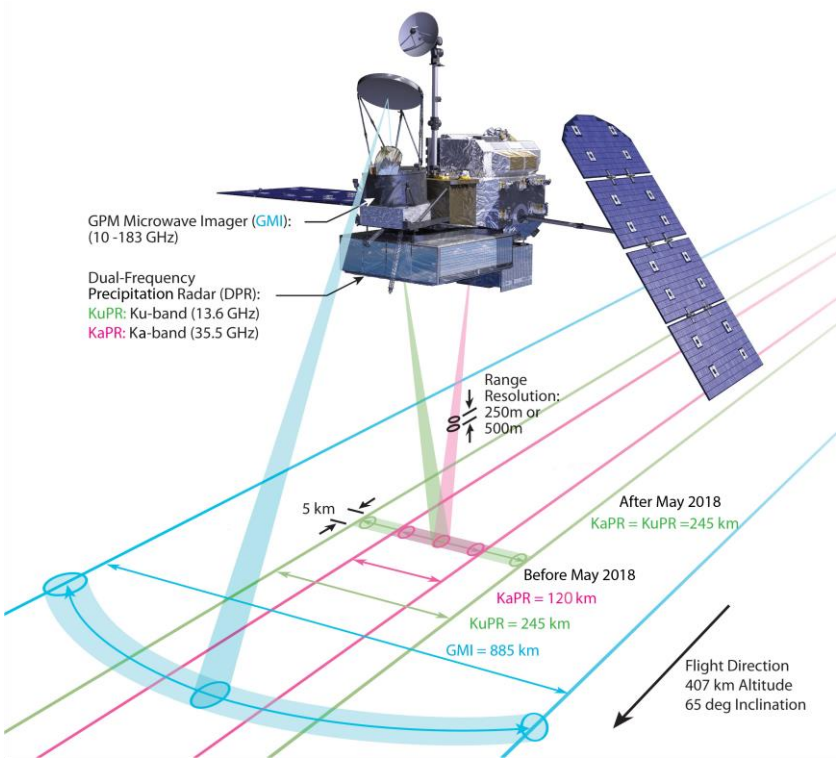

Figure 11. GPM Core Observatory and its coverage dimensions (source: www.gpm.nasa.gov).

1.3.2.3. Snow Cover Observations

The detection of snow on the ground using remote sensing relies on the high reflectivity of the snow in some parts of the electromagnetic spectrum (Figure 12). Depending on its physical and morphological properties in addition to the amounts of impurities, the snow reflects about 30 to 90% of the incident solar energy (Marchane, 2015; WMO, 2008a). These percentages vary with radiation wavelengths. The reflectance of the snowpack in the visible band is the highest. This allows to clearly distinguish snow from most of the natural objects, except clouds. The latter, depending on their type, present high reflectivity in most parts of the electromagnetic spectrum, particularly in the Visible and near IR bands (Hall et al., 1995). The contrast between the two objects is prominent around the Mid-infrared band where the reflectance of snow is significantly low compared to the clouds. Most of the snow cover mapping applications use different approaches that incorporate the Visible and IR bands to discriminate between the snow and no-snow areas (Crane R. G. and Anderson M. R., 1984; WMO, 2008a). The NDSI (Normalized Difference Snow Index), developed by Dozier, (1989), is the most commonly used for snow cover mapping (Boudhar, 2009; Hall et al., 1995). The index is calculated as the ratio of the difference between the Visible (ρ_{VIS}) and the Mid-IR (ρ_{MIR}) reflectance to the sum between Visible and the Mid-IR:

$$NDSI = \frac{\rho_{VIS} - \rho_{MIR}}{\rho_{VIS} + \rho_{MIR}}$$

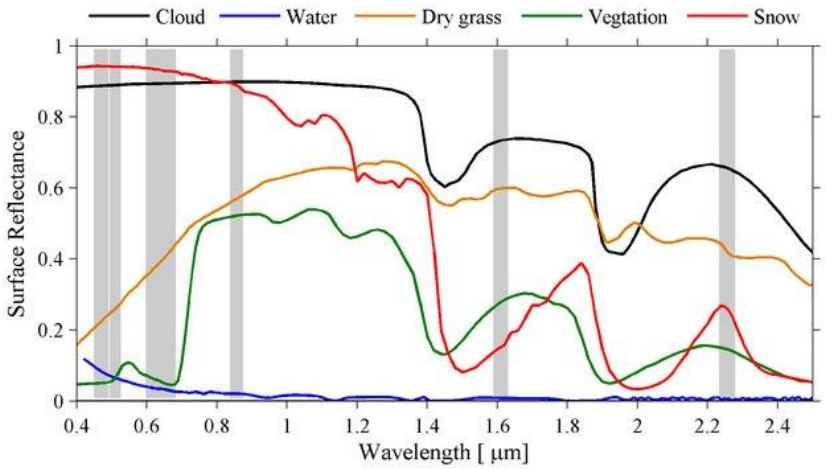

Figure 12. Spectral signatures for five earth's surface objects. created using reflectance data from the ASTER (Advanced Spaceborne Thermal Emission Reflection Radiometer) spectral library (Zhuge et al., 2017).

Chapter 2. Data and Methods

2.1. Study Area

The area of study is the OERB located in the center of Morocco between 31° 15’ N and 33° 22’ N latitudes and 5° 00’ W and 9° 20’ W longitudes (Figure 13). It is one of the largest Moroccan watersheds occupying an area of approximately 35 000 km^2 (7% of the country’s total area). It is bordered from the east by the Atlas Mountains chain, with its two parts, the Middle Atlas (oriented NNE-SSW) and the Hight Atlas (oriented NE-SW). The Atlas mountains constitute the main source of water supply for surrounding lowlands (Boudhar et al., 2020, 2009; Chaponnière, 2005), particularly those located on the western slope of the chain. The watershed is characterized by a marked topography with elevations that vary between 0 meters above sea level (a.s.l.) at the outflow and 3890 meters where it culminates at the High Atlas.

Since 1929, fifteen dams have been built within the watershed’s territory, with a total storage of about 5.3 million cubic meters (Mm^3) (approximately 33% of the national storage capacity). On average, this hydraulic infrastructure allows the mobilization of nearly 3.550 Mm^3 per year for drinking and industrial water supply (10%), and irrigation (90%). The watershed encompasses around 325800 ha of irrigated lands distributed on five irrigated areas, namely Doukkala (96,000 ha), Beni Moussa (69,500 ha), part of the Upstream-Tassaout (52,000 ha), Downstream-Tassaout (44,000 ha), part of the Haouz (35,400 ha), and Beni Ami (28,500 ha). These areas grouped together make 22% of Morocco’s total irrigated lands and play a significant role in the socio-economic development of the watershed. Furthermore, eleven out of the fifteen dams are equipped, with hydropower plants with an installed capacity of 629 MW, allowing an average electricity production of 1800 GWh per year (70% of the national production capacity).

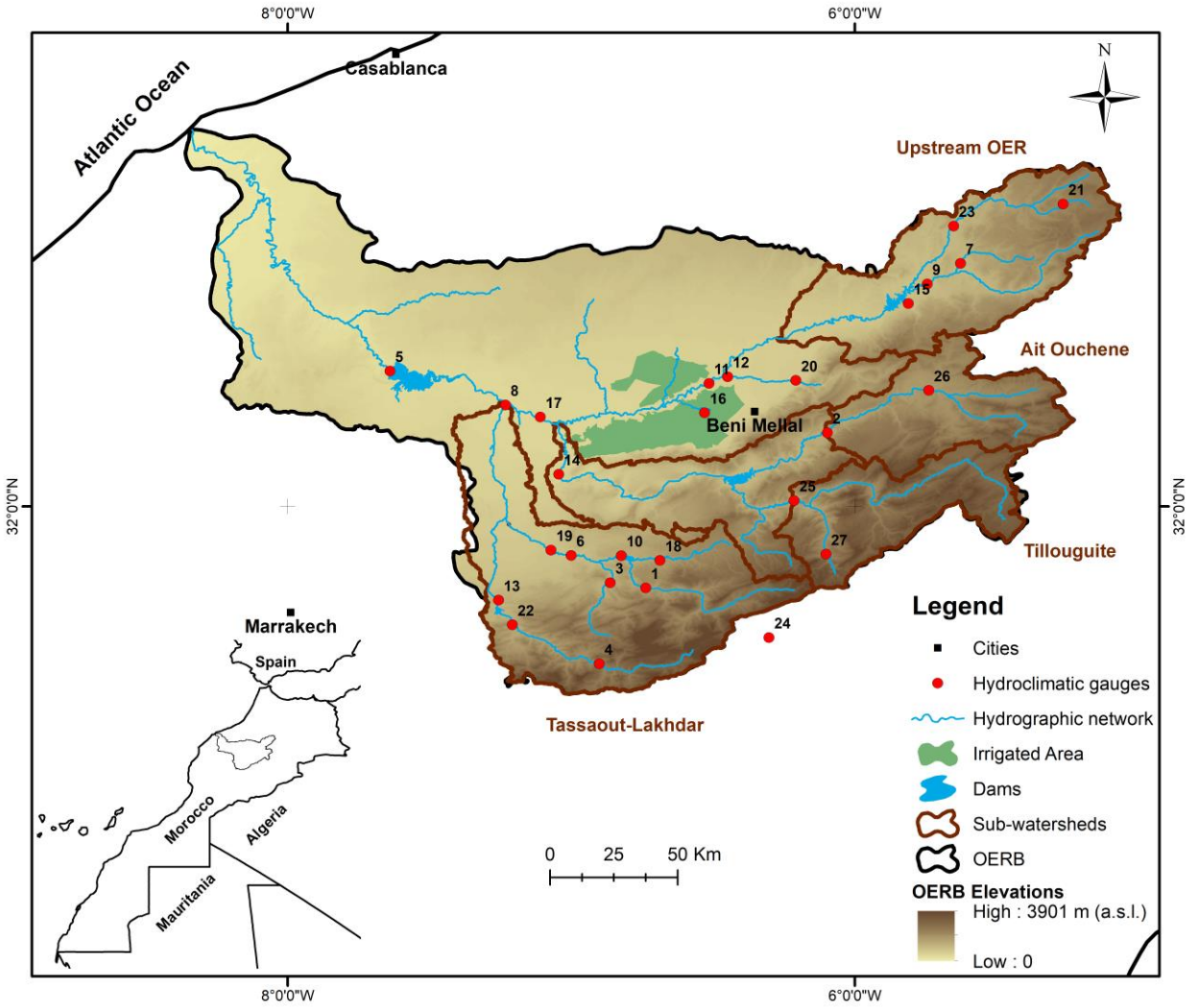

Figure 13. The geographical setting of the study area.

The OERB contains several groundwater reservoirs in full or in part. The most main aquifers are (Figure 14):

The Turonian of Tadla, the largest aquifer of the watershed, covers an area of 10,000 km^2. It consists of karstified and dolomitic limestones with a thickness varying from 20 m in the regions where the aquifer outcrops and 80 m in the South (on the edge of the Atlas chain), and can reach 100 m in some places.

The Eocene aquifer covers an area of 6400 km^2. The aquifer thickness starts from 40 m in the North and gradually increases to reach 100 m in the South. At the foothill of the Atlas range, the aquifer drastically widens to around 300 m. To the north (below the phosphate plateau), the Eocene aquifer is composed of alternating sandy phosphate and phosphate limestones with fissured

flint. To the south, under the Tadla plain, the Maastrichtian-Eocene series occurs in this region in the form of phosphate sands alternating with aquifers of limestones, phosphate dolomites, and flint dolomites. The aquifer ends with a level of dolomitic clay.

The Beni-Moussa-West phreatic aquifer covers an area of 885 km^2 under the west part of the Beni Moussa irrigated area. It is characterized by a heterogeneous geometry with thickness varying between 150 m and 300 m. The aquifer is constituted mostly of limestone and marly-limestone formations of the Villafranchian and ancient quaternary, silts and marls, and upper quaternary sequences with puddingstone of the recent quaternary.

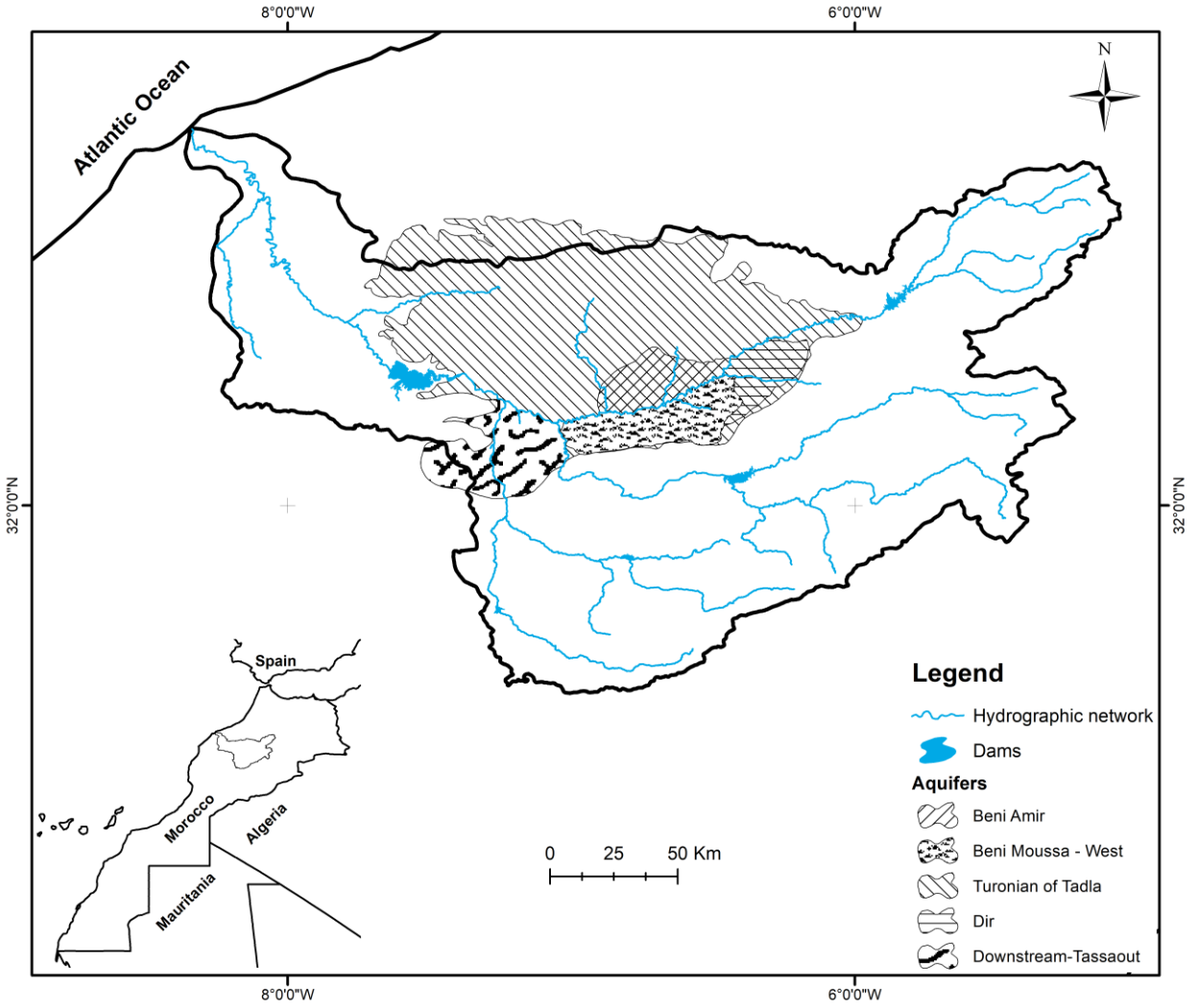

Figure 14. The geographic location of the OERB's main aquifers.

The Beni Moussa-East (also known as Beni Moussa-Dir) phreatic aquifer, with a thickness that varies between 100 and 200m, covers an area of 450 km^2 corresponding to the east part of the

Beni Moussa irrigated area. It contains Mio-Plio-Quaternary sediments essentially composed of alternating limestones, marls, and conglomerates, based on the Cretaceous marl-limestone complex.

The Beni Amir phreatic aquifer spreads mostly under the Beni Amir irrigated area on a surface of around 600 km^2. The aquifer is an alternation of marl-limestone, lacustrine limestone, and conglomerates with a thickness between 10 and 100 m. This thickness follows a North-South increasing gradient and can reach 200 m in some regions near the aquifer's southeastern limit.

The Downstream-Tessaout aquifer occupies an approximate area of 500 km^2 with thickness varying between 10 and 20 m. The aquifer is mainly composed of sandy-clay fill, a plyo-quaternary conglomerate that lies on top of a marly Eocene layer and transgresses into the Turonian limestones. The thickness of the Plio-Quaternary aquifer mostly varies between 10 and 20 m.

The watershed's main draining river, Oum Er-Rbia, takes its source from the Middle Atlas at 1800 m a.s.l. and runs along 550 km until it reaches the outflow in the Atlantic Ocean. Two permanent tributaries (Oued El-Abid and Tassaout-Lakhdar) contribute to feeding the mainstream. Hence, three main sub-watersheds cover the upstream part of OERB, namely Upstream Oum Er-Rbia (OER), Oued El-Abid, and Tassaout-Lakhdar. The Oued El-Abid encompasses two sub-watersheds, Ait Ouchen and Tilouguite drained by Oued El-Abid and Assif'N'Melloul streams, respectively (Table 1). These sub-watersheds contribute to feeding Bin El Ouidane, one of the largest dams in the country. The dam has a storage capacity of 1300 Mm^3 and a regulated volume of 945 $Mm^3.y^{-1}$. It assure the irrigation of Tassaout and Beni Moussa irrigated areas (Htitiou et al., 2019; Lebrini et al., 2019), the water transfer towards the southern neighboring watershed (Tensift), and hydropower generation (El Azhari and Loudyi, 2019). In conjunction with the Afourer hydropower, with an installed capacity of 464 MW (70% of the total installed capacity of the OERB), they allow an annual production that can exceed 718 GWh (El Azhari and Loudyi, 2019).

Table 1. Characteristics of the Ait Ouchene and Tilouguite sub-watersheds.

	Perimeter (km)	Area (km2)	Minimum Elev. (m)	Maximum Elev. (m)	Mean Elev. (m)	Dominant Elev. ranges
Ait Ouchene	390	2427	953	3230	1927	1400-2200
Tilouguite	412	2410	1068	3424	2386	2200-3000

Most of the information and numbers, related to dams and aquifers, reported above are obtained from the official website of the ABHOER (www.abhoer.ma/) and ORMVAT (www.ormva-tadla.ma/) institutions, responsible for water resources and agricultural activities management, respectively.

2.2. In Situ Data

Rainfall records from twenty-six manual RGs, situated within the limits of the OERB, were used in this study (Table 2). Data series from twenty-five stations were provided by the ABHOER and one station was obtained from the ORMVAT. Most of the gauges managed by the ABHOER are intended for measuring both rainfall and streamflow. Hence, all available gauges are situated on the banks of the hydrographic network of the OERB. The ORMVAT (Oulad Gnaou) gauge, which is intended for agricultural studies, is located within the irrigated area of Beni Moussa. The data is used at both daily and monthly timescales. The daily data are available mostly for a short time range (09/1996–08/2012), only three time series (Ait Ouchene, Oulad Gnaou, and Tilouguite) start from the 1970s. The monthly time series, on the other hand, cover longer periods, ranging from 1970 to 2011. This 40-year time coverage was available at fifteen out of the twenty-six RGs. It should be noted that, hereafter, the year term refers to the hydrologic year starting from September and ending in August (e.g., 01/09/2001-31/08/2002, 2001/2002).

The characteristics of the RGs used in this work and data availability are illustrated in Table 2.

Table 2. Characteristics of the RGs used in this work. The column "Chapter" represents the number of the chapter where the gauge data is employed.

ID	Gauge Names	Lon.	Lat.	Elev.	Daily	Time range	Monthly	Time range	Chapter
1	Addammaghene	-6.74	31.71	1098	Yes	09/1996 - 08/2012	-	-	V, VI
2	Ait Ouchene	-6.10	32.26	963	Yes	08/1975 - 08/2012	Yes	01/1970 - 12/2010	III, IV, V, VI
3	Ait Sigmine	-6.86	31.73	1025	Yes	09/1996 - 08/2012	Yes	01/1970 - 12/2010	III, V, VI
4	Ait Tamlilt	-6.90	31.45	1860	Yes	09/1996 - 08/2012	Yes	01/1970 - 12/2010	III, V, VI
5	Al Massira	-7.63	32.48	260	Yes	09/1996 - 08/2012	Yes	01/1970 - 12/2010	III, V, VI
6	Assaka	-7.00	31.83	622	Yes	09/1996 - 08/2012	-	-	V, VI
7	Aval El Heri	-5.62	32.86	830	Yes	09/1996 - 08/2012	Yes	01/1970 - 12/2010	III, V, VI
8	Bissi Bissa	-7.23	32.36	302	Yes	09/1996 - 08/2012	-	-	V, VI
9	Chacha N Amellah	-5.74	32.78	830	Yes	09/1996 - 08/2012	-	-	V, VI
10	Hassan 1st Dam	-6.82	31.83	1009	Yes	09/1996 - 08/2012	-	-	V, VI
11	Mechra Eddahk	-6.51	32.43	414	Yes	09/1996 - 08/2012	-	-	V, VI
12	Moulay Bouzekri	-6.44	32.46	427	Yes	09/1996 - 08/2012	Yes	01/1970 - 12/2010	III, V, VI
13	Moulay Youssef Dam	-7.25	31.67	880	Yes	09/1996 - 08/2012	Yes	01/1970 - 12/2010	III, V, VI
14	Ouaouirinth	-7.04	32.11	370	Yes	09/1996 - 08/2012	Yes	01/1970 - 12/2010	III, V, VI
15	Ouaoumana	-5.81	32.72	697	Yes	09/1996 - 08/2012	-	-	V, VI
16	Oulad Gnaou	-6.53	32.33	450	Yes	09/1970 - 08/2012	-	-	V, VI
17	Ouled Sidi Driss	-7.11	32.32	336	Yes	09/1996 - 08/2012	Yes	01/1970 - 12/2010	III, V, VI
18	Sgat	-6.68	31.81	1150	Yes	09/1996 - 08/2012	Yes	01/1970 - 12/2010	III, V, VI
19	Sidi Driss Dam	-7.07	31.85	642	Yes	09/1996 - 08/2012	-	-	V, VI
20	Taghzirt	-6.21	32.44	565	Yes	09/1996 - 08/2012	Yes	01/1970 - 12/2010	III, V, VI
21	Tamchachate	-5.27	33.07	1696	Yes	09/1996 - 08/2012	-	-	V, VI
22	Tamesmate	-7.21	31.58	920	Yes	09/1996 - 08/2012	Yes	01/1970 - 12/2010	III, V, VI
23	Tarhat	-5.65	32.99	878	Yes	09/1996 - 08/2012	-	-	V, VI
24	Tichki	-6.30	31.54	3250	-	-	-	-	IV, V
25	Tillouguite	-6.21	32.02	1100	Yes	08/1977 - 08/2012	Yes	01/1970 - 12/2010	III, IV, V, VI
26	Tizi N Isly	-5.74	32.41	1347	Yes	09/1996 - 08/2012	Yes	01/1970 - 12/2010	III, IV, V, VI
27	Zaouit Ahansal	-6.10	31.83	1595	Yes	09/1996 - 08/2012	-	-	IV, V, VI

Daily **streamflow** data from two gauges, delivered by the ABHOER, were used in this work (Table 3). The gauges of Ait Ouchene and Tilouguite are located at the outlet and, respectively, record daily streamflow of Ait Ouchene and Tilouguite sub-watersheds. The streamflow observations are made by limnimetric readings converted into actual discharge ($m^3.s^{-1}$) using the rating curve method (the relationship between the flow rate and the stream stage).

Table 3. Characteristics of the streamflow gauges used in this work. The column "Chapter" represents the number of the chapter where the gauge data is employed.

ID	Gauge Names	Lon.	Lat.	Elev.	Daily	Time range	Monthly	Time range	Chapter
2	Ait Ouchene	-6.10	32.26	963	Yes	08/1975 - 08/2011	-	-	III, IV, V, IV
25	Tillouguite	-6.21	32.02	1100	Yes	09/1977 - 08/2011	-	-	III, IV, V, IV

Temperature data were obtained from three gauges (Table 4), namely Sidi Driss Dam (ABHOER), Oulad Gnaou (ORMVAT), and Tichki (IMPETUS; Schulz and de Jong, 2004). The mountainous part of the OERB suffers from the absence of consistent daily temperature data. Therefore, the average temperature of the Ait Ouchene and Tilouguite sub-watersheds was estimated based on the TLR (Temperature Lapse Rate, Equation 1) method using the Tichki (located in the Daraa watershed near Ait Ouchene and Tilouguite) as a reference gauge. The TLR method relies on the fact that temperature variation is influenced by elevation. It is well known that the atmospheric temperature decreases as we go up in the troposphere. This decrease is controlled by a standard TLR of 0.65°C per 100m (Boudhar, 2009). Thus, in the mountainous regions, the rise in elevation induces a drop in air temperature. However, the TLR significantly depends on microclimates changes that may occur from one mountain range to another. Hence, in this work, we did rely on the TLR 0.56°C per 100 m estimated by Boudhar, (2009) for some neighboring watersheds.

The temperature is estimated using the following formula:

$$T_B = T_{TCK} + \frac{TLR\ x\ (TCK_{ELV} - B_{ELV})}{100}\ ;\ TCK_{ELV} > B_{ELV} \qquad \text{Equation 1}$$

Where:

T_B: the average temperature of the watershed;

T_{TCK}: the temperature recorded at the Tichki gauge;

B_{ELV}: the mean elevation of the watershed;

TCK_{ELV}: the elevation of the Tichki gauge.

Table 4. Characteristics of the temperature gauges used in this work. The column "Chapter" represents the number of the chapter where the gauge data is employed.

ID	Gauge Names	Lon.	Lat.	Elev.	Daily	Time range	Monthly	Time range	Chapter
16	Oulad Gnaou	-6.53	32.33	450	Yes	09/1970 - 08/2010	-	-	III
19	Sidi Driss Dam	-7.07	31.85	642	-	-	Yes	09/1985 - 04/2014	III
24	Tichki	-6.30	31.54	3250	Yes	04/2001 - 12/2010	-	-	IV, V

Monthly PET (**potential evapotranspiration**) data series were estimated for Ait Ouchene and Tilouguite using the Thornthwaite model (Thornthwaite, 1948). The latter considers potential evapotranspiration as a function of air temperature (Boudhar et al., 2009; Robinson and Wars, 2017). The only data requirements are mean air temperature and hours of daylight to account for the unequal day lengths in different months (Davie, 2008; Robinson and Wars, 2017).

The first part of the Thornthwaite estimation technique derives a monthly heat index "**i**" for each month based on the mean monthly temperature "**t**" °C (Equation 2).

$$i = \left(\frac{t}{5}\right)^{1.514} \qquad \text{Equation 2}$$

The heat index monthly values are then summed to provide an annual heat index "**I**" (Equation 3).

$$I = \sum_{j=1}^{12} i \qquad \text{Equation 3}$$

Then, according to Thornthwaite the evapotranspiration estimates is derived as (Equation 4):

$$PE = 16K \times \left(\frac{10t}{I}\right)^{a} \qquad \text{Equation 4}$$

Where K is a correction factor to account for unequal hours of daylight between months, determined based on the latitude of the studied site (Table 5).

Table 5. Correction coefficients "K" for the latitude 30° N (Teegavarapu, 2012).

	Sep	Oct	Nov	Dec	Jan	Feb	Mar	Apr	May	Jun	Jul	Aug
K	1.03	0.98	0.88	0.87	0.89	0.86	1.03	1.08	1.19	1.19	1.21	1.15

a is a term of the equation that can be calculated as follow (Equation 5):

$$a = 6.7 \times 10^{-7} I^3 - 7.7 \times 10^{-5} I^2 + 0.018I + 0.49 \quad \text{Equation 5}$$

2.3. Remote Sensing and Ancillary Data

2.3.1. Rainfall

2.3.1.1. TRMM

TRMM is the first space mission dedicated to the quantitative radar-based measurement of rainfall from space (Huffman et al., 2010a; Macritchie, 2015). It was launched from NASDA, the 28th of November 1997 (NASDA, 2001). The mission was developed as a collaboration between NASA and JAXA. The satellite launched as a part of the TRMM mission orbits the earth at 400 km of altitude and 35° of inclination. It embeds five measurement instruments (Kummerow et al., 2000, 1998), the PR (Precipitation Radar), the TMI (TRMM Microwave Imager), VIRS (Visible and Infrared Scanner), CERES (Clouds and the Earth's Radiant Energy System), and LIS (Lightning Imaging Sensor). Out of the five instruments, PR (operating at 13.8 GHz), TMI (operating at five channels 10.65, 19.35, 22.235, 37.0, and 85.5 GHz), and VIRS (Operating at 0.63, 1.6, 3.75, 10.8, and 12 μm) are dedicated to the rainfall measurement system. The TRMM program provides a variety of algorithms, including the TMPA (TRMM Multi-satellite Precipitation Analysis) 3B42 Version 7 (Bolvin and Huffman, 2015; Huffman et al., 2010b), that produce rainfall estimation products through the combination of data from TRMM and various other satellites (LEO and GEO). The use of multisource data is mainly to provide full coverage rainfall estimates in terms of space and time. In addition to TMI, SSMI (on DMSP), SSMIS (on DMSP), AMSR-E (on Aqua), AMSU-B (on NOAA), and MHS (on NOAA and MetOp) are combined to produce global and temporally continuous PMW-based rainfall estimates (Huffman et al., 2010b). The latter are produced by two different service groups based on two different algorithms. At PMM/PPS, the Rainfall estimates are retrieved from TMI, SSMI, SSMIS, and AMSR-E through the physically-based GPROF algorithm (Kummerow et al., 2001), where different versions are used on each of the PMW observations. On the other hand, the NESDIS/MSPPS used the algorithm developed by Zhao and Weng, (2002) and Weng et al., (2003) to compute the AMSU-B and MHS rainfall estimates. Then, the PMW-based rainfall estimates are calibrated using the TMI (adjusted to PR) as a reference calibrator. However, when observations

from more than one sensor are available for the same region, the average of data from all available sensors is used instead. For quality matter in AMSU-B and MHS, precedence is given to the other sensors for average calculation. The GEO IR data from GEOS, GMS, MTSat, and Meteosat were collected and reproduced by NOAA/NCDC and CPC as inputs in TMPA (Huffman et al., 2010b). After being merged as a global grid of cloud top temperature, the GEO IR data are processed for rainfall retrieval in a relatively similar approach as in GPI. The clouds are classified according to their top temperature, where only clouds with top temperatures below a given threshold are considered. The final satellite-based rainfall estimates are mainly created from PMW-based estimates where available, and PMW-based estimates calibrated by IR estimates elsewhere. The combined PMW and IR estimates are adjusted to the GPCP (Adler et al., 2018, 2003) monthly RG analysis to reduce the bias in the satellite-based rainfall estimates.

The final TMPA 3B42 product is provided as quasi-global (50°S to 50°N) rainfall estimates at 0.25°x0.25° spatial resolution and, at 3-hourly and daily temporal resolutions. The data production started in 1998 and ended in 2017. The lifetime of the TRMM mission came to an end officially in 2015, but the TMPA products were maintained until 2017 thanks to the availability of data from the cooperating satellites. The product used in this work was originally obtained as daily (00:00 GMT – 00:00 GMT) rainfall totals at the aforementioned spatial resolution.

2.3.1.2. PERSIANN

PERSIANN-CDR product is developed by the CHRS at the University of California, Irvine for rainfall estimation based on GEO IR and RG data (Ashouri et al., 2015; Sorooshian et al., 2000). The GridSat-B1 data is produced by merging data from multiple GEO satellites (Meteosat, GEOS, GMS, and FY2) collected by NOAA/NCDC under the ISCCP framework (Ashouri et al., 2015). It consists of three subproducts, where IRWIN (InfraRed WINdow), available since 1980, is the one used to feed the PERSIANN algorithm. First, the IRWIN imagery is scanned by a 5x5 regular GCs moving window. And, the IR temperature from the central GC, the mean temperature of 3x3 GCs, the standard deviation temperature of 3x3 GCs, the mean temperature of 5x5 GCs, and the standard deviation temperature of 5x5 GCs are extracted (Sorooshian et al., 2000). These statistical features are then classified, and mapping functions that linearly link the rainfall rate estimates to the aforementioned features are built through calibration against various rainfall observations. Rainfall data from LEO PMW (if available), radars, and ground RGs serve as references to train the model

to build the relationship between the IR top-cloud temperature and rain rate. Lastly, the algorithm's outcome is then bias-adjusted against the GPCP 2.2 using the LS technique (see section 6.2.2.1. for more details about this technique)

The final PERSIANN-CDR product is provided as quasi-global (60°S to 60°N) rainfall estimates at 0.25°x0.25° spatial resolution and, at 3-hourly and daily temporal resolutions. It is available for the period from 1983 to the present, which is long enough to allow relevant climatological analysis after evaluation against the ground RGs. The product used in this work was originally obtained as daily (00:00 GMT – 00:00 GMT) rainfall totals.

2.3.1.3. IMERG

GPM, the successor TRMM, is a space mission jointly launched by NASA and JAXA on February 27th, 2014, in collaboration with other space agencies and programs from around the world (George J Huffman et al., 2019; George J. Huffman et al., 2019). The GPM satellite orbits the earth at an inclination of 65° and an approximate altitude of 408 km. The core observatory of GPM is constituted of active DPR (Dual-frequency Precipitation Radar, operating at Ku and Ku bands) and a multichannel PMW sensor called GMI (GPM Microwave Imager, operating at thirteen channels from 10 GHz to 183 GHz). These instruments provide information about the rainfall rate and distribution (three-dimensionally) within the cloud systems. Also, they serve as a reference for merging rainfall information from other sensors of the GPM constellation to provide quasi-global rainfall estimates. In addition to GMI, the GPM constellation consists of several PMW sensors onboard LEO satellites, namely AMSR-2 (on GCOM-W1), ATMS (on SNPP and NOAA20), SAPHIR (on Megha-Tropiques), MHS (on NOAA19 and MetOp), SSMI (on DMSP), and SSMIS (on DMSP). The IR observations from GEO satellites (GMS, MTSat, Himawari Series-JMA, GOES, Meteosat) complement the relatively limited spatiotemporal coverage of the PMW estimates. The various PMW brightness temperature data are intercalibrated to the GMI-DPR combined product, through a probability matching technique (Krajewski and Smith, 1991), and then merged and converted to rainfall estimates. The estimates from most sensors are computed using one fixed version of the GPROF algorithm (George J. Huffman et al., 2019), except for SAPHIR-based estimates that are produced using the PRPS algorithm (Kidd, 2018). During the merging process, the PMW estimates are combined to one global grid array by retaining the available data. When observations from multiple sensors are available for a given region a

precedence order is applied. The conical-scan radiometers are preferred over the cross-track scanners. In particular, the algorithm prioritizes the sensor that provides the closest observation to the reference reporting time. The monthly calibrated rainfall estimates are distributed to a half-hourly scale using the CMORPH-KF (Joyce and Xie, 2011) quasi-Lagrangian time interpolation scheme and PERSIANN-CCS cloud classification system (Hong et al., 2004), using IR observations from the cooperating GEO satellites (George J. Huffman et al., 2019). Moreover, the CMORPH-KF scheme relies on motion vectors derived from MERRA-2 (Gelaro et al., 2017) and GEOS-FP total precipitable water vapor data (Lucchesi, 2018).

The IMERG estimates are available in Early, Late, and Final releases. The two first releases rely mainly on the on-hands satellite data to provide estimates with the least latency possible. The Final release, on the other hand, is more complete as it uses available data from all cooperating sensors and GPCP monthly data. The latter is used as a reference to bias-adjust the satellite-based rainfall estimates using the same technique as in PERSIANN. The IMERG v6 algorithm combines data collected during the TRMM era with those collected by GPM since 2014 and provides quasi-global (60°S to 60°N) rainfall estimates from 2000 to present. The data is available at 0.1°x0.1° spatial resolution and, at half-hourly and daily temporal resolutions. The final release product used in this work was originally obtained as daily (00:00 GMT – 00:00 GMT) rainfall totals.

2.3.1.4. RFE

The RFE version 2.0 was developed by NOAA's Climate Prediction Center in association with USAID/FEWS-NET (Love et al., 2004). The data is produced via the algorithm based on the Pingping Xie (Xie and Arkin, 1996) method, which incorporates three different data sources. The latter consist of GEO IR, PMW, and RG data. The RFE algorithm works in a merging process of two steps. The first step aims at reducing the random error through the combination of IR and PMW data. A first IR-based rainfall estimate is produced by computing the GPI approach using brightness temperature determined from half-hourly Meteosat imagery (10.5-12.5µm wavelength window). This estimate is derived from the fraction of cloud systems with a top cloud temperature below 235K (Arkin and Meisner, 1987; Love et al., 2004). The GPI-based estimates are then linearly combined with rain rates derived from the SSMI (on DMSP) and the AMSU (on NOAA satellites). The combination consists of a weighted average where the weighting coefficients of each data source are determined by comparing the satellite estimates with the observed rainfall (Love et al.,

2004). The last step is mainly for reducing the bias associated with the satellite-only estimates. Thus, the outcome of the IR and PMW combination is then calibrated against the gauge daily accumulated rainfall provided by the GTS. The calibration procedure relies on attributing the daily observed rainfall to the GCs that correspond to the RGs positions and the satellite estimates elsewhere.

The final products provide daily (06:00 GMT – 06:00 GMT) estimates of rainfall at each 0.1°x0.1° GC over the African continent. The RFE data is available from 2001 to present. The limited temporal coverage of the RFE data is mainly due to the shortage of historical PMW data records.

2.3.1.5. ARC

ARC 2 is the second version of the Africa Rainfall Climatology algorithm produced by the NOAA's Climate Prediction Center in association with USAID/FEWS-NET (Novella and Thiaw, 2013). It was developed mainly to fill the shortage in the dataset record provided by RFE2 and serve sufficient data for long-term climatic analysis. Thus, the ACR2 algorithm operates in a mostly similar way as the one employed in RFE2. The differences between the two datasets mainly concern the input data used for algorithm forcing. ARC2 uses only two data sources out of the three employed in RFE2. It maintains the same GTS gauge data used for calibration and Meteosat IR used for the GPI rainfall estimates production. The GPI calculation relies on a 3-hourly temporal sampling of the geostationary IR data instead of the half-hourly observations, which added extra efficiency in data processing and availability (Novella and Thiaw, 2013). The exclusion of PMW data was mainly motivated by the absence of long and continuous daily records. It allows the construction of consistent and long-term rainfall estimates based on GTS and IR data

The ARC rainfall estimates are available from 1983 to present. The final product is provided as daily (06:00 GMT – 06:00 GMT) rainfall estimates gridded at a 0.1°x0.1° spatial resolution over the African continent.

2.3.1.6. CMORPH

CMORPH algorithm is developed by the NOAA-CPC for rainfall estimation by combining geostationary IR (Meteosat, GEOS, GMS), LEO PMW (TMI, AMSU-B, SSM/I), and daily gauged rainfall data (Joyce et al., 2004). Firstly, rainfall estimates are generated from PMW imagers (TMI,

SSMI) and sounders (AMSU-B) using GPROF (Kummerow et al., 2001) and MSPPS (Ferraro et al., 2005), respectively. The PMW rainfall retrieved from all sources is rescaled to a homogenous spatial resolution of 8 km x 8 km and then calibrated by matching the probability density functions of the PMW estimates. The TMI (on TRMM) sensor serves as a reference calibrator. This operation ensures the homogeneity of the rainfall retrievals from the multiple data sources with different degrees of sensitivity. Since 2015, the year the TRMM mission lifetime ended, the calibration procedure relies on the reference probability functions estimated from the historical data from each sensor (Xie et al., 2017). After calibration, the multisource PMW data is grouped into one global scene and marked with a suffix MWCOMB. In regions where the PMW data scenes are overlapped, only one of the available PWM estimates is used according to the quality precedence ranking (Xie et al., 2017). Even after the combination of multisource images for rainfall retrieval, the spatiotemporal coverage of the PMW data remains very limited. The IR estimates, in contrast, are globally available at finer temporal resolution. Thus, cloud motion vectors computed from the GEO IR images are used to spatiotemporally propagate the PMW-derived rainfall. Lastly, overland, an adjustment against the daily CPC gauge-based analysis rainfalls is performed to account for the bias associated with the Satellite-based CMORPH estimates. It consists of a nonlinear approach that seeks to fit the probability density function of daily CMORPH Raw to that of the CPC daily gauge data (the same principle reported in section 6.2.2.2.).

The final CMORPH product consists of a global (60°S to 60°N) half-hourly rainfall estimates available at 0.08° x 0.08° from 1998 to present. The rainfall estimates are also available at upscaled spatial and temporal resolutions. The daily (00:00 GMT – 00:00 GMT) CMORPH-CRT, gridded at a 0.25° x 0.25° spatial resolution, is used in this work.

2.3.1.7. CHIRPS

The CHIRPS v2.0 rainfall product is developed by the USGS and CHC in collaboration with NASA, USAID, and NOAA (Funk et al., 2015a, 2015b). The dataset was developed to provide long-term rainfall data for trend and drought monitoring to support early warning systems (such as the FEWS-NET framework). The CHIRPS algorithm combines thermal IR, PMW, and RGs rainfall data to produce daily, pentanal, and monthly rainfall estimates at 0.05° x 0.05° spatial resolution. It works in a three steps estimation process that involves the computation of the CHPclim, the CHIRP, and the CHIRPS estimates. First, the CHPclim is created based on long-

term monthly means from FAO and GHCN rainfall historical records, TRMM 2B31 rainfall estimates, CMORPH rainfall estimates, IR, MODIS LST (Land Surface Temperature) in addition to physiographic and geographic information (Funk et al., 2015a, 2015b). A moving window regression approach is adopted to produce CHPclim estimates, where a local regression is performed for each GC considering prediction information derived based on the geographic and physiographic indicators, and satellite observations. The regression models are then fitted to the FAO climate normal and the residuals are used to make a preliminary estimate. The latter are bias-adjusted based on scaling factors estimated from the GHCN stations and CHPclim climate normals (provided at 0.05° x 0.05° GC). IR data from GridSat and CPC are blended and used by CHIRP to calculate the duration, referred to as CCD, for which a cold cloud (temperature below 235°k) has covered a given GC. The CCD is linked to the observed rainfall through regression models calibrated against the TRMM 3B42 rainfall estimates. The developed models are then used to produce estimates of pentanal rainfall normals at a rescaled 0.05° x 0.05° GCs. The final CHIRP product is the pentanal rainfall normals multiplied by the CHPclim normals. The daily CHIRP data are calculated by redistributing the pentanal totals proportionally to the daily CFS data. The CHIRPS data refer to the CHIRP product after bias adjustment. To this end, CHIRPS data incorporate ground RG data from multiple sources at both daily (GTS and NMAs) and monthly (GHCN, GSOD, SASSCAL, and NMAs) time scales. In the first place, the bias-adjustment process relies on GTS and NMA data to provide an early release version of the product. The late release version takes into consideration all RG data sources. The combination process consists of a weighted average of the ratio between five surrounding gauges and the concerned CHIRP GC. The weighting coefficients are mainly calculated adopting the inverse distance weighting principle, a decorrelation slope, and the correlation between CHIRP and the nearest RG.

The CHIRPS rainfall product is available from 1981 to present at daily (00:00 GMT – 00:00 GMT), pentanal, and monthly time resolutions. With a quasi-global spatial coverage (50°S-50°N), the dataset is provided at 0.05° x 0.05° (CHIRPSp5) and 0.25° x 0.25° (CHIRPSp25) spatial resolutions. The daily (00:00 GMT – 00:00 GMT) estimates of both CHIRPSp5 and CHIRPSp25 are considered for evaluation in this work.

2.3.2. Snow Cover

Over the mountainous region of the OERB, there are no gauging stations dedicated to snow depth measurements. Satellite data are the only source available to derive information about snow cover. MOD10A1 version 6 product, from Terra MODIS satellite data (Hall and Riggs, 2016), is used in this study to cope with the lack of snow in situ measurements. Since the early 2000s, the product provides daily maps of SCA at a 500 m spatial resolution. However, daily maps are often affected by cloud coverage. Therefore, the images were processed to fill missing and the cloud-covered GCs adopting the methodology reported by Marchane et al., (2015), specifically developed for the Moroccan Atlas mountain range.

The performance of the MOD10A1 product against in situ data was assessed by Marchane et al., (2015) over the Atlas mountain of Morocco, including the OERB. They have concluded that the SCA product provided by MODIS can be reasonably used to map snow cover over the study area. Moreover, numerous works have used MODIS SCA in hydrologic modeling (e.g., Lee et al., 2005; Li and Williams, 2008; Sorman et al., 2009). Lee et al., (2005) calibrated the HBV model against runoff and SCA from MODIS in Turkey, while Sorman et al., (2009) compared MODIS and NOHRSC SCA products as inputs to simulate streamflow using SRM (Snowmelt Runoff Model) in Colorado and New Mexico. Both studies agreed that SCA from MODIS can provide good simulations of streamflow.

2.3.3. GRACE

GRACE is a joint mission between NASA and DLR, both invested in the build and the launch of the mission back in March 2002 (Tapley et al., 2004). The mission's main goal was to map the Earth's monthly gravity changes provoked by mass redistribution above and below the earth's surface. The GRACE measurements were planned for a five years lifetime. Due to the relevant data and significant insights provided about the Earth system, the mission was extended for additional years of gravitational measurements until October 2017 (Tapley et al., 2019). After GRACE shut down due to battery and fuel problems, the successor mission GRACE-FO was launched in May 2018 to ensure the continuity of measurements based on the same principle and instruments adopted in the GRACE mission. The latter consists of two identical satellites, GRACE-1 (leading) and GRACE-2 (trailing), flying the earth in tandem (220 km apart) on a 500 km polar orbit. The twin satellites, in addition to the telecommunication and maintenance systems, imbed two main

instruments: GPS receivers and microwave K-band antennas (NASA, 2002). The GPS receivers' main role is to provide the precise locations of the two satellites based on the GPS constellation (NASA, 2002). The positioning information is interchanged between the two satellites through carrier signals transmitted and received by the microwave antennas. The received signals are then processed to calculate the changes in the distance (at a micrometric precision) between the twin satellites. The changes in gravity pulls are determined proportionally to the distance between GRACE-1 and GRACE-2 that changes as the satellites fly areas of different gravity fields. When the satellites pass over an area of important gravity the distance between them increases, as the gravity force pulles GRACE-1 farther ahead of GRACE-2. When the GRACE-2 passes over the same area, the satellite is pulled toward the GRACE-1 and the distance between them gets reduced (NASA, 2003).

The gravitational pull is exerted by the earth's mass in its whole, including the mass of its lithosphere, biosphere, and hydrosphere. At small temporal scales, the lithosphere is mostly subject to insignificant changes. Thus, its mass remains relatively constant over time compared to the mass of the hydrosphere. The latter, with both of its liquid and solid components, is in continuous movements between the different Earth's reservoirs. These movements, which can occur at a finer temporal scale, are responsible to a large extent for the variability of the earth's gravity fields (NASA, 2002). The measurements of the gravity changes provided by GRACE are mainly representative of the water mass redistribution over time and space. The GRACE end-user data, provided as Equivalent Water Thickness anomalies, are corrected for most geophysical distortions and ready to use for analyzing the surface and subsurface water variability. They are available as solutions from various centers (CSR, GFZ, JPL, and GSFC) in spherical harmonics and Mascons (mass concentration blocks) versions. The Mascons version is newly released as an alternative for solving the gravity signals. It has advantages over the spherical harmonics. The Mascons solution requires no postprocessing in terms of destriping or smoothing, less subject to leakage errors, and shows better land-ocean signals separation (Luthcke et al., 2013; Save et al., 2016; Watkins et al., 2015).

The GSFS mascons solution (Luthcke et al., 2013) is used in this work. It provides the earth's monthly TWS (Total Water Storage) anomalies from 2003 to the near present, at a spatial resolution of 1°x1°. TWS sums the water masses contained in the different terrestrial reservoirs: SWB

(Surface Water Bodies), SWE (Snow Water Equivalent), SM (Soil Moisture), GWS (Ground Water Storage), Canopy (Ca) (Shen et al., 2015). Thus, the changes in the GWS (Ground Water Storage) can be estimated as:

$$GWS = \text{TWS} - (\text{SWB} + \text{SWE} + \text{SM} + \text{Ca}) \quad \text{Equation 6}$$

One or more of the equation terms (SWB+SWE+SM+Ca) can be omitted according to their significance to the long-term variations in the TWS (Shen et al., 2015).

Table 6. Characteristics and references of the remote sensing data used in this work.

SRP names	Spatial Resolution	Spatial Coverage	Temporal resolution	Temporal Coverage	Unit	Source
RFE	0.1° x 0.1°	40°S–40°N 20°W–55°E	Daily	2001 - present	mm	ftp://ftp.cpc.ncep.noaa.gov/fews/fewsdata/africa/rfe2/
ARC	0.1° x 0.1°	40°S–40°N 20°W–55°E	Daily	1983 - present	mm	ftp://ftp.cpc.ncep.noaa.gov/fews/fewsdata/africa/arc2/
CMORPH-CRT	0.25° x 0.25°	60°S - 60°N	Daily	1998 - present	mm	ftp://ftp.cpc.ncep.noaa.gov/precip/CMORPH_V1.0/
PERSIANN-CDR	0.25° x 0.25°	60°S - 60°N	3-h Daily	1983 - present	mm	ftp://persiann.eng.uci.edu/CHRSdata/PERSIANN-CDR/adj_3hB1
CHIRPS	0.05° x 0.05° And 0.25° x 0.25°	50°S - 50°N	Daily	1981 - present	mm	https://data.chc.ucsb.edu/products/CHIRPS-2.0/global_daily
GPM IMERG	0.1° x 0.1°	60°S - 60°N	30-min Daily	2000 - present	mm	https://gpm1.gesdisc.eosdis.nasa.gov/data/GPM_L3
TRMM 3B42	0.25° x 0.25°	50°S - 50°N	3-h Daily	1998 - 2017	mm	https://disc2.gesdisc.eosdis.nasa.gov/data/TRMM_L3
MOD10A1	500 m	Global	Daily	2000 - present	%	https://earthdata.nasa.gov/
GRACE	1° x 1°	Global	Monthly	2003 - present	cm	https://grace.jpl.nasa.gov/mission/grace/

2.3.4. Soil Moisture

SURFEX (in french Surface Externalisée) is a surface modeling platform developed by Météo-France. It is composed of various physical models for natural land surface (soil and vegetation), urban and artificial areas, natural surface water bodies, and ocean, including chemistry and aerosol surface processes (Albergel et al., 2018a). The platform includes the ISBA land surface model that allows to physically simulate the land-atmosphere exchanges by solving the soil-vegetation energy and water budgets. It also includes the TRIP (Oki and Sud, 1998) hydrologic model, which is coupled to ISBA and uses its outputs to simulate streamflow. The models are implemented through a global land data assimilation system (LDAS-Monde; Albergel et al. 2017). The latter permits the incorporation of surface SM and leaf area index satellite observations to constraint the near-surface variables (including SM) simulated by the ISBA-TRIP coupling model. More information can be found in the scientific literature (Albergel et al., 2019, 2018b, 2017) and on the SURFEX official website (http://www.umr-cnrm.fr/surfex/, last access: August 2019).

Monthly SM simulated at the watershed scale by the SURFEX modeling system is used in this work. The data were computed and delivered by a third party affiliated with Météo-France.

2.4. Gridded Data Processing

In this work, the gridded data processing, as well as the numerical computations and graphical illustrations, were made using the platform of the MATLAB (MATrix LABoratory) programming language developed by Mathworks. The gridded data were freely downloaded from the web in different file formats: NetCDF, HDF, Binary, and tiff. While the data is stored in Binary and tiff files in a standard matrix format, in NetCDF and HDF files, it is structured in one single file as multiple variables (data, attributes, coordinates, and temporal information) that can be extracted and manipulated separately. This kind of storage format facilitates the data organization, but it requires additional computational skills and function libraries to access the data inside the files. Thus, Matlab codes were created to read and access each of the datasets. These codes were written such that to consider the specificity of the different file and storage formats, and thus automate the reading process to overcome the huge amount of data. For some gridded datasets, the time series were available as separate files. Each file contains a two-dimensional matrix that corresponds to a specific day of the study period, which makes it 3287 files to cover the period

between 2001/09/01 and 2010/08/31 (study period). This is the case of ARC and RFE (tiff), CMORPH (Binary), IMERG (NetCDF), TRMM (NetCDF4), and MODISA1 (HDF). The time series of other gridded data sets were stacked as a three-dimensional matrix, where the data files are available in blocks. Each block contains a one-year time series (365/366 images in one file), such as in the case of CHIRPS (NetCDF), or time series of the whole study period, as in the case of PERSIANN (NetCDF) and GRACE (HDF5). The information contained in the images was retrieved using geographical masks prepared based on shapefiles (created vias a GIS software) that describes the position of the RGs and the extent of the sub-watersheds considered in this work. The extraction was done by iteratively read the data files and overlap them with the mask file, making sure that both of them cover the same scene and have compatible dimensions. For the RGs, this step consists of creating satellite time series by retrieving the data from the GCs homologous to each of the RGs (Figure 15a). For the sub-watersheds, the satellite time series were built by averaging the data from the GCs whose centroids were completely within the limits of the studied sub-watersheds (Figure 15b), hereafter referred to as WAvg.

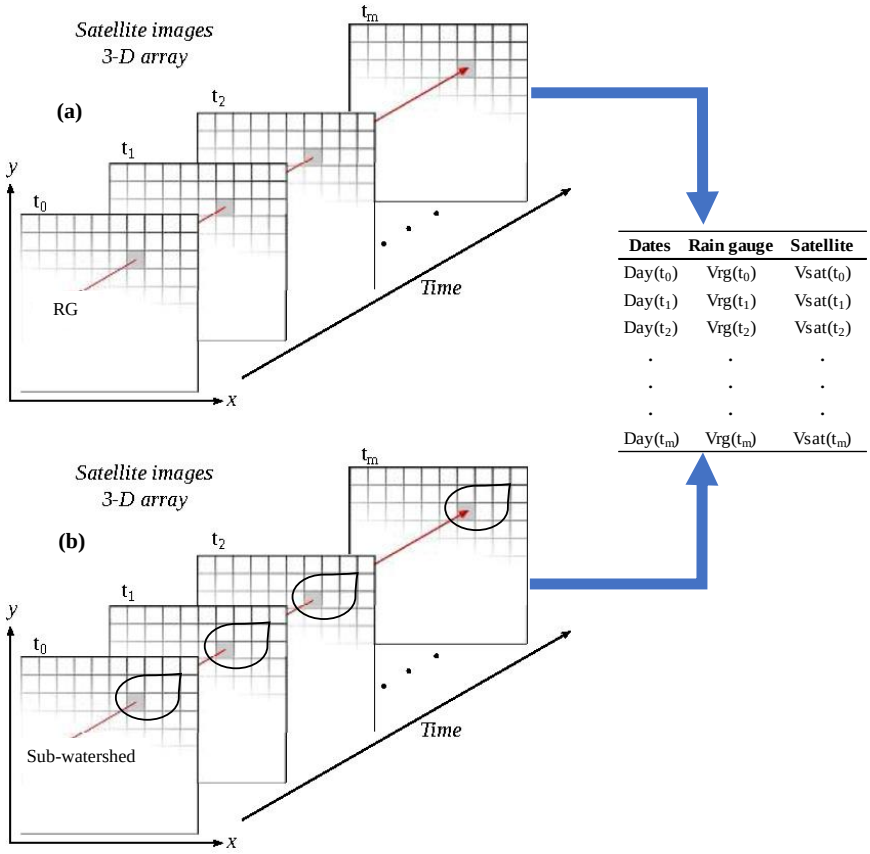

Figure 15. Schematic illustration of the data retrieval from the gridded data files using RG (a) and sub-watershed (b) masks. X, Y, t, Vrg, and Vsat refer to the longitude, latitude, time indices, values obtained from RGs, and the values retrieved from the gridded data, respectively.

2.5. Methodological Summary

The general methodology (aims, study area, and data) is summarized in Figure 16. More detail about the implementation of each of the methodological approaches, including the theoretical basis and formulas of the statistical metrics, can be found in their respective chapters hereinafter. The main aim of this thesis was to evaluate the performance of eight SRP datasets over the OERB. To this end, the capability of the datasets in estimating the daily rainfall was investigated through direct comparison and hydrologic modeling approaches. The first consists of a comparison between the RG and SRP datasets retrieved as GC and WAvg time series. The comparison between the two data sources was held using categorical and standard statistical metrics as indicators of their degree of agreement. In the second approach, the WAvg time series of the eight SRP datasets were used as rainfall inputs to calibrate the HBV conceptual model. The SRPs were then hydrologically evaluated by comparing the simulated daily streamflow against the one gauged at the outlet of the Ait Ouchene and Tilouguite sub-watersheds. Prior to this, the HBV model was tested through a calibration/validation exercise in the Ait Ouchene sub-watershed. In addition, the model's structure was investigated by conducting sensitivity and interdependency analyses of the model's internal parameters. This step that took place before the evaluation processes, firstly, allowed us to evaluate the capability of the model to simulate the daily streamflow in the considered sub-watersheds. Secondly, it helped us to outline the model's structure adequacy to the hydroclimatic context of the study area. Furthermore, depending on the evaluation outcomes, bias correction techniques were applied on certain SRP datasets. The correction operation was considered to account for or reduce the bias contained in the SRP estimates relative to the RG data.

The SRP data evaluation was preceded by a comprehensive analysis of the hydroclimatic variables (rainfall, SCA, temperature, streamflow, TWS, and GWS) over the OERB. The main aim of this analysis was the characterization and understanding of the hydroclimatic context of the OERB.

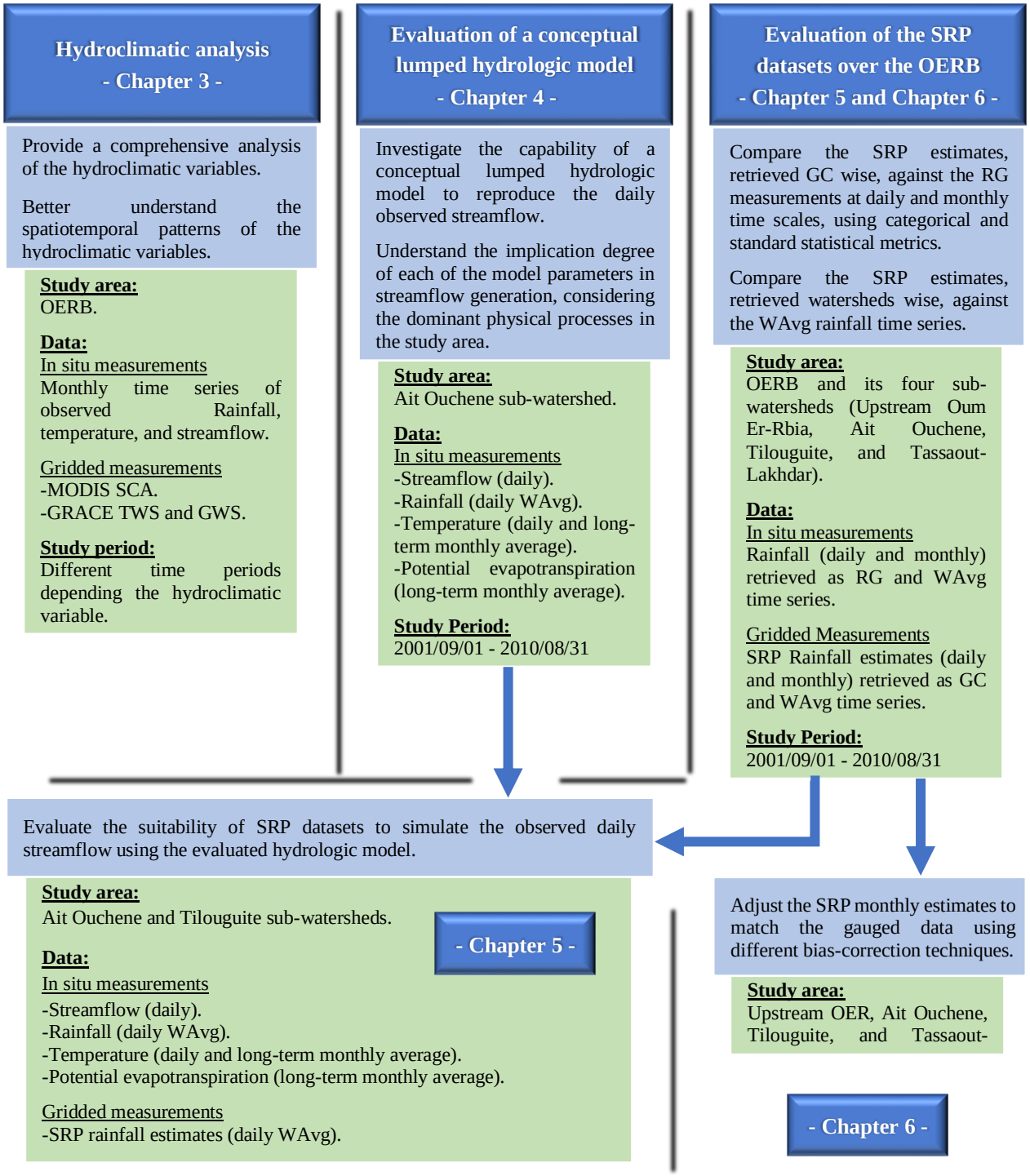

Figure 16. Flowchart of the general methodology of the thesis.

Chapter 3. Analysis of the Hydroclimatic Variables Over the OERB - Anomalies, Drought, and Trends

Ouatiki, H., Boudhar, A., Ouhinou, A., Arioua, A., Hssaisoune, M., Bouamri, H., Benabdelouahab, T., 2019. Trend analysis of rainfall and drought over the Oum Er-Rbia River Basin in Morocco during 1970–2010. Arab. J. Geosci. 12, 1–11. https://doi.org/10.1007/s12517-019-4300-9

3.1. Introduction

The Moroccan kingdom undergoes influences from the Mediterranean, the Atlantic Ocean (locally named Gharbi), and the Sahara (locally named Shergui). The precipitation occurrence is largely influenced by the NAO (North Atlantic Oscillation, Lamb and Peppler 1987; Knippertz, Christoph, and Speth 2003). In addition, the mountain chains that spread over the Moroccan territory considerably affect the spatial distribution of precipitation. It is the case of the Atlas chain that holds the credit for water availability in the OERB and, thus, the socio-economic development driven by agricultural production. The water held in dams contributes to the irrigation of the Tadla perimeter, one of the most important irrigated areas in Morocco. Indeed, it is necessary to investigate the hydroclimatic variables in order to enhance our knowledge about their long-term patterns over the OERB.

In this chapter, we aim to provide an analysis of the temporal variability of the hydroclimatic variables over the OERB by:

- Investigating the annual patterns of temperature, rainfall, SCA, streamflow, TWS, and GWS.
- Analyzing the deficit of annual rainfall using the SPI,
- Assessing temperature, rainfall, SCA, streamflow, TWS, and GWS trends using the Mann–Kendall test.

These analyses were conducted based on a set of monthly in situ data from a total of 15 gauging stations (rainfall, temperature, and streamflow) in addition to satellite data (SCA, TWS, and GWS). The name and number of gauges used for each of the hydroclimatic variables can be found in Table 2, Table 3, and Table 4 (see the column "Chapter"). The study period varies depending on the variables' data availability (as reported in Table 2, Table 3, and Table 4 "Time range" column). It was set such that to maximize the temporal coverage of each variable individually and match the gauge with the shortest time range.

3.2. Methods

3.2.1. Standardized Precipitation Index

The SPI was proposed by McKee et al. (1993) to quantify the rainfall deficit observed during a specific period. In 2009, the WMO recommended the SPI as the standard index for tracking and monitoring meteorological drought (WMO, 2012), through the Lincoln Declaration on Drought Indices (Hayes et al., 2011). Applicable in all climatic regimes, the SPI is classified as a green index due to its simplicity and ease of use (WMO & GWP, 2016). Only rainfall data are required for it to be computed, and it is as good for detecting wet periods as it is for dry periods. The SPI is tolerant of missing data and it can be calculated on time series of at least 20 years of length. However, a period of more than 30 years is ideal and would give more robust results (WMO & GWP, 2016).

The SPI is calculated as the difference of rainfall from the mean of a specified period divided by the standard deviation (Equation 7):

$$\mathrm{SPI} = \frac{\mathrm{P_i} - \overline{\mathrm{P}}}{\sigma} \qquad \text{Equation 7}$$

Where:

P_i: rainfall total of the year i;

$\bar{P}$: mean annual rainfall of the time series;

σ: standard deviation of the time series.

The classes of drought intensity according to the SPI values are reported in Table 7.

Table 7. Classification of drought intensity based on the Standardized Precipitation Index Values

Threshold	Description
ISP ≥ 2	Extremely wet
1.5 ≤ ISP < 2	Very wet
1 ≤ ISP < 1.5	Moderately wet
0 < ISP < 1	Mildly wet
-1 < ISP < 0	Mildly dry
-1,5 < ISP ≤ -1	Moderately dry
-2 < ISP ≤ -1.5	Severely dry
ISP ≤ -2	Extremely dry

3.2.2. Mann Kendall Trend Test

The Mann-Kendall is a statistical test for checking trends in time series. It evaluates whether *X* (observed values) tend to increase or decrease over time. It is essentially limited to test the null hypothesis that no trend exists in the data, without estimating the magnitude of change. It is a free distribution test; no assumption regarding the normality of the data is required. However, there must be no serial correlation for the resulting p-values to be correct (Helsel and Hirsch, 1992)

Mann, (1945) proposed a test for the monotonic trend based on τ (tau), a rank correlation coefficient defined by Kendall, (1938). The τ coefficient assesses the independence between two different variables, where one of them is arranged in an objective order (Kendall, 1970). Mann-Kendall constitutes a particular case of Kendall's test for correlation, where the arranged variable is the time (Hipel and Mcleod, 1994)

To perform the test, Kendall's *S* statistic is computed from the *X* and time data (Kendall, 1970). A subtraction between all consecutive observed data pairs is computed and a value of +1, 0, or –1 is assigned to positive differences, no differences, or negative differences, respectively. Then, the test statistic *S* is calculated as the sum of the computed integers:

$$S = \sum_{i=1}^{n-1} \sum_{j=i+1}^{n} sgn(X_j - X_i) \; ; \; where \; j > i \qquad \text{Equation 8}$$

Where:

$$sgn(X_j - X_i) = \begin{cases} +1 & if \;\; (X_j - X_i) > 0 \\ 0 & if \;\; (X_j - X_i) = 0 \\ -1 & if \;\; (X_j - X_i) < 0 \end{cases} \qquad \text{Equation 9}$$

A positive value of *S* indicates an upward trend and a negative value means a downward trend. When the absolute value of *S* is small, no trend is indicated.

According to Kendall, (1970), for a large sample size (*n* >10) the frequency of distribution tends to be normal. Thus, considering the presence of ties, the mean value of *S* (*E(S)* = 0) and the variance (*var S*) can be defined as:

$$var \; S = \frac{1}{18}\left\{ n(n-1)(2n+5) - \sum_{t} t(t-1)(2t+5) \right\} \qquad \text{Equation 10}$$

Where:

n: sample size;

t: length of the tied group.

Then, the significance of the trend results is evaluated based on the standard normal variate Z. The null hypothesis of no trend is rejected, under a certain significance level α, when $|Z| > |Z_\alpha|$.

$$Z = \begin{cases} \dfrac{S-1}{\sqrt{var \; S}} & if \;\; S > 0 \\ 0 & if \;\; S = 0 \\ \dfrac{S+1}{\sqrt{var \; S}} & if \;\; S < 0 \end{cases} \qquad \text{Equation 11}$$

3.2.3. Theil Sen Slope

Proposed by Theil, (1950) and Sen, (1968), and later extended by Hirsch et al., (1982), the Theil Sen Slope (β) is a useful index to expresses the magnitude of the trend as a slope; change in the data per unit time (Hirsch et al., 1982). The Index (also called Kendall's slope estimator), which is resistant to outliers, is defined as the median of the differences of the ordered data pairs considered in the Mann-Kendall test (Equation 12). The positive/negative β connotes the slope of the upward/downward trend.

$$\beta = median\left(\frac{X_j - X_i}{j - i}\right), \qquad where\ j > i \qquad \text{Equation 12}$$

3.3. Results and Discussion

3.3.1. Temperature

During its annual cycle in the OERB, the temperature reaches a high level in the summer months and a low level in the winter months. As illustrated in Figure 17, between 1985 and 2010, January was the coldest month according to both maximum and minimum temperature with median values around 21 °C (18 °C) and 3 °C (4 °C) at Sidi Driss Dam (Oulad Gnaou), respectively. The highest temperatures mainly appeared in July with maximum and minimum monthly temperatures of 45 °C (40 °C) and 20 °C (22 °C), respectively. The minimum temperature seemed not to show large differences between the two considered gauges. The maximum temperature, on the other hand, was relatively higher at Sidi Driss Dam, situated near the OERB's southern limit, than at Oulad Gnaou. This inlines with the North-to-South gradient characterizing the spatial distribution of temperature over Morocco (Filahi et al., 2015). Moreover, due to the elevation gradient, the temperature significantly decreases in the mountainous region of the OERB. In the winter months, minimum monthly temperatures lower than -5 °C were observed at Tilouguite (Ouatiki et al., 2017).

Annually, the coldest years were recorded in the late 1980s at Sidi Driss Dam (6.5 °C.y^{-1}) and in the first half of the 1990s at Oulad Gnaou (10.43 °C.y^{-1}). Generally, the annual temperature has known an upward tendency during the studied period (Figure 18). Except for the minimum temperature at Sidi Driss Dam, all the trend slopes were statistically significant at the 0.05 level. The maximum temperature exhibited the highest increasing rates, particularly at the gauge located

in the southern part of the OER (Sidi Driss Dam). The temperature at this gauge displayed a significant positive slope of 0.12 °C.y^{-1} against 0.06 °C.y^{-1} at Oulad Gnaou. Hence, the warmest years mainly occurred in the 2000s according to both Sidi Driss Dam (34.72 °C.y^{-1}) and Oulad Gnaou (27.97 °C.y^{-1}). These observations agree with the significant warming trends reported at small and large scales (Donat et al., 2014; Filahi et al., 2015).

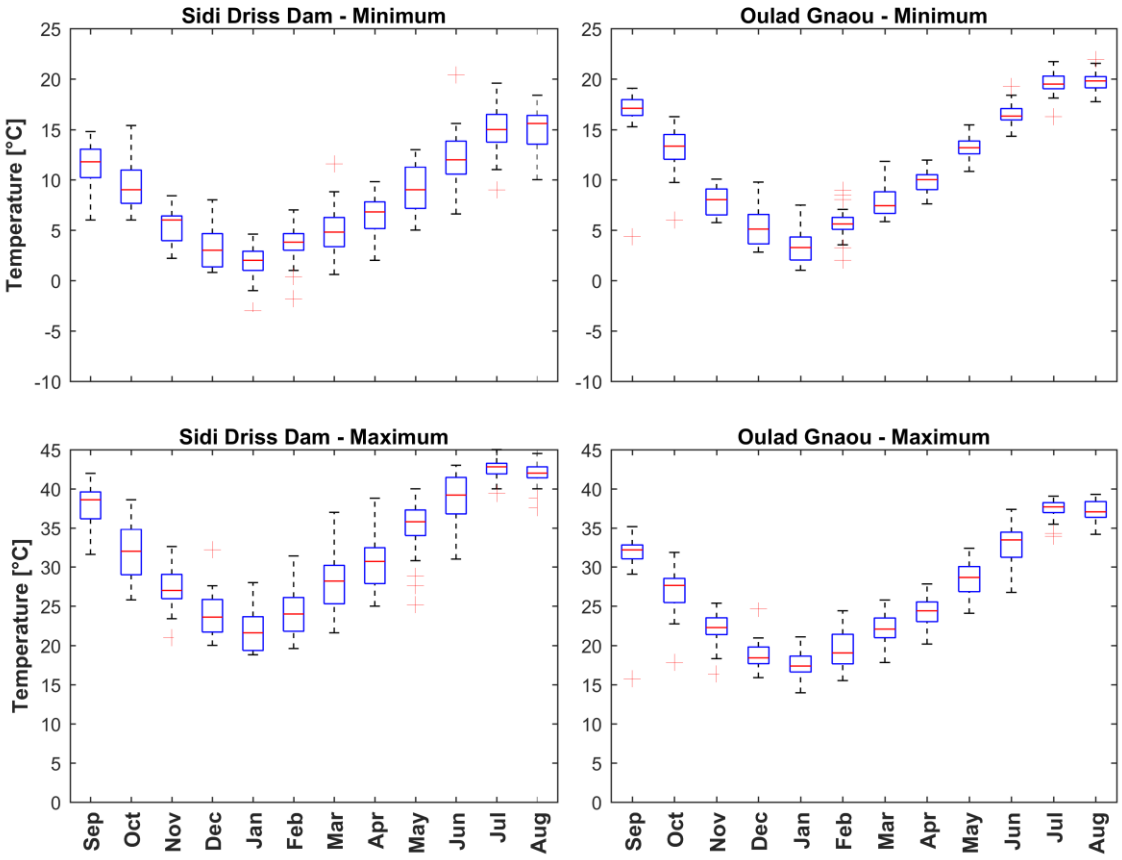

Figure 17. Interannual variability of monthly temperature over the period 1985 – 2010. Each box shows minimum (bottom whisker), 25th percentile (bottom edge of the box), 50th percentile (red line inside the box), 75th percentile (top edge of the box), maximum (top whisker), and extreme values (red plus markers).

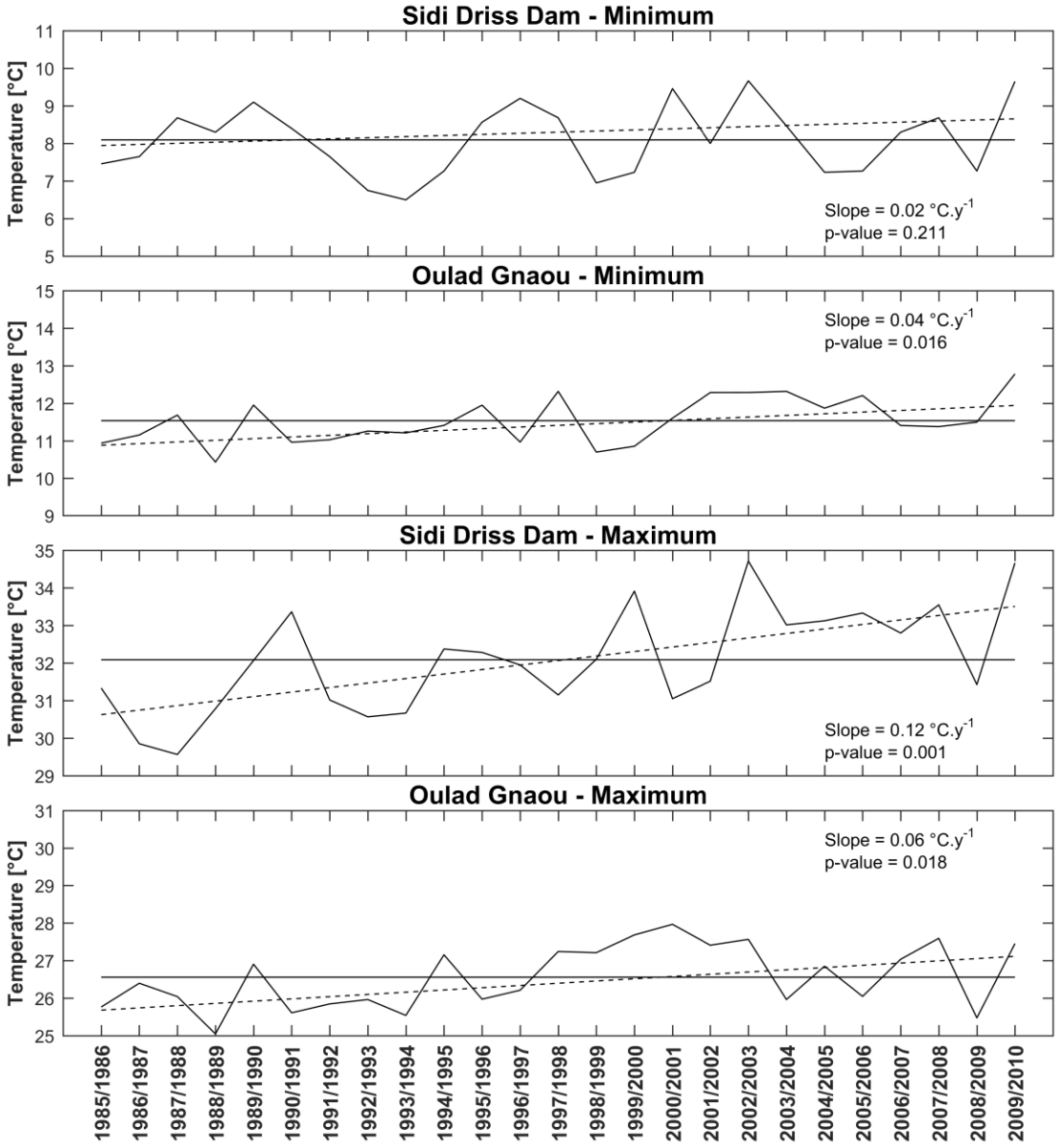

Figure 18. Annual average temperature variability over the period 1985 – 2010. The dashed lines refer to the trend lines, the slopes of which are annotated within the subplots. The solid straight lines refer to the long-term average.

3.3.2. Rainfall

3.3.2.1. Overall Variability

Generally, the study area is characterized by a Mediterranean climate with cold wet winter and hot dry summer. Besides the western advections, which are the dominant source of moisture in the OERB (Moniod and Roche, 1973), the orographic uplifting effect plays a major role in stimulating rainfall generation over the study area. The Atlas chain, which limits the OERB from the east, holds most of the humid advections along its western slope. Hence, a strong contrast marks

the southeastern slope of the Atlas, in terms of rainfall amounts, where the mean interannual is around 100 $mm.y^{-1}$ (Navas et al., 2013).

The OERB is predominantly semi-arid with sub-humid parts on high elevations of the Atlas (Mokhtari et al., 2013). It is characterized by a strong spatiotemporal variability of rainfall. During the period from 1970 to 2010, the total annual rainfall ranged from 80 $mm.y^{-1}$ in the lowlands to about 1100 $mm.y^{-1}$ in the mountainous region (Figure 19.b). An exceptionally wet year, up to 1500 $mm.y^{-1}$ was recorded at Aval El Heri within the wetter region of the OERB. The relationship between the total annual rainfall and elevation was far from being perfectly linear. However, the mountainous region received the largest amounts of rainfall with a regional average of 480 $mm.y^{-1}$. In the lowlands (including Al Massira, Ouled Sidi Driss, Ouaouirinth, and Oulad Gnaou), the average was around 330 $mm.y^{-1}$ with 75% of the years were less than 370 $mm.y^{-1}$ (Figure 19.b).

In the OERB, the annual cycle of rainfall showed a clear seasonal variability with two distinct periods. A wet period spanning from November to April and a dry period extending between the month of June and September. These two periods are separated by the months of October and May that we considered as transitory months. The smallest amounts of rainfall often occurred during the summer (June, July, and August). July was the driest month throughout the study period with monthly values hardly exceeding 15 $mm.m^{-1}$ (Figure 19.a). Nevertheless, sometimes high rainfall amounts, produced as a result of stormy events, were frequently observed in August. During the wet period, the monthly totals generally remained low. Over the entire study area, nearly 60% of the monthly totals recorded during 1970 – 2010 were less than 60 $mm.m^{-1}$, except in the mountainous area where some RGs collected more than 200 $mm.m^{-1}$. From one year to another, the peaks fluctuated over all the months of the wet period. A great number of RGs have known a strong occurrence of maxima, respectively, during April, January, and November. Moreover, 40% of the annual rainfall total was ensured by the winter months (December, January, February), 10% more than those of the spring season (March, April, and May).

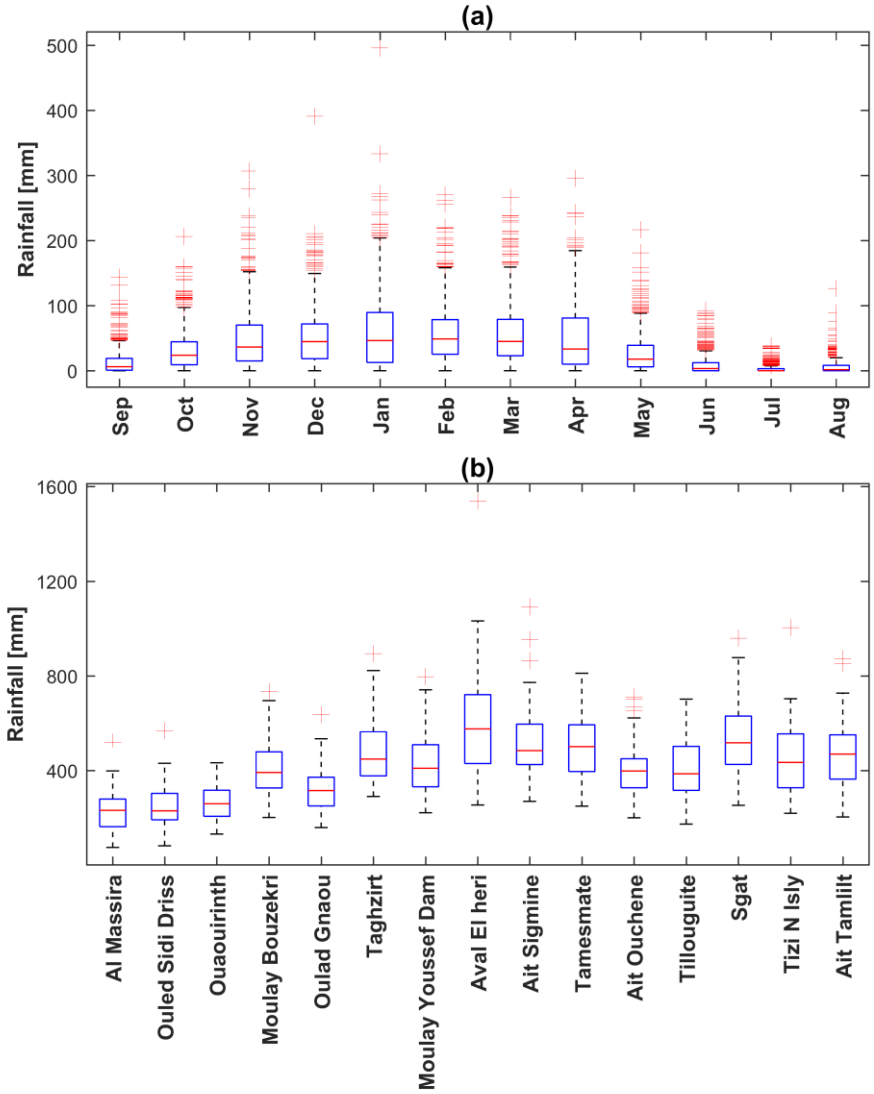

Figure 19. (a) monthly and (b) annual rainfall totals recorded over the OERB (1970 – 2010).

3.3.2.2. Drought Analysis

Since the 1970s decade, the OERB underwent noticeable changes in terms of rainfall, manifested in persistent dry periods and isolated or few consecutive wet years. The watershed experienced an overall deficiency of water supplies, particularly since the early 1980s. As it was identified via the SPIs (Figure 20), during the period extending from 1970 to 2010, the dry years occurred relatively more frequently than the wet years. The percentage of occurrence ranged from 50% at Tamesmate and 63% at Ouled Sidi Driss. However, all the studied RGs exhibited a predominance of small intensity deficits. On average, 72% of the years were mildly dry against 22% moderately dry, while less than 10% were severe. No extremely dry years were reported over

the whole study period. On the other hand, the 1970s were mostly marked by wet years. Five RGs showed a clear and persistent wet period occupying the whole decade, with some very to extremely wet years. Some shorter periods were observed in the rest of the RGs, most of which took place in the second half of the decade. Except in the 1970s, the wet periods were less frequent and generally of small lengths. They were mostly of few successive years that permeate two successive dry periods. However, two wet periods of three years long were observed at several RGs. The first appeared between 1987/1988 and 1989/1990 and the second between 1995/1996 and 1997/1998. The 1995/1996 year was the wettest over much of the study area, particularly at the Tizi N lsly and Aval El Heri, the same as in many regions in Morocco (Driouech, 2010). During the same period (from 1995/1996 to 1997/1998), several places witnessed important flood events that caused human losses and significant damages in the infrastructures and agricultural lands (Daoudi and Saidi, 2008; MEMEE, 2008).

Aval El Heri, Moulay Bouzekri, and Taghzirt were the first to experience a dry period of four years starting in 1971/1972. The 1980/1981 year was of a significant impact at nearly all RGs of the OERB. Starting from the same year, the watershed experienced a succession of dry episodes interspersed by a few moderately to extremely wet years. The first one, which lasted between 5 and 7 years, took place in the early 1980s and was almost widespread over the entire watershed. The second, which counted 3 to 5 years long, occurred between 1990/1991 and 1994/1995. At some RGs, these two periods were almost connected to one another, except for the occurrence of some slightly humid years. These intense multi-year drought periods, identified by Esper et al., (2007) Driouech, (2010) over several areas of Morocco, have led to a dramatic reduction of agricultural production causing the GDP to decline and provoke serious economic instability (Fatna and Handoufe, 1997; Jlibene and Tychon, 2007). Xoplaki et al., (2004) and Sousa et al., (2011) also reported these two periods to be severe over the whole Mediterranean basin. It was suggested that the dry conditions during the 1980s and the 1990s were mostly driven by the NAO positive phase (Hurrell and Van Loon, 1997; Lamb and Peppler, 1987; Physics, 2009). Further, since 1997/1998 a third dry period occurred at all RGs with a length that varied between 4 and 6 years. The last dry period appeared between 2004/2005 and 2007/2008 with a slightly humid year in 2005/2006.

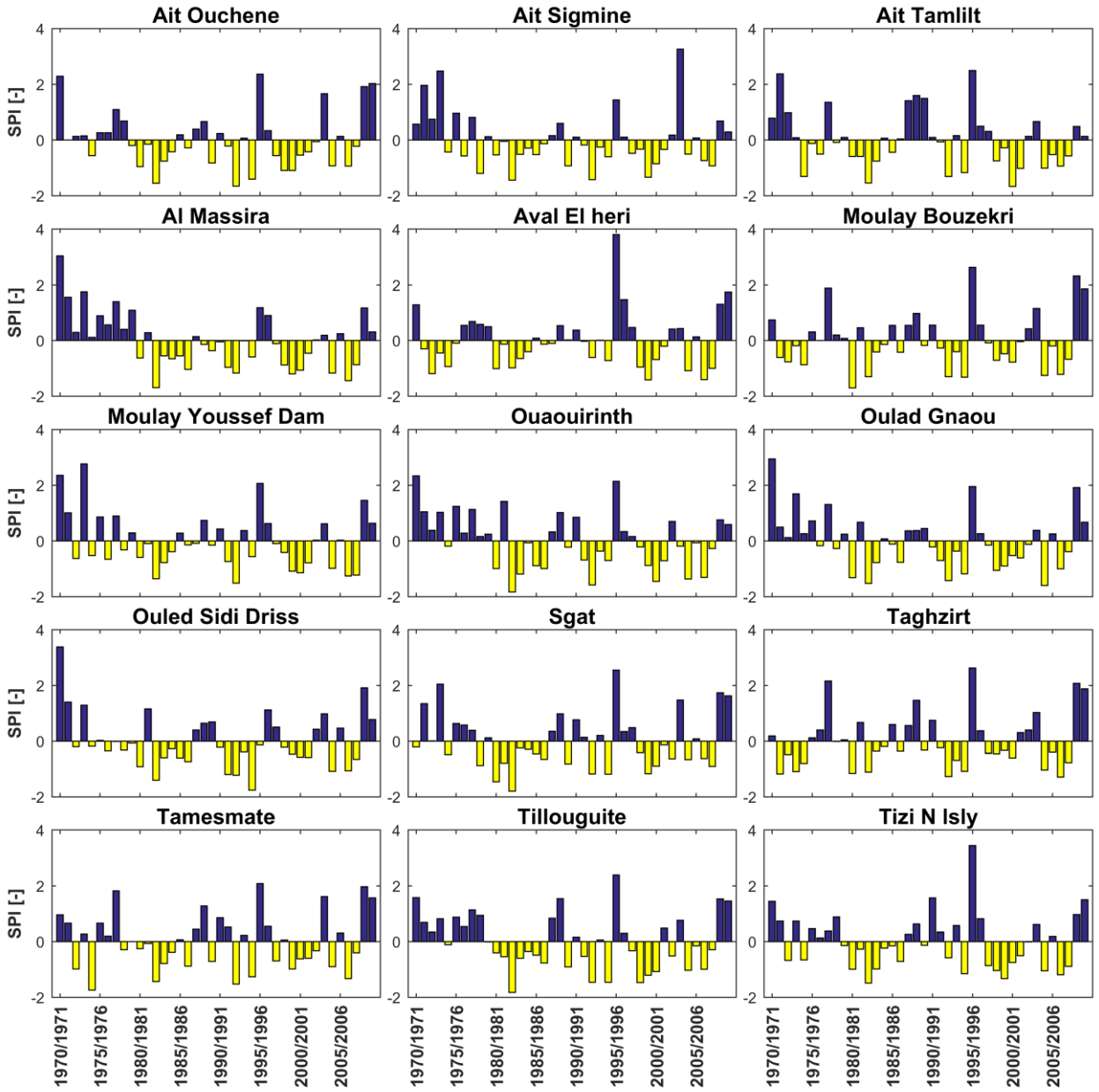

Figure 20. Standardized Precipitation Index computed for the period 1970 – 2010.

3.3.2.3. Trend Analysis

During the study period (1970 – 2010), the annual rainfall showed a predominant decreasing trend over the OERB, except for Aval El Heri, Moulay Bouzekri, and Taghzirt (Table 8). The latter RGs, which are located relatively close to the foothill of the Middle Atlas, exhibited a non-significant increasing trend. Among the fifteen considered RGs, only Al Massira, Ouaouirinth, and Oulad Gnaou experienced a significant decline in rainfall. The rates of decrease at these three RGs, situated in the lowlands, were relatively close. However, the highest magnitude of decrease was

observed at the Oulad Gnaou with about -3.87 mm.y^{-1}. These declining tendencies were mostly accounted for the first two decades. The period from 1970 to the mid-1980s has known the sharpest decrease in the rainfall annual totals (Figure 20). This remark was observed for ten out of fifteen studied RGs. After the 1980s, According to Tramblay et al., (2013), who studied rainfall trends over the North African countries, a slight increase took place over the northern region of morocco. The authors reported this increase as insignificant and linked it to the amply positive anomalies registered in 1995/1996 and 2009/2010.

Table 8. Sen Slop computed for annual and seasonal rainfall time series for the period 1970 – 2010 (Bold values express the significant Slops at α = 0.05).

RG names	Annual	Autumn	Winter	Spring	Summer
Ait Ouchene	-0.92	1.47	0.06	-1.37	0.32
Ait Sigmine	-2.57	1.05	-0.02	-3.14	0.02
Ait Tamlilt	-2.35	0.49	-0.21	**-2.93**	0.67
Al Massira	**-3.49**	-0.03	-0.99	**-1.65**	-0.05
Aval El Heri	0.23	0.29	0.54	-1.15	-0.14
Moulay Youssef Dam	-2.47	0.57	-0.52	**-2.43**	0.18
Moulay Bouzekri	0.33	1.12	1.06	-1.31	-0.01
Ouaouirinth	**-2**	0.06	0	**-1.71**	0
Oulad Gnaou	**-3.87**	-0.14	-0.96	**-2.26**	-0.08
Ouled Sidi Driss	-1.17	0.38	-0.10	-0.85	0
Sgat	-0.76	1.52	0.53	-2.14	0.43
Taghzirt	0.91	1.54	1.50	-1.82	0
Tamesmate	-0.28	1.06	1.13	-1.66	0.13
Tilouguite	-3.27	0.83	-1	**-2.30**	0.25
Tizi N lsly	-1.70	1.14	-0.73	-1.82	0.57

Considering the seasonal and monthly totals, we note that at the same site, rainfall trends showed different directions throughout the year (Table 8 and Figure 21). However, there were more negative instants than positives, suggesting an overall tendency towards drier conditions. The rainfall decreases were mainly concentrated around the winter and spring seasons, while the summer and autumn mostly exhibited increasing trends. In the summer months, except for some isolated points that showed a rainfall decrease during the month of June, all the obtained tendencies were either null or very low positive slopes. The latter were found to be spatially frequent during

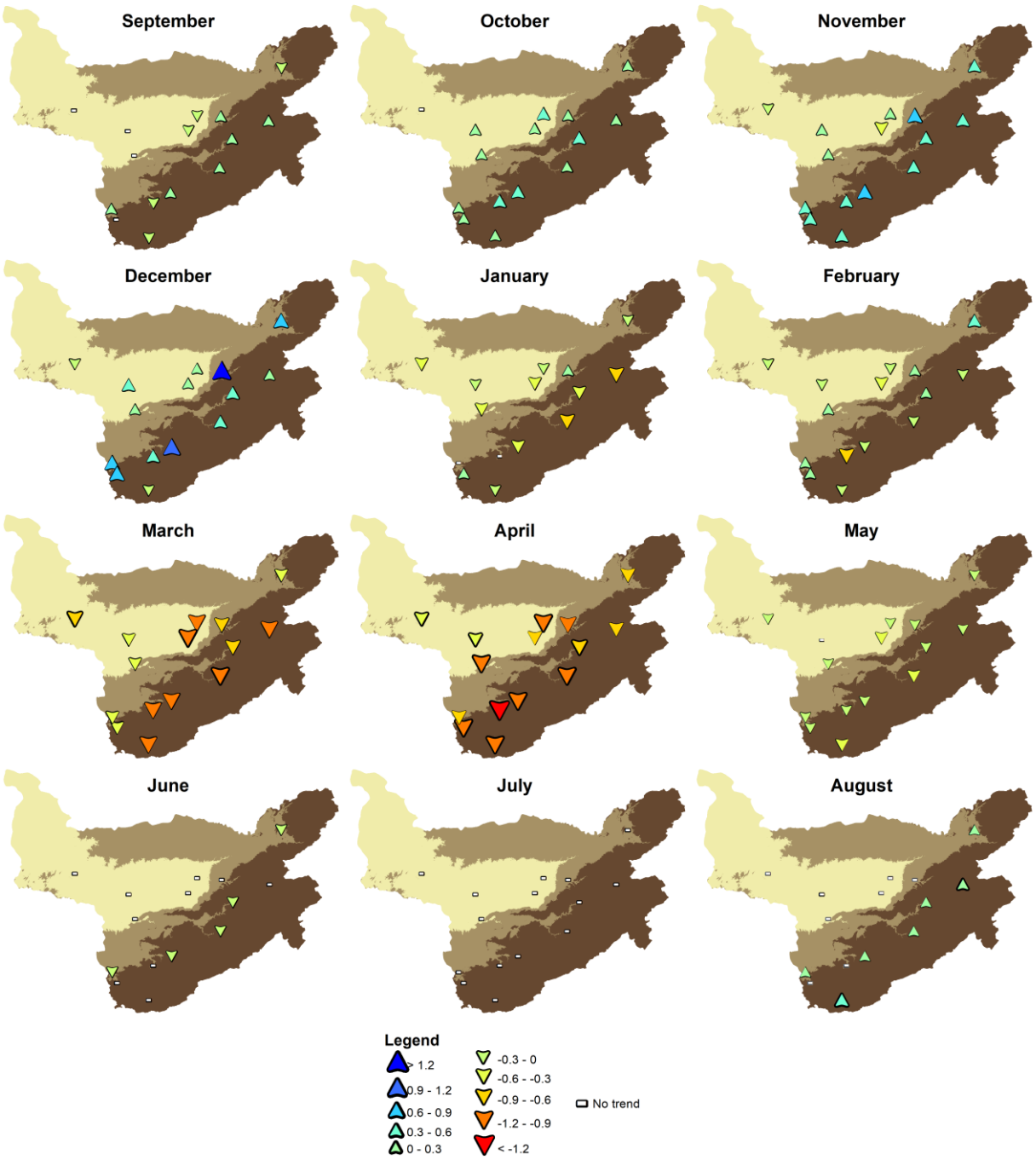

Figure 21. Rainfall trend directions computed for each month over the period 1970 – 2010 (triangles with Bold limits express significant trends at α = 0.05).

the month of August. Only Ait Tamlilt and Tizi N lsly, the highest RGs in terms of elevation, showed notable rainfall increases with statistically significant rates of +0.37 $mm.y^{-1}$ and +0.20 $mm.y^{-1}$, respectively. The rising trends were more prevalent during the autumn season, but none of which were statistically significant. The month of September showed a kind of balance between null, positive, and negative trends. October and November presented widespread positive

trends. The latter were more accentuated around December reaching +1.29 $mm.y^{-1}$ at Taghzirt. Moreover, the falling tendencies started to take place in January and February, except for some positive slopes found at the foothill RGs. The average rate of decrease for these two months was -0.4 $mm.y^{-1}$ (January) and -0.24 $mm.y^{-1}$ (February) with no RG showing a statistically significant decrease. The negative trends were much more spatially homogeneous during spring. All the RGs demonstrated a noticeable decrease in rainfall in all three months of the season, except at Ouled Sidi Driss the slope was almost null in May. The remarkable decline during the spring season was largely driven by the important decreases that occurred during the month of March but mainly by those of the month of April. The latter experienced drastic drops in monthly rainfall totals with slopes up to -1.52 $mm.y^{-1}$ (at Ait Sigmine). The importance of decline was also reflected in the spatial scale, where ten RGs showed statistically significant decreases at an average rate of -1 $mm.y^{-1}$. The impact of the rainfall decrease was noticed in the irrigated perimeter of Tadla. Between 2003 and 2010, the pumped groundwater used in irrigation has increased by 6.28% (ABHOER 2012, Lionboui et al. 2016b), as the farmers relied more on groundwater to compensate for the rainfall deficit.

3.3.3. Snow Cover Area

Over high elevations of the Atlas mountains, part of the precipitation occurs as snow with a strong seasonality (Boudhar et al., 2020). It starts to take place in October and intermittently covers the ground surface through March until it completely vanishes in the late spring (Boudhar et al., 2020). This can be also seen in Figure 22, which represents the daily SCA percentage (SCAp) calculated for each month over the OERB's mountainous region (area above 1000 m a.s.l ≈14 000 km^2). The maximum snow cover often took place between November and December with SCAp that can reach more than 40 %. Moreover, the snowy season is characterized by sudden snowfall episodes that can remarkably increase the snow depth and extent (Boudhar, 2009). Meanwhile, strong ablation that leads to the complete disappearance of snow can occur, even during the wintertime (Marchane, 2015).

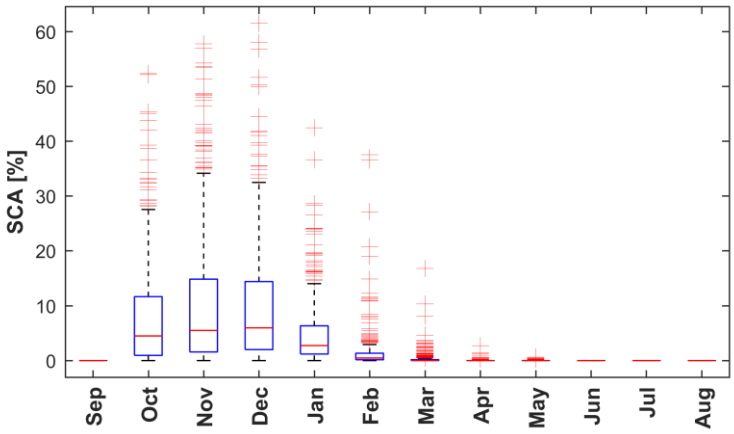

Figure 22. Interannual variability of daily SCAp for each month over the period 2000 – 2015.

Figure 23 shows the annual variability of the SCAp relative to the total area of the mountainous region of the OERB. The top and bottom subplots of the figure represent the annual maximum and median daily SCAp, respectively. From a temporal stand of point, the SCAp demonstrated a strong interannual variability. During the period between 2000 and 2015, the Atlas of the OERB received snow with a maximum extent between 38% (in 2006/2007) and 61% (in 2005/2006). However, nearly half of the snow days observed during the aforementioned period covered less than 6% of the watershed's mountainous region, except in 2008/2009 and 2014/2015. In these two years, snow days of large extents were prevalent with SCAp that fluctuated between a median value of 10% (10 %) and a maximum value of 50% (40 %) in 2008/2009 (2014/2015). Furthermore, the trend lines, calculated based on the Sen slope, suggest that the OERB is experiencing an upward tendency in maximum and median annual snow cover, since the early 2000s. Similar positive tendencies were observed in snow cover duration over the Moroccan Atlas range (Marchane et al., 2015). As shown in Figure 23, SCAp showed a median trend slope of $0.32\%.y^{-1}$ and $0.2\%.y^{-1}$ in maximum and median SCAp, respectively. None of the slopes was statistically significant at the 0.05 significance level. The presence of years with distinctly high snow metrics can be the main reason leading to this increase. Overall, it remains hard to tell whether these observed tendencies are under a long-term increase of snow occurrence or just an apparent tendency driven by the year-to-year unsteady fluctuation of snow cover.

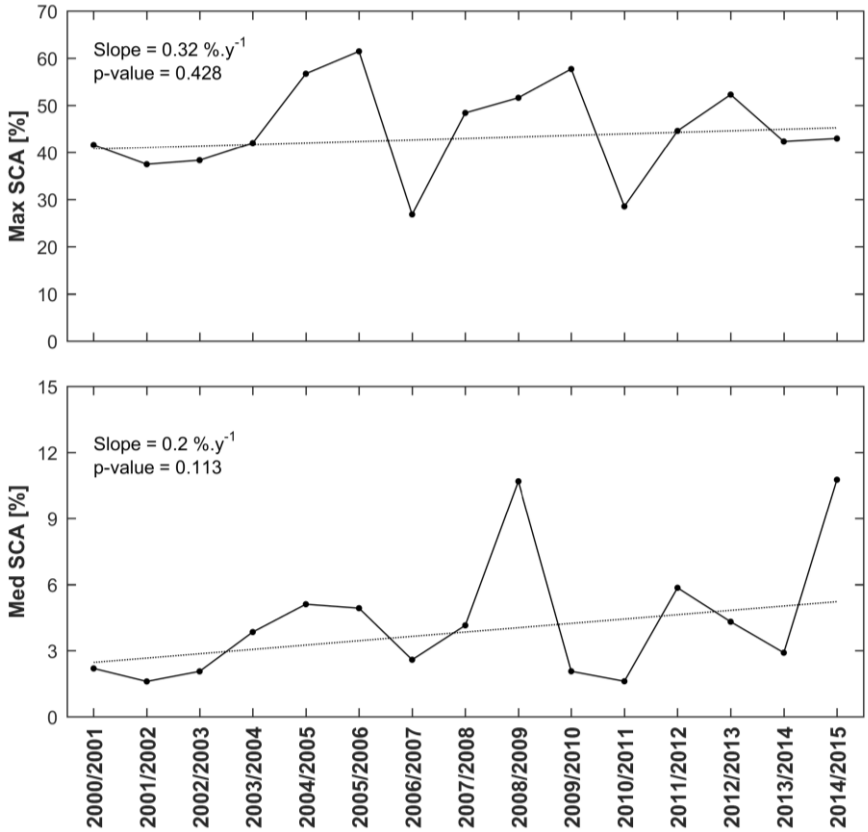

Figure 23. Annual variability of maximum (Max) and median (Med) SCAp for the period 2000 – 2015.

3.3.4. Streamflow

As illustrated in Figure 24, the maximum monthly streamflow tends to occur during the period between late-winter and mid-spring. The monthly streamflow is generally very low between early-autumn and late-summer. It starts to increase in the mid-winter to reach a maximum value in the month of February in Ait Ouchene and March in Tilouguite. Starting from mid-spring the monthly streamflow enters a declining phase until it reaches its lowest level in August. The streamflow peaks seemed to be shifted compared to those of rainfall (Figure 19.b) and SCA (Figure 22). Over both sub-watersheds, they coincide with the declining phase of precipitation. This delay observed in the hydrograph of both sub-watersheds indicates the contribution of snowmelt to the streamflow generation (Boudhar et al., 2020). Annually, the streamflow underwent strong changes since the late-1970s. Several deficient years were reported all along the study period (Figure 25). In Ait Ouchene around 64% of the years were below the long-term average, against 61% in Tilouguite. Long-lasting deficit periods occurred on two occasions in both sub-watersheds: one in the 1980s and the other between the late-1990s and the early-2000s. These temporal patterns concord with what was reported earlier for rainfall using the SPI. Moreover, while the first period

was the largest in terms of length (eight years) and magnitude in Ait Ouchene, the two periods (six years) were relatively close in Tilouguite. Another period of four years hit Tilouguite in the late-2000s, which included the driest year that ever took place during the whole studied period. Accordingly, contrasted tendencies, yet with weak and statistically insignificant slopes (Figure 25), were observed for Ait Ouchene (increasing trend) and Tilouguite (decreasing trend).

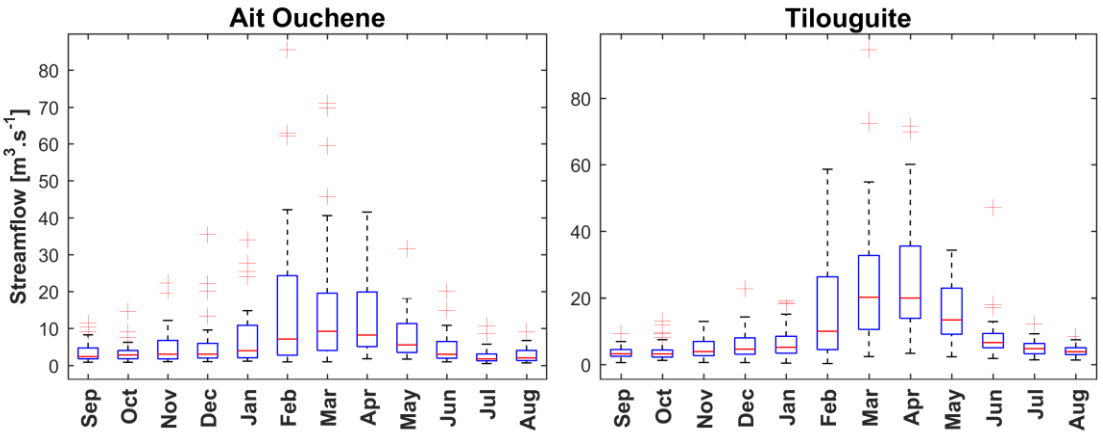

Figure 24. Interannual variability of mean monthly streamflow over the period 1977 – 2010.

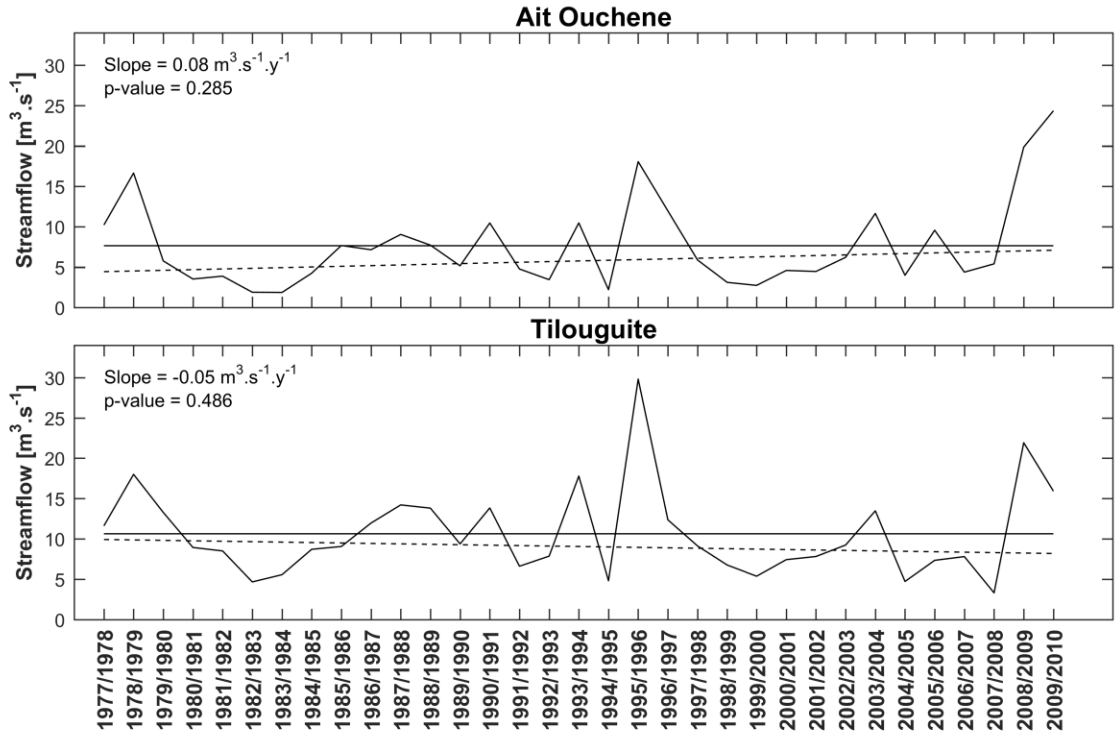

Figure 25. Variability of the annual mean streamflow over the period 1977 – 2010. The dashed lines refer to the trend lines, the slopes of which are annotated within the subplots. The solid straight lines refer to the long-term average.

3.3.5. Total and Ground Water Storages

Figure 26 represents the temporal variability of the TWS as obtained from CSFR mascon GRACE data, SM from the Surfex model, and GWS (after subtracting the SM from the TWS as described in Equation 6) over the OERB. Each of the TWS and GWS time series was tested for trend using the non-parametric seasonal Mann-Kendall test. Three trend lines, based on the Sen slope, were reported on each of the subplots. The first line, in dots, represents the overall trend of the water storage considering the whole study period (09/2003 – 08/2015). The other two lines represent the tendency before and after the 2008/2009 hydrologic year; a potential year of groundwater recharge. The statistics of each of the trend lines are annotated inside the subplots, where the left, middle, right annotations refer to the before, overall, and after trend lines, respectively. As shown in Figure 26 and Figure 27 the TWS and GWS exhibit a clear seasonality over the OERB. Both water storages took lower values during the early-autumn and maximum values in the spring season. The same as the streamflow, the TWS and GWS peaks seemed to be

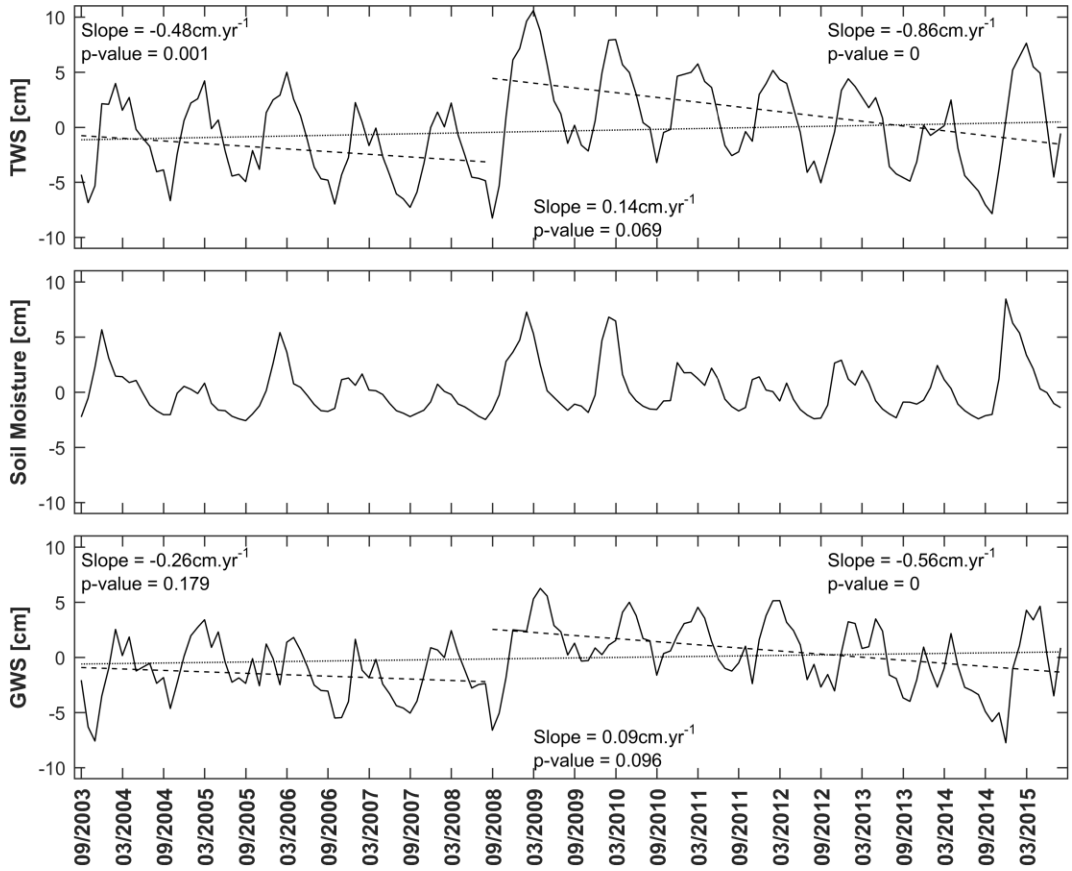

Figure 26. Time series showing the fluctuations in monthly GRACE TWS, soil moisture from Surfex, and GWS over the OERB (2003 - 2015).

shifted compared to the observed peaks in precipitation. This suggests that the rise in TWS and GWS in the spring can be a kind of response to precipitation feeding the continental water reservoirs during the wet period (November – April). Furthermore, annually, it may appear from the full reference period trend lines that the TWS and GWS have known a rising tendency since 2003 (Figure 26). This can be concluded from the positive slopes, yet weaker and insignificant (at the 0.05 significance level). The trend rates were necessarily influenced by the important TWS and GWS recovery in 2008/2009 and 2014/2015. As shown in Figure 26, since 2003 the OERB underwent a persistent and significant decreasing tendency in terms of TWS and GWS. This decline was ruptured in 2008/2009 by a sudden peak that can be induced by a potential recharge of the groundwater storage. After that, the depletion was resumed with a steady annual decline until a second peak that occurred in 2014/2015. The median decreasing rates of the second period (from 2008/2009 to 2014/2015) were also statistically significant and relatively higher than those estimated for the first period (from 2003/2004 to 2007/2008). Remarkably, the GRACE signal showed a temporal pattern closer to that of the precipitation. One of the peaks observed in the GRACE time series actually occurred in a year (2008/2009) that was marked as very wet (according to the SPI) in several regions of the OERB (Figure 20). In the same year, snow events of larger extents have frequently covered the mountainous region of the OERB more than in any other year of the reference period (Figure 23). This may indicate a potential contribution of the precipitation to the relative enhancement of the terrestrial water storage. Overall, the temporal fluctuation of the precipitation and GRACE time series suggests that the terrestrial water resources were subject to intermittent episodes of consistent depletion, interspersed by storage gain from important surface water supplies. This can be deduced from the prevailing storage declines that separately took place after 2003/2004 and 2008/2009. The first falling tendency (after 2003/2004) can be part of a continuous decline that may have started after a susceptible significant storage rise in 1995/1996 (an extremely wet year).

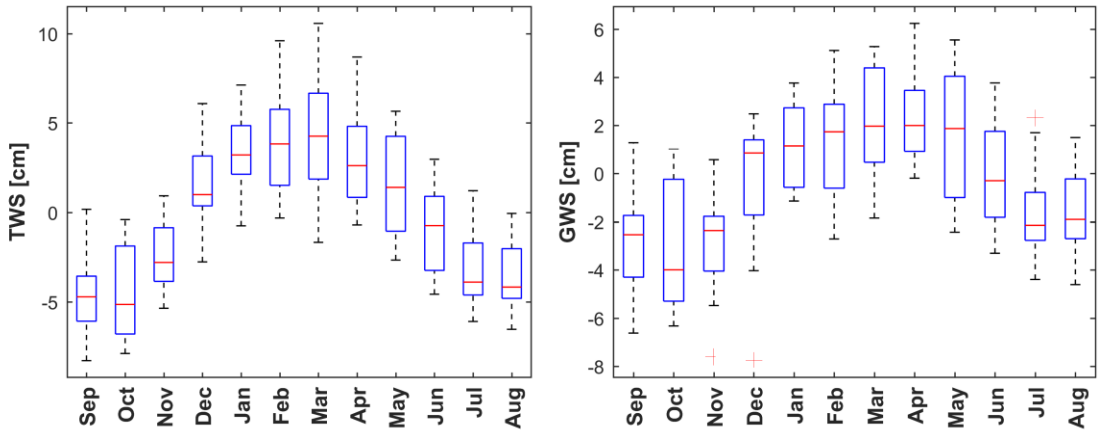

Figure 27. Interannual variability of the monthly TWS and GWS over the period from 2003 to 2015.

Chapter 4. Evaluation of a Conceptual Lumped Hydrologic Model to Simulate the Daily Streamflow: Calibration, Sensitivity, and parameters interdependency

Ouatiki, H., Boudhar, A., Ouhinou, A., Beljadid, A., Leblanc, M., Chehbouni, A., 2020. Sensitivity and Interdependency Analysis of the HBV Conceptual Model Parameters in a Semi-Arid. Water 12, 2440. https://doi.org/10.3390/w12092440

4.1. Introduction

Hydrologic models, with different levels of complexity, have become an inherent tool in water-related studies. However, the availability of hydroclimatic data constitutes one of the main constraints to run and develop such models. Although subject to a certain degree of uncertainty, parsimonious conceptual models with low input data requirements are often the only option for streamflow modeling in poorly gauged semi-arid watersheds. In this context, the objective of this chapter is to evaluate the capability of the HBV model to reproduce the daily streamflow gauged at the outlet of Ait Ouchene. The evaluation was made using a set of nine consecutive years (from 2001/2002 to 2009/2010) of in situ hydroclimatic measurements (rainfall, temperature, and streamflow) and remotely sensed snow SCA (Table 2, Table 3, Table 4, and Table 6). First, the model was calibrated and validated against daily streamflow data and tested for temporal transferability within the same watershed. Then, the sensitivity of the model was examined using the sets of parameters that provided the steadiest performance over much of the study period. Lastly, an interdependency analysis was carried out to emphasize the compensation effect between the model parameters in response to the interannual changes in hydroclimatic conditions.

4.2. Methods

4.2.1. HBV Model

Among the wide range of conceptual hydrologic models available in the literature, HBV (Hydrologiska Byråns Vattenbalansavedlning) has been tested and applied in numerous regions of different physiographic and climatic contexts (Bergström 2006), since its first released version (Bergström and Forsman, 1973). The model was originally developed by the Swedish Meteorological and Hydrological Institute (SMHI) for flood warnings and runoff forecasting in Scandinavian catchments (Bergström, 2006, 1992; Bergström and Forsman, 1973; Bergström and Lindström, 2015). Later on, the model gained trust around the world and multiple versions have become available (Braun and Renner, 1992; Krysanova et al., 1999; Lindström et al., 1997; Seibert, 2005; Stahl et al., 2008). The HBV model demonstrated significant potentials for predicting streamflow in ungauged watersheds (Arheimer, 2006; Bergström, 2006; Johansson, 1992; Samuel et al., 2012; Seibert and Beven, 2009). The model was also used to reproduce the water balance components to analyze their temporal variability (Rientjes et al., 2013; Thapa et al., 2017). In additions, numerous works have used the HBV model in various applications: the assessment of climate change impact on water resources (Bergström et al., 2001; Chen et al., 2012; Roar Saelthun et al., 1998; Vehviläinen and Lohvansuu, 1991), the evaluation of the impact of landscape characteristics and land cover changes on the runoff response (Brandt et al., 1988; Teutschbein et al., 2018), and the investigation of the influence of geomorphologic characteristics on groundwater modeling process (Parra et al., 2019). Overall, the HBV model was found to reliably perform under different climatic and physiographic contexts (Braun and Renner, 1992; Dakhlaoui et al., 2017; Parra et al., 2018; Poméon et al., 2017). Dakhlaoui et al., (2017) have found that HBV was capable to reproduce most of the observed runoff in twelve watersheds in Tunisia. Parra et al., (2018) concluded that the generation of quick runoff was better represented by HBV in two Chilean watersheds. The worldwide applicability of the HBV model was made possible thanks to its low data requirements and its detailed physically sound structure (Bergström, 2006; Bergström and Lindström, 2015). The latter describes most of the significant physical processes that come into play for runoff generation (Bergström, 1992). Although they are of huge attractiveness in hydrologic modeling, these kinds of models can be quite challenging when used to simulate streamflow under certain circumstances. The relatively large number of parameters constitute a

significant constraint in terms of computing power (Beven, 1989). Furthermore, the comprehensive description of the hydrologic process in conceptual rainfall-runoff models increases the risk of overparameterization and provokes parameter interdependency (Beven, 1989; Sorooshian and Gupta, 1983; Uhlenbrook et al., 1999). This reduces the reliability of parameter estimation and increases their uncertainty, where multiple parameter combinations can yield equally good results (Beven, 1989; Keith Beven and Andrew Binley, 1992; Seibert, 1997; Uhlenbrook et al., 1999).

To run the HBV conceptual rainfall-runoff model only daily precipitation, daily temperature, and long-term monthly evapotranspiration average are needed. The lumped version adopted in this work (Figure 28) is based on the early structure reported by Bergström, (1992) and later by Seibert, (2005). It is constituted of three main subroutines (snowmelt routine, soil moisture routine, and response routine), where ten parameters are to be calibrated. This version of the model does not account for snow-rainfall separation, rather it uses SCA from satellite data to simulate snowmelt based on a degree-day factor (DDF) and a fixed temperature threshold (TT). Total water supply (rainfall + snowmelt), which is assumed to infiltrate totally, passes through the soil component and the amount of water contributing to the recharge of the upper reservoir depends on the antecedent SM, maximum SM (FC), and a shape parameter (BETA). A portion of the SM is released towards the atmosphere through actual evapotranspiration. The latter is estimated based on the potential evapotranspiration adjusted against long-term mean temperature and a temperature correction factor (ETF). The actual evapotranspiration equals the potential evapotranspiration when the soil moisture exceeds a threshold LP. Otherwise, it is deducted as a function of the available soil moisture. All excessive water from the soil layer is redirected to fill the upper reservoir. The latter is drained towards a lower reservoir through a percolation rate controlled by KPEEC. The global outflow is a sum of the surface flow (Q0), subsurface flow (Q1), and baseflow (Q2) regulated by the recession coefficients K0, K1, and K2, respectively. However, the outflow from the upper reservoir is continuously controlled by the K1 while the K0 is activated only when the water level exceeds a UZL threshold.

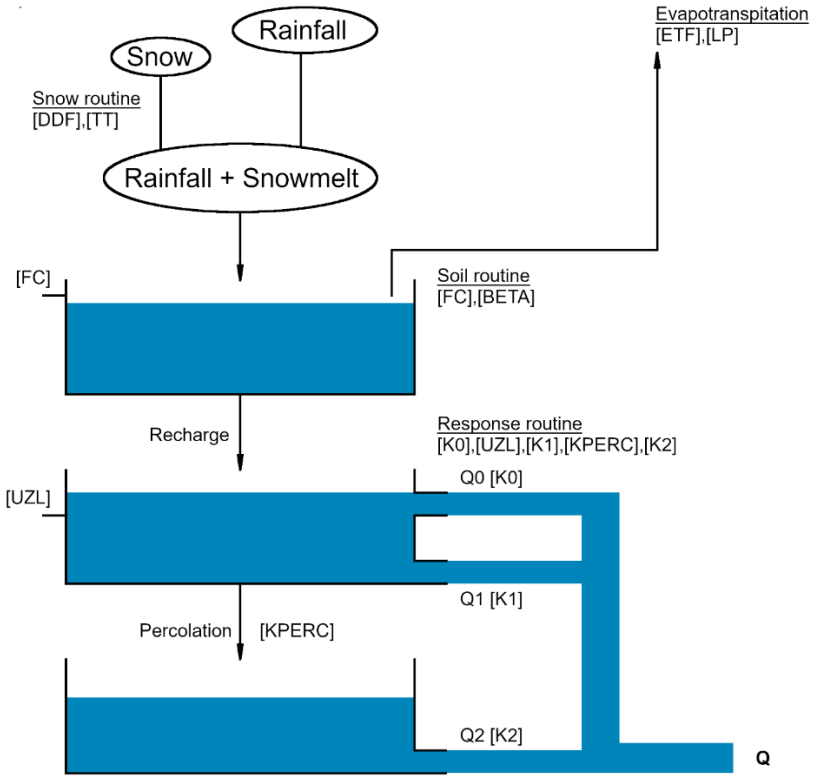

Figure 28. HBV model structure (inspired by Bergström, 1992). The model parameters are enclosed in square brackets.

4.2.2. Evaluation Metrics and Strategy

To evaluate the performance of the HBV rainfall-runoff conceptual model we focused on testing its capability to reproduce the daily gauged streamflow in the Ait Ouchene sub-watershed. First of all, the initial values of the internal state variables of the model were retrieved using the first year (2001/2002) of the reference period for warm-up. Then, the model was calibrated on each of the nine years, using a set of 1.5 Million parameter combinations randomly generated according to the ranges reported in Table 9. The parameter combinations that maximize the NSE (Nash Sutcliff Efficiency, Equation 13) and minimize the RMSE (Root Mean Square Error, Equation 14), as described below, are validated out of their temporal calibration range. We have adopted a cross-validation exercise, which involves using, iteratively, one year for calibration and each of the remaining years for validation.

Table 9. HBV model parameter ranges used in calibration.

Parameter	Definition	Minimum	Maximum	Unit
BETA	Shape coefficient	1	4	-
ETF	Temperature correction factor	0.01	0.3	°C-1
TT	Temperature threshold	0	0	°C
DDF	Degree day factor	0.1	0.6	mm °C-1 d-1
FC	Maximum soil moisture	200	600	mm
K0	Recession coefficient	0.1	0.6	d-1
K1	Recession coefficient	0.01	0.2	d-1
K2	Recession coefficient	0.01	0.15	d-1
KPERC	Percolation coefficient	0.01	0.3	d-1
UZL	Upper reservoir threshold	5	25	mm
LP	Limit for potential evapotranspiration	0.3	0.7	-

Long and consistent time series of meteorological variables are often hard to find worldwide, particularly over mountainous regions (Baba et al., 2018; Boudhar et al., 2016, 2009). Numerous studies have evaluated the effect of the data length on model performance (Anctil et al., 2004; Li et al., 2010; Sorooshian, 1983; Xia et al., 2004). Theoretically, longer data series are expected to give steady optimal parameter estimates and consistent model performance. Various data lengths of three to eight years were recommended by different studies as sufficient for reliable model performance (Anctil et al., 2004; Li et al., 2010; Xia et al., 2004). However, the nature of the data is more of a concern than its length according to numerous studies (Jain, 1993; Sorooshian and Gupta, 1983; Viviroli et al., 2009). The efficient evaluation of a certain model requires that the data series contain all hydroclimatic conditions that may occur within the watershed of interest and not less than one year of length (Sorooshian, 1983; Sorooshian and Gupta, 1983). Gan et al., (1997) found out that in some cases, one to two years could give better-performing models than ten years of calibration, as long as the data contain valuable information about the rainfall-runoff processes. The latter assures the adequate activation of the model parameters and avoids the misinterpretation of the model behavior and sensitivity. Moreover, numerous studies have pointed out that model parameters are time-variant and can be activated during different and short periods in time (Abebe et al., 2010; Tripp and Niemann, 2008). This can be explained by the fact that different kinds of hydrological responses may occur within a short period, depending on rainfall intensities and antecedent wetness conditions (Keith Beven and Andrew Binley, 1992). Therefore, the changes in model parameters can be better captured when using shorter periods (Osuch et al., 2015), particularly under unsteady hydroclimatic conditions.

The reliability of the model outputs was assessed against the daily observed streamflow using the NSE and the RMSE metrics:

$$NSE = 1 - \frac{\sum_{i=1}^{n}(Q_i^{obs} - Q_i^{sim})^2}{\sum_{i=1}^{n}(Q_i^{obs} - \bar{Q}^{obs})^2} \quad \text{Equation 13}$$

$$RMSE = \sqrt{\frac{\sum_{i=1}^{n}(Q_i^{obs} - Q_i^{sim})^2}{n}} \quad \text{Equation 14}$$

Where:

Q_i^{obs}: the observed and simulated streamflow of the day i;
Q_i^{sim}: the simulated streamflow of the day i;
$\bar{Q}^{obs}$: the average value of the observed streamflow;
n: the total number of days.

The NSE is firstly used as an objective function to select the most fitted model simulations to the observed streamflow. This statistical indicator is suggested as one of the most appropriate objective functions to provide reliable information about the overall goodness of fit of model simulations (Legates and McCabe Jr., 1999; Willmott, 2013). This suggestion is later endorsed by numerous studies related to hydrologic modeling (Moriasi et al., 2007; Ritter and Muñoz-carpena, 2013). A good model simulation involves the ability to reproduce the shape of the observed streamflow with the lowest bias possible. Legates and McCabe Jr., (1999) recommended coupling multiple evaluation techniques for more efficient model evaluation. This allows for comprehensive performance assessment and accounts for both qualitative and quantitative aspects (Biondi et al., 2012; Pushpalatha et al., 2012; Ritter and Muñoz-carpena, 2013; Willmott, 2013; Willmott et al., 1985). Thus, in our analysis, the RMSE was incorporated with the NSE to count for the bias between the observed and simulated streamflow.

The main problem related to the use of these metrics is associated with their difficult interpretation out of their range bounds (maximum and minimum values). Thus, a threshold beyond which the model performance can be judged as satisfactory remains hard to set. This issue was raised by many authors who discussed the suitability of available statistical indicators for computer model evaluation (Garrick et al., 1978; Legates and McCabe Jr., 1999; Willmott et al., 1985). Besides, some authors proposed a classification of model performance as ratings to differentiate between poor and satisfactory simulations (Moriasi et al., 2007; Ritter and Muñoz-carpena, 2013;

Singh et al., 2004). However, these classifications are case-specific and highly depend on model applications (Beven, 2006; Klemeš, 1986; Moriasi et al., 2007). Moriasi et al., (2007) conducted a review of several studies related to computer models calibration/validation and proposed performance ratings for several statistical indicators. They suggested that model simulations with $0.5 < NSE \leq 0.65$ and $NSE > 0.65$ can be considered as satisfactory and having good performance, respectively. Furthermore, Singh et al., (2004) recommended that an RMSE of 50% less than the standard deviation of the observed streamflow can be considered as low, while Moriasi et al., (2007) considered this percentage as a reference for a very good model performance. These ratings should present certain flexibility based on the application the model is intended for, the quality of data, and the time step adopted for calibration (Moriasi et al., 2007). For instance, higher evaluation metrics are needed for coarser time step than for finer ones. In the present work, a model simulation will not be considered as satisfactory unless the NSE is greater or equal to 0.5 and the corresponding RMSE is 30% less than the observed streamflow standard deviation. And, the best simulation would be the one produced by the combination of parameters that satisfactorily performs on the majority of the years (the most transferable parameters combination over time).

Lastly, a sensitivity analysis was conducted using one of the most common approaches reported by Hamby, (1994) as “ONE-AT-A-TIME” (OAT) sensitivity measures. The sensitivity analysis allows us to classify the parameters into those that significantly influence the model performance and those that have no such influence. The OAT approach consists of repeatedly varying one parameter at a time while keeping the rest fixed to their optimized values (Hamby, 1994). Furthermore, a “TWO-At-A-TIME” (TAT) version was used as an interdependency analysis in this study to highlight the potential compensation effect between the model parameters. It has the same principle as the OAT approach, except that two parameters are set to be varied instead of one parameter. Both the sensitivity and interdependency are graphically assessed with the reference to the NSE objective function.

4.3. Results and Discussion

4.3.1. Model Calibration and Validation

The model was run using data of nine consecutive years from 2001/2002 to 2009/2010. The calibration exercise was carried out for each year separately. The statistics of simulations corresponding to NSEs above the 99th percentile (hereafter admissible simulations) and the streamflow simulations obtained based on the parameter sets that maximize the NSE during calibration are shown in Figure 29 and Figure 30, respectively. The resulted metrics suggest that, despite the scarcity of climatic data, the model was quite able to reproduce the daily streamflow observed at the outlet of the Ait Ouchene sub-watershed. However, the performance accuracy was highly variable from one year to another (Figure 29). This variability was partly introduced by the fact of using a year-to-year calibration, which highlights the impacts of the interannual changes in hydroclimatic conditions on the model performance. The latter was found to provide the worst simulations in 2001/2002, 2004/2005, and 2006/2007 years with maximum (minimum) NSE (RMSE) of 0.48 (5.30 $m^3.s^{-1}$), 0.44 (3.62 $m^3.s^{-1}$), and 0.43 (4.14 $m^3.s^{-1}$), respectively. The low performance obtained in these three years is largely due to the data quality. The three years present a remarkable discrepancy between the gauged flows and rainfall in terms of event occurrence. From Figure 30, we note that there are instances where large streamflow magnitudes were observed while no rainfall was recorded. This situation often characterizes regions with low-density gauging networks, particularly those that receive local stormy events with smaller extents (Dong et al., 2005; Xu et al., 2013). The performance was relatively higher in 2002/2003 and 2007/2008 with NSE (RMSE) values spanning between 0.46 - 0.79 (6.84 $m^3.s^{-1}$ – 10.20 $m^3.s^{-1}$) and 0.46 – 0.68 (3.70 $m^3.s^{-1}$ - 4.86 $m^3.s^{-1}$), respectively. In the remaining years, the model simulations exhibited good agreement with the observed streamflow where all the NSE values were above 0.66 (in 2008/2009) and reached 0.90 (in 2005/2006), and all corresponding RMSE values were 30% below the annual values of standard deviation. Previous studies reported that the calibration results can be significantly affected by the changes in hydroclimatic conditions, mainly driven by the strong spatiotemporal variability of rainfall (Merz et al., 2011; Osuch et al., 2015). The drier conditions can be more problematic for conceptual models as they often lead to the worst performance compared to humid conditions (Anctil et al., 2004; Li et al., 2010; Merz et al., 2011; Osuch et al., 2015). In the present study, the data series encompasses both drier and humid years without

considering those (2001/2005, 2004/2005, 2006/2007) with remarkable missed events. The performance of the model in wet years agrees with the results from previous studies suggesting the easiness of model calibration during wet conditions compared to the dry ones (Dakhlaoui et al., 2017). In addition to being marked as dry, according to the SPI (see section 3.3.2.2.), the 2002/2003 and 2007/2008 years were characterized by sparse rainfall events often of small magnitudes. Also, they encompass some important rainfall events (around 55 $mm.d^{-1}$) that took place immediately after a period of consecutive dry days. Hence, the simulated streamflow events were largely underestimated, which negatively impacted the model performance. These underestimations may be explained by the fact that a part of the rainfall supplies was converted into soil moisture rather than direct runoff. Moreover, our results are partially in agreement with those of Arsenault and Brissette, (2014) suggesting that a small number of RGs up to two stations can provide acceptable hydrological performances. However, some exceptions exist where important streamflow events were underestimated or not simulated. The use of a low-density gauging network increases the possibility of missing rainfall events (Dong et al., 2005), especially in a semi-arid context. The latter is characterized by stormy events with short duration and smaller spatial coverage, which may require a denser gauging network to be properly captured as stated by Arsenault and Brissette, (2014). In addition, the use of gauging stations located at or near the limits (the outlet in the present work) of the watershed of interest contributes to a further drop-off in the model performance (Xu et al., 2013). However, the overall simulated hydrograph remains close to the observed one, particularly we obtained more accurate results during the wet season.

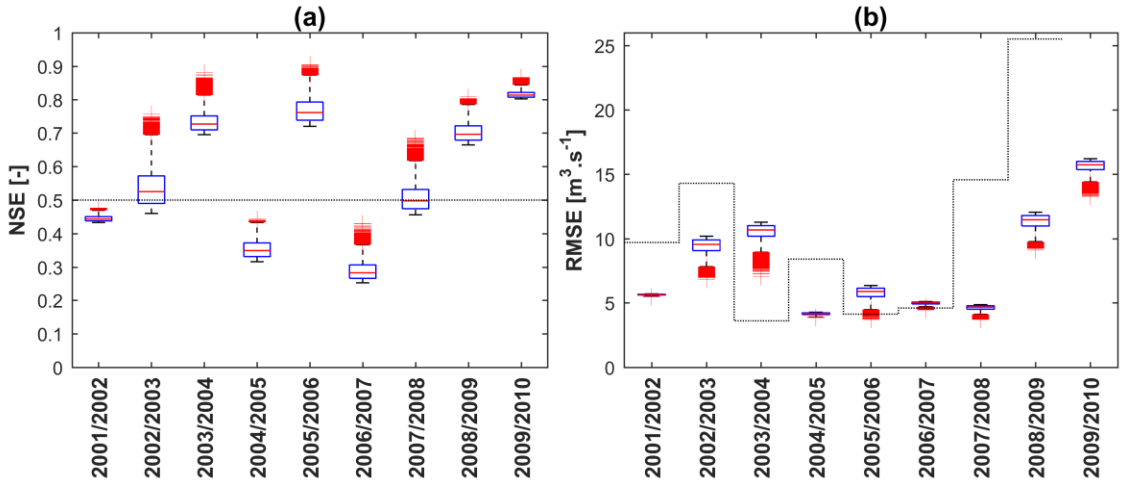

Figure 29. Statistical metrics corresponding to model simulations yielding NSEs above the 99th percentile of the NSE values obtained during calibration. The dashed lines correspond to the 0.5 NSE acceptance threshold (a) and the values of 30% less than the observed streamflow standard deviation (b).

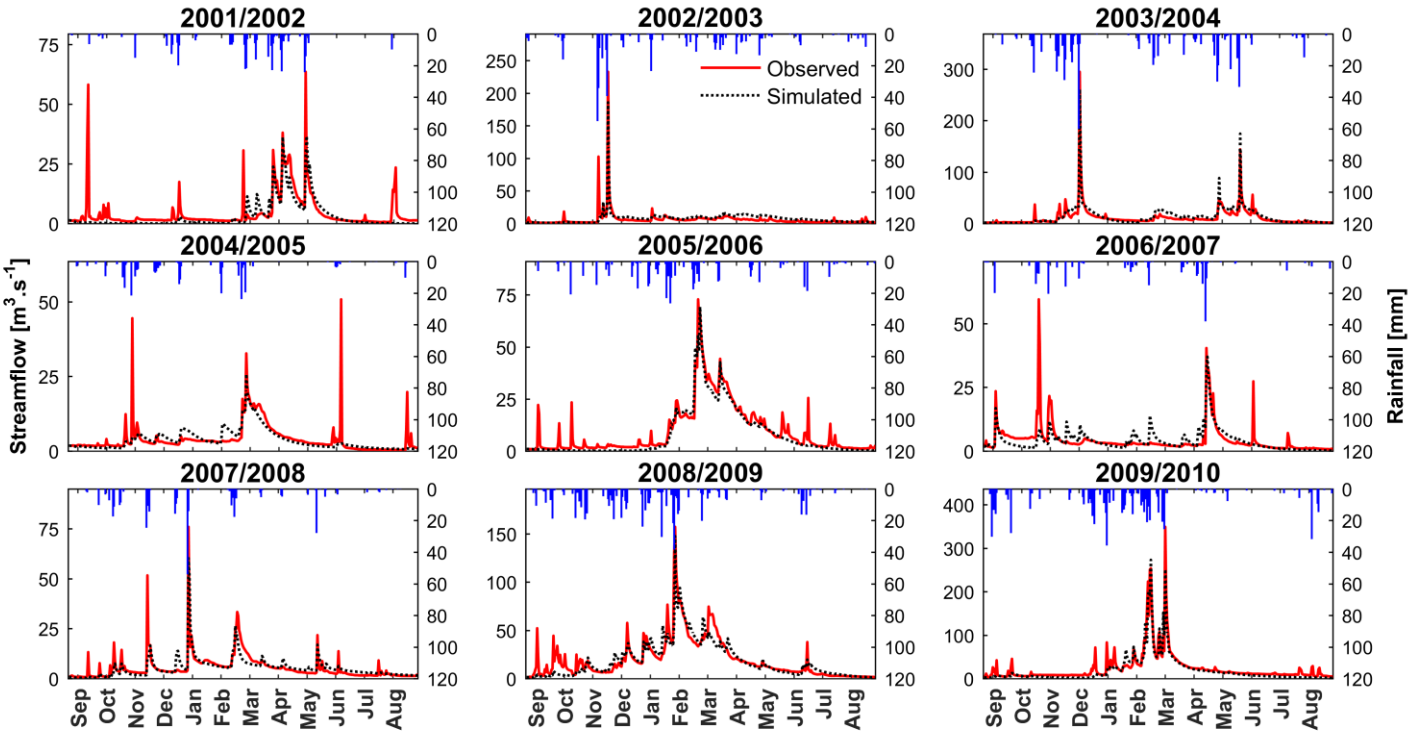

Figure 30. Daily streamflow simulated using the annual optimal parameter combinations obtained during calibration.

Furthermore, the summary of NSEs and RMSEs obtained after validation is illustrated in Table 10. The calibration and validation years are organized in columns and rows, respectively. As shown in Table 10, the parameter combinations from the three years 2001/2002, 2004/2005, and 2006/2007 maintained the same level of poor performance they exhibited during calibration. When the model is validated on one of these years, the NSE remains below the acceptance threshold regardless of the calibration year. However, parameter combinations calibrated on the aforementioned three years lead to improved statistics when validated on other years. These results suggest that when relatively good quality data are available, the HBV model provides streamflow simulations that are fairly close to the streamflow observed at the outlet of the studied sub-watershed. Besides, the model showed reasonable behavior during validation on years with reliable data. Still, we note that there were many instances where the performance of the model decreased rather than increased compared to the calibration runs. The change (decrease/increase) in the objective function mainly depends on the changes in hydroclimatic conditions between the calibration and validation data (Coron et al., 2012; Dakhlaoui et al., 2017; Osuch et al., 2015; Seibert, 1997). The parameter combinations calibrated on 2002/2003 showed the largest NSE and RMSE drop-offs when they were validated on both 2005/2006 and 2008/2009. The drop-offs were

less significant when the admissible simulations were verified against data of 2003/2004 and 2009/2010 (Table 10). 2002/2003 seemed to be the worst calibration/validation year. Moreover, all calibration years provided parameter sets that performed fairly well at least in one of the validation years but, fewer are found to be transferable over more than two years. However, there are sets of parameter combinations that provided acceptable performance over a maximum of five years when the model was calibrated on 2003/2004, 2005/2006, 2007/2008, 2008/2009, or 2009/2010. In contrast, when the model was calibrated on 2002/2003 the parameter sets were found to be less consistent in time after validation.

Table 10. Maximum NSE and minimum RMSE that were obtained after validation (calibration years in columns and validation years in rows).

		01-02	02-03	03-04	04-05	05-06	06-07	07-08	08-09	09-10
01-02	NSE	0.48	0.36	0.47	0.48	0.47	0.45	0.47	0.47	0.48
	RMSE	5.47	6.05	5.5	5.48	5.5	5.61	5.49	5.49	5.48
02-03	NSE	0.34	0.76	0.69	0.69	0.32	0.73	0.67	0.44	0.57
	RMSE	11.25	6.84	7.71	7.71	11.44	7.2	7.91	10.35	9.11
03-04	NSE	0.79	0.84	0.88	0.87	0.86	0.87	0.86	0.8	0.85
	RMSE	9.43	8.15	7.05	7.25	7.77	7.28	7.78	9.11	7.88
04-05	NSE	0.41	0.44	0.44	0.44	0.43	0.44	0.44	0.44	0.44
	RMSE	3.99	3.88	3.87	3.86	3.9	3.88	3.86	3.86	3.88
05-06	NSE	0.84	0.58	0.89	0.9	0.9	0.79	0.85	0.84	0.9
	RMSE	4.78	7.82	4.03	3.74	3.72	5.52	4.67	4.77	3.83
06-07	NSE	0.3	0.42	0.42	0.37	0.36	0.43	0.41	0.41	0.42
	RMSE	4.95	4.48	4.5	4.7	4.71	4.46	4.52	4.52	4.5
07-08	NSE	0.64	0.64	0.68	0.68	0.62	0.68	0.68	0.67	0.59
	RMSE	3.95	3.98	3.7	3.7	4.07	3.7	3.7	3.81	4.24
08-09	NSE	0.8	0.65	0.78	0.81	0.81	0.81	0.81	0.81	0.62
	RMSE	9.3	12.38	9.87	9.12	9.12	9.12	9.12	9.12	12.85
09-10	NSE	0.86	0.83	0.87	0.87	0.87	0.86	0.86	0.79	0.87
	RMSE	13.48	14.9	13.34	13.25	13.25	13.48	13.53	16.57	13.25

Nevertheless, under the inherent interaction between conceptual model parameters, mainly driven by structure inadequacy and data-related uncertainty (Seibert, 1997; Sorooshian and Gupta, 1983), it is difficult to obtain a unique optimal set of parameters (Sorooshian and Gupta, 1983; Uhlenbrook et al., 1999). Multiple simulations that result in equally good performance exist (Seibert, 1997; Uhlenbrook et al., 1999). Therefore, the parameter set that provided the best and consistent performance, according to both NSE and RMSE, was selected (Figure 31). This combination of parameters, not assumed as a realistic description of the physical processes

controlling the hydrologic regime in the studied sub-watershed, was used to investigate the sensitivity and interdependency of the model parameters.

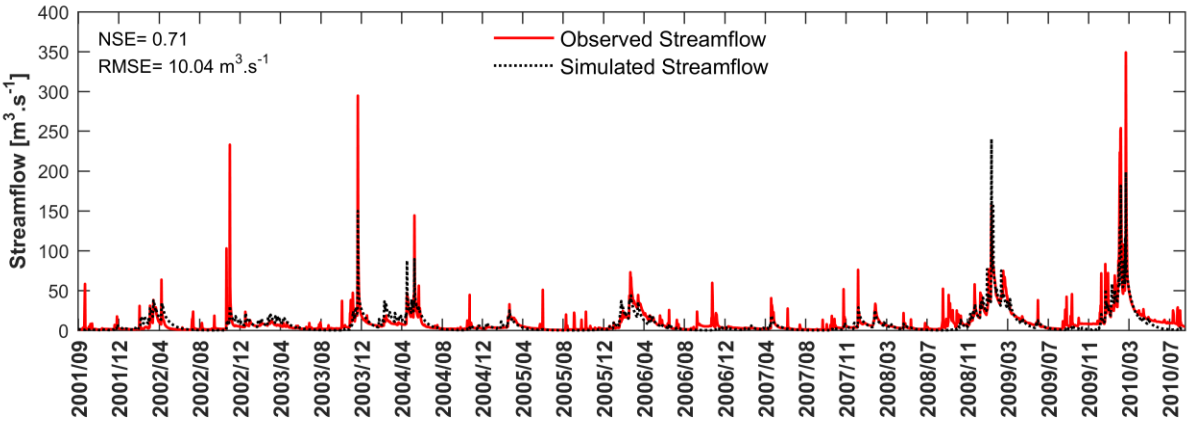

Figure 31. Daily streamflow simulated using the parameters combination that yielded the best statistical metrics (NSE and RMSE) after validation.

4.3.2. Sensitivity Analysis

The sensitivity analysis was performed to quantify the individual effect of the HBV model parameters on streamflow simulation. This analysis was conducted by varying one parameter at a time while the rest are set to their optimized values. The degree of influence of each parameter was assessed according to the changes in the NSE objective function. The analysis covered six years of the reference period, where 2001/2002, 2004/2005, and 2006/2007 were excluded given the poor model performance driven by the low data quality. The sensitivity results are illustrated in Figure 32 where the changes in parameter values are plotted versus the changes in NSE values. From Figure 32, it is clear that there is an important year-to-year variability in the model behavior depending on the parameter changes. Generally, all parameters seemed to impact the model simulations to a certain extent, depending on years and parameters. In our analysis, we observed that the parameter ETF demonstrated no major control over the model performance in most of the years. Except in 2008/2009, the increase in ETF parameter values led to the lowest NSEs. Overall, the model performed the best with smaller ETF values in all the considered years. Whereas, parameters such as DDF and LP seemed to not affect the model response in some years while they showed more influence in others. In most of these years, both parameters demonstrated overall NSE decreasing tendencies as the values of the parameters increased. In contrast, higher LP values in 2002/2003 resulted in higher NSEs, which suggests that the model performs the best under small evapotranspiration rates in such a year. The DDF was more dependent on the availability and extent

of the snow cover over the study area. In previous studies, snowmelt-related parameters, particularly DDF, were found to be more influential on the HBV model response in watersheds with a snow-dominated regime (Seibert, 1997; Uhlenbrook et al., 1998; Zelelew and Alfredsen, 2013). In contrast, the model performance had no clear dependency on the parameter in watersheds with rainfall-dominated regimes due to the small snow portion in these watersheds (Merz et al., 2011; Parra et al., 2018). Furthermore, when varied individually, the FC and BETA parameters seemed to have the most important impact on the model response. They presented the steepest curves in all the studied years. Numerous studies agreed that FC and BETA are the most influential parameters in the HBV conceptual model (Abebe et al., 2010; Osuch et al., 2015; Parra et al., 2018; Seibert, 1997; Uhlenbrook et al., 1998; Zelelew and Alfredsen, 2013). However, the parameter values that maximize the NSE change from one year to another. The FC, for instance, had optimal values within a range of 200 mm to more than 400 mm. It converged more towards the lower edge of the predefined calibration range in 2002/2003 and exceeded 400 mm in 2008/2009. The two years were contrasted in terms of hydroclimatic conditions. The first was marked as a relatively dry year with unevenly distributed rainfall events, one of which caused an extremely high peak flow (Figure 30), while the second was a very wet year with relatively high annual rainfall amount and abundant snow cover (see section 3.3.2. and 3.3.3.). Theoretically, the FC parameter determines the amount of excess water contributing to the upper reservoir recharge. A lower FC, which refers to a soil layer with less water holding capacity, would amplify the portion of excess water compared to larger FC values. Merz et al., (2011) and Osuch et al., (2015) showed that FC positively correlates with precipitation but more significantly with temperature. However, the parameter presents different behaviors in different watersheds depending on the presence or absence of snow cover (Osuch et al., 2015). It tends to increase with temperature in snow-covered watersheds while it shows the opposite tendency in watersheds without snow cover. The findings of Merz et al., (2011) and Osuch et al., (2015) would suggest that the positive correlation between FC and temperature in snow-covered watersheds may be related to increasing snowmelt supplies to the soil subroutine. The latter partly explains the variability in FC optima in our case, where it tended to be larger in years characterized by relatively important snow cover (2005/2006 and 2008/2009). This observation suggests that the FC optima fluctuations are subject to changes in the total water supply, particularly from snowmelt. This interpretation agrees with the finding from Abebe et al., (2010), where the FC was found to take lower values during dry periods and high

values during wet periods with susceptible overestimated rainfall. Contrary to FC, the annual optimal values of BETA varied within a narrower section of its predefined range, throughout the reference period. This may be explained by the adjustment of BETA to the FC optimal values in order to counterbalance the water supply offset provoked by a larger water holding capacity. As shown in Figure 31, the parameter combination obtained after validation often led the model to underestimate high peak flows. The latter would require smaller FCs in order to be correctly simulated. Hence, the bias provoked by the relatively higher optimized FC is accounted for by BETAs that are smaller than those obtained after validation (Figure 32). The smaller BETA values, which mean more recharge water towards the upper reservoir, resulted in higher NSEs, particularly in 2002/2003 and 2003/2004. Moreover, the parameters KPERC and UZL, which control the drainage of the upper reservoir, showed relatively similar behavior to the FC in both 2002/2003 and 2008/2009. As can be seen in Figure 32, in 2002/2003, higher NSEs were obtained by small KPERC and small UZL values, while the opposite was true in 2008/2009. Additionally, the K0 intervened only when the conditions were wet enough to allow the exceedance of the UZL, otherwise, the simulated outflow was mainly the result of the K1 contribution. Generally, a smaller UZL allowed more contribution from the K0 in peak flows generation. This can be seen in the subplots relative to K0 and K1 in Figure 32. Particularly during 2005/2006 and 2007/2008, K0 induced no change in the objective function when varied over its whole range. The K1, in contrast, resulted in steeper curves suggesting a significant control over the model response. The effect of the K0 parameter can be also seen when there was a relatively large water supply from individual rainfall events resulting in important peak flows (Abebe et al., 2010; Ouyang et al., 2014), such as the case of 2002/2003 and 2003/2004. Such peak flows are often driven by extremely intense rainfall events that produce important runoff in a short amount of time. Additionally, the K2, which is responsible for baseflow generation, presented a certain degree of influence on the global flow generation. However, the model sensitivity to K2 highly depended on the simultaneous effect of K1 and KPERC on the water level in the upper reservoir (Seibert, 1997; Uhlenbrook et al., 1999). In the present study, the larger optimized KPERC was the main factor that led to the significant contribution of K2 in the global outflow.

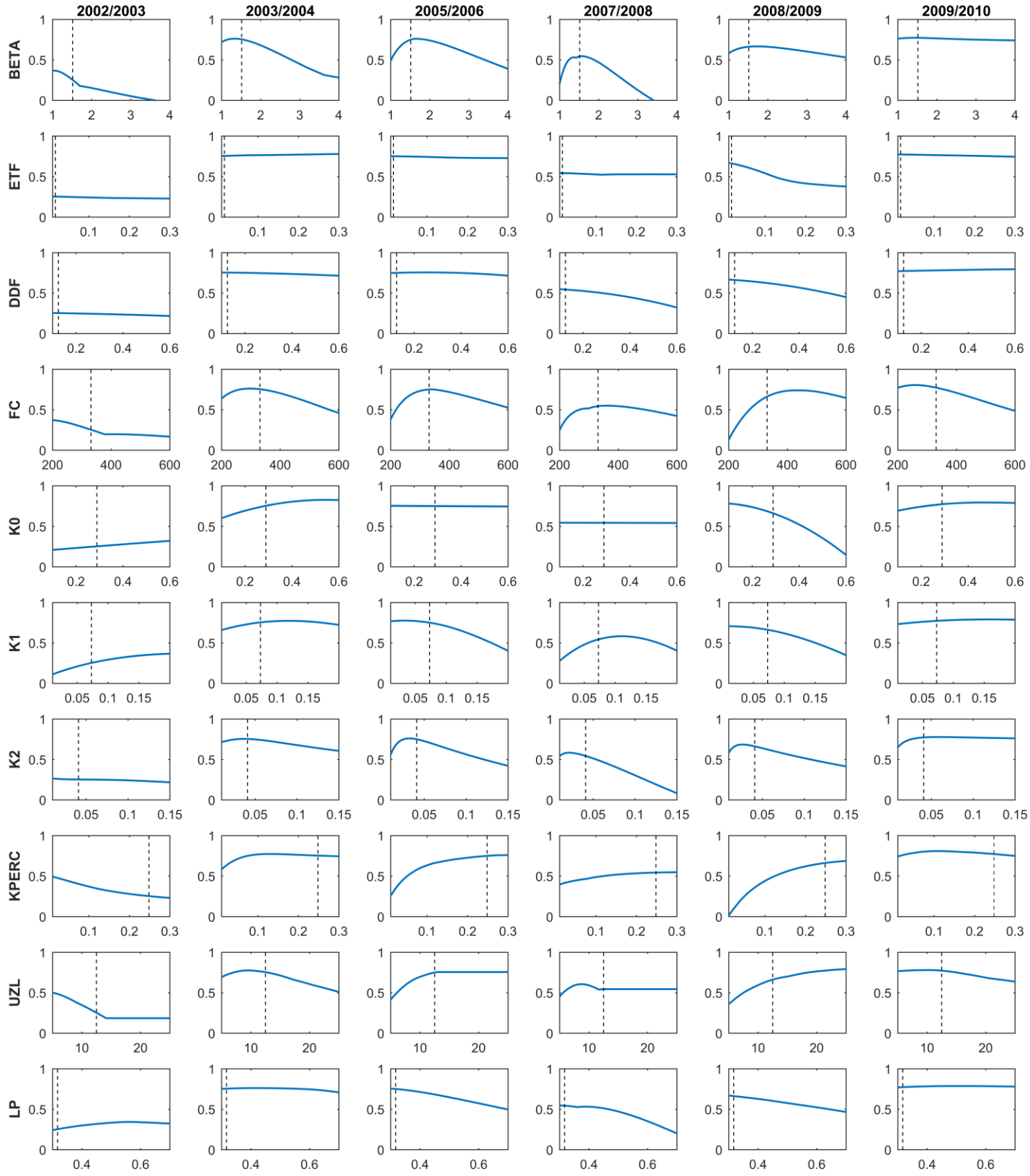

Figure 32. The sensitivity of the model to the changes in parameter values according to the NSE. The dashed lines represent the optimal parameter values obtained after validation.

4.3.3. Parameters Interdependency

Generally, model parameters, as physical as they sound, may not reasonably describe the reality of the physical processes (Seibert, 1999; Uhlenbrook et al., 1998), particularly with conceptual models that are highly subject to parameter interdependency. In the present work, we were able to highlight the potential interdependency of the model parameters through the sensitivity analysis. The findings suggest that the change in one of the model parameters due to hydroclimatic conditions, for instance, would be offset by one or more of the remaining parameters to provide the most fitted model to the observed streamflow. This combining effect is responsible to a large extent for the year-to-year variability of the estimated optimal model parameters (Sorooshian, 1983). To emphasize the interdependency of the HBV model parameters, a bivariate analysis based on the NSE criterion was carried out. It consisted of varying two parameters at a time over their whole predefined range instead of one parameter, while the rest were set to their optimal values. Figure 33 shows the maximum NSE obtained for each couple of parameters, where the diagonal cells of each subplot represent the maximum NSE from the OAT analysis. Previous studies have demonstrated that the use of fewer parameters than the full version has little impact on the model fit (Seibert, 1999; Zelelew and Alfredsen, 2013). Our results showed that combining a minimum of two parameters, while the rest are set to their optimized values, can lead to NSEs comparable to those obtained during calibration. Still, the couple that yielded to the best fit highly depended on the year during which the model is run. Overall, less influential parameters such as ETF, LP, and DDF, when they were combined, brought no significant change compared to the OAT analysis, as shown in Figure 33. However, the incorporation of parameters with more influence on the model response, in the parameter couple, resulted in higher NSEs. The most significant increases were obtained when one or more of the response routine parameters were considered. This remark holds true for all the studied years unless the conditions were not met to allow the engagement of some of the parameters, such as UZL in 2005/2006 and K0 in 2007/2008 hydrologic years. Overall, the results from all the years lead us to conclude that the combination of the response routine parameters, particularly K0, KPERC, and UZL, yielded superior model simulations. Thus, the performance of the model would be more sensitive to the response routine parameters than to those of the soil moisture routine, particularly in years with extremely high peak flows. The impact of the response routine on the model performance was obvious in 2002/2003. As shown in Figure 33, the parameter couples constituted of either UZL or KPERC returned the highest NSEs, especially

when combined with K0. Furthermore, in years with frequent snow cover (2005/2006 and 2008/2009, Figure 23) the couple FC-DDF seemed to provide NSEs as high as those obtained by the response routine parameters.

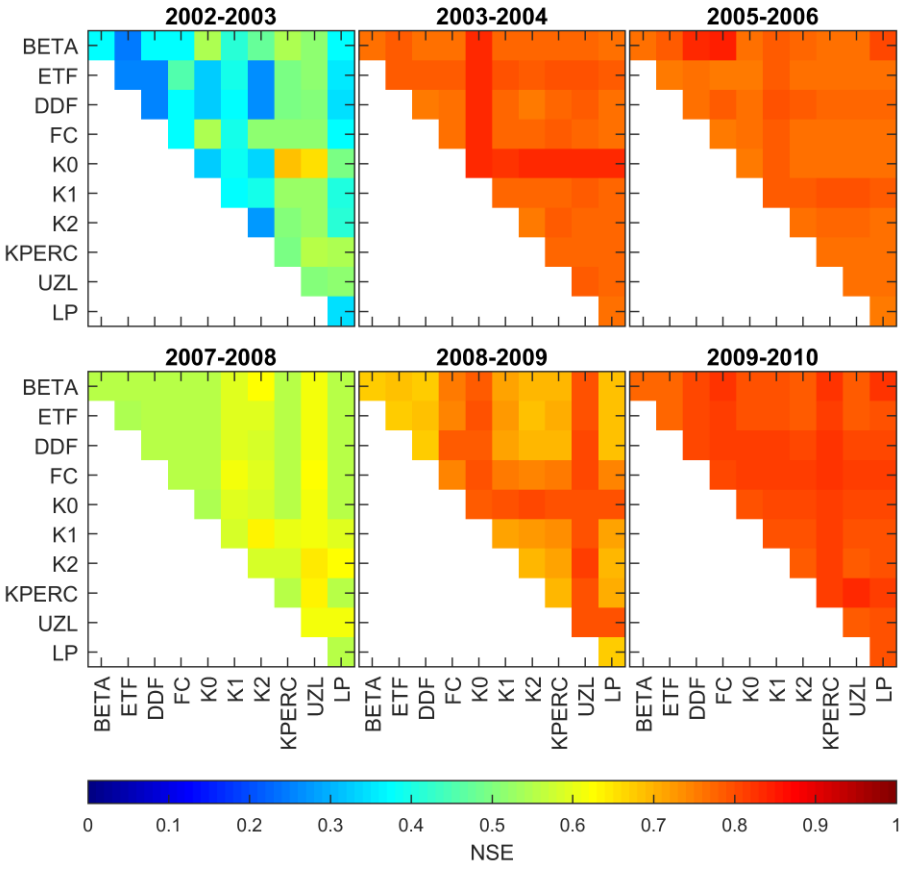

Figure 33. Heatmaps representing the maximum NSE obtained when varying two model parameters at a time while the rest are set to their optimized values.

The interaction between the values of the five parameter couples (FC-DDF, FC-K0, FC-KPERC, K0-KPERC, and K0-UZL) that caused an overall distinct increase in the NSE values, as shown in Figure 33, was further investigated. Figure 34 illustrates the scatter plots of the five parameter couples classified according to the NSE resulted from the combination of each pair of parameter values. Each row represents the results of one parameter couple in four representative years (2002/2003, 2003/2004, 2005/2006, and 2008/2009). Figure 34 confirms that FC was strongly influenced by the year-to-year changes in water supplies. Remarkably, the parameter was positively correlated with the yearly SCAp. Moreover, it seemed to change according to the changes in DDF. As shown in Figure 34, when FC and DDF were varied together, in years with frequent snow cover (2005/2006 and 2008/2009), we observed that both parameters took higher

values to yield the best NSEs. This suggests that important amounts of snowmelt produced under higher DDFs are compensated with higher FCs. In contrast, when varied with other parameters, such as KPERC and K0, the FC significantly decreased, yet the maximal NSE did not change as much. Based on this observation, the higher FC values in both years were set to counterbalance a potentially overestimated snowmelt. This is in line with the interpretation of Abebe et al., (2010) assuming that the parameter takes higher values to reduce the effect of overestimated rainfall. Furthermore, from the scatter plots, we can see that the five considered couples presented contrasting behavior in 2002/2003 and 2008/2009. There was a general tendency where the set of parameter pairs that yield the maximum NSEs, regardless of the actual values, were always on the opposite sides of the parameter ranges. In 2002/2003, the best simulations were the result of the couples that incorporated DDF, FC, KPERC, and UZL parameter values around the lower edge of their predefined range, and larger K0. Conversely, larger values from DDF, FC, KPERC, and UZL, and smaller K0 values provided the best simulations in 2008/2009. The small FC values allowed the small discrete rainfall amounts, in 2002/2003, to fully participate in the upper reservoir recharge. Accordingly, the response subroutine parameters were set in a way to reduce the potential storage of the upper reservoir and percolation rate so that the smaller recharge supplies could significantly contribute to the global outflow. A reverse behavior was observed in 2008/2009. In other words, the combination of the same parameters provoked an enlargement of the upper reservoir storage capacity, which led to a reduction in the excess water from the reservoir. On the one hand, these observations suggest that in addition to FC, all the parameters engaged in the drainage of the upper reservoir compensate for the bias that may take place from an overestimated water supply. On the other hand, under high peak flows, the same parameters are combined to enhance the contribution of small water supplies to the global outflow. In particular, the reduction in the upper reservoir storage capacity may be considered as a mimic of the rapid saturation of the upper soil layer under intense rainfall events, which was the case in 2002/2003 and 2003/2004. Although limited to FC, a similar observation was made by Abebe et al., (2010). They explained the changes in the optimal FC values by the absence of model formulations that account for factors controlling the infiltration-runoff partitioning, such as rainfall intensity and duration.

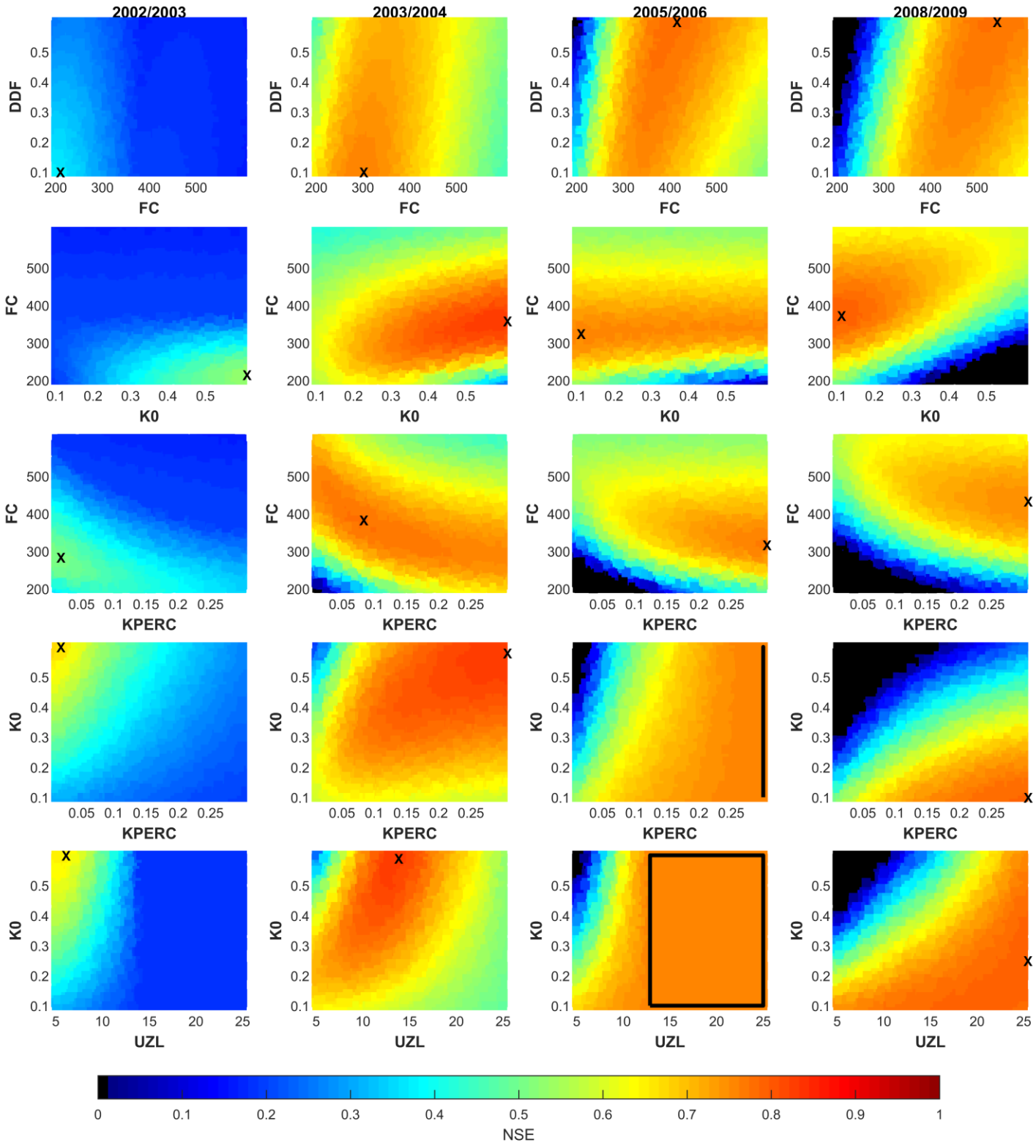

Figure 34. Scatter plots of the five parameter couples FC-DD, FC-K0, FC-KP, K0-KP, and K0-UZL, classified according to the NSE values. The X marker refers to the best-performing pair of parameter values. The continuous black lines enclose the combinations of parameter values that result in the same NSE values.

Chapter 5. Evaluation of the Daily Estimates of the SRP Datasets Using Direct Comparison and Hydrologic Modeling Approaches

5.1. Introduction

The strong spatiotemporal variability of rainfall combined with the low density of the measurement network constitutes real constraints for water resources monitoring and management. As stated earlier, with a low-density gauging network there is a high probability of having rainfall time series with missing rainfall events (Dong et al., 2005). This can be particularly observed in semi-arid contexts where the rainfall events are often stormy, with short duration and small spatial coverage (Arsenault and Brissette, 2014). In recent years, several SRPs have become freely available worldwide. In this chapter, we aim at evaluating the robustness and accuracy of the ARC, CHIRPSp25, CHIRPSp5, CMORPH-CRT v1, GPM IMERG v6, PERSIANN-CDR, RFE, and TRMM 3B42 v7 datasets in estimating the rainfall over the OERB. The SRP estimates were evaluated at a daily time scale over the period from 2001 to 2010. Firstly, the performance of the SRPs was assessed by direct comparison against in situ observations from twenty-six RGs (see Table 2 “Chapter” column). Secondly, we investigated the suitability of the SRPs daily estimates for streamflow simulation over Ait Ouchene and Tilouguite sub-watersheds (Figure 13 and Table 1), using the HBV conceptual lumped model.

5.2. Methods

The SRPs data were evaluated by a direct comparison between rainfall data obtained from RGs and their corresponding GCs and WAvg time series. The SRP datasets were investigated to analyze their capability in detecting rainfall events and reproducing the observed patterns of the daily rainfall using various statistical metrics. First of all, we used the verification indices: POD (Probability Of Detection) and FAR (False Alarm Ratio) (Wilks, 2006). These indices, based on

contingency tables, emphasizes the product's ability to identify rainfall events above a given threshold (Dinku et al., 2008). Different thresholds have been adopted in various studies throughout the world to differentiate between rainy or dry days, including 0.1 mm to define a rainy day in Saudi Arabia (Almazroui, 2011), 0.5 mm in the Korean peninsula (Baik and Choi, 2015), and 1 mm in the Peruvian Andes (Mantas et al., 2014). In this study, we choose to apply 0.1 mm as a rainfall threshold, which corresponds to the minimum amount that can be collected by the RGs.

The POD, also called the success rate, represents the fraction of observed events that were correctly detected by the SRPs. An event is considered as correctly detected when rainfall (greater or equal to 0.1 $mm.d^{-1}$) is reported by both the SRP and the RG (Table 11). The POD is defined as follows:

$$POD = \frac{a}{a + c} \qquad \text{Equation 15}$$

The FAR is the estimated proportion of events that tend to be falsely detected (false alarms). The latter refers to the rainfall events detected by the SRP while no rainfall (lower than 0.1 $mm.d^{-1}$) was recorded at the RGs (Table 11). The FAR is calculated by the following formula:

$$FAR = \frac{b}{a + b} \qquad \text{Equation 16}$$

Where, a, b, and c represent the number of rain events that fulfilled the conditions in Table 11.

Table 11. Contingency table showing the meaning of parameters used in equations 15, and 16 (rain ≥ 0.1 $mm.d^{-1}$ = rainy day; rain <0.1 $mm.d^{-1}$ = dry day).

		RG	
		Rain ≥ threshold	**Rain< threshold**
Satellite	**Rain ≥ threshold**	a	b
	Rain < threshold	c	d

The comparison of the SRP estimates against the RGs data was also conducted through a statistical analysis based on standard indicators. These include the PCC (Equation 17) for evaluating the linear relationship between the SRP and RG time series. There is also the RMSE (Equation 14) in mm, the R-Bias (Relative Bias, Equation 18), and the Bias (Equation 19) that were used to quantify the difference in magnitude between the two data sources.

$$PCC = \frac{\sum_{i=1}^{n}(E_i - \bar{E}_i)(O_i - \bar{O}_i)}{\sqrt{\sum_{i=1}^{n}(E_i - \bar{E}_i)(O_i - \bar{O}_i)^2}} \quad \text{Equation 17}$$

$$R - Bias = \frac{\sum_{i=1}^{n} E_i}{\sum_{i=1}^{n} O_i} \quad \text{Equation 18}$$

$$Bias = E_i - O_i \quad \text{Equation 19}$$

Where:

E_i: the SRP data of the day i with an average of $\bar{E}_i$;
O_i: the RG data of the day i with an average of $\bar{O}_i$;
n: the total number of days in the study period.

Furthermore, the SRPs underwent a hydrologic evaluation using the HBV model. The datasets were used as inputs alongside the RG data to simulate the daily streamflow via the aforementioned model. In this chapter, the calibration/validation process was the same as the one adopted in Chapter 4. The main differences reside in the number of calibration runs and the parameter ranges. For computational purposes, the number of simulations per calibration exercise was set to 100000 instead of 1.5 million (Chapter 4). This allowed us to reduce the effort and time that eight datasets would require to run the model on an annual basis. On the other hand, some changes were made to the model parameters and their respective ranges based on the sensitivity and interdependency analysis reported earlier in Chapter 4. Firstly, the snowmelt subroutine was deactivated and the SCA was not considered as model input. This decision was mainly motivated by the conclusions of the interdependency analysis (Chapter 4). The DDF was found to interact with some of the model parameters, particularly FC (see section 4.3.3.), to account for under or overestimated water supplies. In SRPs evaluation, depending on the DDF coefficients, the snowmelt simulated based on the SCA can compensate for the bias in the SRP daily estimates and, hence, the performance results would be misleading. By disregarding the DDF and the TT, 9 parameters remained to be calibrated. Out of these, six parameters (BETA, ETF, FC, K0, KPERC, and LP) were subject to a range adjustment (Table 12), taking into consideration the sensitivity analysis outcomes. While the ETF was set to a fixed value (0.05), the ranges of three parameters (BETA, FC, and KPERC) were shortened and two (K0 and LP) were widened.

Table 12. HBV model parameter ranges used in the SRP-driven calibration.

Parameter	Definition	Minimum	Maximum	Unit
BETA	Shape coefficient	1	3	-
ETF	Temperature correction factor	0.05	0.05	°C-1
TT	Temperature threshold	-	-	°C
DDF	Degree day factor	-	-	mm °C-1 d-1
FC	Maximum soil moisture	50	400	mm
K0	Recession coefficient	0.01	1	d-1
K1	Recession coefficient	0.001	0.2	d-1
K2	Recession coefficient	0.001	0.15	d-1
KPERC	Percolation coefficient	0.001	0.1	d-1
UZL	Upper reservoir threshold	1	25	mm
LP	Limit for the potential evapotranspiration	0.01	1	-

The performance of the SRP datasets was judged based on their capability to produce daily streamflow that is close enough to the one gauged at the outlet of the Ait Ouchene and Tilouguite sub-watersheds. Thus, the streamflow simulated using the SRP estimates was evaluated against the observed one employing the NSE statistical metric (Equation 13).

5.3. Results and Discussion

5.3.1. Grid Cell based Evaluation

In this section, eight freely available SRP datasets were compared against daily gauged rainfall data. Figure 35 illustrates the performance of the SRPs as described by the statistical metrics (PCC, RMSE, POD, and FAR) computed for each of the twenty-six RGs. The latter are sorted in an ascending order based on the gauges' elevations. As shown in Figure 35, the accuracy of the SRPs in reproducing the daily observed rainfall depends on products and RGs. According to the PCC results, the performance of all products exhibited a strong spatial variability. The obtained daily PCCs ranged from a minimum of 0.11 computed between Addammaghene and its homologous CMORPH GC to a maximum of 0.78 computed between Moulay Bouzekri and RFE. This poor performance is comparable with what was obtained at the daily time scale over Algeria and Egypt (Babaousmail et al., 2019; Nashwan et al., 2019), quantitatively but not in terms of the SRPs performance ranking. Generally, all the products tended to provide the worst performance over the mountainous region. The performance was particularly low (small PCCs and large RMSEs) at high elevations or at those RGs located in the southern part of the OERB (where the

conditions are the aridest). Out of the eight SRPs, PERSIANN, CMORPH, CHIRPSp25, and CHIRPSp5 showed the poorest agreement with the observed data as all the obtained PCCs were lower than 0.48. It was not clear which of these products can be rated as the worst. Nevertheless, CMORPH seemed to have the inferior performance at more RGs than any of the other three products. Moreover, CHIRPSp25 and CHIRPSp5 demonstrated a quite similar spatial pattern. Although the differences were small, the PCCs computed based on the CHIRPSp25 exceeded those computed based on CHIRPSp5 at most of the RGs. Given the fact that both products use the same algorithm, the small GC size (5 km) seemed to provide no significant improvement compared to the overall performance of the 25 km product. The four remaining SRPs (ARC, REF, TRMM, and IMERG) correlate relatively better to the observed data. Still, the performance was spatially consistent in some products more than in others. The PCCs obtained by ARC and RFE were found

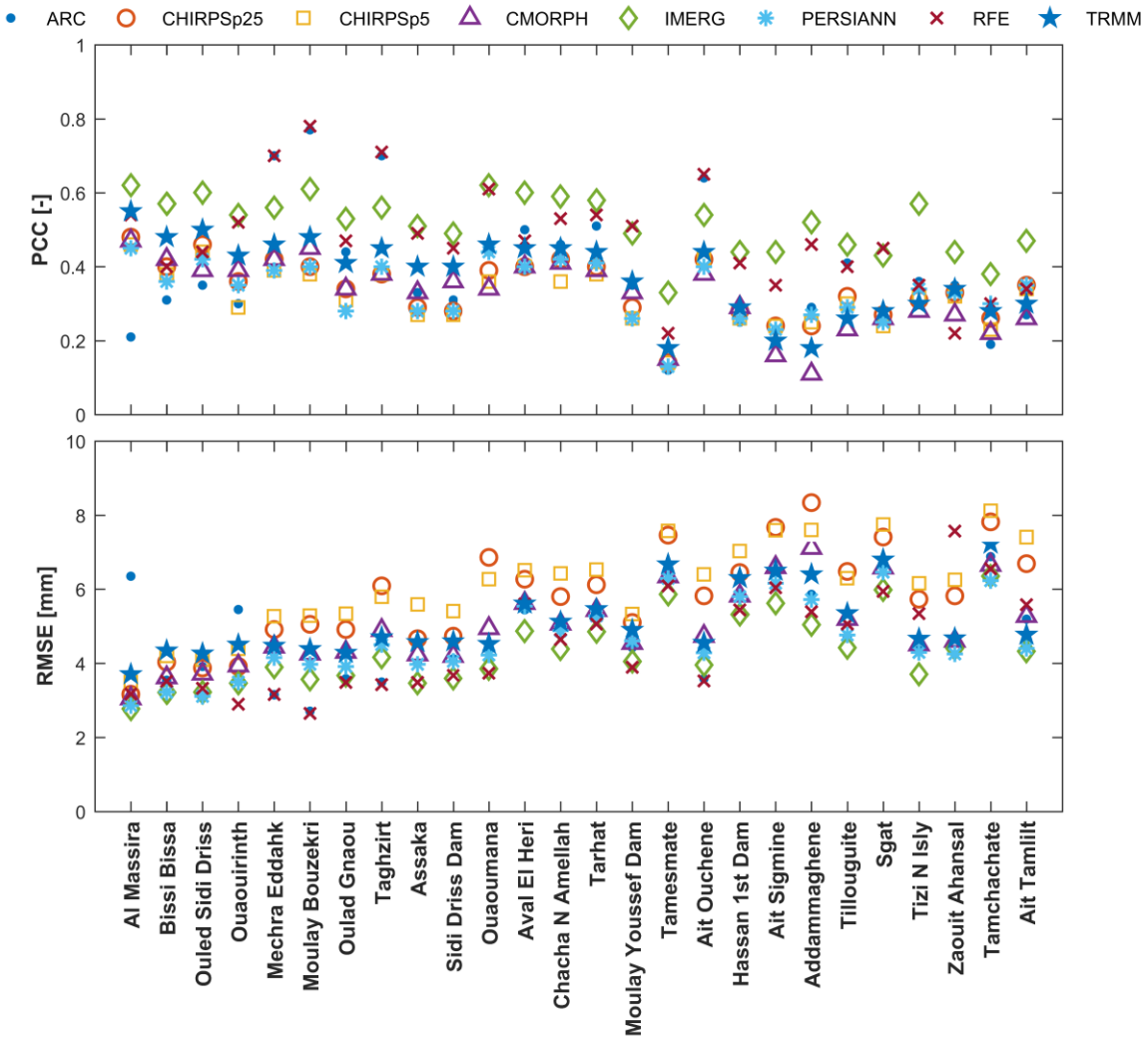

Figure 35. Statistical metrics (PCC and RMSE) computed at the daily time scale. The RGs are sorted in ascending order according to their elevation.

to exceed 0.6 at four neighboring RGs mainly located at the lowlands. As reported earlier, in both ARC and RFE, the calibration procedure relies on attributing the daily observed rainfall to the GCs that correspond to the RG positions and the satellite (IR and PMW) estimates elsewhere. This can explain the high PCCs obtained at these RGs, particularly that they are situated near a meteorological station that belongs to the Moroccan National Weather Administration measurement network. The latter often participate in international data collection programs, such as those used in the calibration of the SRP datasets. At several other sites, the same SRPs (ARC and RFE) were found to exhibit the worst performance among all the products, particularly ARC was predominantly surpassed by RFE in terms of PCCs. On the other hand, the calibrated version of IMERG was spatially the steadiest. It outperformed all the products at all of the studied RGs, except at those sites where ARC and RFE performed the best. In particular, IMERG provided remarkably improved linear correlation coefficients compared to its predecessor TRMM and PERSIANN. The PCCs produced by IMERG ranged over a relatively narrower interval (0.33 – 0.62) where 75% were above 0.46; which were higher than 75% of the PCCs produced by TRMM and all those produced by PERSIANN (Figure 36). The supremacy of IMERG daily estimates over those of CMORPH, CHIRPS, TRMM, PERSIANN, and ARC was reported in several regions of different topographic and climatic contexts (Anjum et al., 2019; Beck et al., 2019; Ma et al., 2020; Tang et al., 2020). In particular, the authors highlighted the remarkable enhancements in IMERG compared to TRMM. However, regarding the other products, the findings of most of these studies oppose ours. For instance, CMORPH outperforming TRMM over China and conterminous US (Beck et al., 2019; Tang et al., 2020), and CHIRPS providing the best performance surpassing TRMM, PERSIANN, and CMORPH over the Lake Titicaca basin (Satgé et al., 2019).

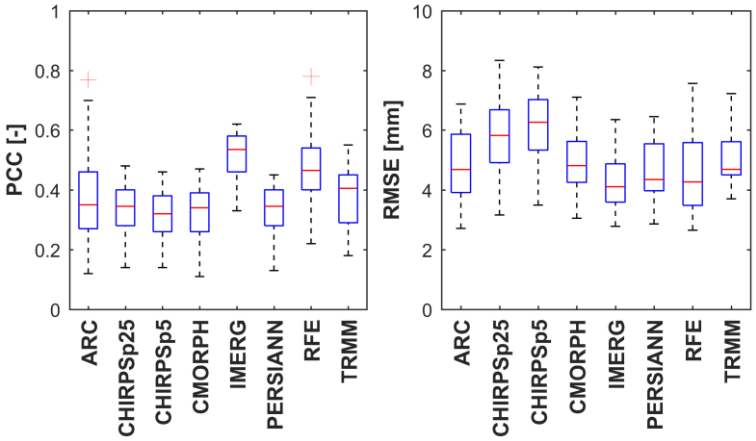

Figure 36. Boxplots summarizing the statistical metrics (PCC and RMSE) obtained at the daily time scale.

Furthermore, the capability of the SRPs to correctly detect the gauged rainfall events, as demonstrated by the POD metric, is illustrated in Figure 37 and Figure 38. According to POD values, the SRPs detection capacity seemed to endure less spatial fluctuation. Overall, the PODs varied from 0.18 to 0.91. ARC and CHIRPSp5 had the worst skill in detecting rainy days among all the products, with a median POD of 0.29 and 0.31, respectively. CHIRPSp25 (0.47) came in fourth rank surpassed by TRMM (0.52), CMORPH (0.54) and RFE (0.60). Throughout the study region, the highest POD values predominately fluctuated between IMERG and PERSIANN products with PODs ranging from 0.52 to 0.91. Both SRPs mostly showed a similar capacity of rainfall events detection with a very close spatial pattern. This can be partly attributed to the fact that IMERG incorporates the output of the PERSIANN-CCS cloud classification system in its newest release. Thus, its detection capacity has remarkably improved compared to its predecessor TRMM. This observation agrees with what was found in other climatic contexts about IMERG being able to detect more rainy days than TRMM (Anjum et al., 2019; Ma et al., 2020). The capability of the SRPs to correctly detect rainfall events as recorded by the RGs is a key factor to judge the suitability of these products to spatially describe the rainfall patterns over a certain region. The low PODs imply an abundance of missed events, which can be of high concern depending on their actual magnitudes. Such events can be mainly provoked by the difference between the time the satellite passed over the location of the RG and the time when the event actually precipitated on the earth's surface (Serrat-capdevila et al., 2016). Generally, the missed events occur when the rain took place moments after the satellite scanned the RG location. This can be actuated depending on the efficiency of the algorithm used for rainfall retrieval and the GC size adopted for the final product. A larger GC size allows more residence time for the clouds within the sensor’s spatial resolution and, hence, enhances the probability of their detection. This can be seen in Figure 37 (subplot 1), for the same RGs CHIRPSp25 was always capable to correctly detect more events than CHIRPSp5.

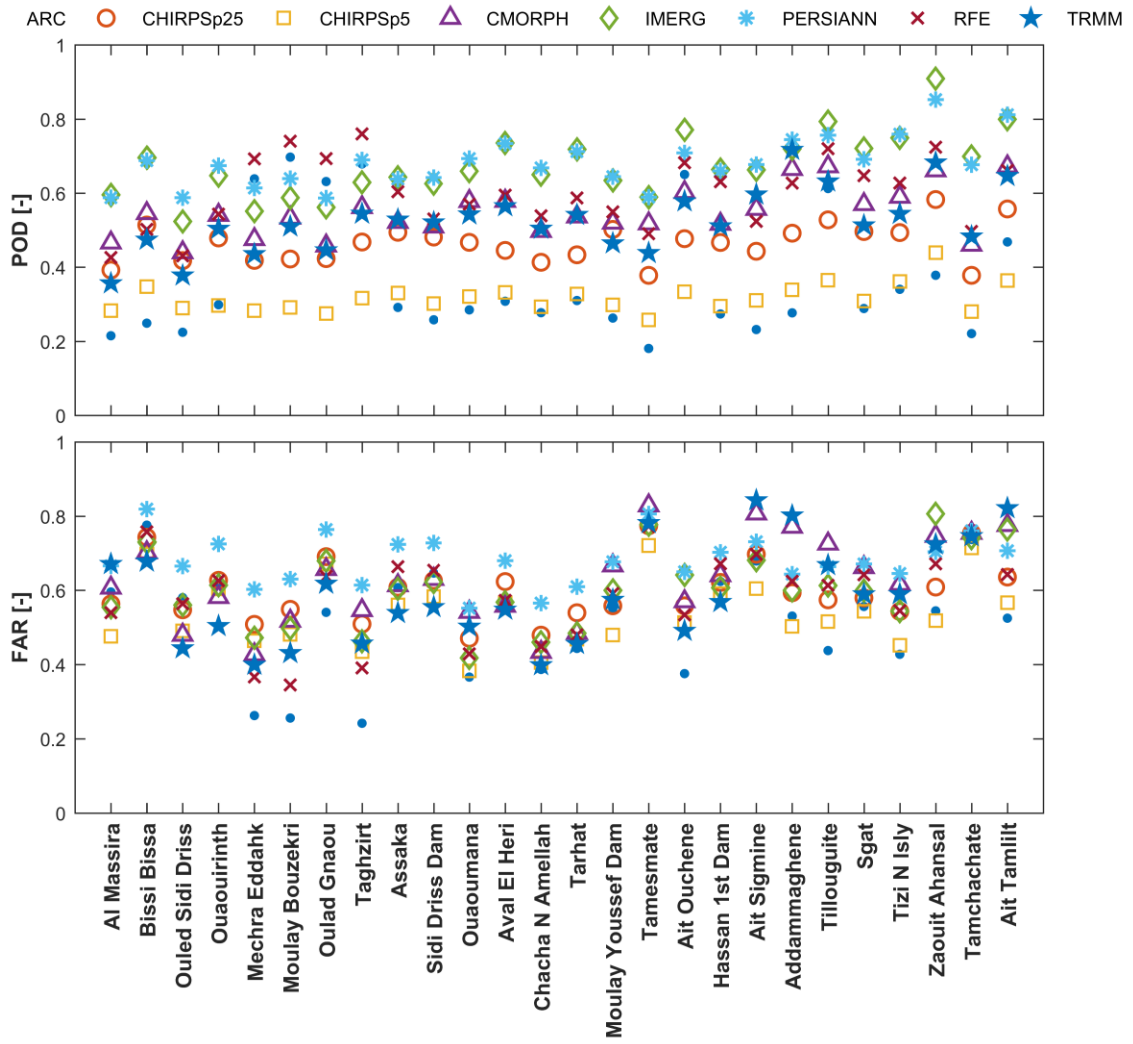

Figure 37. Statistical metrics (POD and FAR), computed at the daily time scale. The RGs are sorted in ascending order according to their elevation.

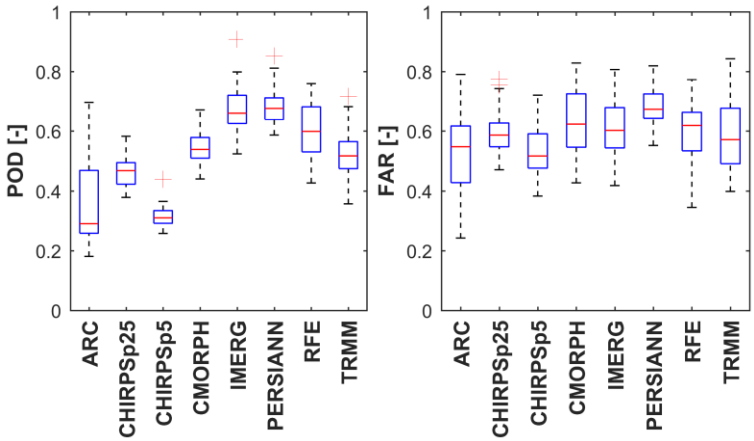

Figure 38. Boxplots summarizing the statistical metrics (POD and FAR) obtained at the daily time scale.

Generally, the missed events are equivalent to a complete loss of water supplies, and depending on their actual magnitudes they can be a potential source of uncertainties in water-related applications. As illustrated in Figure 39.a, during the study period, the SRPs missed rainfall events ranging from less than 1 mm.d^{-1} to more than 80 mm.d^{-1}. The rainfall events within the range of 0 – 5 mm.d^{-1} were the most frequently missed by all the SRPs, with percentages between 20% and 40%. The latter tended to zero as the daily rainfall totals increased. Missing more events of low magnitudes than events of high magnitudes can be related to the frequency-magnitude relationship in rainfall. As described by Davie (2008), this relationship assumes that low magnitude rainfall events tend to occur more often than events of high magnitude, which is the case in the OERB. We note that datasets such as CHIRPS and ARC failed to detect more than half of the rainy days in most of the rainfall ranges (Figure 39.b). This issue is of less extent respectively in CMORPH, TRMM, RFE, and PERSIANN, particularly IMERG showed the lowest missing rates in all the specified rainfall ranges.

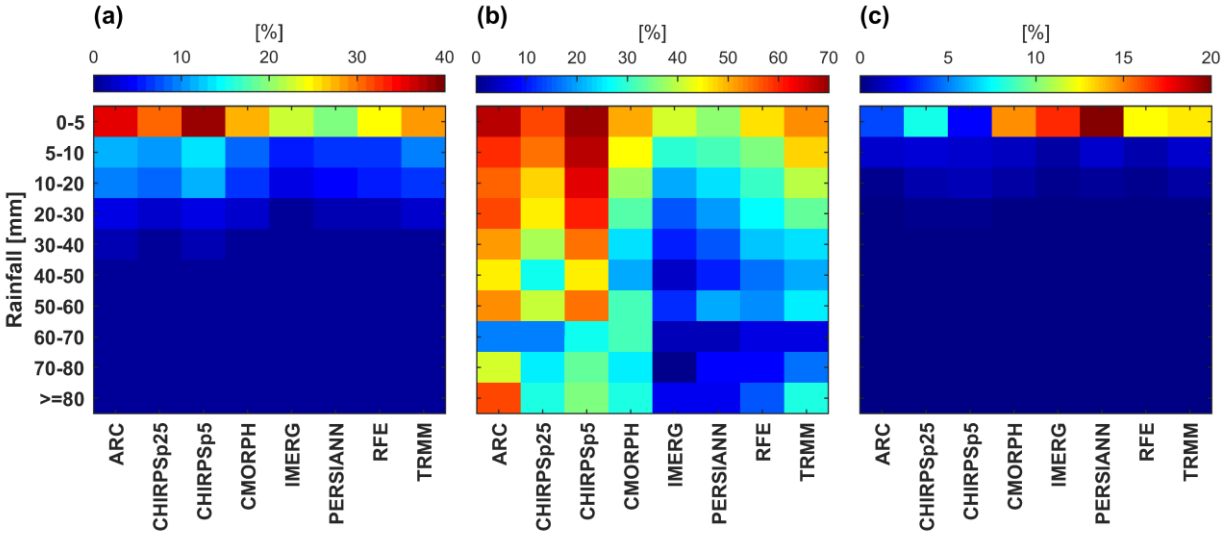

Figure 39. The percentage of correctly detected events (a), missed events (b), and false alarms (c) per rainfall class. The percentages reported in a, b, and c were calculated relative to the total number of rainfall events, the number of rainfall events in each class, and the total number of days in the study period, respectively.

For the false alarms, the FAR values were relatively large for most of the SRPs (Figure 37). They ranged between 0.24 (ARC) and 0.84 (TRMM). The SRPs captured around 40% of the rainfall events as false alarms at more than 75% of the RGs (Figure 38). The product showing the least false alarms often switched between ARC, CHIRPSp5, and TRMM with median FARs of 0.55, 0.52, and 0.58, respectively. PERSIANN, on the other hand, showed the highest rates of false

alarms at much of the RGs with 0.67 as a median value. Moreover, it appeared that the best-performing products in terms of event detection are likely to capture false alarms the most, and vice versa. This can be clearly observed in estimated rainfall totals that fall within 0 – 5 $mm.d^{-1}$, which were the most falsely detected magnitudes for all SRPs (Figure 39). Overall, the presence of false alarms can be the result of numerous factors according to the scientific literature (Mantas et al., 2014; Nashwan et al., 2019; Satgé et al., 2020; Serrat-capdevila et al., 2016). These factors are usually classified as those provoked by the climatic and topographic contexts, such as the impact of the dry hot air layers and desert dust on diminishing rainfall droplets before they reach the RGs (Nashwan et al., 2019). Other authors associated the false alarms with the inefficiency of the satellite sensors (IR and PMW) in differentiating between the rainy cloud systems and certain surface objects in the background (Mantas et al., 2014; Nashwan et al., 2019; Serrat-capdevila et al., 2016). In all these cases the false alarms are considered as unwanted events that deteriorate the performance of the SRPs (Nashwan et al., 2019; Serrat-capdevila et al., 2016). Also, it should be noted that a part of the discrepancies between the RGs and SRPs, related to the false alarms, can be attributed to the reliability of the RG network density relative to the intra-GC variability (Mantas et al., 2014; Satgé et al., 2020). Therefore, false alarms are to be expected given the differences in the spatial resolution of measurement between the SRP GCs (areal) and the RGs (punctual). The small coverage area combined with the low density of the measurement network can lead the RGs to miss a certain amount of rainfall events. Thus, the false alarms can actually be rainfall events that precipitated within the products' GCs areas, but distant enough to be covered by the homologous RGs. In this case, their presence would constitute a source of information to complement the RG data. The effect of the GC size on the ratio of false alarms can be observed by comparing the FARs obtained for CHIRPSp5 and CHIRPSp25 in Figure 37 and Figure 38. CHIRPSp5, with the smallest GC size, predominantly showed low FAR values compared to CHIPRPSp25. This indicates that the small GC size can help to reduce the number of falsely detected rainfall events.

Furthermore, to highlight the impact of the spatial resolution discrepancies on the occurrence of the false alarms, we analyzed the FAR values obtained considering GCs enclosing at least two RGs (Figure 40). The CHIRPSp5, RFE, and ARC datasets were not taken into account in this analysis owing to the complete absence of GCs that contain more than one RG. Five groups (G) constituted of two or three RGs were defined for the SRPs with 25 km^2 GCs, and one group of two

RGs was defined for IMERG. The groups' details are presented in Table 13. Each group includes FAR coefficients obtained based on the GC versus RG comparison (blue bars) and those obtained based on the comparison between the GC time series and the average of all RG situated within the same GC (yellow bars, Figure 40). As illustrated in the figure, the FARs obtained based on the average data were either less or equal to the minimum FARs obtained based on the individual RGs belonging to each of the groups. In other words, certain rainfall events, within the same GC, considered as false alarms in the first RG were correctly detected in the second one. These findings confirm that some of the false alarms were actually rainy events that precipitated out without being captured by the RGs (Satgé et al., 2019). Some of the gauges showed more uncaptured events than others. For instance, the average data in G4 and G5 yielded false alarms way fewer than Bissi Bissa (G4) and Oulad Gnaou (G5), but very close to Ouled Sidi Driss (G4) and Mechra Eddahk (G5). For G3, which happened to contain three RGs, the average data produced FARs that were noticeably less than those of the other groups.

Table 13. RG names per GC group.

	G1	G2	G3	G4	G5
Rain gauges	Ait Ouchene Taghzirt	Assaka Sidi Driss	Aval El Heri Chacha N Amlah Tarhat	Bssi Bissa Oulad Sidi Driss	Mechra Eddahk Oulad Gnaou

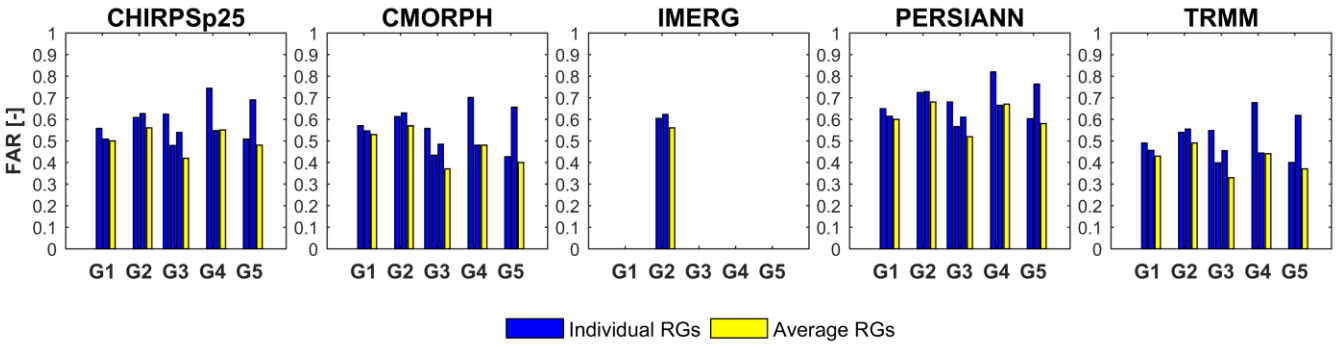

Figure 40. The blue bars represent the FARs computed through the comparison between the GC data series and each of the corresponding RGs. The yellow bars represent the FARs computed through the comparison between the GC data series and the average of all gauges corresponding to the GC.

In addition, all SRPs tended to misestimate the magnitude of most of the correctly detected rainfall events (Figure 41). They were found to frequently underestimate rainfall. Only CHIRPS datasets showed more overestimated than underestimated daily totals, with around 70% of the events were positively biased. The SRPs strongly underestimated rainfalls of high magnitude,

especially the totals greater than 40 mm.d^{-1}. The Bias values varied between -1 mm.d^{-1} to more than -30 mm.d^{-1}. For each rainfall range, the large biases were the most frequently obtained. At least 50% of the correctly detected rainy days belonging to the ranges above 40 mm.d^{-1} were underestimated by more than 30 mm.d^{-1}. The percentage appeared to decrease as we move towards low bias values to reach a minimum of 5% or less at the 0 – -5 mm.d^{-1} range. Nonetheless, IMERG and CHIRPSp5 seemed to have a relatively better capacity to accurately estimate the events of high magnitude than the other products. They both provided more estimates of less than -5 mm.d^{-1} bias

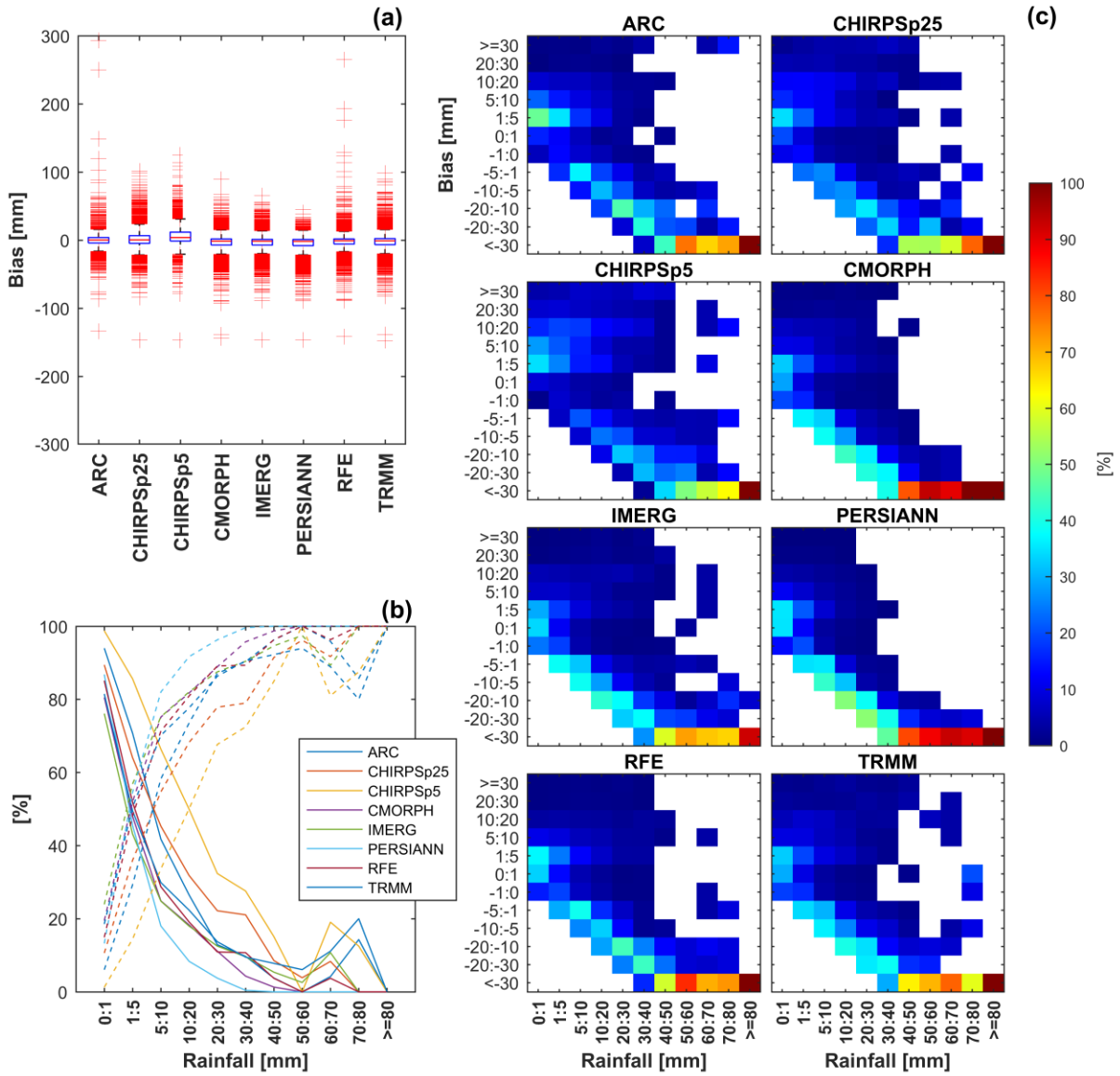

Figure 41. (a): boxplots summarizing the bias values calculated at the daily time scale considering data from all the studied RGs. (b): the percentage of daily rainfall totals that were overestimated (solid line) and underestimated (dashed lines) per rainfall class. (c): the percentage of correctly detected events classified according to the bias values and rainfall classes.

for such magnitudes. On the other hand, the overestimations mostly concerned smaller rainfall events, less than 40 $mm.d^{-1}$. Particularly, the SRPs tended to overestimate the rainfall events within the range of 0 – 5 $mm.d^{-1}$.

5.3.2. Watershed Average based Evaluation

In this section, the evaluation was held at a watershed basis using observed and SRP WAvg time series (Figure 42). Overall, in terms of the correlation between the two data sources, no major improvement was found compared to the GC-based comparison. Nevertheless, the agreement between the RG and SRPs predominantly increased, for all sub-watersheds, compared to the watershed-based average of the PCCs. The latter was obtained as the average of the metric values computed using the GC and the RG time series situated within the limits of each of the sub-watersheds (Figure 42.a). Still, the PCCs remained below 0.5 in most cases, except for ARC, RFE, and IMERG, which exhibited a relatively significant increase in PCC (Figure 42.b). These were mainly observed for Upstream OER and Tassaout-Lakhdar. In particular, IMERG showed the best correlations and outperformed the other products in most of the sub-watersheds, followed by RFE. The low performance obtained here highlights that a part of the mismatch between the SRP and the RG datasets can be related to the difference in their respective reporting times (Mantas et al., 2014). Besides, all the SRPs seemed to follow a downward performance gradient from north to south. The rainfall estimates achieved a higher agreement with the RG time series in Upstream OER (the wettest) than in Tassaout-Lakhdar (the driest), except for RFE and IMERG as the PCCs obtained in both sub-watersheds were comparable. A reverse behavior was observed for the RMSE. The SRPs showed low RMSE values in Tassaout-Lakhdar compared to Upstream OER, suggesting that the rainfall estimates tended to be less biased in relatively drier regions. This remark is in line with what was mentioned earlier about the increasing tendency of RMSE with the total water supplies. Still, the performance ranking based on the RMSE demonstrated similar patterns as the PCC, with IMERG and RFE exhibiting the lowest values.

The detection capacity of the SRPs improved compared to the GC-based evaluation. The relatively larger area of the sub-watersheds has led the SRPs to correctly capture more rainfall events. The increase in the detection capacity was more apparent for low-performing products in terms of POD, such as ARC and CHIRPSp5. On average, around 23% of additional rainy days were detected by ARC, with a maximum of 35% in Upstream OER, and at least 22% were

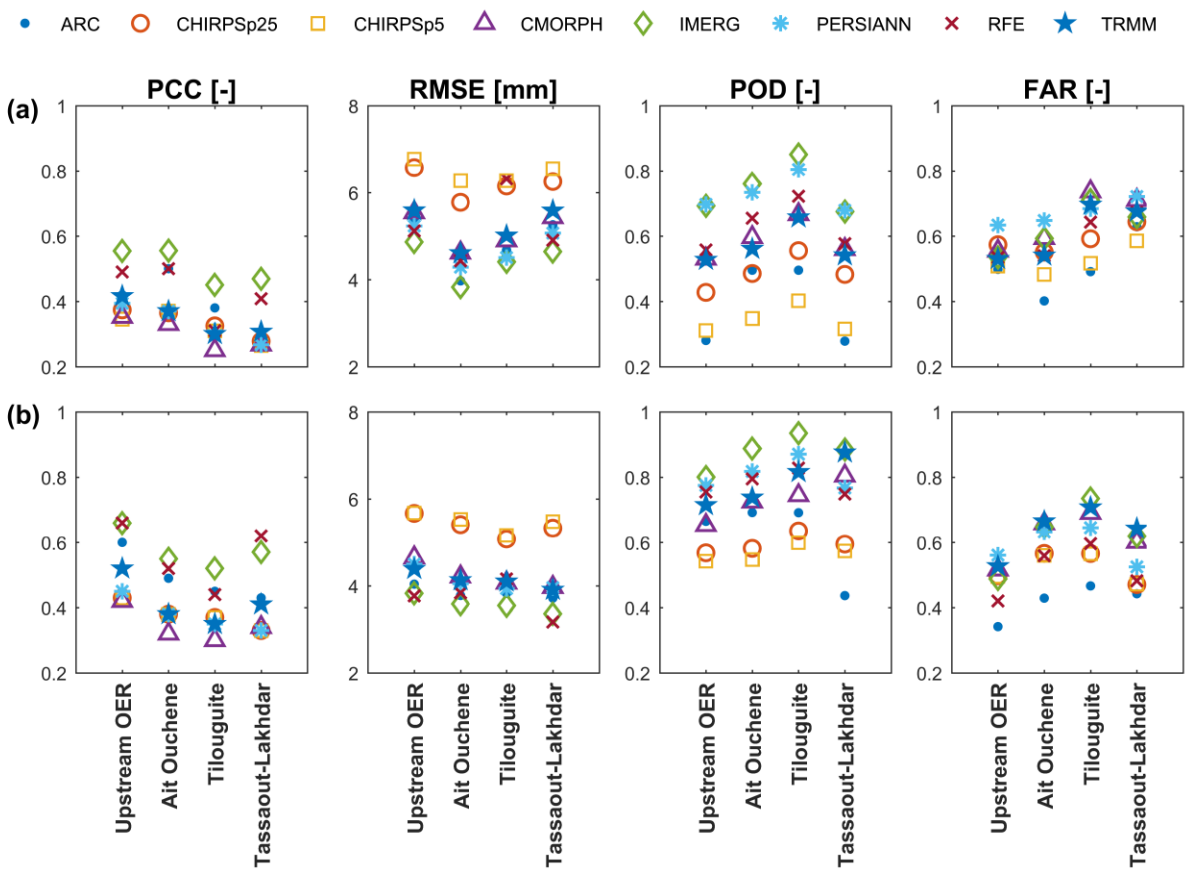

Figure 42. (a) Statistical metric values obtained by averaging the metrics computed for the GCs and RGs situated within each of the sub-watersheds. (b) Statistical metrics computed using the WAvg daily time series.

detected by CHIRPSp5 in the four sub-watersheds. Furthermore, the difference in GC size between CHIRPSp5 and CHIRPSp25 became less significant at the watershed scale. An average difference of 15% between both datasets (at the GC scale) was reduced to less than a 3% difference (At the watershed scale). Nevertheless, CHIRPSp5 detection capacity remained the lowest out of all the products with a median POD of 0.56, while IMERG exhibited the highest rate of correctly detected events with a median POD of 0.89. In contrast, as suggested by the FAR values, the watershed-based averaging option allowed a reduction of the false alarms in Upstream OER and Tassaout-Lakhdar, while it induced more of them in Ait Ouchene and Tilouguite. The increase in the FARs, in this case, can be partly explained by the gauging network density, which was found to have a significant impact on the percentage of false alarms (see section 5.3.1.). Depending on SRPs, the sub-watersheds with the fewest RGs (Ait Ouchene and Tilouguite) experienced the most noticeable increase in FARs. However, as demonstrated earlier, a non-negligible portion of these false alarms can be actual rainfall events that were missed by the spatially limited gauging network.

Bias-wise, the SRPs' performance slightly improved compared to the GC-based evaluation (Figure 43). The maximum bias values exhibited by the SRPs were remarkably reduced. In particular, some of the exaggeratedly overestimated daily events by ARC and RFE were significantly lessened when the estimates were regionally averaged. Overall, the overestimated totals were the most significantly decreased. Thus, the products maintained the same tendency of predominantly underestimating the rainfall totals, especially in the northern sub-watershed.

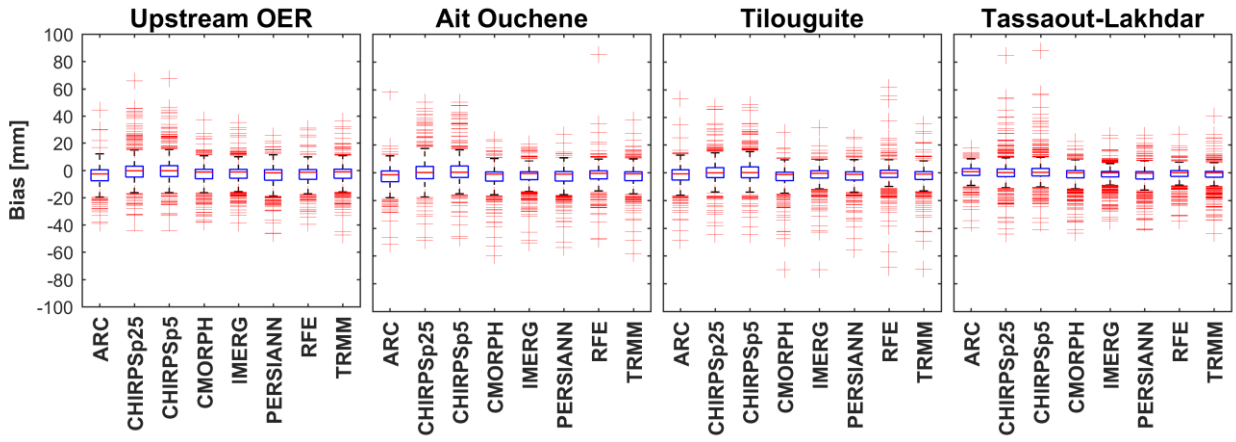

Figure 43. Boxplots summarizing the watershed-based bias values calculated at the daily time scale.

5.3.3. Suitability of the Spatial Rainfall Products in Simulating Daily Streamflow

In this section, we investigated the capability of the SRPs to simulate the daily streamflow using the HBV hydrologic model. Such an approach allows overcoming the gauging network limitations and cop with the difference in the measurement spatial resolutions (Poméon et al., 2017). It affords comprehensive and indirect consideration of the SRP's ungauged GCs (Satgé et al., 2019). The accuracy of the SRP-driven simulations was evaluated, against the daily gauged streamflow, using the NSE statistical metric. Figure 44.a and Figure 44.b illustrate the NSE values corresponding to the admissible simulations selected out of 100000 calibration runs in Ait Ouchcene and Tilouguite, respectively. In the figure, each box (boxplot) refers to the results of an SRP dataset while each group of nine boxes represents the NSE values obtained using a one-year calibration time series. The extreme left box in all groups shows the top simulations obtained based on the RG dataset. The horizontal dashed line is the 0.5 NSE baseline set as the threshold below which the corresponding simulations are rated as unsatisfactory (Moriasi et al., 2007). Based on the RG dataset, the HBV model performance varied from one sub-watershed to another. Overall,

the model performed better in Ait Ouchene than in Tilouguite, except in 2001/2002 where the NSE obtained in Tilouguite exceeded 0.5 contrary to those obtained in Ait Ouchene. In the latter sub-watershed, the HBV model provided good performance in five out of the nine studied years with NSEs between 0.65 and 0.88. In the four remaining years, the model performance was relatively low. While in 2007/2008 the NSE values did not exceed 0.57 and were mostly within an unsatisfactory range, they were fully below 0.5 in 2001/2002, 2004/2005, and 2006/2007. In these three years, the unsatisfactory results obtained after calibration were mainly due to data quality. They were mainly marked by frequent missed rainfall events induced by the RG's sparsity, as reported earlier (in section 4.3.1.). Numerous peak flows were measured at the watershed outlet while no rainfall was recorded at the RGs. Also, the low density as well as the poor distribution of the gauging network can partly explain the significant difference in performance between the two studied sub-watersheds. While the available RGs are well distributed over the Ait Ouchene, covering both of its upstream and downstream parts, they are mainly concentrated around the outlet of Tilouguite with no rainfall recorded for a considerable portion of its high elevated regions. Hence, in Tilouguite the HBV model performed poorly in most of the studied years, as the obtained NSEs were predominantly rated as unsatisfactory. Relatively higher NSEs were only found in 2001/2002 and 2009/2010. This can be due to far more missed rainfall events in Tilouguite compared to Ait Ouchene. This remark agrees with the findings of Xu et al. (2013), Arsenault and Brissette (2014), and Zeng et al. (2018) who reported that the gauging network distribution can play a major role in providing optimal model performance.

Regarding the SRP-driven model simulations, in Ait Ouchene the calibration results were seldom satisfactory. As shown in Figure 44, most of the SRPs performed the best in 2005/2006. In this year, the NSEs achieved by ARC, CHIRPSp5, and CHIRPSp25, IMERG, PERSIANN, and TRMM were predominantly unsatisfactory but can reach maximum values between 0.60 and 0.73. RFE, on the other hand, exhibited better performance compared to the rest of the products with NSEs ranging between 0.55 and 0.85. However, the SRPs accuracy appeared to be inconsistent and varied throughout the reference period. No product steadily provided reliable simulations for more than three years (Figure 44). This unsteadiness can be due to the changes in the availability and accuracy of the satellite data sources, particularly the PMW estimates, used as inputs to feed the algorithms of the different products (Huffman et al., 2010a). While CHIRPSp5, CHIRPSp25, and IMERG showed satisfactory NSEs in 2009/2010, they performed relatively poorly in other years

as only RFE (in 2002/2003 and 2008/2009) and IMERG (in 2003/2004) achieved NSEs that barely surpassed the baseline. The SRPs were mostly significantly outperformed by the RG dataset, except in those years where the RG-driven simulations were very low during calibration. On the one hand, the NSEs obtained by certain SRPs were found to be close to those obtained by the RGs, such as the case in 2001/2002 (ARC and RFE), 2004/2005 (IMERG and RFE), and in 2006/2007 (IMERG). Interestingly, in 2004/2005 and 2007/2008, the model simulations produced by ARC dataset suggested better performance than the RGs. More than 50% of the top simulations driven by ARC yielded NSE values greater than the maximum NSEs obtained using the RG dataset.

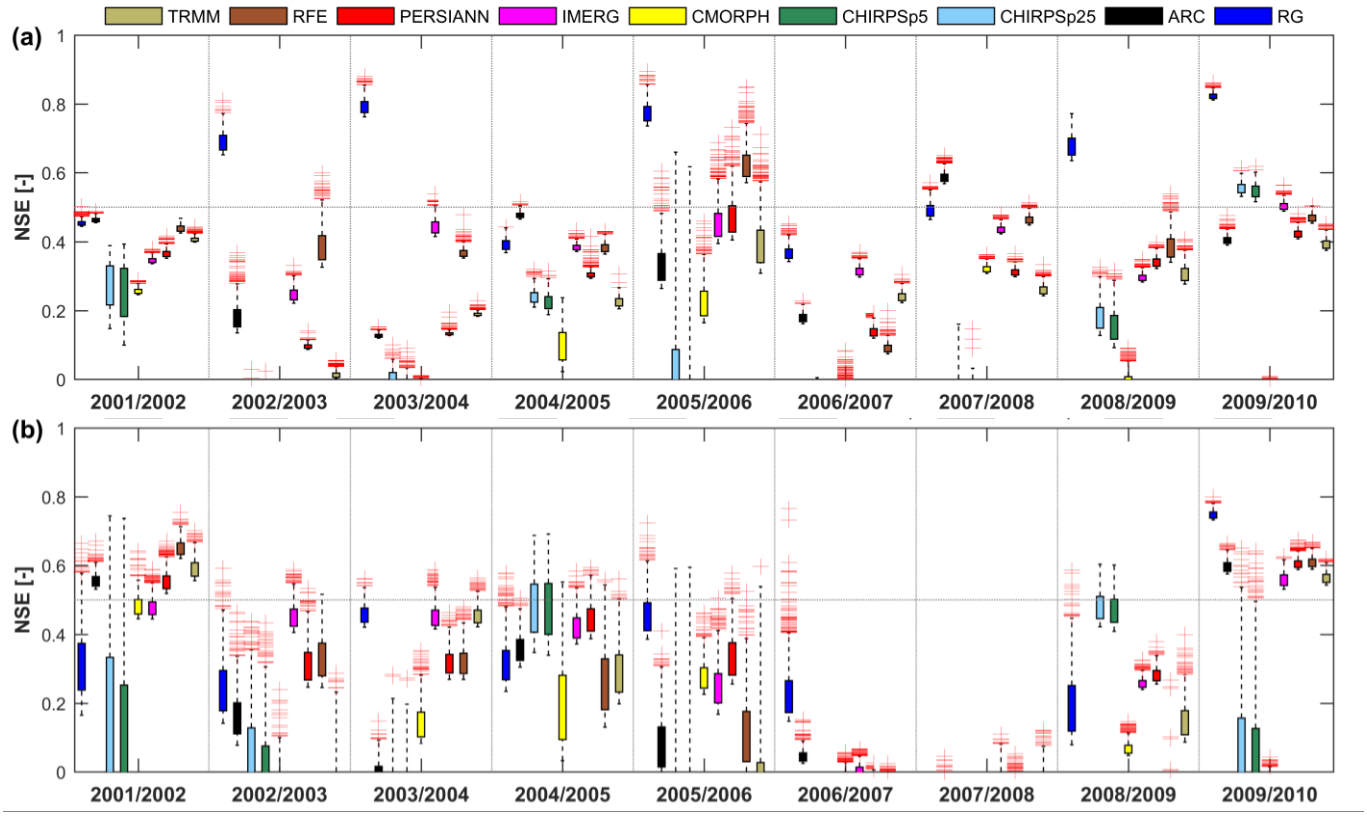

Figure 44. Boxplots representing the admissible simulations obtained over Ait Ouchene (a) and Tilouguite (b) sub-watersheds. The dark blue box (the extreme left) refers to the RG data while the remaining boxes refer to the eight SRPs datasets.

Moreover, the temporal inconsistency of the SRPs performance was also observed in the Tilouguite. Except for CMORPH, most of the products produced satisfactory simulations in 2001/2002 and 2009/2010, with median NSEs greater than 0.5. The accuracy of the rainfall estimates noticeably decreased in the remaining years, particularly in 2006/2007 and 2007/2008 where the majority of the obtained NSEs were negative. The performance deterioration seemed to be of less extent for CHIRPS datasets. The latter, followed by IMERG, steadily performed

satisfactorily in more years than any other product and achieved either close or better NSEs than those obtained by the RGs. Nevertheless, given the strong spatiotemporal fluctuations of the SRPs performance, it is not clear which product can be considered as the best performing. However, while CMORPH exhibited the poorest performance over both of the studied sub-watersheds and often yielded NSEs below zero, products such as ARC, RFE, IMERG, and CHIRPS frequently outperformed the remaining SRPs and worth further investigation. Given the overall low performance of the SRPs in calibrating the HBV model, the validation exercise was omitted and the products' hydrologic examination relied only on the NSEs obtained after calibration.

The poor performance exhibited by the SRPs in streamflow simulations can be the result of the combined effect of missed events and the important bias contained in the different rainfall estimates. As demonstrated earlier, the majority of the products underestimated most of the correctly detected events. Particularly, they tended to largely underestimate rainfall totals of high magnitudes. The latter, which often correspond to significant peak flows, can strongly reduce the robustness of the SRP-driven simulations. Hence, an alternative solution that relies on the combination of the SRP estimates and the RG dataset was needed in order to reduce the effect of the uncertainties related to the presence of bias and missed events. Figure 45 illustrates the NSEs corresponding to the top calibrated simulations driven by RG-SRPs combined datasets. The latter consists of a simple merger of the two data sources, where the SRPs estimates were used to complement the original RG dataset. The rainfall events captured as false alarms, with no additional alteration, were directly inserted into the RG data series. This combination approach was considered in an attempt to take advantage of possible correct false alarms (the false alarms that correspond to actual rainfall events). If present, the latter, can reduce the uncertainties induced by the peak flows that were not captured by the RGs and, thus enhances the overall performance of the model. Figure 45 displays the NSEs of the admissible streamflow simulations obtained after calibration. Figure 45.a and Figure 45.b correspond to the results obtained in Ait Ouchcene and Tilouguite, respectively. According to the figure, it is obvious that the direct merge of the false alarms does not necessarily imply an improvement of the model performance. Indeed, the maximum NSE values obtained by most RG-SRPs significantly increased compared to the SRP-only datasets. Still, the increase was not important enough to allow the exceedance of the RG-only results. On the other hand, the data combination has led to a regression of the overall performance of certain RG-SRPs. This can be clearly seen in 2004/2005 (for ARC, CHIRPSp5, CHIRPSp25,

and CMORPH) and 2007/2008 (for ARC) in Ait Ouchene, but mostly observed in 2001/2002 (all RG-SRPs) in Tilouguite. Additionally, the 99th NSE values have decreased for almost all data combinations over both sub-watersheds.

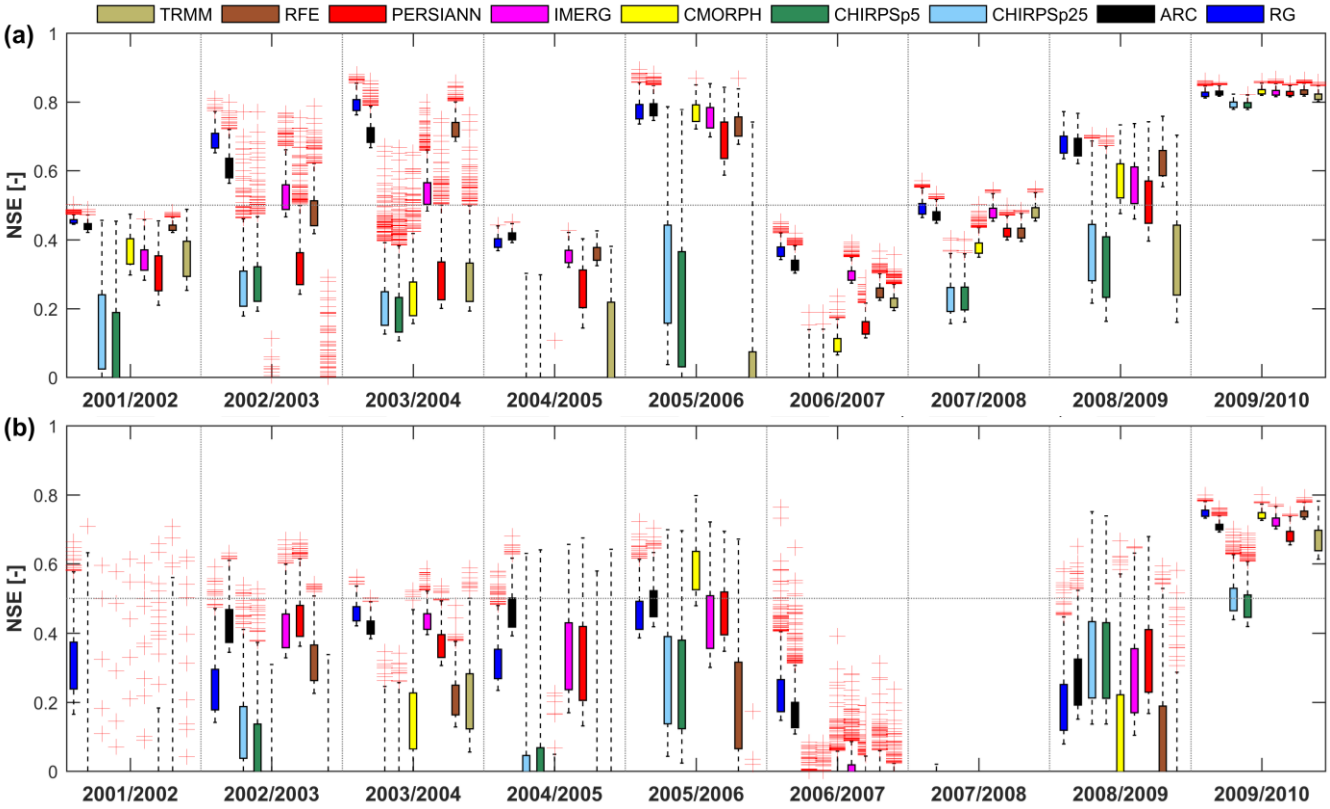

Figure 45. Boxplots representing the admissible simulation obtained over Ait Ouchene (a) and Tilouguite (b) sub-watersheds using the RG-SRP combined time series. The dark blue box (the extreme right) refers to the RG data while the remaining boxes refer to the combination between the RG and the SRP datasets.

The regression in performance of the RG-SRP compared to the RG-only datasets can be related to the occurrence of falsely detected events that were quite large relative to the corresponding streamflow records (hereafter insignificant false alarms). These can lead the model to simulate false peak flows and thus overestimate the gauged streamflow. The impact of the IFA (Insignificant False Alarms) can be deduced by comparing the results from Figure 45 and Figure 46. The latter (Figure 46) illustrates the daily totals of rainfall events captured by the SRPs as false alarms classified according to their homologous daily streamflow, in Ait Ouchene (Figure 46.a) and Tilouguite (Figure 46.b). Each circle refers to a rainfall event that was falsely detected on a certain day, where their sizes are proportional to the peak flow recorded on the same day. Considering the figures, it can be seen that the decrease of NSEs can be largely attributed to the presence of IFA. The latter was observed for the majority of the SRPs, but most frequently for

CHIRPS datasets. Their abundance in RG-CHIRPS combination has contributed to either significant drop-offs in NSEs, such as the case in 2004/2005 (Ait Ouchene) and 2001/2002 (Tilouguite), or a relatively slight increase in NSEs compared to that observed for the other data combinations, as in 2005/2006 and 2006/2007 in both sub-watersheds. When they were fewer, in 2009/2010 for instance, the combined data performance was less affected. These remarks hold true for the other products as well. Furthermore, the presence of the IFA can be of different degrees of impact depending on the time they have occurred. During summer when the model's upper reservoir is subject to excessive evapotranspiration, the incoming water contributes more to the

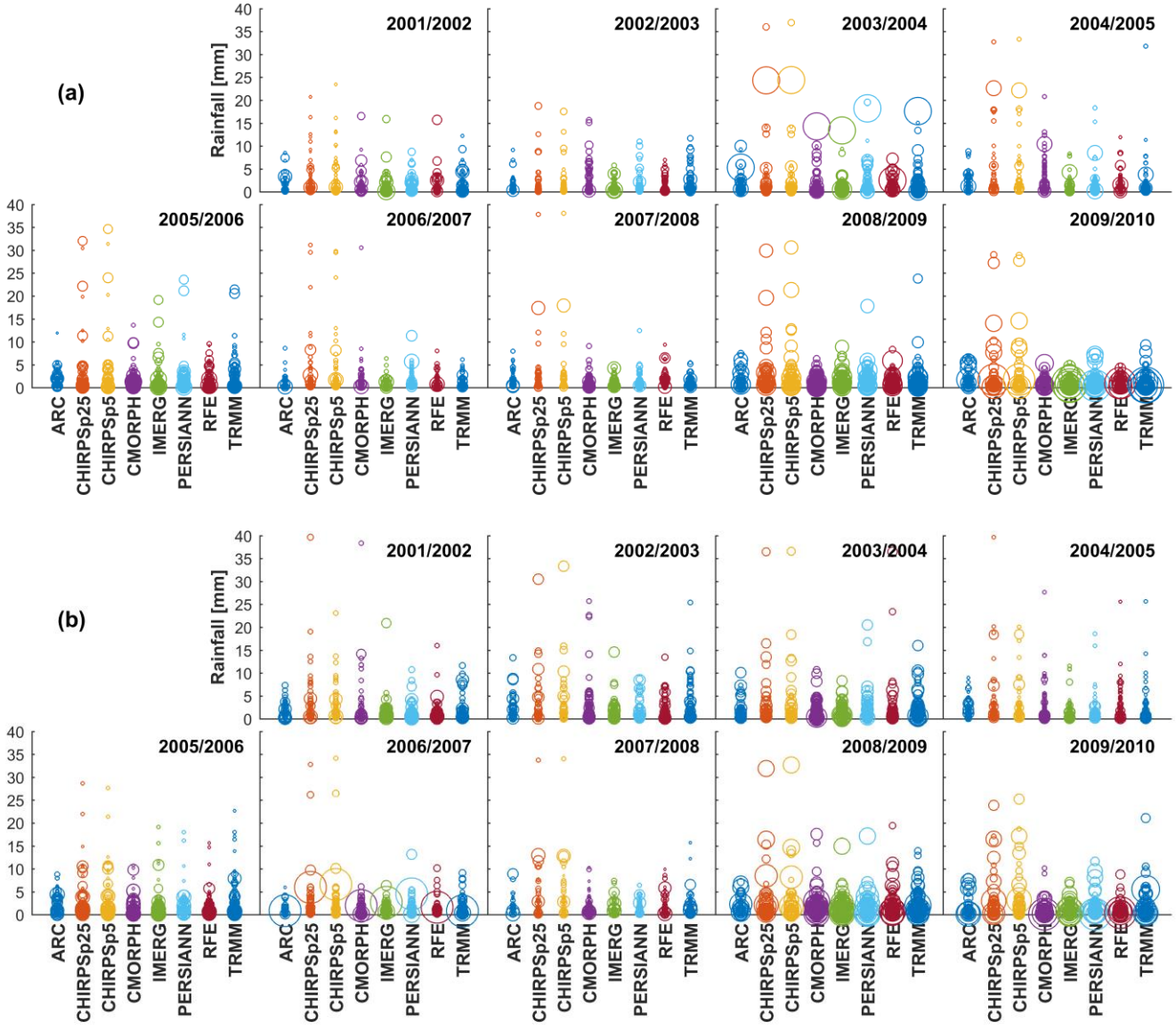

Figure 46. The daily rainfalls that were detected by the SRPs as false alarms in Ait Ouchene (a) and Tilouguite (b). The false alarms are classified based on the daily streamflow magnitudes. The size of the circles is proportional to the daily streamflow.

filling of the reservoir rather than to the rapid surface flow generation. Thus, the false alarms would be of less impact compared to the case when they have occurred during winter. Poméon, Jackisch, and Diekkrüger (2017), who evaluated several SRPs in West Africa, stated that the HBV model parameters governing the infiltration and evaporation can dampen the effects of over or underestimated rainfall. This may explain the improvement in the performance of certain data combinations despite the presence of large IFAs. This can be also the result of a trade-off between the IFAs and the significant ones (SFA). In Figure 46 we can note that the SRPs can capture some false alarms that correspond to relatively large peak flows. These can be of important interest in hydrologic modeling if correctly used to complement the RG datasets. The correct selection of the SFAs would require the implementation of a reliable classification scheme of the false alarms based on their significance to the streamflow generation. Hence, in future works, more focus should be given to the analysis of the false alarms to determine some key characteristics of the SFAs. This would allow us to efficiently select and merge the SRPs with the RG datasets through an assimilation scheme.

Chapter 6. The Spatial Rainfall Products' Capability to Reproduce the Monthly Rainfall Patterns over The OERB: Evaluation and Bias Correction

6.1. Introduction

In this chapter, we aim at evaluating the capability of the eight SRP datasets (ARC, CHIRPSp25, CHIRPSp5, CMORPH-CRT v1, GPM IMERG v6, PERSIANN-CDR, RFE, and TRMM 3B42 v7) to reproduce the rainfall patterns, observed over the OERB, at a monthly time scale. The SRPs were evaluated against the RG observations through a direct comparison considering both the GC and the WAvg time series. The evaluation was held using nine hydrologic years (from 2001 to 2010) of monthly rainfall measurements obtained from twenty-six RGs in addition to WAvg time series of four mountainous sub-watersheds (Upstream OER, Ait Ouchene, Tilouguite, and Tassaout-Lakhdar).

In the second part of this chapter, four bias correction techniques were adopted and applied to the SRPs in an attempt to reduce the bias contained in these datasets. In the bias-correction procedure, we focused only on the WAvg time series. We used the Ait Ouchcene and Tilouguite as the reference sub-watersheds to build the parameters required for each of the bias-correction techniques. The latter was then tested and spatially validated by verifying their capability to provide reliable bias removal in three out of the four sub-watersheds (Upstream OER, Ait Ouchene, Tilouguite, and Tassaout-Lakhdar) of the OERB. For instance, the parameters estimated for Ait Ouchene were used and validated on the Upstream OER, Tilouguite, and Tassaout-Lakhdar, and vice versa.

6.2. Methods

6.2.1. Evaluation Metrics

At the monthly time scale, the SRP datasets were evaluated against the RG data following the same approach used earlier (Chapter 5). Except for the categorical statistical metrics, the PCC (Equation 17) was used to assess the linear relationship between the SPRs and the RG data, and the RMSE (Equation 14), R-Bias (Equation 18), and Bias (Equation 19) were used to investigate the offset that the SRPs present relative to the RGs.

6.2.2. Bias Correction Techniques

As demonstrated earlier, for the daily timescale, the SRPs can be significantly biased with regard to the in-situ rainfall measurements. These biases, stemmed from different sources, prevent the absolute matching between the two data sources. Several adjustment techniques have been developed to count for the bias between the observed and SRP data. They were originally designed and extensively used for empirical transformation and bias correction of the rainfall estimated under the regional climate models and future projection scenarios (Lafon et al., 2013; Lenderink et al., 2007; Luo et al., 2018; Mendez et al., 2020; Teutschbein and Seibert, 2012). Recently, the application fields of these bias correction techniques have been widened to cover the adjustment of other hydroclimatic gridded datasets to match the in-situ observations. They were applied for datasets like the SRPs (Almazroui, 2011; Gumindoga et al., 2019; Ji et al., 2020; Liu et al., 2016; Xiang Soo et al., 2020; Yeggina et al., 2020; Yeh et al., 2020; Zad et al., 2018) and the soil moisture (Brocca et al., 2011; Reichle and Koster, 2004). These techniques range from simple linear scaling to more sophisticated and distribution-based approaches (Luo et al., 2018; Mendez et al., 2020; Teutschbein and Seibert, 2012).

Our aim is to bias correct the considered SRPs data to match the RG measurements using four different techniques: LS (Linear Scaling), QM (Quantile Mapping), a combination of LS and QM, and the SLR (Simple Linear Regression).

6.2.2.1. Linear Scaling

The LS is one of the simplest techniques. It has low data requirements and no assumption about the distribution is needed. It corrects the rainfall estimates using a constant scaling factor. The latter is calculated as the ratio of long-term mean monthly observed rainfall to the mean

monthly estimated rainfall (Teutschbein and Seibert, 2012). The scale factor, calculated for each month's time series, is applied to daily or monthly biased estimates of the same month. The technique is particularly powerful in correcting the mean monthly values but not in the wet-day frequency and intensity (Teutschbein and Seibert, 2012). The corrected rainfall time series are generated by multiplying the SRP monthly values by their respective scaling factor (Equation 20).

$$R_{LS} = R_{SRP} \times \left[\frac{\mu_m(R_{RG})}{\mu_m(R_{SRP})}\right] \quad \text{Equation 20}$$

Where:

R_{LS}: rainfall corrected using the LS technique;
R_{SRP}: raw SRPs data;
R_{RG}: observed rainfall;
μ_m: long-term mean monthly values.

6.2.2.2. Quantile Mapping

The principle behind the QM, an enhanced non-linear technique for bias removal, resides in adjusting the distribution function of the SRP estimates to match that of the RGs. It assumes that both SRPs and RG datasets have similar cumulative frequencies and the distribution characteristics of the data are stationary (Ji et al., 2020). Thus, the QM is also known as the CDF (cumulative distribution function) matching approach, as the CDF of one data source is rescaled to agree with the other one's CDF. This is done by building a transfer function (a non-linear polynomial) to shift the SRPs' CDF based on the statistical moments (mean, variance, skewness, and kurtosis) of the observed data (Mendez et al., 2020; Teutschbein and Seibert, 2012). Contrary to the LS technique, which focuses on the mean values, the QM (hereafter CDF) adjusts all the moments of the estimated data.

$$R_{CDF} = CDF_{RG}^{-1}(CDF_{SRP}(R_{SRP})) \quad \text{Equation 21}$$

Where:

R_{CDF}: rainfall corrected using the QM technique;
CDF_{RG}^{-1}: the inverse of the CDF built based on RG data;
CDF_{SRP}: CDF built based on the raw SRPs data;

The combination between the LS and CDF, referred to as LSCDF, was done by applying the CDF technique on the R_{LS} instead of the R_{SRP}.

6.2.2.3. Linear Regression Model

The simple linear regression is a statistical approach used to model the relationship between two variables (a dependent (y) and an independent (x) one). The latter is built based on a linear function of two parameters (β0 and β1) estimated from the variable data series. Above all, the technique requires that the relationship between the two considered variables must be linear. Thus, the adjustment exercise mainly relies upon a preliminary correlation analysis. Only time series showing high and significant correlation coefficients could lead to useful and reliable linear models, and hence adequate to be used. The linear function can be written in a simple format as:

$$y=\beta0+\beta1x+\varepsilon. \quad \text{Equation 22}$$

Through Equation 22, the "y" variable can be predicted from "x" using a linear relationship described by the parameters β1 (slope) and β0 (intercept). For bias correction, the linear regression is used to adjust the SRPs to the RG data by fitting the predictive model based on the least-squares approach. In our case, we were trying to build a linear model that, based on the SRP dataset, can provide rainfall estimates that are the closest possible to the RG measurements. Thus, the parameters β1 and β0 are estimated considering the R_{RG} as the dependent (response) variable and the R_{SRP} as the independent (predictor) variable.

$$R_{RG} = \beta0 + \beta1 \times R_{SRP} + \varepsilon \quad \text{Equation 23}$$

After being built and tested, the linear model can be henceforth used to provide corrected SRPs data regardless of the availability of the in-situ measurements. The corrected rainfall estimates can be determined through the linear combination of the raw SRPs estimates and the regressions model's parameters:

$$R_{SLR} = \beta0 + \beta1 \times R_{SRP} + \varepsilon \quad \text{Equation 24}$$

Where:

R_{SRP}: rainfall from the raw SRPs data;
R_{SLR}: rainfall corrected using the SLR technique;
$\beta0$: the intercept;
$\beta1$: the slope of the regression line;
ε: a random error term representing the deviation from the underlying regression line.

6.3. Results and Discussion

6.3.1. Grid Cell based Evaluation

In the following, we present the results of the SRP estimates' monthly evaluation against the RG observations. Figure 47 and Figure 48 display the statistical metrics (PCC, RMSE, and R-BIAS) computed using the monthly rainfall totals obtained from both data sources. In terms of PCC, the performance of the SRPs remarkably enhanced compared to the daily estimates. This improvement tendency, observed as we aggregate the data from the daily to the monthly time scale, was also highlighted in previous studies from different topographic and climatic contexts (Almazroui, 2011; Anjum et al., 2019; Babaousmail et al., 2019; Xue et al., 2013). Mantas et al. (2014) reported that the SRP estimates can be especially reliable when aggregated to time scales of 16-day to monthly. The enhancement in performance, when the monthly estimates are considered, can be the result of different factors. For instance, it can be related to the fact that the aggregation to coarser time scales dampens the mismatch introduced by the difference in reporting times (Mantas et al., 2014; Satgé et al., 2020). Also, It can be due to the use of monthly RG records during the calibration of the raw IR and PMW estimates (Anjum et al., 2019; Gao and Liu, 2013; Mantas et al., 2014). CMORPH showed the worst performance, with a maximum PCC of around 0.71 and a median below 0.5. ARC performed relatively better than CMORPH with 25% of the PCCs between 0.68 and 0.92, but it was outperformed by RFE that showed PCC values between 0.68 and 0.92 at 50% of the RGs. The prevalence of RFE over ARC can be attributed to the fact that the product uses PMW rainfall estimates in addition to the data that it has in common with ARC, namely the IR and RG datasets. Generally, the SRPs that incorporate the IR and PWM datasets are often better than those relying on the IR only (Poméon et al., 2017; Tang et al., 2020). The agreement of the rainfall estimates with the RG data was more consistent for the other products, as most of the correlation coefficients were between 0.7 and 0.93. The PCCs were the highest over the lowlands and tended to decrease with elevation to reach the lowest values in the mountainous region. Spatially, CHIRPSp5 and CHIRPSp25 showed the same pattern throughout the study area, and only small differences were found at fewer RGs. The same behavior was observed for PERSIANN, TRMM, and IMERG, between which the highest PCCs mostly alternate. Nevertheless, IMERG outperformed the other SRPs at most of the gauging stations. While the PCC values were the highest at only 2 and 6 RGs for PERSIANN and TRMM, respectively, they were

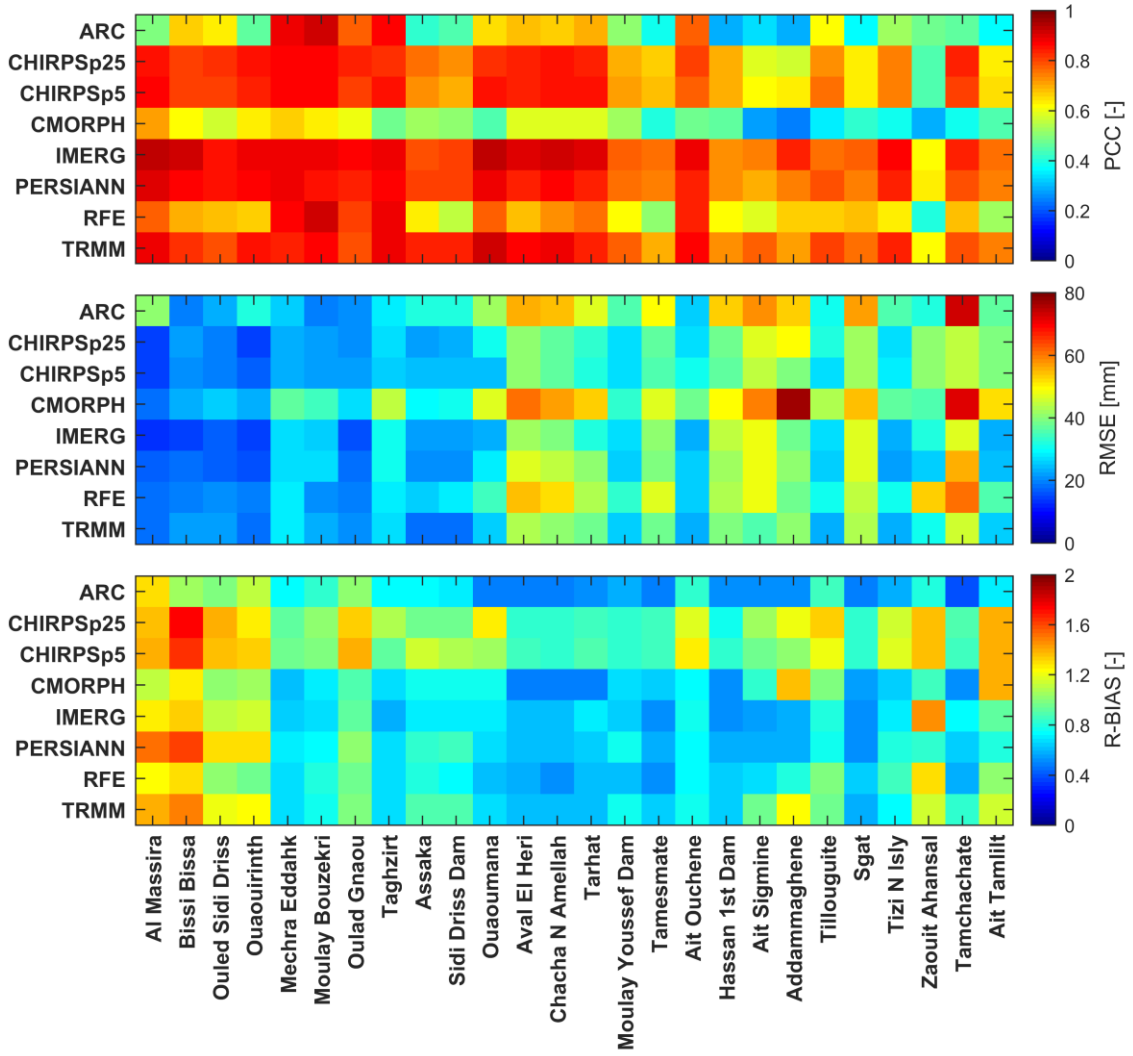

Figure 47. Heatmaps of the statistical metrics (R2, RMSE, R-BIAS) computed at the monthly time scale using the GC time series.

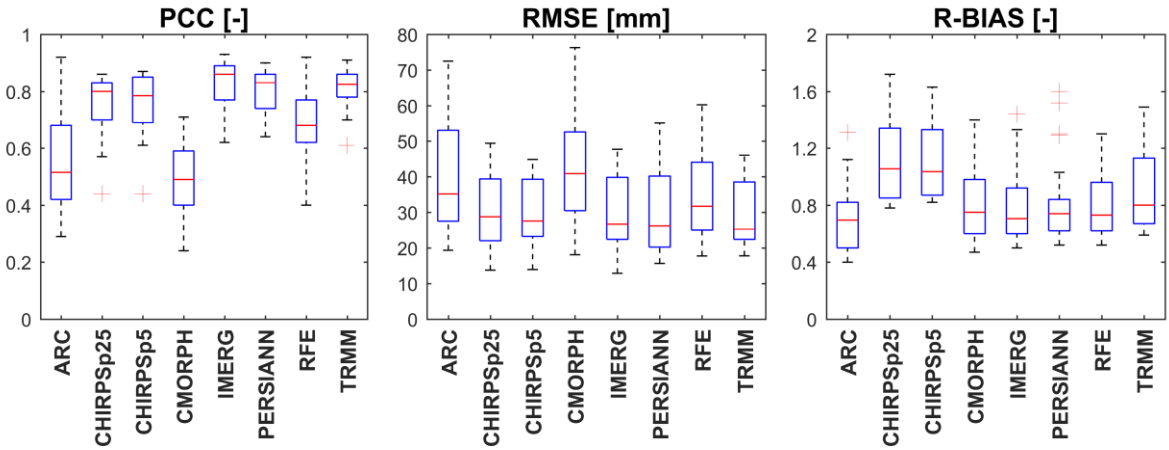

Figure 48. Boxplots summarizing the statistical metrics (R2, RMSE, R-BIAS) computed at the monthly time scale using the GC time series.

the best at 18 gauges for IMERG. The supremacy of IMERG over the other products, particularly TRMM, can be related to the advancements introduced in its rainfall retrieval algorithm (Anjum et al., 2019; Beck et al., 2019; Ma et al., 2020; Tang et al., 2020). These advancements can be summarized in the incorporation of recent PMW data sources (Beck et al., 2019; Tang et al., 2020), the use of new algorithms (such as the propagation approach from CMORPH motion vectors and the cloud classification system from PERSIANN-CCS) (George J. Huffman et al., 2019), and the adoption of a finer time reporting interval (30 min) that increases the chance of capturing short-duration events (Anjum et al., 2019). Moreover, no general conclusion can be drawn regarding the performance of the SRPs based on the RMSE. Except for ARC and CMORPH, which exhibited the largest RMSEs, no product seemed to show distinct and steady precedence compared to the others. However, all SRPs showed large RMSE values in most of the mountainous regions than in the lowlands. No SRP has fulfilled the requirement of a low RMSE, as recommended by Singh et al., (2004) and Moriasi et al., (2007). Furthermore, most SRPs tended to underestimate rainfall throughout the region, except at fewer gauges mostly of low elevations (Figure 47). This is not the case for CHIRPSp25 and CHIRPSp5 where the bias values were relatively evenly distributed around the baseline (R-BIAS = 1). Both SRP datasets showed the closest biases to the optimum with around 75% of the gauges were within a +/- 0.2 offset, and median values of 1.06 (CHIRPSp25) and 1.04 (CHIRPSp5) against medians between 0.7 and 0.8 for the other SRPs (Figure 48).

In terms of Bias, the monthly estimates were prevalently deviated compared to the observed monthly data (Figure 49.a). The actual bias values varied depending on products and rainfall totals. They showed similar patterns to the daily estimates. The SRPs tended to overestimate low rainfall totals and underestimate the larger ones. The same behavior was reported by Mantas et al. (2014) and Anjum et al. (2019) over the Peruvian Andes and the Tianshan Mountains, respectively. From one product to another, 70% to 86% out of the total number of monthly rainfall totals belonging to the 0 – 5 $mm.m^{-1}$ range were overestimated (Figure 49.b). As the rainfall ranges increased, these percentages steadily decreased against an increase in the percentage of the underestimated totals. The latter became predominant starting from the 10 – 20 $mm.m^{-1}$ range to reach more than 90% for the rainfall ranges above 100 $mm.m^{-1}$. For CHIRPSp5 and CHIRPSp25, the percentage of the overestimated rainfalls overpassed that of the underestimated rainfalls in much more ranges. For instance, around 58 % of the rainfall totals between 40 $mm.m^{-1}$ and 60 $mm.m^{-1}$ were found to be

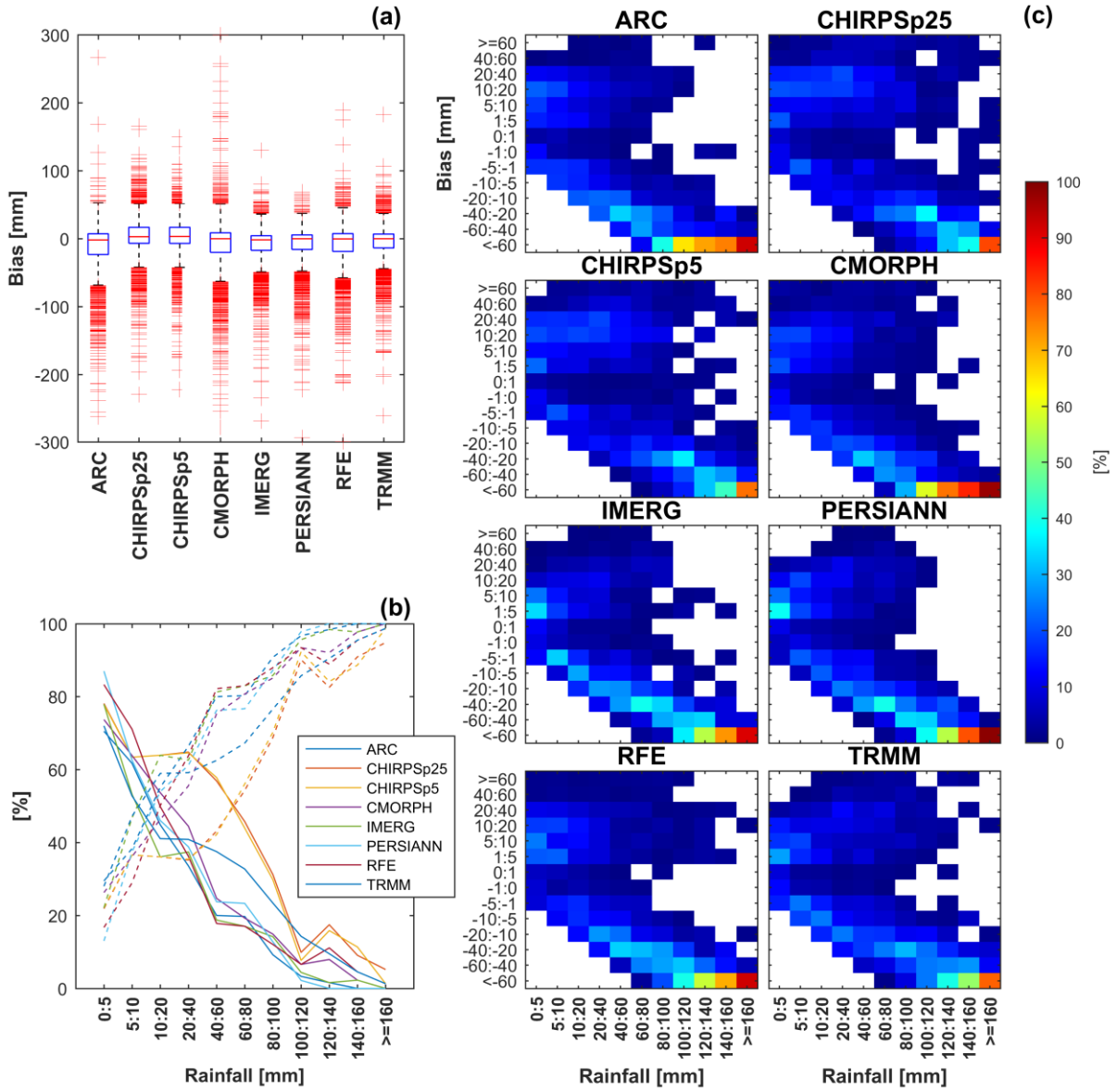

Figure 49. (a): boxplots summarizing the bias values calculated at the monthly time scale considering data from all the studied RGs. (b): the percentage of monthly rainfall totals that were overestimated (solid line) and underestimated (dashed lines) per rainfall class. (c): the percentage of monthly totals classified according to the bias values and rainfall classes.

overestimated by CHIRPS datasets against a maximum of 37% for the rest of the datasets. Moreover, most of the SRPs tended to significantly underestimate larger rainfall totals (Figure 49.c). The majority of the monthly SRP estimates exhibited negative biases up to 60 $mm.m^{-1}$, and often exceeded 150 $mm.m^{-1}$, for observed rainfalls greater than 100 $mm.m^{-1}$. The small biases for such ranges were rarely found. For instance, the maximum occurrence percentage

of the -/+10 $mm.m^{-1}$ bias values seldom surpassed 5%. This general tendency of remarkably misestimating the rainfall totals of high magnitudes, mostly gauged at the high elevated RGs, can partly explain the large RMSEs at the RGs located in the mountainous region (see Figure 47). According to previous studies the rough topography can undermine the rainfall estimates over such regions (Huffman and Bolvin, 2015; Mantas et al., 2014). Therefore, the SRPs provide better agreement in low elevated regions and tended to be more biased over the high lands (Anjum et al., 2019; Mantas et al., 2014; Wang et al., 2020).

6.3.2. Watershed Average based Evaluation

The statistical metrics (PCC, RMSE, and Bias) computed using the RG and SRP WAvg monthly rainfall time series are illustrated in Figure 50 and Figure 51. The comparison between the WAvg-based and the GC-based statistics revealed that when retrieved and averaged over watersheds, the SRP estimates can show a relatively better and consistent agreement with the RG dataset. This enhancement can be noticed in terms of correlation and bias (Figure 50 and Figure 51). The PCCs computed based on the WAvg data were generally larger than those computed based on the GC time series, except for ARC, IMERG, and PERSIANN in Ait Ouchene. The degree of increase in PCC varied depending on products and watersheds. The smallest increases were often associated with Ait Ouchene while the largest ones were mainly found in Tilouguite, particularly for CHIRPSp25 and RFE. The latter has known the most noticeable and widespread correlation improvement. For the same product, a PCC rise of between 0.13 and 0.18 was observed in three (Upstream OER, Tilouguite, and Tassaout-Lakhdar) out of the four considered sub-watersheds. Besides, comparing Figure 50.a with Figure 50.b and Figure 51 with Figure 49.a the WAvg time series seemed to exhibit relatively smaller Biases than the GCs ones. Thus, except for ARC and PERSIANN in Tilouguite, all of the SRPs showed a decrease in RMSE in all sub-watersheds. But no particular product appeared to provide a distinguishable improvement over the others. Although the observed drops in Bias, the SRPs remained significantly deviated from the RG measurements. The majority of the bias values that remained among the WAvg time series correspond to

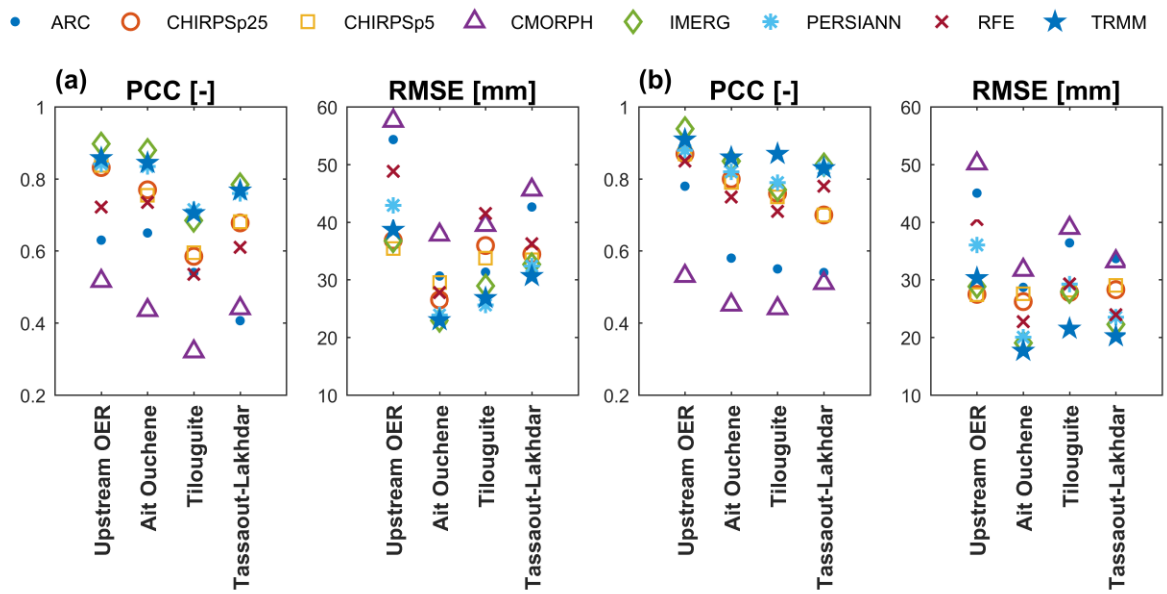

Figure 50. Statistical metrics computed at the monthly time scale using the WAvg time series. (a): the PCC and RMSE values, calculated as the average of the statistical metrics computed based on the RGs and the GCs situated within each of the sub-watersheds. (b): the PCC and RMSE values computed based on the RG and SRP WAvg time series.

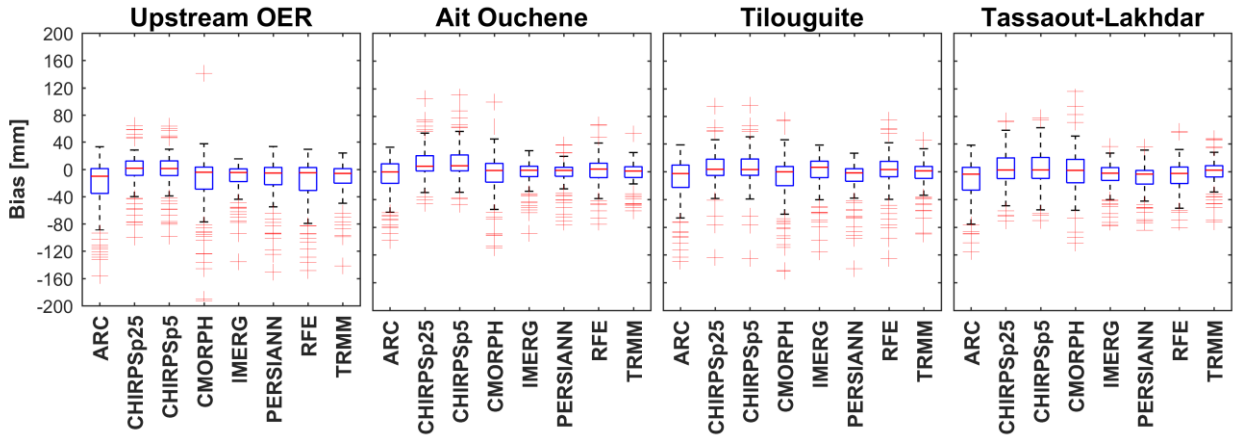

Figure 51. Boxplots summarizing the watershed-based bias values calculated at the monthly time scale.

underestimated rainfall totals. A non-negligible amount of these values frequently exceeded 60 mm.m^{-1} (Figure 43). As can be seen in Table 14, the underestimations mainly occurred during the period between October and April (except for CHIRPS datasets), which encompasses the wettest months that largely contribute to the annual rainfall totals in the OERB. During the same period, the SRPs happened to exhibit the largest RMSE values (Table 15). This confirms the struggle of the SPRs in estimating the important rainfall totals that occur during the months of the aforementioned period. The persistence of the bias in the SRP datasets highlights the inefficiency of the calibration process implemented in their respective algorithms. This can be due to the

scarcity of the RGs available within the framework of the international data collection programs, such as the case of the GPCP. The calibration RGs scarcity constrains the calibration process in numerous regions of the African continent (Poméon et al., 2017). Thus, a bias adjustment operation would be required before any use of these products in water-related applications.

Table 14. R-Bias metric computed using rainfall time series of each month. The values reported in the table refer to the average R-Bias of the four mountainous sub-watersheds (Upstream OER, Ait Ouchene, Tilouguite, and Tassaout-Lakhdar).

	Sep	Oct	Nov	Dec	Jan	Feb	Mar	Apr	May	Jun	Jul	Aug
ARC2	1.52	0.82	0.36	0.48	0.51	0.52	0.57	0.65	0.86	1.83	3.06	1.42
CHIRPSp25	1.08	1.28	0.81	1.07	1.27	1.33	1.47	1.25	1.08	0.93	0.69	0.67
CHIRPSp5	1.09	1.28	0.81	1.09	1.29	1.36	1.49	1.26	1.10	0.93	0.71	0.68
CMORPH	1.08	0.79	0.53	0.63	0.95	0.66	0.83	0.93	0.62	1.22	2.78	1.44
IMERG	1.45	1.15	0.64	0.84	0.62	0.67	0.68	0.97	0.92	1.41	3.59	1.44
PERSIANN	1.48	1.03	0.50	0.69	0.56	0.72	0.81	0.97	0.80	1.10	1.01	1.03
RFE	1.69	0.90	0.68	0.70	0.80	0.67	0.75	0.79	0.86	2.17	3.66	2.15
TRMM	1.38	1.12	0.79	0.82	0.78	0.74	0.81	0.95	0.93	1.13	2.05	1.08

Table 15. RMSE (mm) metric computed using rainfall time series of each month. The values reported in the table refer to the average RMSE of the four mountainous sub-watersheds (Upstream OER, Ait Ouchene, Tilouguite, and Tassaout-Lakhdar).

	Sep	Oct	Nov	Dec	Jan	Feb	Mar	Apr	May	Jun	Jul	Aug
ARC2	15.77	27.58	61.28	50.94	49.04	47.49	31.75	31.52	20.82	14.52	13.93	12.17
CHIRPSp25	10.93	24.61	39.68	29.97	32.16	46.23	31.59	25.03	16.29	6.95	7.23	10.77
CHIRPSp5	10.98	24.71	39.46	30.54	33.30	47.82	32.90	25.20	16.33	6.91	7.24	10.78
CMORPH	10.69	21.58	61.84	53.27	64.07	54.44	35.25	29.02	24.90	8.31	10.94	11.07
IMERG	10.56	13.77	37.91	29.03	37.32	34.16	28.37	15.33	14.01	8.21	13.97	11.06
PERSIANN	12.11	18.55	50.74	37.48	42.12	34.03	17.51	18.51	15.39	7.30	6.86	8.19
RFE	21.02	18.12	43.64	45.13	31.13	36.60	25.03	25.48	16.24	21.56	14.14	16.23
TRMM	9.82	13.78	29.36	31.59	34.32	35.80	24.71	11.81	12.46	5.63	7.42	8.82

6.3.3. Bias Correction of the Spatial Rainfall Products

6.3.3.1. Application of the Bias Correction Techniques

Four bias-correction techniques were adopted to account for the bias in the raw SRP datasets. The correction procedures concerned the WAvg time series only, considering their superior performance at the monthly time scale in terms of correlation and bias. Figure 52 illustrates the statistical metrics (PCC, RMSE, and R-BIAS) computed using the raw data, as provided by the original products' estimates, and the four bias-corrected time series. The latter were obtained by

adjusting the R_{SRP} monthly estimates to the observed R_{RG} based on the LS (R_{LS}), SLR (R_{SLR}), CDF (R_{CDF}), and LSCDF (R_{LSCDF}) techniques. All of these techniques were applied to the SRPs each month separately. Thus, the full data series were decomposed into twelve time series, one for each month, and then reassembled after the correction was done. This procedure mainly allowed us to deal with the seasonality that characterizes the rainfall patterns over the study area. Thus, twelve scaling factors, linear models, and polynomial models were built for each of the SRP data series. It should be noted that only six out of the eight SRP datasets were considered in this analysis; CHIRPSp25 and TRMM datasets were excluded. The CHIRPSp25 performance metrics were generally similar to those of CHIRPSp5 and TRMM showed relatively inferior performance compared to its successor IMERG. The TRMM data, in addition, is no longer available for recent dates as the mission's lifetime was ended back in 2015. For that, the bias correction of both datasets would be of no viable usefulness. The results suggest that the bias correction significantly enhanced the SRP estimates. This can be noticed for all statistical metrics considered here (Figure 52). As demonstrated by the R-BIAS, the overall bias values were completely neutralized. After being corrected, the R-BIAS of all six SRPs matches the perfect value of 1. This does not necessarily mean a complete removal of the bias between the SRP estimates and the RG dataset. It does mean, instead, that the over/underestimation tendencies of the products were set to an equilibrium, and no predominance can be reported. However, the application of the bias correction techniques has led to a non-negligible reduction in the average bias values. As can be seen in Figure 52, the RMSEs have decreased by about 10 mm on average, depending on products and correction techniques. The highest bias decrease was observed for CHIRPS in Ait Ouchene and PERSIANN in Tilouguite. Still, the lowest RMSEs obtained after bias correction were computed by IMERG and PERSIANN in the two studied sub-watersheds. For both products, the RMSE moved from more than 20 mm to around 10 mm in Ait Ouchene and from around 30 mm to less than 20 mm in Tilouguite. We noted that the performance of the four bias correction techniques was very close, particularly the LSCDF seemed to show no improvement compared to the CDF alone. Furthermore, the bias attenuation has contributed to a significant improvement in the linear relationship between the SRP and RG datasets. The computed PCCs remarkably increased for all SRPs. The bias-corrected time series produced by all techniques yielded better correlations than the raw estimates, with some differences depending on products and techniques. The highest increase in PCC values was obtained for ARC and CMORPH by about 0.23 points on average. However, their performance in terms of linear

correlation remained the weakest. For both SRPs, all corrected time series showed PCCs lower than those obtained by the other products' raw data, except for ARC's R_{SLR} that barely surpassed the raw estimates in Ait Ouchene and Tilouguite. For the remaining products, the PCCs were fairly close with the precedence of CDF and SLR, respectively, over the LS. This was of less importance for IMERG and PERSIANN, which were found to be the best performing products after bias correction. They showed a PCC rise ranging from about 0.1 to 0.14, which means an increase of the correlation coefficients from 0.85 to 0.95 (IMERG) and from 0.82 to 0.93 (PERSIANN) in Ait Ouchene. In Tilouguite, the PCCs increased from 0.77 to 0.91 (IMERG) and from 0.79 to 0.92 (PERSIANN). Thus, out of the six products, IMERG and PERSIANN were selected to be retained for further investigation.

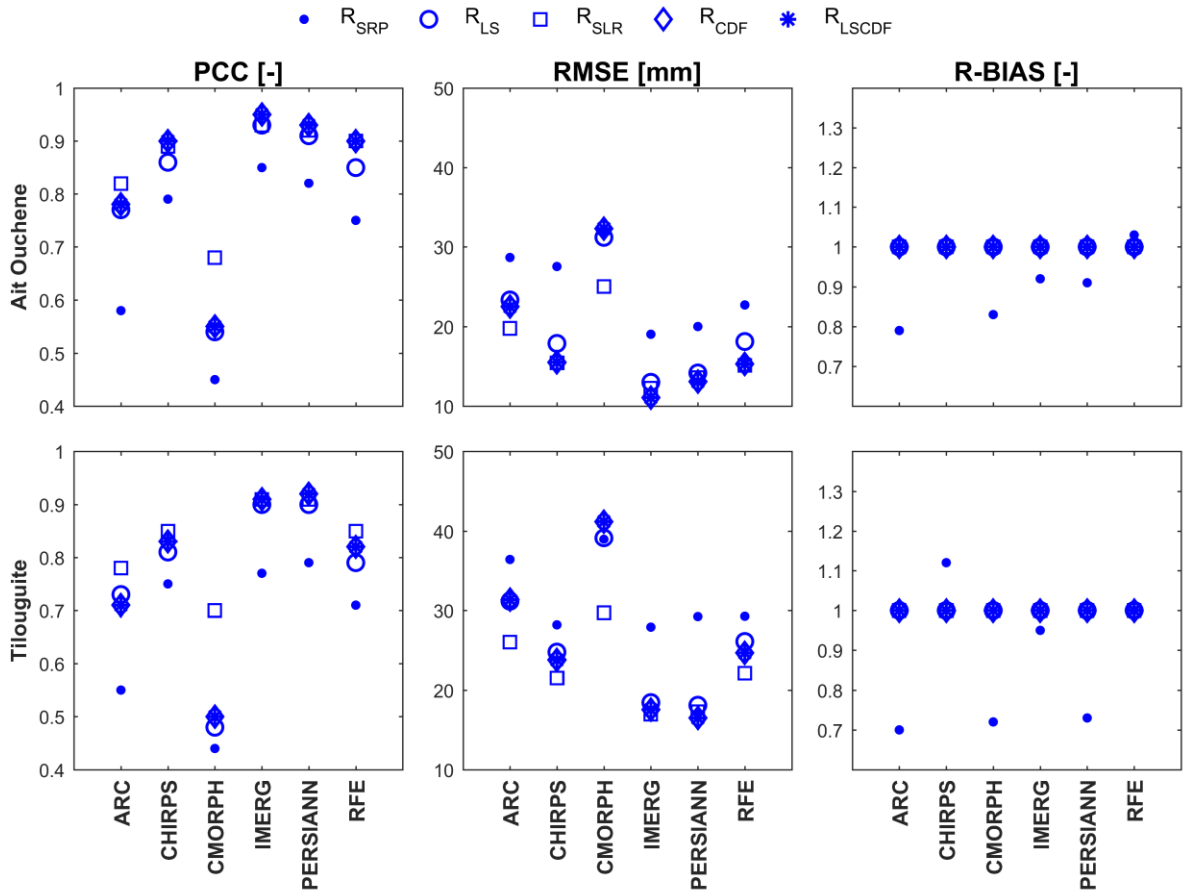

Figure 52. Monthly statistical metrics (PCC, RMSE, R-BIAS) computed using RG data against raw SRP estimates and SRPs corrected based on the four considered bias correction techniques. The illustrated metrics cover six SRPs (ARC, CHIRPS, IMERG, PERSIANN, and RFE) in Ait Ouchene and Tilouguite sub-watersheds.

Figure 53 and Figure 54 illustrate the scatter plots of RG versus SRP data in Ait Ouchene and Tilouguite, respectively. In one same plot, the red points represent the RG versus raw SRP

estimates and the blue points represent the RG versus the SRP estimates corrected using one of the four bias-correction techniques (annotated within the subplots). As can be seen in Figure 53 and Figure 54, in both sub-watersheds, the large monthly rainfall totals were mostly underestimated while the small totals tended to be overestimated. According to both figures, IMERG and PERSIANN underestimated the majority of the monthly totals above 40 $mm.m^{-1}$ while they overestimated those that were less. Particularly, the rainfall totals below 20 $mm.m^{-1}$ were the most frequently significantly overestimated. This observation was more prominent in IMERG than in PERSIANN. As reported earlier, all the bias correction techniques have contributed to improving the agreement between the RG and SRP datasets. With variable degrees, they were all found to act on both small and large rainfall totals. Out of the four techniques, CDF provided the best fit to the observed data compared to LS and SLR. The SRP estimates became better aligned around the y=x line for both rainfall classes (small and large). In particular, the CDF well adjusted the majority of the monthly rainfall totals greater than 60 $mm.m^{-1}$. For instance, using the CDF, estimated totals of 30 – 60 $mm.m^{-1}$ and 60 – 90 $mm.m^{-1}$ were raised to 60 – 90 $mm.m^{-1}$ and more than 100 $mm.m^{-1}$, respectively. This can be observed in the two studied sub-watersheds for PERSIANN, and with less extent for IMERG in Tilouguite. Overall, the raw SRP estimates were significantly redressed such that the cumulative distribution function of the SRP dataset became near-perfectly superimposed on that of the RG dataset (Figure 55).

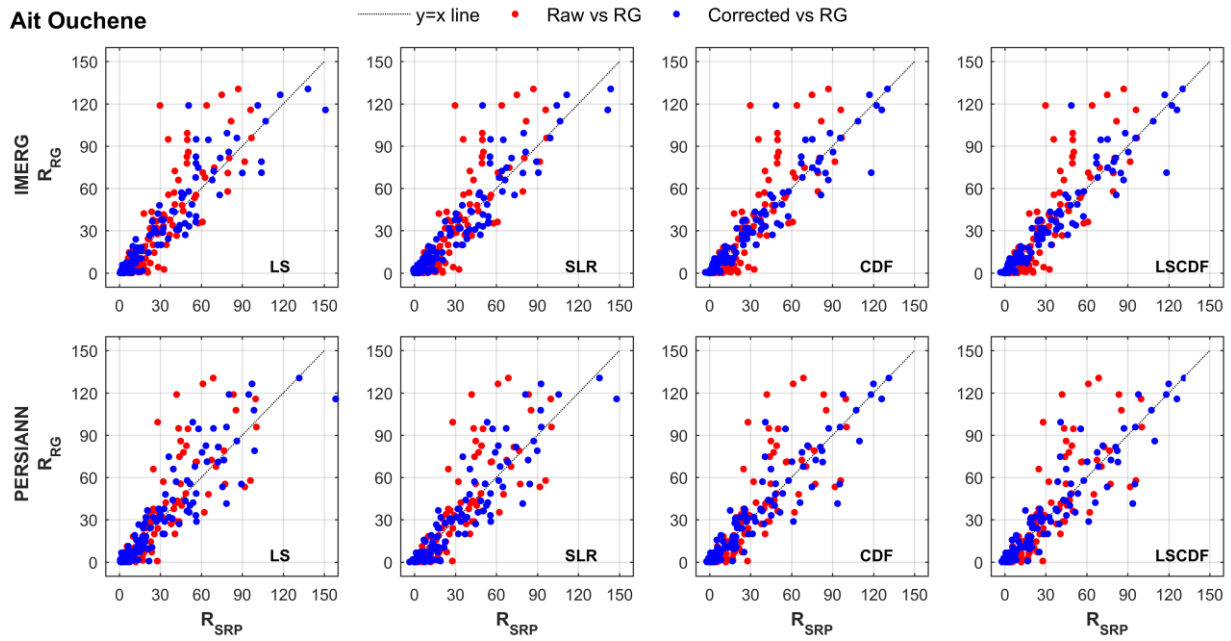

Figure 53. Scatterplots of RG data (in mm) versus SRPs estimates (in mm) corrected (blue points) based on the four bias correction techniques (LS, SLR, CDF, and LSCDF) in the Ait Ouchene sub-watershed. The red scattered points represent the RG data versus the raw SRPs estimates.

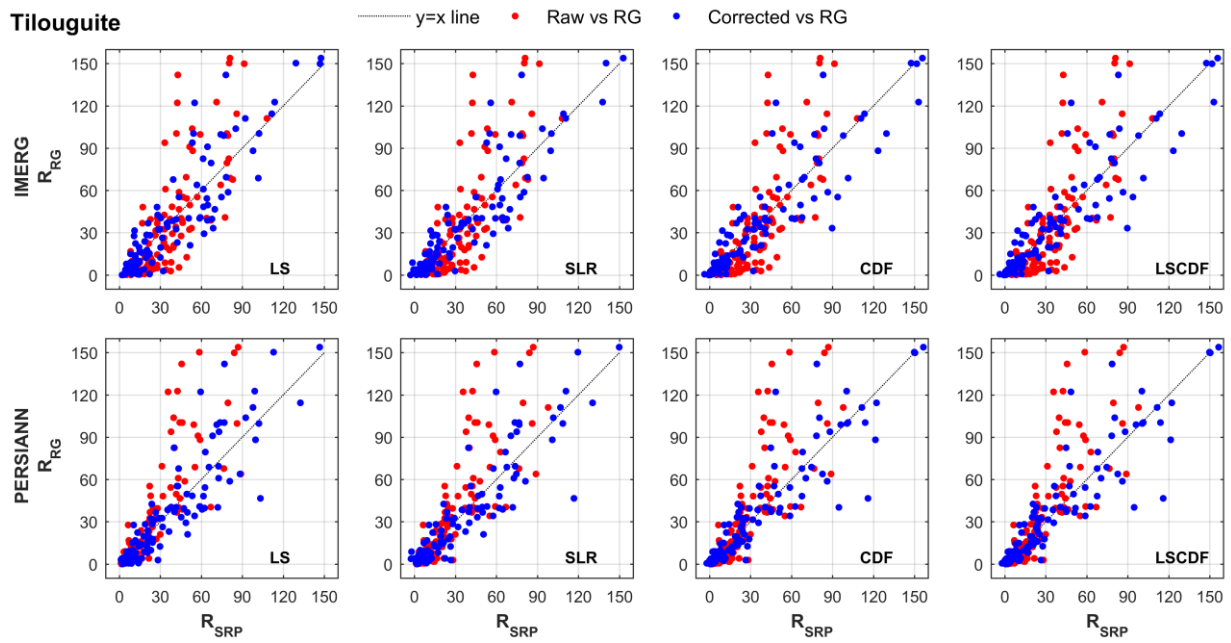

Figure 54. Scatterplots of RG data (in mm) versus SRPs estimates (in mm) corrected (blue points) based on the four bias correction techniques (LS, SLR, CDF, and LSCDF) in the Tilouguite sub-watershed. The red scattered points represent the RG data versus the raw SRPs estimates.

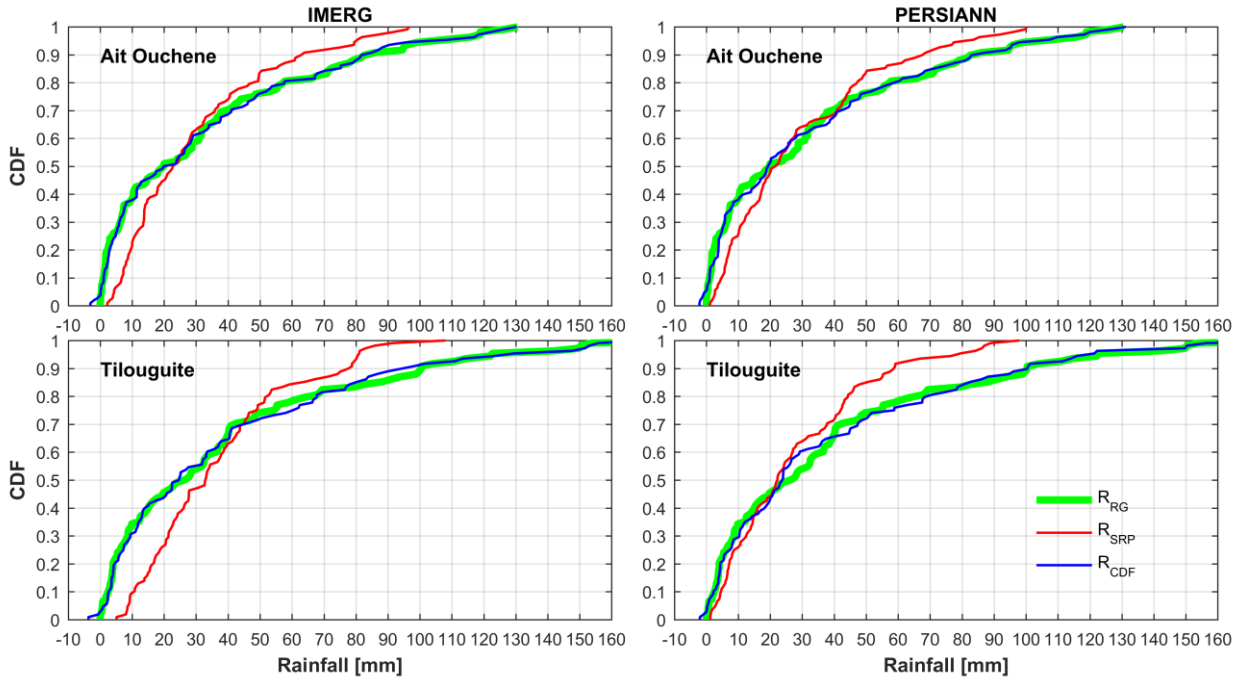

Figure 55. CDF curves build using RG (green), raw SRPs (red), and corrected SRPs (blue) in Ait Ouchene and Tilouguite sub-watersheds.

It must be outlined that, contrary to LS, the bias correction employing the SLR and CDF techniques resulted in time series that contain negative values (Figure 56). For SLR, these values

occurred in cases where the raw SRP estimates were substantially staggered relative to the long-term monthly average. In particular, the very low rainfall totals recorded during the months where the SRP frequently overestimated the RG dataset (Table 14) were the ones that became negative after correction. Generally, in such months, the raw SRP estimates are supposed to be greater than those collected by the RGs. Thus, the linear models were built such that they subtract a certain quantity from the raw estimates in order to produce corrected rainfalls that match the RGs. Any time the models meet raw estimates that are too small than the quantity to be subtracted the negative values occur. This situation was mainly associated with the early-autumn, late spring, and summer months. For the CDF, on the other hand, the negative values appeared every month of the hydrologic year where the raw SRP rainfalls were relatively low and corresponded to very small observed rainfall totals. For the two bias-correction techniques, around 5% of IMERG and PERSIANN data series were affected by this issue. Also, the latter, concerned only SRP rainfall totals that were below 10 $mm.m^{-1}$. Therefore, and given the fact that SRP data seldom misestimates the small totals (as demonstrated earlier), the negative values can be overcome by simply replacing them with their homologous from the raw data.

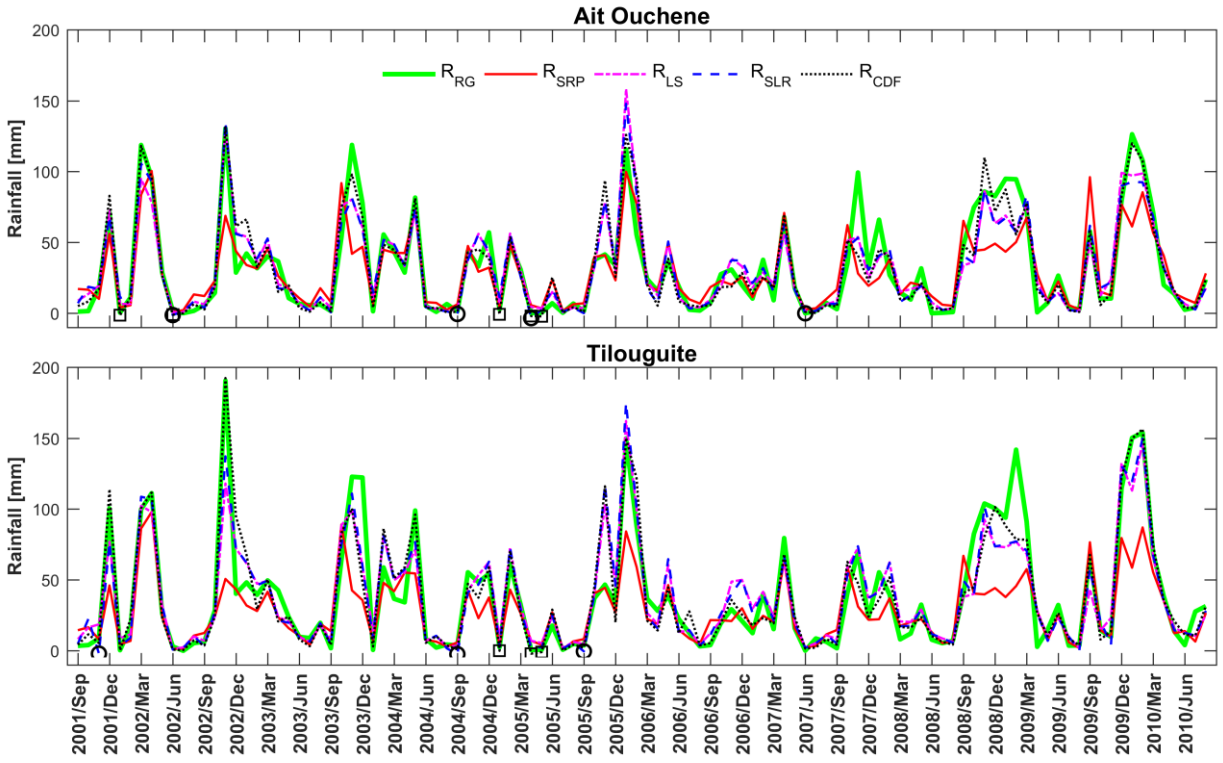

Figure 56. Monthly time series of RG, raw PERSIANN, and corrected PERSIANN using the SL, SLR and CDF techniques. The circle and square markers refer to the negative monthly values that occurred after the bias correction using SLR and CDF, respectively.

6.3.3.2. Spatial Validation and Transferability of the Bias Correction Techniques

In this section, the spatial validity of the three bias correction techniques (LS, SLR, and CDF) was tested. Our main aim here was to determine which of the techniques was able to maintain good performance when its estimation parameters (LS scaling factors, the parameters of the SLR, and the parameters of CDF models) were applied out of the reference sub-watersheds (Ait Ouchcene and Tilouguite). To this end, the estimation parameters built for IMERG and PERSIANN in Ait Ouchcene and Tilouguite were alternatively used to bias adjust the SRP raw datasets in three sub-watersheds among the four considered in this work (Upstream OER, Ait Ouchene, Tilouguite, and Tassaout-Lakhdar). The transferability of each of the techniques was evaluated based on the statistical metrics (PCC, RMSE, and R-BIAS) obtained for the validation sub-watersheds. The techniques that showed the best statistical metrics in the maximum number of sub-watersheds were considered as spatially transferable, and thus reliable for SRP bias correction in the OERB. The summary of the validation results is displayed in Figure 57, where the dot, circle, and pentagram markers represent the statistical metrics computed based on the raw SRP data, the SRP data corrected using the Tilouguite's estimation parameters, and the SRP data corrected using the Ait Ouchene's estimation parameters, respectively. The results suggest that the performance of the CDF correction technique was spatially inconsistent compared to that of LS and SLR. This was observed for PCC and RMSE evaluation metrics. As we can note from Figure 57, the correlation between the RGs and the corrected SRPs decreased by about 0.54 (0.74) points when the Tilouguite's (Ait Ouchene) parameters were applied to bias-adjust the IMERG estimates in the Upstream OER. Similar regression, yet of less magnitude, was observed for PERSIANN in addition to 0.13 and 0.36 points decrease that, respectively, concerned Ait Ouchene and Tassaout-Lakhdar when the Tilouguite's parameters were adopted as the reference. Moreover, the correlation deterioration was matched by an increase in the bias between the CDF-based corrected data and the RGs, which was manifested as remarkably large RMSE values (Greater than 50 $mm.m^{-1}$). On the other hand, the transferability of the LS and SLR was relatively better than that of the CDF. They showed no abrupt drop-offs in the overall performance for both IMERG and PERSIANN. In contrast, while no noticeable change in PCC was reported in Upstream OER and Tassaout-Lakhdar, the LS and SLR adjustments contributed to a non-negligible decrease in the RMSEs. This remark holds true in all cases, except when the Tilouguite's parameters were applied in Tassaout-Lakhdar,

as the RMSE slightly increased. In the same sub-watershed, the Ait Ouchene's parameters outperformed those of Tilouguite and yielded RMSE that was 2 $mm.m^{-1}$ smaller than that computed by the raw SRP data. A reverse situation was observed for the Upstream OER sub-watershed. In terms of RMSE, the Tilouguite's parameters were found to perform the best considering both IMERG and PERSIANN. For PERSIANN, using the Tilouguite's (Ait Ouchene) parameters, the LS technique allowed RMSE to decrease from 36 $mm.m^{-1}$ to around 20 $mm.m^{-1}$ (27 $mm.m^{-1}$), while the SLR-induced decrease was to around 22 $mm.m^{-1}$ (28 $mm.m^{-1}$). The gap in performance between the two reference parameters (Ait Ouchcene and Tilouguite) was of less importance for IMERG. Both of them yielded RMSE of less than 20 $mm.m^{-1}$, using LS, and nearly 21 $mm.m^{-1}$, using SLR.

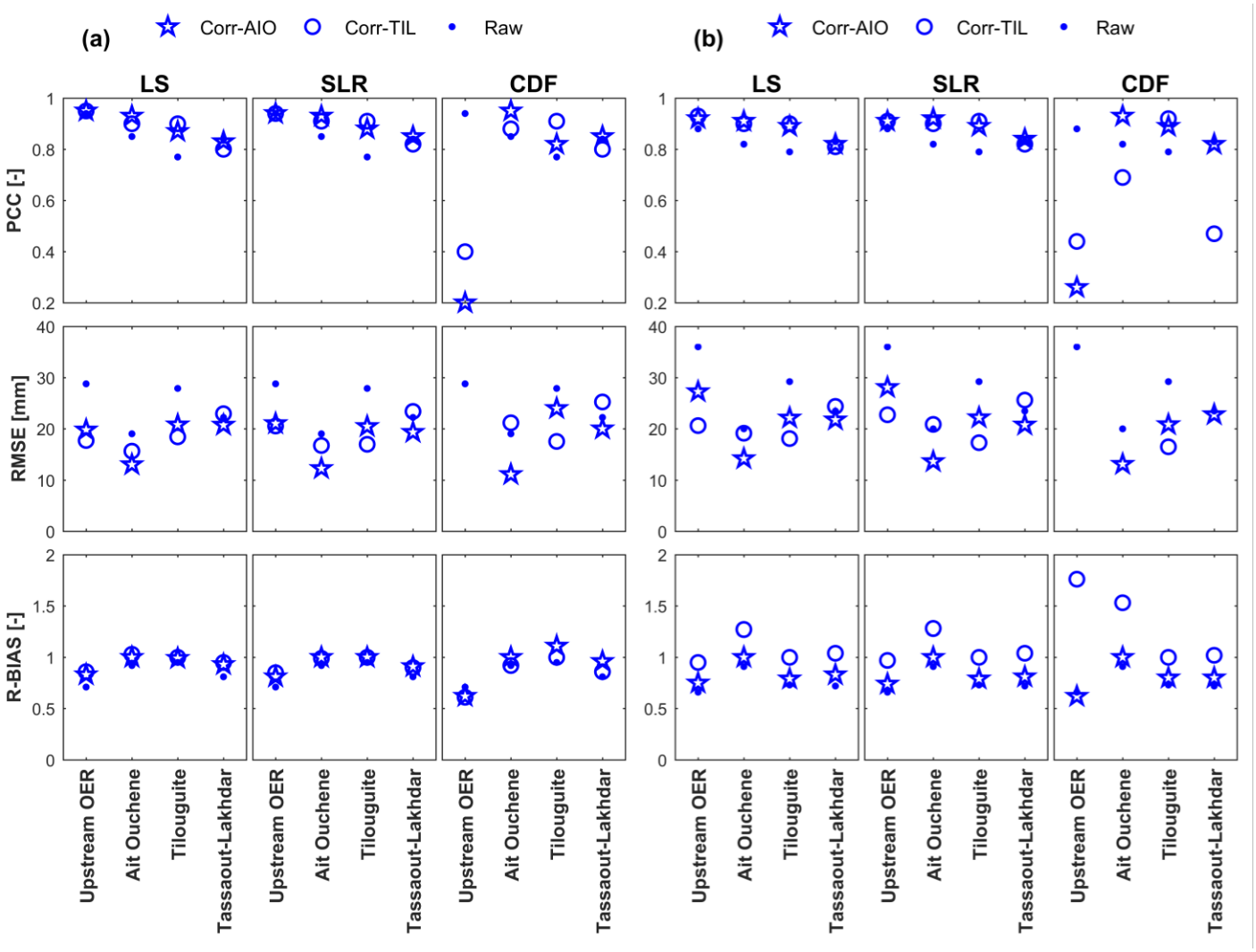

Figure 57. Monthly statistical metrics (PCC, RMSE, R-BIAS) computed for IMERG (a) and PERSIANN (b) to test the transferability of the bias correction techniques (LS, SLR, CDF) to other sub-watersheds. AIO and TIL refers to Ait Ouchene and Tilouguite sub-watersheds, respectively.

General Conclusions

Accurate rainfall measurements are crucial for spatiotemporal monitoring and quantifying water supplies for water management purposes. These measurements are mainly provided by in situ point scale RGs. The latter, which are generally representative of only small areas, are implemented in networks of more than one RG in order to allow larger scale coverage. Thus, gauging network density and distribution can play a limiting role in terms of reliability in water-related studies. However, topographic and financial factors often lead to sparse and unevenly distributed measurement networks, which is the case of many Moroccan watersheds. Freely available gridded datasets that provide rainfall estimates, at an interesting spatiotemporal resolution with global coverage, can be an alternative source of information to overcome the aforementioned limitations. In this context, the main aim of our thesis work was to evaluate the capability of eight SRP datasets in reproducing the daily and monthly gauged rainfall over the OERB in Morocco. In this work we have addressed the following points:

First, we have studied the variability of hydroclimatic variables to understand and characterize the hydroclimatic context of the OERB. Besides the classic statistical exploration of the observed variables, we have employed the SPI and the Mann-Kendall trend test. The first was used to analyze the drought and the second to assess the monotonic trends in time series, with an emphasis on precipitation (RG Rainfall and MODIS SCA) and terrestrial water storage (GRACE anomalies). The analysis results suggest that the OERB, mostly semi-arid, has known strong year-to-year rainfall variability during the period 1970 – 2010. Deficit years were prevalent since the early 1980s. This decade was distinguished with one of the most severe and long-lasting dry periods over the study area. It counts up to seven consecutive years of mildly to severe dryness. Since then, three dry periods took place with relatively short lengths. In addition, the wet spells were less frequent and mainly of small temporal extents, except for the 1970 decade that was characterized by abundant wet years but spatially incoherent wet periods. Furthermore, the annual rainfall

amounts demonstrated an overall decline since 1970/1971 year. However, only three stations, situated in the lowlands, experienced statistically significant decreasing trends. Seasonally, the rainfall totals exhibited a mixture of trend directions, even at the same site. While the summer and autumn showed a non-significant increasing trend, the winter and spring were dominated by strong decreasing tendencies. In particular, widespread significant decreases were observed for the spring months, mainly in April. Moreover, the strong temporal variability of rainfall and SCA were found to have an impact on terrestrial water availability. The latter exhibited a consistent decreasing tendency interspersed by potential storage recharge ensured by important water supplies from precipitation. The findings of this analysis, which fill an important gap of hydroclimatic studies in the OERB, emphasize that the region encounters a serious issue regarding water availability. The observed decrease in rainfall and terrestrial water storage should be considered as alarming signs for future difficulties that the area may face. The situation challenges the decision-makers and managers to take measures to guide alternative management practices to mitigate the decrease in water supplies.

Second, we have assessed the performance of the ARC, CHIRPSp25, CHIRPSp5, CMORPH-CRT v1, GPM IMERG v6, PERSIANN-CDR, RFE, and TRMM 3B42 v7 SRPs compared to the in situ measurements of twenty-six RGs at daily and monthly time scales over the OERB. The assessment was performed GC-wise through direct comparison against in situ data and watershed-wise through two approaches: a direct comparison between the WAvg datasets of four mountainous sub-watersheds (Upstream OER, Ait Ouchene, Tilouguite, and Tassaout-Lakhdar) and daily hydrologic modeling in two sub-watersheds (Ait Ouchene and Tilouguite). To hydrologically evaluate the daily SRP estimates the conceptual lumped version of the HBV hydrologic model was chosen. Therefore, the suitability of the model to simulate the daily streamflow was tested over Ait Ouchene. A set of nine years, from 2001 to 2009, of hydroclimatic measurements and remotely sensed SCA were used. The model performance was firstly tested through a cross-validation exercise. Then, the best performing combination of parameters was chosen to run sensitivity and interdependency analyses using the “ONE-AT-A-TIME” and “TWO-AT-A-TIME” approaches, respectively. The investigation of the HBV showed that the model can fairly reproduce the daily streamflow at the outlet of Ait Ouchene. The statistical metrics obtained during calibration exhibited a significant variability from one year to another. The worst model

performance was obtained in relatively dry years with unevenly distributed rainfall events. The performance was better in the remaining years with good agreements between simulated and observed streamflow. The results of the sensitivity analysis indicated that each of the model parameters can influence the simulated streamflow to a certain extent. However, the degree of influence varied depending on parameters and years. We found that the parameter ETF had no major influence on the model performance in most of the years. The model was found to be more sensitive to FC and Beta parameters. Furthermore, we noted that the optimal parameters present significant annual variability, which is mainly driven by the changes in hydroclimatic conditions. During years with extremely high peak flows, the soil routine parameters assumed values that lead to amplify the amount of water drained towards the upper reservoir. Meanwhile, the upper reservoir-related parameters (UZL and KPERC) were found to combine to reduce the storage capacity of the reservoir to ensure important excess water from smaller amounts of water supplies. The same parameters presented a reverse behavior in years with abundant snow cover. In particular, the FC showed higher sensitivity to the total water supply, mainly to the portion produced from the snowmelt. In summary, the results of our analyses highlight the main challenges associated with hydrological modeling studies in our context, especially the high interdependency between model parameters and the strong impact of changes in hydroclimatic conditions. However, despite the lack of efficient ground datasets, the relatively good streamflow simulations obtained using the HBV model at the daily time scale are very promising.

The SRPs evaluation results indicated that at the daily time scale, the estimated and gauged data showed poor agreement, with PCCs often less than 0.5. The poor performance was also observed for daily streamflow simulation. The SRPs' performance, during calibration of the HBV model, seemed unsteady and varied depending on years and products. Particularly, CMORPH consistently showed the lowest results in both temporal and spatial dimensions. Although their overall low capability of streamflow simulation, the SRPs appeared to yield better streamflow estimates than the RG data over the Tilouguite sub-watershed. The latter is characterized by a low gauging network density with poor distribution. For the aggregated time scale (monthly), the products' estimates and RG data showed a stronger agreement compared to the daily time scale. The two data sources were generally well correlated for most of the study area, except for some sites located in the mountainous region of the OERB. Overall, at the monthly time scale, IMERG

and PERSIANN outperformed all the studied rainfall products. Although IMERG showed a certain precedence over PERSIANN, at this stage it remained difficult to choose out of the two products considering their spatial and temporal characteristics. while IMERG provides rainfall estimates at a spatial resolution of 10 km with short time records, PERSIANN estimates are available at a bit coarser spatial resolution (25 km) but in longer data records (the feature that is required in several hydroclimatic studies). Additionally, if we consider grouping the SRPs into short-term (products with short data record: CMORPH, IMERG, RFE, and TRMM) and long-term (products with long data record: ARC, CHIRPSp5, CHIRPSp25, and PERSIANN) products, in terms of PCCs, IMERG and PERSIANN would top the ranking of their respective groups. Nevertheless, the monthly rainfall estimates exhibited a non-negligible bias relative to the RGs. The important rainfall amounts were predominantly underestimated for all SRPs, except CHIRPS. Also, we noticed that most SRPs tended to overestimate rainfall in dry conditions (mostly over the lowlands) and underestimate it as the conditions became wetter (mostly at height elevations). Although the obtained correlations were high, the bias results suggested that the SRPs were unable to accurately estimate the monthly gauged rainfall, particularly in the mountainous region of the OERB.

To remove or reduce the bias in the monthly SRP estimates, multiple bias correction techniques were applied and tested over the four mountainous sub-watersheds of the OERB. The estimation parameters of each of the correction techniques were built using the WAvg time series of Ait Ouchene and Tilouguite sub-watersheds. To account for the seasonality in the rainfall data, for each technique, the full time series were decomposed, and thus the bias adjustment was applied to each month's (twelve) time series. After that, the estimation parameters were validated on all sub-watersheds, except on the one used in the building process. In other words, the parameters of Ait Ouchene were validated on the Upstream OER, Tilouguite, and Tassaout-Lakhdar, vice versa. All the considered techniques allowed a remarkable improvement in the SRPs performance. The bias was significantly reduced, particularly for the large totals of rainfall. After the bias was corrected, an enhancement in the agreement between the SRPs and RG was observed as the PCCs significantly increased. It should be noted that the ranking of the SRPs remained the same with PERSIANN and IMERG performing the best. Besides, the results of the considered correction techniques were relatively close. The CDF seemed to relatively surpass the LS and SLR techniques, yielding better PCCs and RMSEs. However, the superiority of CDF was only limited to the case

where the technique was applied to the same sub-watershed it was tested for (Ait Ouchcene and Tilouguite). The LS and SLR techniques, on the other hand, were spatially more consistent than the CDF, when validated on the other sub-watersheds. These findings lead to the conclusion that, in the OERB, either LS or SLR can be used to reduce the bias contained in the SRP estimates.

In perspective, some research subjects remained open and can be dealt with in future works. They can be generally summarized as follows:

- The daily evaluation revealed that the poor performance of the SRPs can be the result of multiple factors related to both the data sources and algorithms. These factors led the products to miss rainfall events, misestimate (overestimate or overestimate) rainfall totals, and detect events as false alarms. Further investigations will be taken into consideration to improve the reliability of the SRPs' daily estimates. For instance, in addition to the SFA, the SRP time series were found to include many IFA, which negatively impact the overall performance of the products. Hence, any future works should focus more on building a classification scheme that allows distinguishing the SFAs from the total false alarms. This will help remove or reduce the uncertainty provoked by the IFAs and facilitate the implementation of other enhancements.
- The monthly evaluation results suggest that IMERG and PERSIANN datasets, after being corrected for bias, can provide reliable rainfall estimates at the monthly time scale. These estimates can satisfy the need for spatiotemporally consistent data in many water-related applications. They would be of significant usefulness in overcoming the data shortage in poorly gauged regions, which is the case of several Moroccan river basins. Therefore, a wider spatial validation would be required to test the stability of the bias-corrected SRPs (IMERG and PERSIANN) performance and, thus, the consistency of the bias correction techniques in other regions, particularly within the Moroccan territory. In addition to the direct comparison against the RG observations, the validation exercises would include the incorporation of the bias-corrected estimates in monthly-based hydrologic models.

References

Abahous, H., Ronchail, J., Sifeddine, A., Kenny, L., Bouchaou, L., 2017. Trend and change point analyses of annual precipitation in the Souss-Massa Region in Morocco during 1932 – 2010.

Abdulla, F., Al-Badranih, L., 2010. Application of a rainfall-runoff model to three catchments in Iraq. Hydrol. Sci. J. 45, 13–25. https://doi.org/10.1080/02626660009492303

Abebe, N.A., Ogden, F.L., Pradhan, N.R., 2010. Sensitivity and uncertainty analysis of the conceptual HBV rainfall-runoff model: Implications for parameter estimation. J. Hydrol. 389, 301–310. https://doi.org/10.1016/j.jhydrol.2010.06.007

ABHOER, 2012. Etude du plan directeur d'aménagement intégré des ressources en eau du bassin de l'Oum-Rr-Rbia et des bassins côtiers atlantiques. Rabat, Maroc.

Adler, R.F., Huffman, G.J., Chang, A., Ferraro, R., Xie, P.P., Janowiak, J., Rudolf, B., Schneider, U., Curtis, S., Bolvin, D., Gruber, A., Susskind, J., Arkin, P., Nelkin, E., 2003. The version-2 global precipitation climatology project (GPCP) monthly precipitation analysis (1979-present). J. Hydrometeorol. 4, 1147–1167. https://doi.org/10.1175/1525-7541(2003)004<1147:TVGPCP>2.0.CO;2

Adler, R.F., Huffman, G.J., Keehn, P.R., 1994. Global tropical rain estimates from microwave-adjusted geosynchronous IR data. Remote Sens. Rev. 11, 125–152. https://doi.org/10.1080/02757259409532262

Adler, R.F., Negri, A.J., Keehn, P.R., Hakkarinen, I.M., 1993. Estimation of monthly rainfall over Japan and surrounding waters from a combination of low-orbit microwave and geosynchronous IR data. J. Appl. Meteorol. https://doi.org/10.1175/1520-0450(1993)032<0335:EOMROJ>2.0.CO;2

Adler, R.F., Sapiano, M.R.P., Huffman, G.J., Wang, J.J., Gu, G., Bolvin, D., Chiu, L., Schneider, U., Becker, A., Nelkin, E., Xie, P., Ferraro, R., Shin, D. Bin, 2018. The Global Precipitation Climatology Project (GPCP) monthly analysis (New Version 2.3) and a review of 2017 global precipitation. Atmosphere (Basel). 9, 1–14. https://doi.org/10.3390/atmos9040138

Ahmad, I., Tang, D., Wang, T., Wang, M., Wagan, B., 2015. Precipitation trends over time using Mann-Kendall and Spearman's rho tests in Swat river basin, Pakistan. Adv. Meteorol. 2015, 15. https://doi.org/http://dx.doi.org/10.1155/2015/431860

Albergel, C., Boone, A., Belamari, S., Decharme, B., Dumont, M., Le Moigne, P., Masson, V., 2018a. SURFEX Scientific Documentation (No. 3). Toulouse, France.

Albergel, C., Dutra, E., Bonan, B., Zheng, Y., Munier, S., Balsamo, G., de Rosnay, P., Muñoz-Sabater, J., Calvet, J.C., 2019. Monitoring and forecasting the impact of the 2018 summer heatwave on vegetation. Remote Sens. 11, 1–22. https://doi.org/10.3390/rs11050520

Albergel, C., Dutra, E., Munier, S., Calvet, J.C., Munoz-Sabater, J., De Rosnay, P., Balsamo, G., 2018b. ERA-5 and ERA-Interim driven ISBA land surface model simulations: Which one performs better? Hydrol. Earth Syst. Sci. 22, 3515–3532. https://doi.org/10.5194/hess-22-3515-2018

Albergel, C., Munier, S., Jennifer Leroux, D., Dewaele, H., Fairbairn, D., Lavinia Barbu, A., Gelati, E., Dorigo, W., Faroux, S., Meurey, C., Le Moigne, P., Decharme, B., Mahfouf, J.F., Calvet, J.C., 2017. Sequential assimilation of satellite-derived vegetation and soil moisture products using SURFEX-v8.0: LDAS-Monde assessment over the Euro-Mediterranean area. Geosci. Model Dev. 10, 3889–3912. https://doi.org/10.5194/gmd-10-3889-2017

Almazroui, M., 2011. Calibration of TRMM rainfall climatology over Saudi Arabia during 1998–2009. Atmos. Res. 99, 400–414. https://doi.org/10.1016/j.atmosres.2010.11.006

References

Anctil, F., Perrin, C., Andréassian, V., 2004. Impact of the length of observed records on the performance of ANN and of conceptual parsimonious rainfall-runoff forecasting models. Environ. Model. Softw. 19, 357–368. https://doi.org/10.1016/S1364-8152(03)00135-X

Andréasson, J., Bergström, S., Carlsson, B., Graham, L.P., Lindström, G., 2004. Hydrological Change – Climate Change Impact Simulations for Sweden. Ambio 33, 228–234. https://doi.org/10.1579/0044-7447-33.4.228

Anjum, M.N., Ahmad, I., Ding, Y., Shangguan, D., Zaman, M., Ijaz, M.W., Sarwar, K., Han, H., Yang, M., 2019. Assessment of IMERG-V06 Precipitation Product over Different Hydro-Climatic Regimes in the Tianshan Mountains, North-Western China. Remote Sens. 11, 2314. https://doi.org/10.3390/rs11192314

Arheimer, B., 2006. Evaluation of water quantity and quality modelling in ungauged European basins, in: Predictions in Ungauged Basins: Promise and Progress. IAHS Publ. 303, Foz do Iguaçu, Brazil, pp. 99–107.

Arkin, P.A., 1979. The relationship between fractional coverage of high cloud and rainfall accumulations during GATE over the B-scale array. Mon. Weather Rev. https://doi.org/10.1175/1520-0493(1979)107<1382:TRBFCO>2.0.CO;2

Arkin, P.A., Meisner, B.N., 1987. The Relationship between Large-Scale Convective Rainfall and Cold Cloud over the Western Hemisphere during 1982- 84. Mon. Weather Rev. 115, 51–74. https://doi.org/10.1017/CBO9781107415324.004

Arnold, J.G., Fohrer, N., 2005. SWAT2000: Current capabilities and research opportunities in applied watershed modelling. Hydrol. Process. 19, 563–572. https://doi.org/10.1002/hyp.5611

Arsenault, R., Brissette, F., 2014. Determining the Optimal Spatial Distribution of Weather Station Networks for Hydrological Modeling Purposes Using RCM Datasets : An Experimental Approach. J. Hydrometeorol. 15, 517–526. https://doi.org/10.1175/JHM-D-13-088.1

Ashouri, H., Hsu, K.L., Sorooshian, S., Braithwaite, D.K., Knapp, K.R., Cecil, L.D., Nelson, B.R., Prat, O.P., 2015. PERSIANN-CDR: Daily precipitation climate data record from multisatellite observations for hydrological and climate studies. Bull. Am. Meteorol. Soc. 96, 69–83. https://doi.org/10.1175/BAMS-D-13-00068.1

Baba, M.W., Gascoin, S., Jarlan, L., Simonneaux, V., Hanich, L., 2018. Variations of the snow water equivalent in the ourika catchment (Morocco) over 2000-2018 using downscaled MERRA-2 data. Water 10, 1–18. https://doi.org/10.3390/w10091120

Babaousmail, H., Hou, R., Ayugi, B., Tchalim Gnitou, G., 2019. Evaluation of Satellite-Based Precipitation Estimation over Algeria During Journal of Atmospheric and Solar-Terrestrial Physics Evaluation of satellite-based precipitation estimates over Algeria during 1998 – 2016. J. Atmos. Solar-Terrestrial Phys. 195, 105139. https://doi.org/10.1016/j.jastp.2019.105139

Baik, J., Choi, M., 2015. Spatio-temporal variability of remotely sensed precipitation data from COMS and TRMM: Case study of Korean peninsula in East Asia. Adv. Sp. Res. 56, 1125–1138. https://doi.org/10.1016/j.asr.2015.06.015

Bates, B., Kundzewicz, Z.W., Wu, S., Palutikof, J., 2008. Climate change and water, Technical Paper of the Intergovernmental Panel on Climate Change. Geneva, Switzerland.

Beck, H.E., Pan, M., Roy, T., Weedon, G.P., Pappenberger, F., van Dijk, A.I.J.M., Huffman, G.J., Adler, R.F., Wood, E.F., 2019. Daily evaluation of 26 precipitation datasets using Stage-IV gauge-radar data for the CONUS. Hydrol. Earth Syst. Sci. 23, 207–224.

Benabdelouahab, T., Balaghi, R., Hadria, R., Lionboui, H., Minet, J., Tychon, B., 2015. Monitoring surface water content using visible and short-wave infrared SPOT-5 data of wheat plots in irrigated semi-arid regions. Int. J. Remote Sens. 36, 4018–4036. https://doi.org/10.1080/01431161.2015.1072650

Bennartz, R., Thoss, A., Dybbroe, A., Michelson, D.B., 2002. Precipitation analysis using the Advanced Microwave Sounding Unit in support of nowcasting applications. Meteorol. Appl. 9, 177–189. https://doi.org/10.1017/S1350482702002037

Bergström, s., Carlsson, B., Gardelin, M., Lindström, G., Petterson, A., Rummukainen, M., 2001. Climate change impacts on runoff in Sweden - Assessments by global climate models, dynamical downscalling and hydrological modelling. Clim. Res. 16, 101–112. https://doi.org/10.3354/cr016101

Bergström, S., 2006. Experience from applications of the HBV hydrological model from the perspective of prediction in ungauged basins, MOPEX Experiments. IAHS Publ. 307.

References

Bergström, S., 1992. The HBV Model - its structure and applications (No. RH No.4). Norrköping, Sweden.

Bergström, S., Forsman, A., 1973. Development of a Conceptual Deterministic Rainfall-Runoff Model. Nord. Hydrol. 4, 147–170.

Bergström, S., Lindström, G., 2015. Interpretation of runoff processes in hydrological modelling-experience from the HBV approach. Hydrol. Process. 29, 3535–3545. https://doi.org/10.1002/hyp.10510

Beven, K., 2006. A manifesto for the equifinality thesis. J. Hydrol. 320, 18–36. https://doi.org/10.1016/j.jhydrol.2005.07.007

Beven, K., 1989. Changing ideas in hydrology - The case of physically based models. J. Hydrol. 105, 157–172. https://doi.org/10.1016/0022-1694(90)90161-P

Beven, K., Freer, J., 2001. Equifinality, data assimilation, and uncertainty estimation in mechanistic modelling of complex environmental systems using the GLUE methodology. J. Hydrol. 249, 11–29. https://doi.org/10.1016/S0022-1694(01)00421-8

Beven, K.J., Wood, E.F., Sivapalan, M., 1988. On hydrological heterogeneity - catchment morphology and catchment response. J. Hydrol. 100, 353–375.

Biondi, D., Freni, G., Iacobellis, V., Mascaro, G., Montanari, A., 2012. Validation of hydrological models : Conceptual basis, methodological approaches and a proposal for a code of practice. Phys. Chem. Earth 42–44, 70–76. https://doi.org/10.1016/j.pce.2011.07.037

Bolvin, D.T., Huffman, G.J., 2015. Transition of 3B42 / 3B43 Research Product from Monthly to Climatological Calibration / Adjustment 2015.

Bonell, M., 1993. Progress in the understanding of runoff generation dynamics in forests. J. Hydrol. 150, 217–275. https://doi.org/10.1016/0022-1694(93)90112-M

Bouchaou, L., Tagma, T., Boutaleb, S., Hssaisoune, M., El Morjani, Z.E.A., 2011. Climate change and its impacts on groundwater resources in Morocco: the case of the Souss-Massa basin, in: Treidel, H., Martin-Bordes, J.L., Gurdak, J.J. (Eds.), Climate Change Effects on Groundwater Resources: A Global Synthesis of Findings and Recommendations. Taylor & Francis, London, England, pp. 129–144.

Boudhar, A., 2009. Télédétection du manteau neigeux et modélisation de la contribution des eaux de fonte des neiges aux débits des Oueds du Haut Atlas de Marrakech (Ph.D). Marrakech, Morocco. https://doi.org/10.1016/j.jag.2009.09.008

Boudhar, A., Boulet, G., Hanich, L., Sicart, J.E., Chehbouni, A., 2016. Energy fluxes and melt rate of a seasonal snow cover in the Moroccan High Atlas. Hydrol. Sci. J. 61, 931–943. https://doi.org/10.1080/02626667.2014.965173

Boudhar, A., Hanich, L., Boulet, G., Duchemin, B., Berjamy, B., Chehbouni, A., 2009. Evaluation of the Snowmelt Runoff model in the Moroccan High Atlas Mountains using two snow-cover estimates. Hydrol. Sci. J. 54, 1094–1113. https://doi.org/10.1623/hysj.54.6.1094

Boudhar, A., Ouatiki, H., Bouamri, H., Lebrini, Y., Karaoui, I., Hssaisoune, M., Arioua, A., Benabdelouahab, T., 2020. Hydrological Response to Snow Cover Changes Using Remote Sensing over the Oum Er Rbia Upstream Basin, Morocco, in: Rebai, N., Mastere, M. (Eds.), Mapping and Spatial Analysis of Socio-Economic and Environmental Indicators for Sustainable Development. Springer, Cham, Cham, Switzerland, pp. 95–102. https://doi.org/10.1007/978-3-030-21166-0_9

Boyles, R.P., Raman, S., 2003. Analysis of climate trends in North Carolina (1949-1998). Environ. Int. 29, 263–275. https://doi.org/10.1016/S0160-4120(02)00185-X

Brandt, M., Bergström, S., Gardelin, M., 1988. Modelling the effects of clearcutting on runoff - Examples from central Sweden. Ambio 17, 307–313.

Braun, J.N., Renner, C.B., 1992. Application of a conceptual runoff model in different physiographic regions of Switzerland. Hydrol. Sci. J. 37, 217–231. https://doi.org/10.1080/02626669209492583

Brocca, L., Hasenauer, S., Lacava, T., Melone, F., Moramarco, T., Wagner, W., Dorigo, W., Matgen, P., Martínez-Fernández, J., Llorens, P., Latron, J., Martin, C., Bittelli, M., 2011. Soil moisture estimation through ASCAT and AMSR-E sensors: An intercomparison and validation study across Europe. Remote Sens. Environ. 115, 3390–3408. https://doi.org/10.1016/j.rse.2011.08.003

References

Brooks, K.N., Ffolliott, P.F., Magner, J.A., 2013. Hydrology and the Management of Watersheds, 4th ed, Hydrology and the Management of Watersheds: Fourth Edition. John Wiley & Sons, Inc, Iowa, USA. https://doi.org/10.1002/9781118459751

Burns, D.A., Klaus, J., McHale, M.R., 2007. Recent climate trends and implications for water resources in the Catskill Mountain region, New York, USA. J. Hydrol. 336, 155–170. https://doi.org/10.1016/j.jhydrol.2006.12.019

Campbell, J.B., Wynne, R.H., 2011. Introduction to Remote Sensing, 5th ed. Guilford Publications, Inc., New York, USA.

CESE, 2014. La gouvernance par la gestion intégrée des ressources en eau au Maroc : Levier fondamental de développement durable. Rabat, Maroc.

Chaponnière, A., 2005. Fonctionnement hydrologique d'un bassin versant montagneux semi-aride Cas du bassin versant du Rehraya (Haut Atlas marocain).

Chen, H., Xiang, T., Zhou, X., 2012. Impacts of climate change on the Qingjiang Watershed ' s runoff change trend in China. Stoch. Environ. Res. Risk Assess. 26, 847–858. https://doi.org/10.1007/s00477-011-0524-2

Coron, L., Andréassian, V., Perrin, C., Lerat, J., Vaze, J., Bourqui, M., Hendrickx, F., 2012. Crash testing hydrological models in contrasted climate conditions: An experiment on 216 Australian catchments. Water Resour. Res. 48, 1–17. https://doi.org/10.1029/2011WR011721

Crane R. G., Anderson M. R., 1984. Satellite discrimination of snow/cloud surfaces. Int. J. Remote Sens. 5, 213–223.

Dakhlaoui, H., Ruelland, D., Tramblay, Y., Bargaoui, Z., 2017. Evaluating the robustness of conceptual rainfall-runoff models under climate variability in northern Tunisia. J. Hydrol. 550, 201–217. https://doi.org/10.1016/j.jhydrol.2017.04.032

Daoudi, L., Saidi, M., 2008. Floods in semi-arid zone: example of the Ourika (High Atlas of Marrakech, Morocco). Int. Sci. J. Altern. Energy Ecol. 5, 117–123.

Davie, T., 2008. Fundamentals of Hydrology, 2nd ed, Routledge Fundamentals of Physical Geography Series. Routledge, New York, USA. https://doi.org/10.1353/sgo.2004.0016

Dinku, T., Chidzambwa, S., Ceccato, P., Connor, S.J., Ropelewski, C.F., 2008. Validation of high-resolution satellite rainfall products over complex terrain. Int. J. Remote Sens. 29, 4097–4110. https://doi.org/10.1080/01431160701772526

Donat, M.G., Peterson, T.C., Brunet, M., King, A.D., Almazroui, M., Kolli, R.K., Boucherf, D., Al-Mulla, A.Y., Nour, A.Y., Aly, A.A., Nada, T.A.A., Semawi, M.M., Al Dashti, H.A., Salhab, T.G., El Fadli, K.I., Muftah, M.K., Dah Eida, S., Badi, W., Driouech, F., El Rhaz, K., Abubaker, M.J.Y., Ghulam, A.S., Erayah, A.S., Mansour, M. Ben, Alabdouli, W.O., Al Dhanhani, J.S., Al Shekaili, M.N., 2014. Changes in extreme temperature and precipitation in the Arab region: Long-term trends and variability related to ENSO and NAO. Int. J. Climatol. 34, 581–592. https://doi.org/10.1002/joc.3707

Dong, X., Dohmen-Janssen, C.M., Booij, M.J., 2005. Appropriate spatial sampling of rainfall for flow simulation. Hydrol. Sci. J. 50, 279–297. https://doi.org/10.1623/hysj.50.2.279.60656

Dooge, J.C.I., 1988. Hydrology past and present. J. Hydraul. Res. 26, 5–26. https://doi.org/10.1080/00221688809499231

Dozier, J., 1989. Spectral signature of alpine snow cover from the landsat thematic mapper. Remote Sens. Environ. 28, 9–22. https://doi.org/10.1016/0034-4257(89)90101-6

Driouech, F., 2010. Distribution des précipitations hivernales sur le Maroc dans le cadre d'un changement climatique: descente d'échelle et incertitudes (PhD). Institut National Polytechnique de Toulouse, Toulouse, France.

Dunnen, T., Black, R.D., 1970. Partial area contributions to storm runoff in a small New England watershed. Water Resour. Res. 6, 1296–1311.

Egan, W.G., 2003. Optical remote sensing: Science and technology. Marcel Dekker, Inc., New York, USA.

El Azhari, M., Loudyi, D., 2019. Analysis of the Water-Energy nexus in central Oum Er-Rbia sub-basin - Morocco. Int. J. River Basin Manag. 17, 13–24. https://doi.org/10.1080/15715124.2018.1446966

Esper, J., Frank, D., Bu, U., Verstege, A., Xoplaki, E., 2007. Long-term drought severity variations in Morocco 34, 1–5. https://doi.org/10.1029/2007GL030844

Fatna, B., Handoufe, A., 1997. La sécheresse agricole au Maroc, in: Sustainability of Water Resources under Increasing Uncertainty. Rabat, Maroc, pp. 31–41.

Ferket, B.V.A., Samain, B., Pauwels, V.R.N., 2010. Internal validation of conceptual rainfall-runoff models using baseflow separation. J. Hydrol. 381, 158–173. https://doi.org/10.1016/j.jhydrol.2009.11.038

Ferraro, R.R., Weng, F., Grody, N.C., Zhao, L., Meng, H., Kongoli, C., Pellegrino, P., Qiu, S., Dean, C., 2005. NOAA operational hydrological products derived from the advanced microwave sounding unit. IEEE Trans. Geosci. Remote Sens. 43, 1036–1048. https://doi.org/10.1109/TGRS.2004.843249

Filahi, S., Tanarhte, M., Mouhir, L., Morhit, M. El, Tramblay, Y., 2015. Trends in indices of daily temperature and precipitations extremes in Morocco. Theor. Appl. Climatol. 124, 959–972. https://doi.org/10.1007/s00704-015-1472-4

Frédéric FRAPPART, 2006. Développement d' applications pour l' utilisation de la télédétection sur les grands bassins fluviaux.

Funk, C., Peterson, P., Landsfeld, M., Pedreros, D., Verdin, J., Shukla, S., Husak, G., Rowland, J., Harrison, L., Hoell, A., Michaelsen, J., 2015a. The climate hazards infrared precipitation with stations - A new environmental record for monitoring extremes. Sci. Data 2, 1–21. https://doi.org/10.1038/sdata.2015.66

Funk, C., Verdin, A., Michaelsen, J., Peterson, P., Pedreros, D., Husak, G., 2015b. A global satellite assisted precipitation climatology. Earth Syst. Sci. Data Discuss. 8, 401–425. https://doi.org/10.5194/essdd-8-401-2015

Gan, T.Y., Dlamini, E.M., Biftu, G.F., 1997. Effects of model complexity and structure, data quality, and objective functions on hydrologic modeling. J. Hydrol. 192, 81–103. https://doi.org/10.1016/S0022-1694(96)03114-9

Gao, Y.C., Liu, M.F., 2013. Evaluation of high-resolution satellite precipitation products using rain gauge observations over the Tibetan Plateau. Hydrol. Earth Syst. Sci. 17, 837–849. https://doi.org/10.5194/hess-17-837-2013

Garrick, M., Cunnane, C., Nash, J.E., 1978. A criterion of efficiency for rainfall-runoff models. J. Hydrol. 36, 375–381.

Gelaro, R., McCarty, W., Suárez, M.J., Todling, R., Molod, A., Takacs, L., Randles, C.A., Darmenov, A., Bosilovich, M.G., Reichle, R., Wargan, K., Coy, L., Cullather, R., Draper, C., Akella, S., Buchard, V., Conaty, A., da Silva, A.M., Gu, W., Kim, G.K., Koster, R., Lucchesi, R., Merkova, D., Nielsen, J.E., Partyka, G., Pawson, S., Putman, W., Rienecker, M., Schubert, S.D., Sienkiewicz, M., Zhao, B., 2017. The modern-era retrospective analysis for research and applications, version 2 (MERRA-2). J. Clim. 30, 5419–5454. https://doi.org/10.1175/JCLI-D-16-0758.1

Gnouma, R., 2006. Aide à la calibration d'un modèle hydrologique distribué au moyen d'une analyses des processus hydrologiques: appliquation au bassin cersant de l'Yzeron.

Gosain, A.K., Rao, S., Basuray, D., 2006. Climate change impact assessment on hydrology of Indian river basins. Curr. Sci. 90, 346–353.

Graham, S., 1999. Remote Sensing [WWW Document]. URL https://earthobservatory.nasa.gov/features/RemoteSensing (accessed 8.1.20).

Gumindoga, W., Rientjes, T.H.M., Tamiru Haile, A., Makurira, H., Reggiani, P., 2019. Performance of bias-correction schemes for CMORPH rainfall estimates in the Zambezi River basin. Hydrol. Earth Syst. Sci. 23, 2915–2938. https://doi.org/10.5194/hess-23-2915-2019

Hall, D.K., Riggs, G.A., 2016. MODIS/Terra Snow Cover Daily L3 Global 500m SIN Grid, Version 6. [h17v5]. Boulder, Colorado USA. NASA National Snow and Ice Data Center Distributed Active Archive Center. https://doi.org/https://doi.org/10.5067/MODIS/MOD10A1.006. [2018-02-04]

Hall, D.K., Riggs, G.A., Salomonson, V. V., 1995. Development of Methods for Mapping Global Snow Cover Using Moderate Resolution Imaging Spectroradiometer Data. Remote Sens. Environ. 54, 127–140.

Hamby, D.M., 1994. A review of techniques for parameter sensitivity analysis of environmental models. Environ. Monit. Assess. 32, 135–154.

Hayes, M., Svoboda, M., Wall, N., Widhalm, M., 2011. The lincoln declaration on drought indices: Universal meteorological drought index recommended. Bull. Am. Meteorol. Soc. 92, 485–488. https://doi.org/10.1175/2010BAMS3103.1

Helsel, D.R., Hirsch, R.M., 1992. Statistical methods in water resources, 1st ed. Elsevier, New York, United States.

Hernandez, M., Miller, S.N., Goodrich, D.C., Goff, B.F., Kepner, W.G., Edmonds, C.M., Jones, K.B., 2000. Modeling runoff response to land cover and rainfall spatial variability in semi-arid watersheds. Environ. Monit. Assess. 64, 285–298. https://doi.org/10.1023/A:1006445811859

Hewlett, J.D., Hibbert, A.R., 1965. Factors affecting the reponse of small watersheds to precipitation in humid areas, in: Sopper, W.E., Lull, H.W. (Eds.), International Symposium on Forest Hydrology. Pergamon, Pennsylvania, USA, pp. 275–290. https://doi.org/10.1016/S0040-4039(00)86233-4

Hipel, keith W., Mcleod, A.I., 1994. Time series modelling of water resources and environmental systems, 1st ed. Elsevier, Amsterdam, Netherlands.

Hirsch, R.M., Slack, J.R., Smith, R.A., 1982. Techniques of trend analysis for monthly water-quality data. Water Resour. Res. 18, 107–121. https://doi.org/10.1029/WR018i001p00107

Hong, Y., Hsu, K.L., Sorooshian, S., Gao, X., 2004. Precipitation estimation from remotely sensed imagery using an artificial neural network cloud classification system. J. Appl. Meteorol. 43, 1834–1852. https://doi.org/10.1175/jam2173.1

Horton, R.E., 1933. The Role of Infiltration in the Hydrologic cycle. Trans. Am. Geophys. Union 446–460.

Htitiou, A., Boudhar, A., Lebrini, Y., Hadria, R., Lionboui, H., Elmansouri, L., Tychon, B., Benabdelouahab, T., 2019. The Performance of Random Forest Classification Based on Phenological Metrics Derived from Sentinel-2 and Landsat 8 to Map Crop Cover in an Irrigated Semi-arid Region. Remote Sens. Earth Syst. Sci. 2, 208–224. https://doi.org/10.1007/s41976-019-00023-9

Huffman, G.J., Adler, R.F., Bolvin, D.T., Nelkin, E.J., 2010a. The TRMMMulti-Satellite Precipitation Analysis (TMPA), in: Gebremichael, M., Hossain, F. (Eds.), Satellite Rainfall Applications for Surface Hydrology. Springer, Netherlands, pp. 3–22. https://doi.org/10.1007/978-90-481-2915-7

Huffman, G.J., Adler, R.F., Bolvin, D.T., Nelkin, E.J., 2010b. The TRMM Multi-satellite Precipitation Analysis (TMPA). Satell. Rainfall Appl. Surf. Hydrol. 3–22. https://doi.org/10.1007/978-90-481-2915-7_1

Huffman, G.J., Adler, R.F., Morrissey, M.M., Bolvin, D.T., Curtis, S., Joyce, R., McGavock, B., Susskind, J., 2001. Global Precipitation at One-Degree Daily Resolution from Multisatellite Observations. J. Hydrometeorol. 2, 36–50. https://doi.org/10.1175/1525-7541(2001)002<0036:GPAODD>2.0.CO;2

Huffman, G.J., Bolvin, D.T., 2015. TRMM and Other Data Precipitation Data Set Documentation [WWW Document]. TRMM 3B42_3B43 Doc. https://doi.org/10.1111/fcre.12141

Huffman, George J., Bolvin, D.T., Braithwaite, D., Hsu, K.-L., Joyce, R.J., Kidd, C., Nelkin, E.J., Sorooshian, S., Stocker, E.F., Tan, J., Wolff, D.B., Xie, P., 2019. NASA Global Precipitation Measurement (GPM) Integrated Multi-satellitE Retrievals for GPM (IMERG) (No. 06). Greenbelt, USA. https://doi.org/10.1007/978-3-030-24568-9_19

Huffman, George J, Bolvin, D.T., Nelkin, E.J., Tan, J., 2019. Integrated Multi-satellitE Retrievals for GPM (IMERG) Technical Documentation. Greenbelt, USA. https://doi.org/10.36548/jucct.2019.1

Hurrell, J.W., Van Loon, H., 1997. Decadal variations in climate associated with the North Atlantic Oscillation. Clim. Change 36, 301–326. https://doi.org/10.1023/a:1005314315270

IPCC, 2014. Climate change 2014 synthesis report. Geneva, Switzerland.

IPCC, 2012. Managing the Risks of Extreme Events and Disasters to Advance Climate Change Adaptation. Cambridge, New York, United Kingdom, United States. https://doi.org/10.1017/CBO9781139177245

Jain, S.K., 1993. Calibration of conceptual models for rainfall-runoff simulation. Hydrol. Sci. J. 38, 431–441. https://doi.org/10.1080/026266693099492692

Ji, X., Li, Y., Luo, X., He, D., Guo, R., Wang, J., Bai, Y., Yue, C., Liu, C., 2020. Evaluation of bias correction methods for APHRODITE data to improve hydrologic simulation in a large Himalayan basin. Atmos. Res. 242, 104964. https://doi.org/10.1016/j.atmosres.2020.104964

JICA, 2007. Etude du plan de gestion intégrée des ressources en eau dans la plaine du Haouz royaume du Maroc. Rabat, Maroc.

Jlibene, M., Tychon, B., 2007. Gestion du risque de sécheresse agricole au Maroc 1 18, 1–8.

Johansson, B., 1992. Runoff calculations in ungauged catchments - An evaluation of the Pulse model. Vatten 48, 111–116.

Joyce, R.J., Janowiak, J.E., Arkin, P.A., Xie, P., 2004. CMORPH: A Method that Produces Global Precipitation Estimates from Passive Microwave and Infrared Data at High Spatial and Temporal Resolution. J. Hydrometeorol. 5, 487–503. https://doi.org/10.1175/1525-7541(2004)005<0487:CAMTPG>2.0.CO;2

Joyce, R.J., Xie, P., 2011. Kalman filter-based CMORPH. J. Hydrometeorol. 12, 1547–1563. https://doi.org/10.1175/JHM-D-11-022.1

Keith Beven, Andrew Binley, 1992. The future of distributed models: Model calibration and uncertainty prediction. Hydrol. Process. 6, 279–298.

Kendall, M.G., 1970. Rank correlation methods, 4th ed. Charles Griffin, London, England.

Kendall, M.G., 1938. A new measure of rank correlation. Biometrika 30, 81–93. https://doi.org/10.2307/2332226

Khomsi, K., Mahe, G., Tramblay, Y., Sinan, M., Snoussi, M., Hassania, E., 2016. Regional impacts of global change : seasonal trends in extreme rainfall , run-off and temperature in two contrasting regions of Morocco. Nat. Hazards Earth Syst. Sci. 16, 1079–1090. https://doi.org/10.5194/nhess-16-1079-2016

Kidd, C., 2018. Algorithm Theoretical Basis Document (ATBD) Version 01-02 NASA Global Precipitation Measurement (GPM) Precipitation Retrieval and Profiling Scheme (PRPS) Prepared for : Prepared by : (No. 01–02). Greenbelt, USA.

Klemeš, V., 1986. Operational testing of hydrological simulation models. Hydrol. Sci. J. 31, 13–24. https://doi.org/10.1080/02626668609491024

Knippertz, P., Christoph, M., Speth, P., 2003. Long-term precipitation variability in Morocco and the link to the large-scale circulation in recent and future climates. Meteorol. Atmos. Phys. 83, 67–88. https://doi.org/10.1007/s00703-002-0561-y

Koivusalo, H., 2003. Process-oriented investigation of snow accumulation, snowmelt and runoff generation in forested sites in Finland.

Krajewski, W.F., Smith, J.A., 1991. On the Estimation of Climatological Z–R Relationships. J. Appl. Meteorol. 30, 1436–1445. https://doi.org/10.16309/j.cnki.issn.1007-1776.2003.03.004

Krysanova, V., Bronstert, A., Müller-wohlfeil, D.-I., 1999. Modelling river discharge for large drainage basins : from lumped to distributed approach. Hydrol. Sci. J. 44, 313–331. https://doi.org/10.1080/02626669909492224

Kummerow, C., Barnes, W., Kozu, T., Shiue, J., Simpson, J., 1998. The tropical rainfall measuring mission(TRMM) sensor package. J. Atmos. Ocean. Technol. 15, 809–817. https://doi.org/10.1175/1520-0426(1998)015<0809:TTRMMT>2.0.CO;2

Kummerow, C., Hong, Y., Olson, W.S., Yang, S., Adler, R.F., McCollum, J., Ferraro, R., Petty, G., Shin, D.B., Wilheit, T.T., 2001. The evolution of the Goddard profiling algorithm (GPROF) for rainfall estimation from passive microwave sensors. J. Appl. Meteorol. 40, 1801–1820. https://doi.org/10.1175/1520-0450(2001)040<1801:TEOTGP>2.0.CO;2

Kummerow, C., Simpson, J., Thiele, O., Barnes, W., Chang, a. T.C., Stocker, E., Adler, R.F., Hou, a., Kakar, R., Wentz, F., Ashcroft, P., Kozu, T., Hong, Y., Okamoto, K., Iguchi, T., Kuroiwa, H., Im, E., Haddad, Z., Huffman, G., Ferrier, B., Olson, W.S., Zipser, E., Smith, E. a., Wilheit, T.T., North, G., Krishnamurti, T., Nakamura, K., 2000. The Status of the Tropical Rainfall Measuring Mission (TRMM) after Two Years in Orbit. J. Appl. Meteorol. 39, 1965–1982. https://doi.org/10.1175/1520-0450(2001)040<1965:TSOTTR>2.0.CO;2

Lafon, T., Dadson, S., Buys, G., Prudhomme, C., 2013. Bias correction of daily precipitation simulated by a regional climate model: A comparison of methods. Int. J. Climatol. 33, 1367–1381. https://doi.org/10.1002/joc.3518

Lamb, P.J., Peppler, R.A., 1987. North atlantic oscillation: concept and an application. Am. Meteorol. Soc. https://doi.org/10.1175/1520-0477(1987)068<1218:NAOCAA>2.0.CO;2

Lebrini, Y., Boudhar, A., Hadria, R., Lionboui, H., Elmansouri, L., Arrach, R., Ceccato, P., Benabdelouahab, T., 2019. Identifying Agricultural Systems Using SVM Classification Approach Based on Phenological Metrics in a Semi-arid Region of Morocco. Earth Syst. Environ. 3, 277–288. https://doi.org/10.1007/s41748-019-00106-z

Ledesma, J.L.J., Futter, M.N., 2017. Gridded climate data products are an alternative to instrumental measurements as inputs to rainfall – runoff models. Hydrol. Process. 31, 3283–3293. https://doi.org/10.1002/hyp.11269

Lee, S., Klein, A.G., Over, T.M., 2005. A comparison of MODIS and NOHRSC snow-cover products for simulating

streamflow using the Snowmelt Runoff Model. Hydrol. Process. 19, 2951–2972. https://doi.org/10.1002/hyp.5810

Legates, D.R., McCabe Jr., G.J., 1999. Evaluating the use of "Goodness of Fit" measures in hydrologic and hydroclimatic model validation. Water Resour. Res. 35, 233–241. https://doi.org/10.1029/1998WR900018

Lenderink, G., Buishand, A., Van Deursen, W., 2007. Estimates of future discharges of the river Rhine using two scenario methodologies: Direct versus delta approach. Hydrol. Earth Syst. Sci. 11, 1145–1159. https://doi.org/10.5194/hess-11-1145-2007

Li, C.Z., Wang, H., Liu, J., Yan, D.H., Yu, F.L., Zhang, L., 2010. Effect of calibration data series length on performance and optimal parameters of hydrological model. Water Sci. Eng. 3, 378–393. https://doi.org/10.3882/j.issn.1674-2370.2010.04.002

Li, F., Zhang, G., Xu, Y.J., 2014. Spatiotemporal variability of climate and streamflow in the Songhua River Basin, northeast China. J. Hydrol. 514, 53–64. https://doi.org/10.1016/j.jhydrol.2014.04.010

Li, L., Shen, H., Dai, S., Li, H., Xiao, J., 2013. Response of water resources to climate change and its future trend in the source region of the Yangtze River. J. Geogr. Sci. 23, 208–218. https://doi.org/10.1007/s11442-013-1004-z

Li, X., Williams, M.W., 2008. Snowmelt runoff modelling in an arid mountain watershed , Tarim Basin , China. Hydrol. Process. 3940, 3931–3940. https://doi.org/10.1002/hyp

Liang, X., Lettenmaier, D.P., Wood, E.F., Burges, S.J., 1994. A simple hydrologically based model of land surface water and energy fluxes for general circulation model. J. Geophys. Res. 99, 14415–14428.

Lindström, G., Johansson, B., Persson, M., Gardelin, M., Bergström, S., 1997. Development and test of the distributed HBV-96 hydrological model. J. Hydrol. 201, 272–288. https://doi.org/10.2166/wst.2009.488

Lionboui, H., Benabdelouahab, T., Elame, F., Hasib, A., Boulli, A., 2016a. Multi-year agro-economic modelling for predicting changes in irrigation water management indicators in the Tadla sub-basin. Int. J. Agric. Manag. 5, 96–105. https://doi.org/https://doi.org/10.5836/ijam/2016-05-96

Lionboui, H., Benabdelouahab, T., Hasib, A., Boulli, A., 2016b. Analysis of Farms Performance Using Different Sources of Irrigation Water : A Case Study in a Semi-Arid Area. Int. J. Agric. Manag. Dev. 6, 145–154.

Liu, S., Yan, D., Qin, T., Weng, B., Li, M., 2016. Correction of TRMM 3B42V7 Based on Linear Regression Models over China. Adv. Meteorol. 2016, 13–17. https://doi.org/10.1155/2016/3103749

Liu, X., Xu, Z., Yu, R., 2011. Trend of climate variability in China during the past decades. Clim. Change 109, 503–516. https://doi.org/10.1007/s10584-011-0097-6

Love, T.B., Kumar, V., Xie, P.P., Thiaw, W., 2004. A 20-year daily Africa precipitation climatology using satellite and gauge data, in: AMS Conference on Applied ClimatologyBulletin of The. pp. 5213–5216.

Lu, H., Bryant, R.B., Buda, A.R., Collick, A.S., Folmar, G.J., Kleinman, P.J.A., 2015. Long-term trends in climate and hydrology in an agricultural, headwater watershed of central Pennsylvania, USA. J. Hydrol. Reg. Stud. 4, 713–731. https://doi.org/10.1016/j.ejrh.2015.10.004

Lucchesi, R., 2018. File Specification for GEOS FP (No. GMAO Office Note No. 4 (Version 1.2)). Greenbelt, USA.

Luo, M., Liu, T., Meng, F., Duan, Y., Frankl, A., Bao, A., De Maeyer, P., 2018. Comparing bias correction methods used in downscaling precipitation and temperature from regional climate models: A case study from the Kaidu River Basin in Western China. Water 10, 1–21. https://doi.org/10.3390/w10081046

Luthcke, S.B., Sabaka, T.J., Loomis, B.D., Arendt, A.A., McCarthy, J.J., Camp, J., 2013. Antarctica, Greenland and Gulf of Alaska land-ice evolution from an iterated GRACE global mascon solution. J. Glaciol. 59, 613–631. https://doi.org/10.3189/2013JoG12J147

Ma, Q., Li, Y., Feng, H., Yu, Q., Zou, Y., Liu, F., Pulatov, B., 2020. Performance evaluation and correction of precipitation data using the 20-year IMERG and TMPA precipitation products in diverse subregions of China. Atmos. Res. 249, 105304. https://doi.org/10.1016/j.atmosres.2020.105304

Macritchie, K., 2015. README Document for the Tropical Rainfall Measurement Mission (TRMM) (No. 610.2). Greenbelt, USA.

Mann, H.B., 1945. Nonparametric tests against trend. Econometrica 13, 245–259. https://doi.org/10.2307/1907187

Mantas, V.M., Liu, Z., Caro, C., Pereira, A.J.S.C., 2014. Validation of TRMM multi-satellite precipitation analysis (TMPA) products in the Peruvian Andes. Atmos. Res. 163, 132–145. https://doi.org/10.1016/j.atmosres.2014.11.012

Marchane, A., 2015. Outils spatiaux pour le suivi de la dynamique de la neige sur l'Atlas marocain : changement climatique et ressources en eau (Ph.D). Cadi Ayyad, Marrakech, Morocco.

Marchane, A., Jarlan, L., Hanich, L., Boudhar, A., Gascoin, S., Tavernier, A., Filali, N., Le Page, M., Hagolle, O., Berjamy, B., 2015. Assessment of daily MODIS snow cover products to monitor snow cover dynamics over the Moroccan Atlas mountain range. Remote Sens. Environ. 160, 72–86. https://doi.org/10.1016/j.rse.2015.01.002

Mathevet, T., 2005. Quels modèles pluie-débit globaux au pas de temps horaire ? Développements empiriques et comparaison de modèles sur un large échantillon de bassins versants.

Mckee, T.B., Doesken, N.J., Kleist, J., 1993. The relationship of drought frequency and duration to time scales. AMS 8th Conf. Appl. Climatol. 179–184. https://doi.org/citeulike-article-id:10490403

MEMEE, 2008. Etude pour la réalisation d'une cartographie et d'un système d'information géographique sur les risques majeurs au Maroc. Rabat, Maroc.

Mendez, M., Maathuis, B., Hein-Griggs, D., Alvarado-Gamboa, L.F., 2020. Performance evaluation of bias correction methods for climate change monthly precipitation projections over Costa Rica. Water (Switzerland) 12. https://doi.org/10.3390/w12020482

Merz, R., Parajka, J., Blöschl, G., 2011. Time stability of catchment model parameters: Implications for climate impact analyses. Water Resour. Res. 47, 1–17. https://doi.org/10.1029/2010WR009505

Milewski, A., Elkadiri, R., Durham, M., 2015. Assessment and Comparison of TMPA Satellite Precipitation Products in Varying Climatic and Topographic Regimes in Morocco. Remote Sens. 7, 5697–5717. https://doi.org/10.3390/rs70505697

Mokhtari, N., Mrabet, R., Lebailly, P., Bock, L., 2013. Spatialisation des bioclimats, de l'aridité et des étages de végétation du Maroc. Rev. Marocaine des Sci. Agron. Vétérinaires 2, 50–66.

Moniod, F., Roche, M., 1973. Étude hydrologicpe de l'Oum Er-Rbia. Cah. l'ORSTOM série Hydrol. 10, 153–170.

Moriasi, D.N., Arnold, J.G., Liew, M.W. Van, Bingner, R.L., Harmel, R.D., Veith, T.L., 2007. Model evaluation guidelines for systematic quantification of accuracy in watershed simulations. Am. Soc. Agric. Biol. Eng. 50, 885–900.

Mougou, R., Mansour, M., Iglesias, A., Chebbi Zitouna, R., Battaglini, A., 2011. Climate change and agricultural vulnerability: a case study of rain-fed wheat in Kairouan, Central Tunisia. Reg. Environ. Chang. 11, 137–142. https://doi.org/https://doi.org/10.1007/s10113-010-0179-4

Muñoz, E.A., Paola, F. Di, Lanfri, M.A., Arteaga, F.J., 2016. Observing the Troposphere through the Advanced Microwave Technology Sensor (ATMS) to Retrieve Rain Rate 586–594.

NASA, 2003. Studying the Earth's Gravity from Space : The Gravity Recovery and Climate Experiment (GRACE) (No. FS-2002-1-029-GSFC). Greenbelt, USA.

NASA, 2002. GRACE Launch Press Kit. Washington, USA.

NASDA, 2001. TRMM Users Handbook. Earth Observation Center.

Nashwan, M.S., Shahid, S., Dewan, A., Ismail, T., 2019. Performance of five high resolution satellite-based precipitation products in arid region of Egypt : An evaluation. Atmos. Res. 236, 104809. https://doi.org/10.1016/j.atmosres.2019.104809

Navas, A., Machin, J., Gaspar, L., Sadiki, A., Kabiri, L., Faleh, A., 2013. Les sols dans le pays du Ziz (Sud-est marocain) Caractéristiques et aspects de dégradation. Fès, Maroc.

Novella, N.S., Thiaw, W.M., 2013. African rainfall climatology version 2 for famine early warning systems. J. Appl. Meteorol. Climatol. 52, 588–606. https://doi.org/10.1175/JAMC-D-11-0238.1

NRCAN, 2019. Remote Sensing Tutorials [WWW Document]. URL https://www.nrcan.gc.ca/maps-tools-publications/satellite-imagery-air-photos/tutorial-fundamentals-remote-sensing/9309

Oki, T., Sud, Y.C., 1998. Design of Total Runoff Integrating Pathways (TRIP)—A Global River Channel Network. Earth Interact. 2, 1–36. https://doi.org/10.1175/1087-3562(1998)002<0001:dotrip>2.3.co;2

OMM, 1994. Guide Des Pratiques Hydrologiques Omm-N° 168. Organisation météorologique mondiale.

Orth, R., Staudinger, M., Seneviratne, S.I., Seibert, J., Zappa, M., 2015. Does model performance improve with complexity? A case study with three hydrological models. J. Hydrol. 523, 147–159.

https://doi.org/10.1016/j.jhydrol.2015.01.044

Osuch, M., Romanowicz, R.J., Booij, M.J., 2015. The influence of parametric uncertainty on the relationships between HBV model parameters and climatic characteristics. Hydrol. Sci. J. 60, 1299–1316. https://doi.org/10.1080/02626667.2014.967694

Ouatiki, H., Boudhar, A., Tramblay, Y., Jarlan, L., Benabdelouhab, T., Hanich, L., El Meslouhi, M., Chehbouni, A., 2017. Evaluation of TRMM 3B42 V7 Rainfall Product over the Oum Er Rbia Watershed in Morocco. Climate 5, 1–17. https://doi.org/10.3390/cli5010001

Oudin, L., 2005. Recherche d'un modèle d'évapotranspiration potentielle pertinent comme entrée d'un modèle pluie-débit global Ludovic Oudin To cite this version : HAL Id : pastel-00000931 POTENTIELLE PERTINENT COMME ENTREE D ' UN MODELE PLUIE-DEBIT GLOBAL.

Ouyang, S., Puhlmann, H., Wang, S., von Wilpert, K., Sun, O.J., 2014. Parameter uncertainty and identifiability of a conceptual semi-distributed model to simulate hydrological processes in a small headwater catchment in Northwest China. Ecol. Process. 3, 1–17. https://doi.org/10.1186/s13717-014-0014-9

Parra, V., Arumí, J.L., Muñoz, E., 2019. Identifying a Suitable Model for Low-Flow Simulation in Watersheds of South-Central Chile : A Study Based on a Sensitivity Analysis. Water 11, 1–18. https://doi.org/10.3390/w11071506

Parra, V., Fuentes-Aguilera, P., Muñoz, E., 2018. Identifying advantages and drawbacks of two hydrological models based on a sensitivity analysis: a study in two Chilean watersheds. Hydrol. Sci. J. 63, 1831–1843. https://doi.org/10.1080/02626667.2018.1538593

Penman, H.L., 1961. Weather, Plant and Soil Factors in Hydrology. Weather 16, 207–219. https://doi.org/10.1002/j.1477-8696.1961.tb01934.x

Perrin, C., 2000. Vers une amélioration d'un modèle global pluie-débit au travers d'une approche comparative. https://doi.org/10.1051/lhb/2002089

Petty, G.W., 1994. Physical retrievals of over-ocean rain rate from multichannel microwave imagery. Part I: Theoretical characteristics of normalized polarization and scattering indices. Meteorol. Atmos. Phys. 54, 79–99. https://doi.org/10.1007/BF01030053

Petty, G.W., Katsaros, K.B., 1992. The Response of the SSM/I to the Marine En- vironment. Part I: An Analytic Model for the Atmospheric Component of Observed Brightness Temperatures. J. Atmos. Ocean. Technol. 9, 746–761.

Physics, A., 2009. Prediction of Dry-Season Precipitation in Tropical West Africa and Its Relation to Forcing from the Extratropics 1064–1084. https://doi.org/10.1175/2009WAF2222221.1

Pilgrim, D.H., Chapman, T.G., Doran, D.G., 1988. Problèmes de la mise au point de modèles pluie-écoulement dans les régions arides et semi-arides. Hydrol. Sci. J. 33, 379–400. https://doi.org/10.1080/02626668809491261

Poméon, T., Jackisch, D., Diekkrüger, B., 2017. Evaluating the performance of remotely sensed and reanalysed precipitation data over West Africa using HBV light. J. Hydrol. 547, 222–235. https://doi.org/10.1016/j.jhydrol.2017.01.055

Pushpalatha, R., Perrin, C., Le, N., Andréassian, V., 2012. A review of efficiency criteria suitable for evaluating low-flow simulations. J. Hydrol. 420–421, 171–182. https://doi.org/10.1016/j.jhydrol.2011.11.055

Rango, A., Martinec, J., 1979. Application of a Snowmelt-Runoff Model Using Landsat Data. Nord. Hydrol. 10, 225–238.

Reichle, R.H., Koster, R.D., 2004. Bias reduction in short records of satellite soil moisture. Geophys. Res. Lett. 31, 2–5. https://doi.org/10.1029/2004GL020938

Rientjes, T.H.M., Muthuwatta, L.P., Bos, M.G., Booij, M.J., Bhatti, H.A., 2013. Multi-variable calibration of a semi-distributed hydrological model using streamflow data and satellite-based evapotranspiration. J. Hydrol. 505, 276–290. https://doi.org/10.1016/j.jhydrol.2013.10.006

Ritter, A., Muñoz-carpena, R., 2013. Performance evaluation of hydrological models : Statistical significance for reducing subjectivity in goodness-of-fit assessments. J. Hydrol. 480, 33–45. https://doi.org/10.1016/j.jhydrol.2012.12.004

Roar Saelthun, N., Aittoniemi, P., Bergström, S., 1998. Climate change impacts on runoff and hydropower in the Nordic countries Final report from the project "Climate change and energy production" (No. NEI-DK--3366).

Kobenhavn, Denmark.
Robinson, M., Wars, R.C., 2017. Hydrology : Principles and processes, 1st ed. IWA, London, United Kingdom.
Rozante, J.R., Moreira, D.S., de Goncalves, L.G.G., Vila, D. a., 2010. Combining TRMM and Surface Observations of Precipitation: Technique and Validation over South America. Weather Forecast. 25, 885–894. https://doi.org/10.1175/2010WAF2222325.1
Samuel, J., Coulibaly, P., Metcalfe, R.A., 2012. Identification of rainfall-runoff model for improved baseflow estimation in ungauged basins. Hydrol. Process. 26, 356–366. https://doi.org/10.1002/hyp.8133
Saouabe, T., El Khalki, E.M., Saidi, M.E.M., Najmi, A., Hadri, A., Rachidi, S., Jadoud, M., Tramblay, Y., 2020. Evaluation of the GPM-IMERG precipitation product for flood modeling in a semi-arid mountainous basin in Morocco. Water (Switzerland) 12. https://doi.org/10.3390/w12092516
Satgé, F., Defrance, D., Sultan, B., Bonnet, M., Seyler, F., Rouché, N., Pierron, F., Paturel, J., 2020. Evaluation of 23 gridded precipitation datasets across West Africa. J. Hydrol. 581, 1–19. https://doi.org/10.1016/j.jhydrol.2019.124412
Satgé, F., Ruelland, D., Bonnet, M., Molina, J., Pillco, R., 2019. Consistency of satellite-based precipitation products in space and over time compared with gauge observations and snow- hydrological modelling in the Lake Titicaca region. Hydrol. Earth Syst. Sci. 23, 595–619.
Save, H., Bettadpur, S., Tapley, B.D., 2016. High-resolution CSR GRACE RL05 mascons. J. Geophys. Res. Solid Earth 121, 7547–7569. https://doi.org/10.1002/2016JB013007
Schilling, J., Freier, K.P., Hertig, E., Scheffran, J., 2012. Climate change, vulnerability and adaptation in North Africa with focus on Morocco. Agric. Ecosyst. Environ. 156, 12–26. https://doi.org/10.1016/j.agee.2012.04.021
Seibert, J., 2005. HBV light version 2 User's Manual. Stockholm, Sweden.
Seibert, J., 1999. Regionalisation of parameters for a conceptual rainfall-runoff model. Agric. For. Meteorol. 98, 279–293.
Seibert, J., 1997. Estimation of parameter uncertainty in the HBV model. Nord. Hydrol. 28, 247–262.
Seibert, J., Beven, K.J., 2009. Gauging the ungauged basin : how many discharge measurements are needed ? Hydrol. Earth Syst. Sci. 13, 883–892.
Sen, P.K., 1968. Estimates of the Regression Coefficient Based on Kendall'S Tau. J. Am. Stat. Assoc. 63, 1379–1389. https://doi.org/http://dx.doi.org/10.1080/01621459.1968.10480934
Serrat-capdevila, A., Merino, M., Valdes, J.B., Durcik, M., 2016. Evaluation of the Performance of Three Satellite Precipitation Products over Africa. Remote Sens. 8, 836. https://doi.org/10.3390/rs8100836
Shen, H., Leblanc, M., Tweed, S., Liu, W., 2015. Groundwater depletion in the Hai River Basin, China, from in situ and GRACE observations. Hydrol. Sci. J. 60, 671–687. https://doi.org/10.1080/02626667.2014.916406
Singh, J., Knapp, H.V., Demissie, M., 2004. Hydrologic Modeling of the Iroquois River Watershed Using HSPF and SWAT (No. 2004– 08). Illinois, USA.
Sorman, A.A., Sensoy, A., Tekeli, A.E., Sorman, A.Ü., Akyurek, Z., 2009. Modelling and forecasting snowmelt runoff process using the HBV model in the eastern part of Turkey. Hydrol. Process. 23, 1031–1040. https://doi.org/10.1002/hyp
Sorooshian, S., 1983. Evaluation of Maximum Likelihood Parameter Estimation Techniques for and Length on Model Credibility. Water Resour. Res. 19, 251–259.
Sorooshian, S., Gupta, V.K., 1983. Automatic calibration of conceptual rainfall-runoff models: The question of parameter observability and uniqueness. Water Resour. Res. 19, 260–268. https://doi.org/10.1029/WR019i001p00260
Sorooshian, S., Hsu, K.L., Gao, X., Gupta, H. V., Imam, B., Braithwaite, D., 2000. Evaluation of PERSIANN system satellite-based estimates of tropical rainfall. Bull. Am. Meteorol. Soc. 81, 2035–2046. https://doi.org/10.1175/1520-0477(2000)081<2035:EOPSSE>2.3.CO;2
Sousa, P.M., Trigo, R.M., Aizpurua, P., Nieto, R., Gimeno, L., Garcia-Herrera, R., 2011. Trends and extremes of drought indices throughout the 20th century in the Mediterranean. Nat. Hazards Earth Syst. Sci. 11, 33–51. https://doi.org/10.5194/nhess-11-33-2011

Stahl, K., Moore, R.D., Shea, J.M., Hutchinson, D., Cannon, A.J., 2008. Coupled modelling of glacier and streamflow response to future climate scenarios. Water Resour. Res. 44, 1–13. https://doi.org/10.1029/2007WR005956

Stout, J.E., Martin, D.W., Sikdar, D.N., 1979. Estimating GATE rainfall with geosynchronous satellite images. Mon. Weather Rev. 107, 585–598.

Tang, G., Clark, M.P., Michael, S., Ma, Z., Hong, Y., 2020. Have satellite precipitation products improved over last two decades? A comprehensive comparison of GPM IMERG with nine satellite and reanalysis datasets. Remote Sens. Environ. 240, 111697. https://doi.org/10.1016/j.rse.2020.111697

Tapley, B.D., Bettadpur, S., Watkins, M.M., Reigber, C., 2004. The gravity recovery and climate experiment: Mission overview and early results. Geophys. Res. Lett. 31, 1–4. https://doi.org/10.1029/2004GL019920

Tapley, B.D., Watkins, M.M., Flechtner, F., Reigber, C., Bettadpur, S., Rodell, M., Sasgen, I., Famiglietti, J.S., Landerer, F.W., Chambers, D.P., Reager, J.T., Gardner, A.S., Save, H., Ivins, E.R., Swenson, S.C., Boening, C., Dahle, C., Wiese, D.N., Dobslaw, H., Tamisiea, M.E., Velicogna, I., 2019. Contributions of GRACE to understanding climate change. Nat. Clim. Chang. 9, 358–369. https://doi.org/10.1038/s41558-019-0456-2

Teegavarapu, R.S.V., 2012. Hydrologic modeling and design, in: Floods in a Changing Climate: Extreme Precipitation, International Hydrology Series. Cambridge University Press, Cambridge, England, pp. 225–240. https://doi.org/DOI: 10.1017/CBO9781139088442.010

Terêncio, D.P.S., Sanches Fernandes, L.F., Cortes, R.M.V., Moura, J.P., Pacheco, F.A.L., 2018. Rainwater harvesting in catchments for agro-forestry uses: A study focused on the balance between sustainability values and storage capacity. Sci. Total Environ. 613–614, 1079–1092. https://doi.org/10.1016/j.scitotenv.2017.09.198

Terêncio, D.P.S., Sanches Fernandes, L.F., Cortes, R.M.V., Pacheco, F.A.L., 2017. Improved framework model to allocate optimal rainwater harvesting sites in small watersheds for agro-forestry uses. J. Hydrol. 550, 318–330. https://doi.org/10.1016/j.jhydrol.2017.05.003

Teutschbein, C., Grabs, T., Laudon, H., Karlsen, R.H., Bishop, K., 2018. Simulating streamflow in ungauged basins under a changing climate: The importance of landscape characteristics. J. Hydrol. 561, 160–178. https://doi.org/10.1016/j.jhydrol.2018.03.060

Teutschbein, C., Seibert, J., 2012. Bias correction of regional climate model simulations for hydrological climate-change impact studies: Review and evaluation of different methods. J. Hydrol. 456–457, 12–29. https://doi.org/10.1016/j.jhydrol.2012.05.052

Thapa, B.R., Ishidaira, H., Pandey, V.P., Shakya, N.M., 2017. A multi-model approach for analyzing water balance dynamics in Kathmandu Valley, Nepal. J. Hydrol. Reg. Stud. 9, 149–162. https://doi.org/10.1016/j.ejrh.2016.12.080

Theil, H., 1950. A rank-invariant method of linear and polynomial regression analysis. I, II, III. Ned. Akad. van Wet. Proc. 53, 386–392, 521–525, 1397–1412.

Thornthwaite, C.W., 1948. An Approach toward a Rational Classification of Climate. Geogr. Rev. 38, 55–94.

Todini, E., 1996. The ARNO rainfall-runoff model. J. Hydrol. 175, 339–382. https://doi.org/10.1016/S0022-1694(96)80016-3

Tramblay, Y., El Adlouni, S., Servat, E., 2013. Trends and variability in extreme precipitation indices over Maghreb countries. Nat. Hazards Earth Syst. Sci. 13, 3235–3248. https://doi.org/10.5194/nhess-13-3235-2013

Tramblay, Y., Thiemig, V., Dezetter, A., Hanich, L., 2016. Evaluation of satellite-based rainfall products for hydrological modelling in Morocco. Hydrol. Sci. J. 61, 2509–2519. https://doi.org/10.1080/02626667.2016.1154149

Tripp, D.R., Niemann, J.D., 2008. Evaluating the parameter identifiability and structural validity of a probability-distributed model for soil moisture. J. Hydrol. 353, 93–108. https://doi.org/10.1016/j.jhydrol.2008.01.028

Uhlenbrook, S., Holocher, J., Leibundgut, C., Seibert, J., 1998. Using a conceptual rainfall-runoff model on different scales by comparing a headwater with larger basins, in: Hydrology, Water Resources and Ecology in Headwaters. IAHS Publ. 248, Meran/Merano, Italy, pp. 297–305.

Uhlenbrook, S., Seibert, J., Leibundgut, C., Rodhe, A., 1999. Prediction uncertainty of conceptual rainfall- runoff models caused by problems in identifying model parameters and structure. Hydrol. Sci. J. 44, 779–797. https://doi.org/10.1080/02626669909492273

USAID, 2010. Morocco economic competitiveness Moulouya and Oum Er-Rbia watersheds: organizational it and

management system needs. Rabat, Morocco.
Vandewiele, G.L., Xu, C.Y., Ni-Lar-Win, 1992. Methodology and comparative study of monthly water balance models in Belgium, China and Burma. J. Hydrol. 134, 315–347. https://doi.org/10.1016/0022-1694(92)90041-S
Vehviläinen, B., Lohvansuu, J., 1991. The effects of climate change on discharges and snow cover in Finland. Hydrol. Sci. J. 36, 109–121. https://doi.org/10.1080/02626669109492493
Viessman, W.J., Lewis, G.L., 1996. Introduction to Hydrology, 4th ed. HarperCollins College, New York, USA.
Vila, D.A., de Goncalves, L.G.G., Toll, D.L., Rozante, J.R., 2009. Statistical Evaluation of Combined Daily Gauge Observations and Rainfall Satellite Estimates over Continental South America. J. Hydrometeorol. 10, 533–543. https://doi.org/10.1175/2008JHM1048.1
Viviroli, D., Zappa, M., Schwanbeck, J., Gurtz, J., Weingartner, R., 2009. Continuous simulation for flood estimation in ungauged mesoscale catchments of Switzerland – Part I : Modelling framework and calibration results. J. Hydrol. 377, 191–207. https://doi.org/10.1016/j.jhydrol.2009.08.023
Wang, Y., Xie, X., Meng, S., Wu, D., Chen, Y., Jiang, F., Zhu, B., 2020. Magnitude Agreement , Occurrence Consistency , and Elevation Dependency of Satellite-Based Precipitation Products over the Tibetan Plateau. Remote Sens. 12, 1750.
Watkins, M.M., Wiese, D.N., Yuan, D.-N., Boening, C., Landerer, F.W., 2015. Improved methods for observing Earth's time variable mass distribution with GRACE using spherical cap mascons. J. Geophys. Res. Solid Earth 120, 2648–2671. https://doi.org/10.1002/2014JB011547.
Weng, F., Zhao, L., Ferraro, R.R., Poe, G., Li, X., Grody, N.C., 2003. Advanced microwave sounding unit cloud and precipitation algorithms. Radio Sci. 38, 1–13. https://doi.org/10.1029/2002rs002679
Wilk, J., Hughes, D.A., 2002. Calibrating a rainfall-runoff model for a catchment with limited data. Hydrol. Sci. J. 47, 3–17. https://doi.org/10.1080/02626660209492903
Wilks, D.S., 2006. Statistical methods in the atmospheric sciences, International Geophysics Series. Elsevier. https://doi.org/10.1002/met.16
Willmott, C.J., 2013. On the validation of models. Phys. Geogr. 2, 37–41. https://doi.org/10.1080/02723646.1981.10642213
Willmott, C.J., Ackleson, S.G., Davis, R.E., Feddema, J.J., Klink, K.M., Legates, D.R., O'Donnell, J., Rowe, C.M., 1985. Statistics for the evaluation and comparison of models. J. Geophys. Res. 90, 8995. https://doi.org/10.1029/JC090iC05p08995
WMO-UNESCO, 2012. International Glossary of Hydrology, 3rd ed, WMO-No. 385. WMO-UNESCO, Geneva, Switzerland.
WMO, 2012. Standardized precipitation index user guide, WMO-No. 10. ed. Geneva. https://doi.org/10.1175/2007JCLI1348.1
WMO, 2008a. Guide to Hydrological Practices : Hydrology – From Measurement to Hydrological Information, 6th ed, WMO-No. 168. World Meteorological Organization, Geneva, Switzerland. https://doi.org/10.1017/CBO9781107415324.004
WMO, 2008b. Guide to Meteorological Instruments and Methods of Observation, 2008th ed, WMO-No. 8. Geneva, Switzerland. https://doi.org/10.1017/cbo9780511794285.002
WMO, GWP, 2016. Handbook of drought indicators and indices, WMO-No. 11. ed. Geneva. https://doi.org/10.1007/s00704-016-1984-6
Xia, Y., Yang, Z.-L., Jackson, C., Stoffa, P.L., Sen, M.K., 2004. Impacts of data length on optimal parameter and uncertainty estimation of a land surface model. J. Geophys. Res. 109, 1–13. https://doi.org/10.1029/2003jd004419
Xiang Soo, E.Z., Wan Jaafar, W.Z., Lai, S.H., Othman, F., Elshafie, A., Islam, T., Srivastava, P., Othman Hadi, H.S., 2020. Evaluation of bias-adjusted satellite precipitation estimations for extreme flood events in Langat river basin, Malaysia. Hydrol. Res. 51, 105–126. https://doi.org/10.2166/nh.2019.071
Xie, P., Arkin, P.A., 1996. Analyses of Global Monthly Precipitation Using Gauge Observations, Satellite Estimates, and Numerical Model Predictions. J. Climatol. 9, 840-858. https://doi.org/10.1017/CBO9781107415324.004
Xie, P., Joyce, R., Wu, S., Yoo, S.H., Yarosh, Y., Sun, F., Lin, R., 2017. Reprocessed, bias-corrected CMORPH global

high-resolution precipitation estimates from 1998. J. Hydrometeorol. 18, 1617–1641. https://doi.org/10.1175/JHM-D-16-0168.1

Xoplaki, E., González-Rouco, J.F., Luterbacher, J., Wanner, H., 2004. Wet season Mediterranean precipitation variability: influence of large-scale dynamics and trends. Clim. Dyn. 23, 63–78. https://doi.org/10.1007/s00382-004-0422-0

Xu, H., Xu, C., Chen, H., Zhang, Z., Li, L., 2013. Assessing the influence of rain gauge density and distribution on hydrological model performance in a humid region of China Hongliang. J. Hydrol. 505, 1–12. https://doi.org/10.1016/j.jhydrol.2013.09.004

Xue, X., Hong, Y., Limaye, A.S., Gourley, J.J., Huffman, G.J., Khan, S.I., Dorji, C., Chen, S., 2013. Statistical and hydrological evaluation of TRMM-based Multi-satellite Precipitation Analysis over the Wangchu Basin of Bhutan: Are the latest satellite precipitation products 3B42V7 ready for use in ungauged basins? J. Hydrol. 499, 91–99. https://doi.org/10.1016/j.jhydrol.2013.06.042

Yeggina, S., Teegavarapu, R.S.V., Muddu, S., 2020. Evaluation and bias corrections of gridded precipitation data for hydrologic modelling support in Kabini River basin, India. Theor. Appl. Climatol. 140, 1495–1513. https://doi.org/10.1007/s00704-020-03175-7

Yeh, N.C., Chuang, Y.C., Peng, H.S., Hsu, K.L., 2020. Bias Adjustment of Satellite Precipitation Estimation Using Ground-Based Observation: Mei-Yu Front Case Studies in Taiwan. Asia-Pacific J. Atmos. Sci. 56, 485–492. https://doi.org/10.1007/s13143-019-00152-7

Zad, S.N.M., Zulkafli, Z., Muharram, F.M., 2018. Satellite Rainfall (TRMM 3B42-V7) Performance Assessment and Adjustment over Pahang River Basin, Malaysia. Remote Sens. 10, 388. https://doi.org/10.3390/rs10030388

Zelelew, M.B., Alfredsen, K., 2013. Sensitivity-guided evaluation of the HBV hydrological model parameterization. J. Hydroinformatics 15, 967–990. https://doi.org/10.2166/hydro.2012.011

Zeng, Q., Chen, H., Xu, C.Y., Jie, M.X., Chen, J., Guo, S.L., Liu, J., 2018. The effect of rain gauge density and distribution on runoff simulation using a lumped hydrological modelling approach. J. Hydrol. 563, 106–122. https://doi.org/10.1016/j.jhydrol.2018.05.058

Zhao, L., Weng, F., 2002. Retrieval of ice cloud parameters using the advanced microwave sounding unit. J. Appl. Meteorol. 41, 384–395. https://doi.org/10.1175/1520-0450(2002)041<0384:ROICPU>2.0.CO;2

Zhao, R.J., 1992. The Xinanjiang model applied in China. J. Hydrol. 135, 371–381. https://doi.org/10.1016/0022-1694(92)90096-E

Zhuge, X.Y., Zou, X., Wang, Y., 2017. A Fast Cloud Detection Algorithm Applicable to Monitoring and Nowcasting of Daytime Cloud Systems. IEEE Trans. Geosci. Remote Sens. 55, 6111–6119. https://doi.org/10.1109/TGRS.2017.2720664